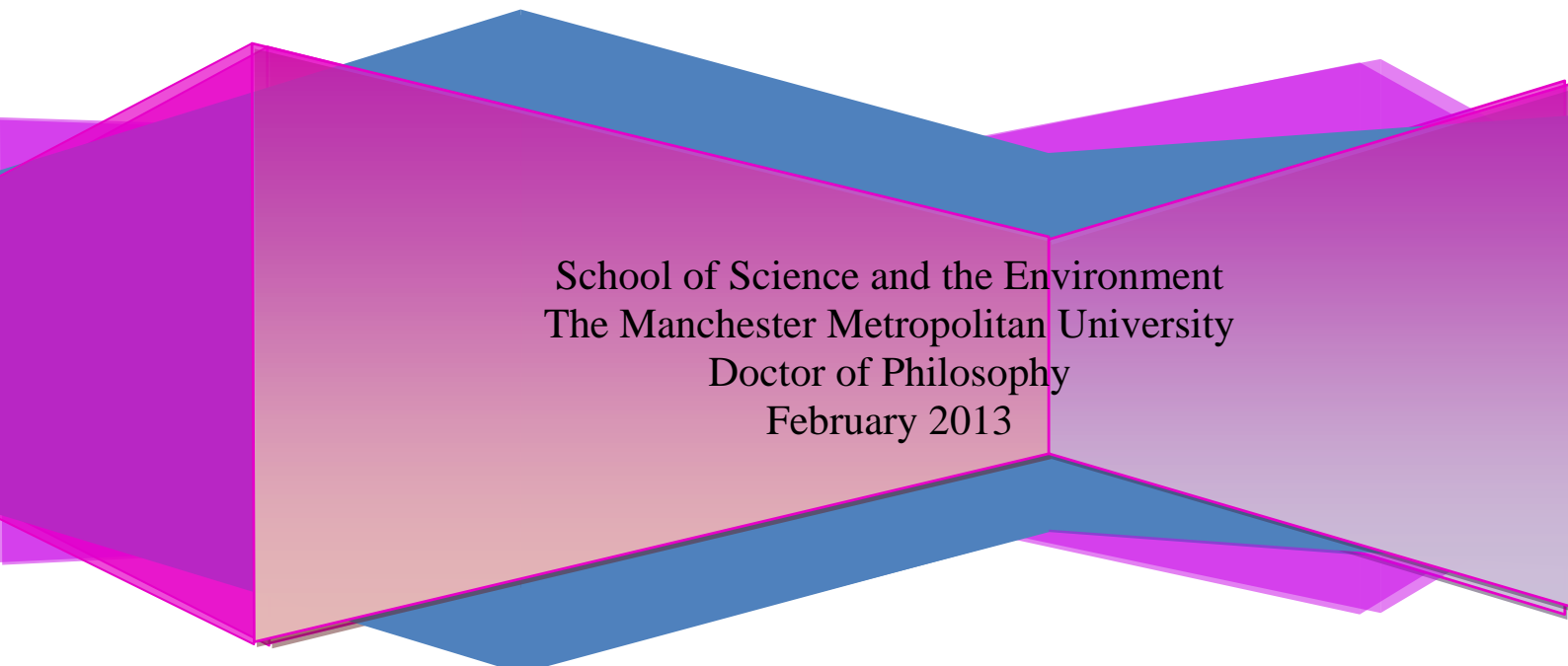


# **Preparation of Inorganic Nanoparticles for Sensor and Bioapplications**

**Asima Farooq**

**Supervised by Dr. D. Whitehead, Dr. M. Azzawi,  
Prof. P. Kelly and Dr. L. Tosheva**



School of Science and the Environment  
The Manchester Metropolitan University  
Doctor of Philosophy  
February 2013

# ***Table of Contents***

---

<i>Declaration</i> .....	I
<i>Ethical consideration for experimental animals</i> .....	II
<i>Dedication</i> .....	III
<i>Acknowledgments</i> .....	IV
<i>Publications</i> .....	V
<i>List of abbreviations</i> .....	VI
<i>List of figures</i> .....	IX
<i>List of equations</i> .....	XIX
<i>List of tables</i> .....	XX
<i>Abstract</i> .....	XXIII
<i>Aims and objectives</i> .....	XXIV
<i>Thesis structure</i> .....	XXV

## **CHAPTER 1. INTRODUCTION.....1**

1.1. Nanotechnology .....	1
1.2. Synthesis Methods of Silica Nanoparticles .....	2
1.2.1. Sol-gel method .....	3
1.2.1.1. Controlled growth of silica nanoparticles .....	5
1.2.2. Microemulsion method .....	7
1.3. Stability of Colloidal Silica .....	10
1.3.1. Stabilisation .....	12
1.3.1.1. Surface charge .....	12
1.3.1.1.1. Debye Landau Verwey Overbeek theory .....	14
1.3.1.1.2. Non-Debye Landau Verwey Overbeek interactions ...	16
1.3.1.1.3. Ion specificity .....	17
1.3.1.2. Surface stabilisation .....	17
1.3.1.2.1. Hairy model theory .....	18
1.4. Mesoporous Nanoparticles .....	18
1.4.1. M41S family .....	18
1.5. Characterisation .....	20
1.5.1. Electron Microscopy .....	20

1.5.1.1. Scanning electron microscopy.....	21
1.5.1.2. Transmission electron microscopy .....	22
1.5.2. Photon correlation spectroscopy.....	23
1.5.3. Laser Doppler Velocimetry .....	25
1.5.3.1. Electrical double layer.....	25
1.5.4. Diffuse reflectance infra-red Fourier transform spectroscopy.....	27
1.5.5. Thermogravimetric analysis .....	28
1.5.6. Nitrogen sorption.....	30
1.5.7. Atomic absorption spectroscopy.....	33
1.5.8. Fluorescence spectroscopy .....	35

## **CHAPTER 2. NANOPARTICLE PREPARATION.....37**

2.1. Amorphous Silica Nanoparticles via Sol-gel .....	39
2.1.1. Materials .....	39
2.1.2. Methodology.....	39
2.1.3. Physiological salt solution preparation.....	40
2.1.4. Characterisation .....	40
2.1.5. Results .....	41
2.1.6. Discussion.....	43
2.2. Dye Encapsulated Silica Nanoparticles via Sol-gel.....	44
2.2.1. Materials .....	44
2.2.2. Methodology.....	44
2.2.2.1. Sol-gel precipitation of fluorophore encapsulated silica nanoparticles.....	44
2.2.2.2. Direct coating of fluorophore encapsulated silica nanoparticles with silica shell by seeding technique .....	45
2.2.2.3. Functionalising silica nanoparticles with carboxylic acid groups ...	46
2.2.2.4. Quantifying the amount of fluorophore within the nanoparticles ...	47
2.2.3. Results .....	47
2.2.3.1. Nanoparticles prepared via the sol-gel method .....	47
2.2.3.2. Nanoparticle seeds coated with silica shell .....	49
2.2.4. Discussion.....	53
2.2.4.1. Nanoparticles prepared via the sol-gel method .....	53
2.2.4.2. Nanoparticle seeds coated with silica shell .....	53

2.3. Silica Nanoparticles via Microemulsion .....	55
2.3.1. Materials .....	55
2.3.2. Methodology .....	55
2.3.3. Characterisation .....	56
2.3.4. Results .....	56
2.3.5. Discussion.....	58
2.4. Mesoporous Nanoparticles.....	59
2.4.1. Materials .....	59
2.4.2. Methodology.....	59
2.4.2.1. RBITC encapsulated mesoporous nanoparticles: synthetic route 1 (sample 1) .....	59
2.4.2.2. Mesoporous nanoparticles: synthetic route 2 (sample 2-7).....	60
2.4.2.2.1. Silica mesoporous nanoparticles (sample 2-6) .....	60
2.4.2.2.2. Synthesis of mesoporous nanoparticles with RBITC dye (sample 7).....	61
2.4.2.3. Mesoporous nanoparticles: synthetic route 3 (sample 8-12).....	61
2.4.2.3.1. RBITC encapsulated mesoporous nanoparticles (sample 8).....	62
2.4.2.3.2. Mesoporous nanoparticles (sample 9) .....	62
2.4.2.3.3. RBITC encapsulated mesoporous nanoparticles (sample 10).....	63
2.4.2.3.4. FITC encapsulated mesoporous nanoparticles (sample 11).....	64
2.4.2.3.5. RBITC/ FITC encapsulated mesoporous nanoparticles (sample 12).....	65
2.4.3. Results .....	66
2.4.3.1. Quantification of dye molecules within the mesoporous nanoparticles .....	80
2.4.4. Discussion.....	82
2.5. Silicate-1 Nanoparticles .....	84
2.5.1. Materials .....	84
2.5.2. Methodology.....	84
2.5.3. Results .....	85
2.5.4. Discussion.....	88

**CHAPTER 3. APPLICATIONS.....89**

3.1. Introduction to Fluorescence Sensing .....	90
3.1.1. Fluorescence mechanics .....	90
3.1.2. Quenching modes .....	92
3.1.3. Intensity-based fluorescent sensor vs. lifetime .....	92
3.1.4. The Stern-Volmer relationship to dynamic quenching.....	93
3.2. Gas Sensor.....	95
3.2.1. Experimentation.....	102
3.2.1.1. Nanosensor film formation.....	102
3.2.1.2. Gas sensing techniques.....	102
3.2.2. Results and discussions .....	103
3.2.2.1. Dual gas sensor analysis.....	104
3.2.3. Conclusions .....	107
3.3. Introduction to the Bioapplications.....	108
3.3.1. Aortic vessel structure .....	109
3.3.2. Aortic vessel function and contractility .....	111
3.3.2.1. Vasoconstrictors .....	111
3.3.2.2. Vasodilators.....	113
3.3.3. Cellular uptake mechanisms of nanoparticles .....	116
3.4. Biocompatibility of Silica Nanoparticles .....	121
3.4.1. Experimentation.....	124
3.4.1.1. Tissue preparation .....	124
3.4.1.2. Organ-bath setup .....	125
3.4.1.3. Tissue fixation and processing .....	127
3.4.2. Results .....	128
3.4.2.1. Detection of silica nanoparticles within vascular tissue.....	128
3.4.2.2. Influence of silica nanoparticles on vasoconstrictor responses of aortic vessels.....	132
3.4.2.3. Aortic vessel responses to vasodilator agonists.....	133
3.4.2.4. Influence of silica nanoparticles on endothelium-dependent and independent vasodilator responses .....	135
3.4.2.5. Effect of nanoparticle number on vascular function .....	136
3.4.2.6. Effect of nanoparticle size on vascular function .....	138

3.4.2.7. Effect of dye encapsulated silica nanoparticle on vascular responses.....	139
3.4.2.8. Restoration of dilator response using SOD .....	141
3.4.3. Discussion.....	142
3.4.4. Conclusions .....	146
3.5. Pressurised System for the Aortic vessel .....	148
3.5.1. Experimentation.....	148
3.5.2. Results .....	150
3.5.2.1. Detection of silica nanoparticles within vascular tissue .....	150
3.5.2.2. Influence of silica nanoparticles on endothelium-dependent vasodilator responses .....	150
3.5.3. Discussion.....	151
3.5.4. Conclusions .....	152
3.6. Drug Release Study of Mesoporous Nanoparticles .....	153
3.6.1. Diffusion of drug release .....	156
3.6.2. Sodium nitroprusside .....	156
3.6.3. Experimentation.....	157
3.6.3.1. Materials .....	157
3.6.3.2. Release profile of sodium nitroprusside from mesoporous nanoparticles.....	157
3.6.3.2.1. Drug loading efficiency .....	159
3.6.3.2.2. Drug loading capacity .....	160
3.6.3.3. Release of sodium nitroprusside from mesoporous nanoparticles <i>in vitro</i> .....	160
3.6.4. Results .....	161
3.6.4.1. Detection of mesoporous nanoparticles within vascular tissue .....	161
3.6.4.2. Sodium nitroprusside release from mesoporous nanoparticles .....	161
3.6.4.3. Drug release study of sodium nitroprusside <i>in vitro</i> .....	164
3.6.5. Discussion.....	170
3.6.6. Conclusions .....	171

**CHAPTER 4. CONCLUSIONS..... 172**

4.1. Future work ..... 172

*References* ..... 174

*Appendix*..... 195

## *Declaration*

---

This thesis contains no material which has been accepted for the award of any other degree or diploma in any university, to the best of my knowledge and belief, contains no material previously published or written by another, except where due reference has been made in the text. In addition, no parts of this thesis have been copied from other sources. I understand that any evidence of plagiarism and/or the use of unacknowledged third party data will be dealt with as a very serious matter.

Signature: \_\_\_\_\_

Date: \_\_\_\_\_

## ***Ethical consideration for experimental animals***

---

The physiological functional experiments in this study were performed using animal tissue excised from dead animals (Male Wistar rats, 200-300 g in weight, aged 7-13 weeks), obtained from the BSU, University of Manchester. The Wistar rats were housed under standardised conditions (12 hour light/ dark cycles at 24 °C). The animals were humanely killed by stunning and cervical dislocation. All procedures are conducted in accordance with institutional guidelines of the MMU and the University of Manchester and the United Kingdom Animals (Scientific Procedures) Act of 1986 (schedule 1 killing- Experiments were performed with the approval of the Review Board of the University of Manchester and the Home Office. A risk assessment for the use and handling of animal tissue was conducted.

## ***Dedication***

---

This study is dedicated to my wonderful and loving father, Farooq Mahmud. Thank you for giving me the freedom and confidence to pursue my dreams, especially through the difficult times. *'I miss you every day'*

## *Acknowledgments*

---

The content within this thesis contains my research studies which has taken duration of four years. I am truly blessed for Allah (S.W.T) to have granted me the opportunity to conduct my research and for the successful completion. The Quran is the guidance to mankind which includes scientific facts that were only discovered in recent centuries. I am truly indebted to my beloved Prophet Muhammad (S.A.W), who 1400 years ago received guidance the first word revealed by Arch angel Gabriel “Iqra!” (Read). Study, discovery, research and endless learning are a beacon of light to a brighter future.

Firstly, I would like to express my heartfelt gratitude to my first supervisor Dr. Debra E. Whitehead. I was also fortunate enough to have the support and patience of my second supervisor Dr. May E. Azzawi without whom this research would not have been possible. They are my dearest supervisors who are truly inspirational and left a remarkable impression in my life.

I would also like to express my sincere gratitude to my co-supervisor Professor Peter Kelly and Dr. Lubomira Tosheva. Your research experience has provided me with a sound basis for developing research practices. I am deeply grateful for the technical help from Mr Dave Maskew, Mr Bill Ellison and Dr. Maira Guzman. I would like to thank Dr. Ramaier Narayanaswamy, Phil Roche and Raed Al-Jowder for the work we did in collaboration.

On a personal note, to my parents, a special thanks. Without them I would not be the person I am today, who have always encouraged me to aim high and follow my dreams, and without their constant support I would not be able to achieve my academic goals. Also, I am thankful for having a loving husband, Abbas, it takes a special person to tolerate the long hours and stress as a result of this thesis. I am also thankful to my dearly loved son, Saif, who I owe a lot of lost time and due to his young age it difficult for him to understand my relentless research work. Finally, I must thank my sisters, Saleena and Sara, and nephews, Junaid, Jamal and Jawad, for their moral support and encouragement over the past four years. I would like to thank my good friends Teba Mohamed, Rehana Akhtar and Ali Shukur for making a better and interesting laboratory experience. Thank you all for your love and support.

## ***Publications***

---

- Farooq, A., Whitehead, D. and Azzawi, M., '*Attenuation of endothelial dependent vasodilator responses, induced by dye encapsulated silica nanoparticles, in aortic vessels*', Future Medicine, 2012, in press.
- Farooq, A., Al-Jowder, R., Narayanaswamy, R., Azzawi, M., Roche, P. J. R. and Whitehead, D., '*Ultrasensitive gas detection using quenching fluorescence of dye-immobilized silica nanoparticles*', Sensors and Actuators B: Chemical, 2012, accepted minor revisions.

## *List of abbreviations*

---

Acetylcholine	ACh	Delayed rectifier potassium channels	K <sub>DR</sub>
Adaptor protein-2	AP2	Derivative thermogravimetric	DTG
Alkoxide silica	Si(OR) <sub>4</sub>	Diacylglycerol	DAG
(3-aminopropyl)triethoxy silane	APTES	Diffuse reflectance infra-red Fourier transform spectroscopy	DRIFTS
(3-aminopropyl)trimethoxy silane	APTMS	Dimethylformamide	DMF
Ammonium hydroxide	NH <sub>4</sub> OH	Drug loading capacity	DLC
Ammonium nitrate	NH <sub>4</sub> NO <sub>3</sub>	Drug loading efficiency	DLE
ATP-sensitive potassium channels	K <sub>ATP</sub>	Dynamic light scattering	DLS
Back-scattered electrons	BSE	Electrochemical double layer	EDL
Bradykinin	BK	Endothelium	ECs
Brunauer-Emmett-Teller	BET	Endothelium –delivered hyperpolarizing factor	EDHF
Calcium	Ca <sup>2+</sup>	Epoxyeicosatrienoic acids	EETs
Calcium chloride	CaCl <sub>2</sub> .2H <sub>2</sub> O	Ethanol	EtOH
Converting the binding protein	GTP	Ethylenediaminetetraacetic acid dipotassium salt dihydrate	K <sub>2</sub> EDTA.2H <sub>2</sub> O
Cyclic adenosine monophosphate	cAMP	Ethylene glycol	EG
Cyclic guanosine monophosphate	cGMP	Flame atomic absorption spectroscopy	FAAS
Cyclooxygenase	COX	Fluorescein isothiocyanate	FITC
Debye Landau Verwey Overbeek	DLVO	Graphite furnace atomic absorption spectroscopy	GFAAS

Hexadecyltrimethyl ammonium bromide	CTMAB	Nitric oxide synthase	NOS
Inductively coupled plasma mass spectroscopy	ICP-MS	<i>N<sub>ω</sub></i> -Nitro-L-arginine	L-NNA
Inductively coupled plasma optical emission spectroscopy	ICP-OES	Octyltriethoxy silane	OTEOS
Inner Helmholtz plane	IHP	Organically modified sol-gels	ormosil
Insitol triphosphate	IP <sub>3</sub>	Outer Helmholtz plane	OHP
Internal elastic lamina	IEL	Perivascular adipose tissue	PVAT
Isoelectric point	IEP	Phosphatidyl insitol diphosphate	PIP <sub>2</sub>
Isopropanol	IP	Phospholipase A <sub>2</sub>	PLA <sub>2</sub>
L-Arginine	L-Arg	Phospholipase C	PL-C
Laser Doppler velocimetry	LDV	Phospholipid	PL
L-Citruline	L-Cit	Photon Correlation Spectroscopy	PCS
Ligand centered	LC	Physiological salt solution	PSS
Magnesium sulphate heptahydrate	MgSO <sub>4</sub> .7H <sub>2</sub> O	Potassium channels	K <sub>CA</sub>
Mesoporous nanoparticles	MNP	Potassium chloride	KCl
Metal centered	MC	Potassium dihydrogen phosphate (monobasic)	KH <sub>2</sub> PO <sub>4</sub>
Metal-to-ligand-charge-transfer	MLCT	Potassium physiological salt solution	KPSS
Methanol	MeOH	Prostaglandin I <sub>2</sub>	PGI <sub>2</sub>
Methyltriethoxy silane	MTEOS	Protein kinase G	PKG
Nanoparticle	NP	Reactive oxygen species	ROS
Nanoparticles	NPs	Rhodamine B isothiocyanate	RBITC
Nitric oxide	NO	Rhodamine B isothiocyanate silica nanoparticles	SiRBITC NPs

Ruthenium-tris (4, 7-diphenyl-1, 10-phenanthroline) dichloride	$\text{Ru(dpp)}_3$	Sodium nitroprusside	SNP
Ruthenium-tris (4, 7-diphenyl-1, 10-phenanthroline) dichloride silica nanoparticles	$\text{SiRu(dpp)}_3$ NPs	Soluble guanylate cyclase	sGC
Sacroendoplasmic reticulum	SR	Standard error of mean	S.E.M
Scanning electron microscope	SEM	Sulphur dioxide	$\text{SO}_2$
Secondary electron imaging	SEI	Superoxide dismutase	SOD
Silica nanoparticles	SiNPs	Tetraethyl orthosilicate	TEOS
Smooth muscle cells	SMCs	Tetrapropylammonium hydroxide solution	TPAOH
Sodium bicarbonate	$\text{NaHCO}_3$	Thermogravimetric analysis	TGA
Sodium chloride	$\text{NaCl}$	Transmission electron microscope	TEM
Sodium hydroxide	$\text{NaOH}$	Virus particles	SV40

## *List of figures*

---

<i>Figure Number</i>	<i>Legend title</i>	<i>Page number</i>
1.1	Diagram of A) crystalline silicon dioxide in a quartz structure and B) amorphous structure.	3
1.2	The reaction scheme for the fabrication of silica nanoparticle; where (1) is the initial hydrolysis reaction step, (2) is the alcohol condensation reaction step and (3) is the water condensation reaction step. The overall reaction is given in step (4), where R denotes C <sub>2</sub> H <sub>5</sub> .	4
1.3	Schematic illustration of the Stöber sol-gel reaction for the production of silica spheres.	5
1.4	Schematic illustration of the micelle and reversed micelle.	8
1.5	An illustration of the silica nanoparticle formation from microemulsion reaction.	9
1.6	Stable colloidal nanoparticles undergoing the flocculation and coagulation process of aggregation.	11
1.7	Stabilisation process of nanoparticles, where C abbreviates capping agent.	12
1.8	Electrochemical double layer on a particle surface in a solution containing electrolytes.	13
1.9	The total energy of interaction (V(1), V(2) and V(3)) between two particles, acquired from the sum of attraction curve (V <sub>A</sub> ) and repulsion curves (V <sub>R</sub> (1), V <sub>R</sub> (2) and V <sub>R</sub> (3)).	15
1.10	Illustration for the fabrication of mesoporous nanoparticles (MCM-41).	19
1.11	Illustration of the difference between the imaging process of scanning electron and transmission electron microscope.	20
1.12	Image of a scanning electron microscope (JEOL 5600LV).	21
1.13	Image of a transmission electron microscope (Philips Technai 12 Biotwin TEM).	22
1.14	Image of Malvern zetasizer used for photon correlation spectroscopy and zeta potential.	23
1.15	The scattering of light being detected as it interacts with the particle.	24
1.16	Zeta potential gives an indication of the colloidal systems stability.	26
1.17	Micro-electrophoresis cell attachment used to measure the samples velocity by a laser Doppler velocimetry within the Malvern Zetasizer Nano series.	26

<i>Figure Number</i>	<i>Legend title</i>	<i>Page number</i>
1.18	Image of diffuse reflectance infra-red Fourier transform spectroscopy.	27
1.19	Image of thermogravimetric analysis set-up.	28
1.20	An illustration of the components within the thermogravimetric instrument.	29
1.21	An illustration of a volumetric apparatus set-up when measuring gas adsorption at 350 °C.	30
1.22	Classification of Brunauer's isotherm.	31
1.23	Image of the Brunauer-Emmett-Teller nitrogen sorption instrumentation.	32
1.24	Image of A) the graphite furnace atomic absorption spectroscopy and B) the sample loading bay.	34
1.25	Simplified illustration of the graphite furnace atomic absorption set-up.	34
1.26	An image of A) fluorescence spectrophotometer F-2500 and B) the sample holder where the cuvette is held.	35
1.27	An illustration of the components within a fluorescence spectrophotometer.	36
2.1	Schematic illustration of the experimental set-up for the silica nanoparticles synthesis.	39
2.2	Transmission electron microscope images of A) 71±6 nm silica nanoparticles and B) 27±7 nm silica nanoparticles.	41
2.3	Photon correlation spectroscopy analysis of A) 71±6 nm silica nanoparticles in water (dotted) and in PSS (straight), and B) 27±7 nm silica nanoparticles in water (dotted) and in PSS (straight).	42
2.4	An image of the fluorophore encapsulated silica nanoparticles of A) the seeds, B) half way through the silica shell formation and C) nanoparticles when the desired size have been reached, with their SEM images indicated below ( <b>500 nm</b> ). The pink solution is of the rhodamine B isothiocyanate encapsulated silica nanoparticles and orange solution is of the ruthenium-tris (4, 7-diphenyl-1, 10-phenanthroline) dichloride encapsulated silica nanoparticles.	46
2.5	Schematic illustration of the surface modification of silica nanoparticles with carboxylic acid group.	47
2.6	Transmission electron microscope images of A) 61±7 nm rhodamine B isothiocyanate encapsulated silica nanoparticles and B) 31±10 nm rhodamine B isothiocyanate encapsulated silica nanoparticles.	48

<b>Figure Number</b>	<b>Legend title</b>	<b>Page number</b>
2.7	Photon correlation spectroscopy analysis of A) $61\pm 7$ nm rhodamine B isothiocyanate encapsulated silica nanoparticles in water (dotted) and in PSS (straight), and B) $31\pm 10$ nm rhodamine B isothiocyanate encapsulated silica nanoparticles in water (dotted) and in PSS (straight).	49
2.8	Transmission electron microscope images of A) ruthenium-tris (4, 7-diphenyl-1, 10-phenanthroline) dichloride encapsulated silica nanoparticles and B) rhodamine B isothiocyanate encapsulated silica nanoparticles.	50
2.9	Photon correlation spectroscopy analysis of ruthenium-tris (4, 7-diphenyl-1, 10-phenanthroline) dichloride encapsulated silica nanoparticles and rhodamine B isothiocyanate encapsulated silica nanoparticles.	50
2.10	Schematic illustration of the hydrolysis of TEOS causing it to become hydrophilic.	51
2.11	Bar chart graph illustrating the surface modification of silica dye encapsulated nanoparticles by change in zeta potential.	51
2.12	Fluorescence calibration graph of A) rhodamine B isothiocyanate and B) ruthenium-tris (4, 7-diphenyl-1, 10-phenanthroline) dichloride dye molecules.	52
2.13	Transmission electron microscope images of rhodamine B isothiocyanate encapsulated silica nanoparticles; A) sample 1, B) sample 2, C) sample 3 and D) sample 4.	57
2.14	Photon correlation spectroscopy analysis of rhodamine B isothiocyanate encapsulated silica nanoparticles synthesised via microemulsion precipitation process.	57
2.15	Image of mesoporous nanoparticles A) before and B) after acid template extraction.	63
2.16	Image of rhodamine B isothiocyanate encapsulated mesoporous nanoparticles A) before and B) after acid template extraction.	64
2.17	Image of fluorescein isothiocyanate encapsulated mesoporous nanoparticles A) before and B) after acid template extraction.	64
2.18	Image of rhodamine B isothiocyanate/ fluorescein isothiocyanate encapsulated mesoporous nanoparticles A) before and B) after acid template extraction.	65
2.19	Image of A) silica mesoporous nanoparticles, B) fluorescein isothiocyanate encapsulated mesoporous nanoparticles; C) rhodamine B isothiocyanate encapsulated mesoporous nanoparticles and D) rhodamine B isothiocyanate/ fluorescein isothiocyanate encapsulated mesoporous nanoparticles.	66

<b>Figure Number</b>	<b>Legend title</b>	<b>Page number</b>
2.20	Photon correlation spectroscopy analysis of rhodamine B isothiocyanate encapsulated mesoporous nanoparticles; sample 1.	66
2.21	Transmission electron microscope image of rhodamine B isothiocyanate encapsulated mesoporous nanoparticles; sample 1 where A) is at 46000 magnification and B) is at 10500 magnification.	67
2.22	Photon correlation spectroscopy analysis of mesoporous nanoparticles; sample 2 was 292.3 nm, sample 3 was 173.6 nm, sample 4 was 160.1 nm, sample 5 was 106.7 nm and sample 6 was 123.2 nm.	68
2.23	Scanning electron microscope image of mesoporous nanoparticles of A) sample 2, B) sample 3, C) sample 4, D) sample 5, E) sample 6 and F) sample 7.	69
2.24	Photon correlation spectroscopy analysis of mesoporous nanoparticles, sample 5, with a hydrodynamic diameter of 106.7 nm and is increased to 8139 nm when calcined.	70
2.25	Transmission electron microscope image of template removed mesoporous nanoparticles, sample 5, at A) lower magnification and B) higher magnification.	70
2.26	Nitrogen sorption isotherm, of absorption (diamond curve) and desorption (circle curve), and pore distribution (insert) for mesoporous nanoparticles (sample 5).	71
2.27	Scanning electron microscope image of rhodamine B isothiocyanate encapsulated mesoporous nanoparticles (sample 8).	72
2.28	Scanning electron microscope image of A) mesoporous nanoparticles (sample 9), B) rhodamine B isothiocyanate encapsulated mesoporous nanoparticles (sample 10), C) fluorescein isothiocyanate encapsulated mesoporous nanoparticles (sample 11) and D) rhodamine B isothiocyanate/ fluorescein encapsulated isothiocyanate mesoporous nanoparticles (sample 12).	73
2.29	Diffuse reflectance infra-red Fourier transform spectroscopy of template intact (dotted) and template removed (straight line) mesoporous nanoparticles; where A) mesoporous nanoparticles (sample 9), B) rhodamine B isothiocyanate mesoporous nanoparticles (sample 10), C) fluorescein isothiocyanate mesoporous nanoparticles (sample 11) and D) rhodamine B isothiocyanate/ fluorescein isothiocyanate mesoporous nanoparticles (sample 12).	74

<b>Figure Number</b>	<b>Legend title</b>	<b>Page number</b>
2.30	Thermogravimetric analysis (solid line) and derivative thermogravimetric curve (dotted line) of A) mesoporous nanoparticles (sample 9), B) rhodamine B isothiocyanate mesoporous nanoparticle (sample 10), C) fluorescein isothiocyanate mesoporous nanoparticles (sample 11) and D) rhodamine B isothiocyanate/ fluorescein isothiocyanate mesoporous nanoparticles (sample 12).	76
2.31	Nitrogen sorption isotherm for gas adsorption (diamond curve) and desorption (circle curve) of A) mesoporous nanoparticles (sample 9), B) rhodamine B isothiocyanate mesoporous nanoparticles (sample 10), C) fluorescein isothiocyanate mesoporous nanoparticles (sample 11) and D) rhodamine B isothiocyanate/ fluorescein isothiocyanate mesoporous nanoparticles (sample 12).	77
2.32	Transmission electron microscope image of A) mesoporous nanoparticles, B) side-view of the mesopore channels and C) front-view of the mesopores.	78
2.33	Photon correlation spectroscopy analysis of mesoporous nanoparticles with and without dye molecules in water and potassium physiological salt solution media.	79
2.34	Calibration spectra of fluorescence for A) rhodamine B isothiocyanate and B) fluorescein isothiocyanate dye molecules.	81
2.35	Scanning electron microscope images of A) sample 1 and B) sample 2.	85
2.36	Photon correlation spectroscopy analysis of silicate-1; sample 1 and sample 2.	86
2.37	Thermogravimetric analysis (solid line) and derivative thermogravimetric curve (dotted line) of sample 1.	86
2.38	Thermogravimetric analysis (solid line) and derivative thermogravimetric curve (dotted line) of sample 2.	87
2.39	Nitrogen sorption isotherm analysis for gas adsorption (diamond curve) and desorption (circle curve) of silicate-1; where A) sample 1 and B) sample 2.	88
3.1	The Jablonski energy level diagram of the fluorescence mechanism.	91
3.2	Illustration of the fluorescent nanoparticle film which is capable of sensing gaseous oxygen and sulphur dioxide.	95
3.3	Illustration of rhodamine B isothiocyanate core silica shell nanoparticle.	96

<b>Figure Number</b>	<b>Legend title</b>	<b>Page number</b>
3.4	Schematic diagram of the incorporation of rhodamine B isothiocyanate dye within the silica nanoparticles and the penetration of gaseous SO <sub>2</sub> through the silica shell.	97
3.5	Schematic diagram of the incorporation of the ruthenium-tris (4, 7-diphenyl-1, 10-phenanthroline) dichloride dye within the silica nanoparticles and the penetration of gaseous O <sub>2</sub> through the silica shell.	98
3.6	Structure of the ruthenium complex.	99
3.7	Energy-level diagram of the ruthenium complex, were LC abbreviates ligand centered.	100
3.8	Reactions of the ruthenium complex being quenched by oxygen, where * represents an electron.	100
3.9	Diagram of the gas sensing instrumentation.	103
3.10	Fluorescence spectra of ruthenium-tris (4, 7-diphenyl-1, 10-phenanthroline) dichloride encapsulated silica nanoparticles and rhodamine B isothiocyanate encapsulated silica nanoparticles alone and mixed.	104
3.11	Fluorescence quenching of dual nanoparticles slide subjected to A) cycling concentration of oxygen in nitrogen atmosphere, B) higher oxygen concentration and C) lower oxygen concentration.	105
3.12	Calibration curve of normalised intensity versus oxygen concentration in % (v/v) for dual nanoparticle slide.	106
3.13	Fluorescence quenching of dual nanoparticles slide subjected to A) cycling concentration of SO <sub>2</sub> in nitrogen atmosphere and B) 100 and 60 % of SO <sub>2</sub> in nitrogen atmosphere.	107
3.14	The arterial wall structure of the aortic vessel.	109
3.15	Molecular structure of vasoconstrictor L-phenylephrine.	111
3.16	Mechanism of the contraction of the smooth muscle cells due to L-phenylephrine.	112
3.17	Molecular structure of vasodilator A) acetylcholine and B) sodium nitroprusside.	113
3.18	Mechanism of acetylcholine (endothelium dependent relaxation) agonist releasing nitric oxide from endothelium cells leading to the relaxation of smooth muscle cells; and sodium nitroprusside (endothelium independent relaxation) agonist which directly donates nitric oxide to the smooth muscle cells, leading to relaxation.	115
3.19	Illustration of the inhibition of the production of eNOS and thus blocking acetylcholine induced relaxation.	116

<b>Figure Number</b>	<b>Legend title</b>	<b>Page number</b>
3.20	Possible uptake mechanisms of nanoparticles into cells.	117
3.21	Clathrin-mediated endocytosis mechanism.	119
3.22	Illustration of the initialisation of nanoparticles via the caveolae-mediated pathway.	120
3.23	Illustration of the attenuation of endothelial-dependent vasodilator responses, induced by dye encapsulated silica nanoparticles, <i>in vitro</i> .	121
3.24	Image of the aortic vessel A) attached to organelles, B) with perivascular adipose tissue intact, C) with perivascular adipose tissue removed and D) magnified 3 mm ring.	124
3.25	Organ-bath system for the endothelium-dependent and independent vasodilation experimentation of aortic vessel.	126
3.26	Example of a trace that was obtained when evaluating the influence of constrictor and dilator effects on the aortic ring.	127
3.27	Transmission electron microscope image of the aortic vessel where the layers are illustrated.	128
3.28	Transmission electron microscope images of $71\pm 6$ nm silica nanoparticles within the endothelial cell lining of the aortic vessel.	129
3.29	Transmission electron microscope image of $61\pm 7$ nm rhodamine B isothiocyanate encapsulated silica nanoparticles within the endothelial cell lining of the aortic vessel	130
3.30	Transmission electron microscope images of $27\pm 7$ silica nanoparticles within the endothelial cell lining of the aortic vessel.	130
3.31	Transmission electron microscope images of $31\pm 10$ nm rhodamine B isothiocyanate encapsulated silica nanoparticles within the endothelial cell lining of the aortic vessel.	131
3.32	Transmission electron microscope images of $71\pm 6$ nm silica nanoparticles incubated at 4 °C in the presence of an aortic vessel.	132
3.33	The influence on potassium physiological salt solution constrictor response of the aortic vessels before and after incubation, where $p > 0.05$ for all the experiments. ‘ <i>n</i> ’ is the number of vessels.	133
3.34	The influence on acetylcholine dilator responses of the aortic vessels before and after incubation in physiological salt solution. ‘ <i>n</i> ’ is the number of vessels, where $p > 0.05$ for all the experiments.	134

<b>Figure Number</b>	<b>Legend title</b>	<b>Page number</b>
3.35	The influence on sodium nitroprusside dilator responses of the aortic vessels before and after incubation in physiological salt solution. ‘ <i>n</i> ’ is the number of vessels, where $p > 0.05$ for all the experiments.	134
3.36	The influence of both amorphous (SiNPs) and rhodamine B isothiocyanate encapsulated silica nanoparticles (SiRIBTC NPs) on endothelium-dependent vasodilator responses. The control is incubation in PSS alone. A) Effect of medium-size SiNP number at $1.31 \times 10^{11}$ NP/ mL and $1.96 \times 10^{12}$ NP/ mL. B) Effect of SiNP size at $1.96 \times 10^{12}$ NP/ mL; medium-size SiNPs and small-size SiNPs. C) Effect of medium-size SiRBITC NPs at $1.96 \times 10^{12}$ NP/ mL; medium-size SiNPs and medium-size SiRBITC NPs. D) Effect of small-size SiRBITC NPs at $1.96 \times 10^{12}$ NP/ mL; small-size SiNPs and small-size SiRBITC NPs. ‘ <i>n</i> ’ is number of vessels. *= $p < 0.05$ , #= $p < 0.01$ and §= $p < 0.001$ , error bars=S.E.M.	135
3.37	The influence of medium-size silica nanoparticles on sodium nitroprusside dilator responses of the aortic vessels; where A) $1.31 \times 10^{11}$ NP/ mL and B) $1.96 \times 10^{12}$ NP/ mL. ‘ <i>n</i> ’ is the number of vessels, where $p > 0.05$ for all the experiments.	137
3.38	The influence on sodium nitroprusside dilator responses of the aortic vessels when incubated with A) medium-size silica nanoparticles and B) small-size silica nanoparticles at $1.96 \times 10^{12}$ NP/ mL. ‘ <i>n</i> ’ is the number of vessels, where $p > 0.05$ for all the experiments.	139
3.39	The influence on sodium nitroprusside dilator responses of the aortic vessels when incubated with A) medium-size silica nanoparticles and B) medium-size rhodamine B isothiocyanate encapsulated silica nanoparticles at $1.96 \times 10^{12}$ NP/ mL. ‘ <i>n</i> ’ is the number of vessels, where $p > 0.05$ for all the experiments.	140
3.40	The influence on sodium nitroprusside dilator responses of the aortic vessels when incubated with A) small-size silica nanoparticles and B) small-size rhodamine B isothiocyanate encapsulated silica nanoparticles at $1.96 \times 10^{12}$ NP/ mL. ‘ <i>n</i> ’ is the number of vessels, where $p > 0.05$ for all the experiments.	141

<b>Figure Number</b>	<b>Legend title</b>	<b>Page number</b>
3.41	The influence on acetylcholine dilator responses after: A) small-size rhodamine B isothiocyanate encapsulated silica nanoparticle co-incubation with superoxide dismutase in comparison to small-size rhodamine B isothiocyanate encapsulated silica nanoparticles alone, or PSS, B) small-size silica nanoparticle co-incubation with superoxide dismutase in comparison to small-size silica nanoparticles alone, or PSS and C) <i>N</i> <sub>ω</sub> -Nitro-L-arginine incubation in PSS alone. ‘ <i>n</i> ’ is number of vessels. *= <i>p</i> <0.05, #= <i>p</i> <0.01 and §= <i>p</i> <0.001, error bars=S.E.M.	142
3.42	Image of the pressurised system set-up for the large aortic vessels.	149
3.43	Transmission electron microscope images of 71±6 nm silica nanoparticles pressurised into the aortic vessel.	150
3.44	The influence on acetylcholine dilator responses after incubation in 71±6 nm silica nanoparticles at 1.31×10 <sup>11</sup> NP/mL under pressurised system in comparison to the passive process. ‘ <i>n</i> ’ is number of vessels. *= <i>p</i> <0.05, #= <i>p</i> <0.01 and §= <i>p</i> <0.001, error bars=S.E.M.	151
3.45	Schematic illustration of the relaxation of constricted aortic vessels via the release of endothelial-independent vasodilators, <i>in vitro</i>	153
3.46	Schematic illustration of the interaction between sodium nitroprusside and the mesopore channel.	158
3.47	Image of the experimental set-up for the drug release study of rhodamine B isothiocyanate encapsulated mesoporous nanoparticles.	158
3.48	Transmission electron microscope image of mesoporous nanoparticles within the endothelial cell lining of the aortic vessel.	161
3.49	The drug loading capacity altering as the sodium nitroprusside concentration increases.	162
3.50	Release profile of sodium nitroprusside from mesoporous nanoparticles using atomic absorption spectroscopy.	163
3.51	An example trace of the influence of sodium nitroprusside loaded mesoporous nanoparticles at low concentration on constricted aortic vessels in real-time.	164
3.52	An example trace of the influence of sodium nitroprusside loaded mesoporous nanoparticles at high concentration on constricted aortic vessels in real-time.	165

<i>Figure Number</i>	<i>Legend title</i>	<i>Page number</i>
3.53	An example trace of the influence of sodium nitroprusside loaded fluorescein isothiocyanate encapsulated mesoporous nanoparticles at low concentration on constricted aortic vessels in real-time.	166
3.54	An example trace of the influence of sodium nitroprusside loaded fluoresein isothiocyanate encapsulated mesoporous nanoparticles at high concentration on constricted aortic vessels in real-time.	166
3.55	The influence of sodium nitroprusside loaded mesoporous nanoparticles on endothelium-independent vasodilator responses. ‘ <i>n</i> ’ is number of vessels.	167
3.56	The influence of sodium nitroprusside loaded fluoresein isothiocyanate encapsulated mesoporous nanoparticles on endothelium-independent vasodilator responses. ‘ <i>n</i> ’ is number of vessels.	168
3.57	Calibration spectra of endothelium-independent vasodilator response against known concentrations of sodium nitroprusside.	169

## *List of equations*

---

<i>Equation number</i>	<i>Equation explanation</i>	<i>Page number</i>
1.1	Bogush equation to determine the diameter of silica nanoparticles using the reactant concentration.	6
1.2	The calculation for the term <i>A</i> specified in Bogush's equation for the determination of silica nanoparticle diameter.	6
1.3	The calculation for the term <i>B</i> specified in Bogush's equation for the determination of silica nanoparticle diameter.	6
1.4	Bogush equation to determine the total volume of TEOS required for the seeded growth of silica nanoparticle.	6
1.5	DLVO theory explanation via the sum of attractive and repulsive forces because of double layer of counterions.	14
1.6	Beer-Lambert law	33
1.7	Beer-Lambert law; alternative expression of absorbance.	33
3.1	Stern-Volmer equation, which described the relationship between the fluorescence emission intensity and the concentration of the fluorophore.	93
3.2	The bimolecular quenching constant.	93
3.3	Stokes-Einstein equation describing the diffusion coefficient of a particle.	93
3.4	The Stern-Volmer equation simplified.	94
3.5	The drug loading efficiency of mesoporous nanoparticles.	160
3.6	The drug loading capacity of mesoporous nanoparticles.	160

## *List of tables*

---

<i>Table number</i>	<i>Table title</i>	<i>Page number</i>
1.1	The limit of detection for Fe using different atomic absorption techniques, values obtained from the Perkin Elmer guide for selecting the appropriate techniques and systems.	34
2.1	Overview of the types of nanoparticles fabricated in this Chapter.	37
2.2	The molar ratio of the reagent required to synthesise silica nanoparticles of a given composition and size.	40
2.3	Hydrodynamic size and stability measurements of silica nanoparticles, in water and physiological salt solution.	42
2.4	Hydrodynamic size and stability measurements of rhodamine B isothiocyanate encapsulated silica nanoparticles, in water and physiological salt solution.	48
2.5	Hydrodynamic size and stability measurements of silica dye encapsulated nanoparticles and their surface modification with amine and carboxylic acid groups.	52
2.6	Quantifying the amount of dye molecules within the nanoparticles.	53
2.7	The solution amounts of the reagent required to synthesise rhodamine B isothiocyanate encapsulated silica nanoparticles of a given composition and size.	56
2.8	Hydrodynamic size and stability measurements of silica nanoparticles in water media.	58
2.9	The solution amounts of the reagent required to synthesise mesoporous nanoparticles of required composition and size.	60
2.10	Overview of the amount of reactants needed to synthesise mesoporous nanoparticles.	62
2.11	Diffuse reflectance infra-red Fourier transform spectroscopy analysis of the functional groups within the mesoporous nanoparticles.	75
2.12	Hydrodynamic size and stability measurements of mesoporous nanoparticles, in water and high potassium physiological salt solution.	80
2.13	Quantification of dye molecules within the nanoparticles.	82
2.14	Overview for the fabrication of silicate-1 nanoparticles as the temperature and aging time alters.	85
3.1	Overview of the types of nanoparticles used for specific applications.	89

<b><i>Table number</i></b>	<b><i>Table title</i></b>	<b><i>Page number</i></b>
3.2	Calculated surface area and mass of nanoparticles added to an experiment.	136
3.3	The half-maximal relaxation to the endothelial-dependent vasodilator (acetylcholine).	137
3.4	Half-maximal relaxation of aortic vessels due to the endothelial-independent vasodilator, sodium nitroprusside, before and after incubation with different types of nanoparticles	138
3.5	Summary of the reactant concentration used for the release profile.	159
3.6	The total concentration of SNP released from the MNP matrix, <i>in vitro</i> .	169

## ***Abstract***

---

A wide variety of silica based nanoparticles (NPs) were synthesised to engineer materials with properties for specific applications by manipulating the nanoparticle composition. These include luminescent core shell NPs and luminescent mesoporous silica which have been successfully synthesised. The particle size distribution and characteristics of the NPs were determined by photon correlation spectroscopy. The laser Doppler velocimetry was used to determine the NPs stability in suspension. Transmission and scanning electron microscopy analysis were used to assess morphology and size of the NPs. Diffuse reflectance infra-red Fourier transform spectroscopy was used to study the template removal to produce porous NPs.

The particles were then utilized for assessing different applications. A novel dual oxygen (O<sub>2</sub>) and sulphur dioxide (SO<sub>2</sub>) gas sensor was produced by incorporating fluorophores within SiNPs. The fluorophore rhodamine B isothiocyanate (RBITC) was encapsulated within SiNPs (208±9 nm) to produce a nanosensor that is sensitive to SO<sub>2</sub>, while ruthenium-tris(4,7-diphenyl-1,10-phenanthroline) dichloride (Ru(dpp)<sub>3</sub>) was encapsulated within SiNPs (192±8 nm) to sense O<sub>2</sub>. The sensor utilises the fluorescence quenching phenomena as a detection mechanism and had high sensitivity for detection of low O<sub>2</sub> gas concentrations (0.018 %). These novel nanosensors demonstrate potential to develop multisensor systems to capable of detecting multiple gasses simultaneously in a single matrix for a magnitude of future applications that require small robust gas sensing. Biocompatibility of SiNP number, size (smaller than 100 nm), and dye encapsulation on conduit arterial function, *in vitro* was assessed. Their effects on endothelial-dependent [acetylcholine (ACh); 0.01-200 µM] and independent [sodium nitroprusside (SNP); 0.001-10 µM] dilator responses were examined. When incubated with 1.96×10<sup>12</sup> NP/ mL, both 30 nm, 70 nm SiNPs and RBITC encapsulated in silica nanoparticles (SiRBITC NPs) significantly reduced endothelium-dependent, but not independent vasodilation. Furthermore, attenuated dilation due to SiRBITC NPs, but not SiNPs, could be partially restored using superoxide dismutase. Our results suggest that the mechanism of attenuated dilation is different for SiNPs and SiRBITC NPs which has implications for the future fabrication of biocompatible nanoparticles for imaging diagnostics. Spherical mesoporous nanoparticles (MNP) and dye encapsulated MNP were synthesised via a sol-gel method in

the presences of organic template. The template was removed using an acidic extraction. The average diameters of the MNP were 100 nm. The interior pores were loaded with SNP, these drug loaded MNP were placed in live tissue and release in real-time was observed, *in vitro*. We demonstrate that the initial instantaneous release is due to the surface adsorption of the drug followed by released from the pores. Furthermore, these drug loaded MNP were placed in live tissue and release in real-time was observed, *in vitro*.

## ***Aims and objectives***

---

### **Aims**

The aim of this thesis is to fabricate silica base nanoparticles and utilise them for potential sensor and bioapplications.

### **Objective 1 - Fabrication of nanoparticles.**

To determine suitable methods for synthesis of amorphous and porous fluorescent silica nanoparticles of various monodispersed sizes. To achieve nanoparticle surface functionalisation to enable them to be utilised for their purpose built applications.

### **Objective 2 - Characterisation of the nanoparticles.**

The size and characteristics of nanoparticles will be determined by the use of specialist analytical apparatus such as the Malvern Zetasizer, to measure the zeta potential.

### **Objective 3 - Gas sensing via fluorescent core shell silica nanoparticles.**

These nanoparticles will be utilized as gas sensors through the fluorescence quenching phenomena. The nanoparticles interaction with gaseous molecules will be examined with real-time fluorescence spectrophotometer.

### **Objective 4 - Biocompatibility of fluorescent silica nanoparticles.**

Their toxicological influence on the live aortic blood vessels will be determined by assessing their effect on the vascular function. This will be conducted with a specialist organ-bath system for the *in vitro* studies, whereby transmission electron microscopy will determine uptake within the ultra-structure.

### **Objective 5 - Drug delivery system using fluorescent mesoporous nanoparticles.**

Determine the parameters for optimal drug loading, release and decomposition protection under simulated biological conditions. Determine the dynamics of drug release by drug-loaded nanoparticles using isolated live blood vessels *in vitro*.

# Thesis structure

## 1) Particle Synthesis and Characterisation

- A. To fabricate monodispersed nanoparticles (NPs), via sol-gel precipitation technique, and the sizes will be determined with electron microscopy and photon correlation spectrophotometer.
- B. NPs stability will be determine through the laser Doppler velocimetry.
- C. Characterisation of NPs will be conducted with thermogravimetric analysis for decomposition analysis, infra-red spectroscopy for surface groups attachment or removal, quantification of dye molecules within NPs via fluorescence spectroscopy, surface area and porosity quantification with N<sub>2</sub> sorption and atomic absorption spectroscopy for quantification of Fe from the drug release profile of mesoporous NPs.

## 2) Gas Sensor Application

- Introduction to fluorescence
- Experimentation

### Aims

- Produce a film consisting of both Ru(dpp)<sub>3</sub> core and silica shell and RBITC core and silica shell NPs.
- Determine Ru(dpp)<sub>3</sub> NPs sensitivity to gaeous O<sub>2</sub> and RBITC NPs sensitivity to SO<sub>2</sub>.

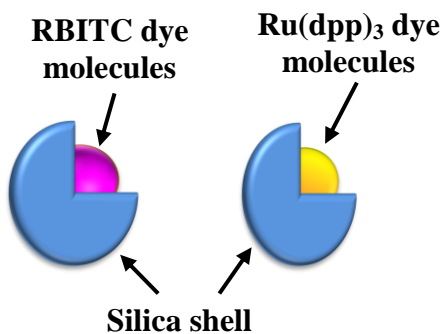
## 3) Biological Application

- Introduction to aortic vessel structure and function
- Experimentation

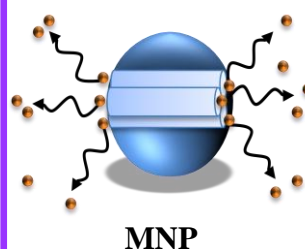
### Aims

- Determine the influence of size and concentration of silica NPs with and without dye molecules on vascular function.
- Determine the dynamic of drug release by drug-loaded mesoporous nanoparticles *in vitro*.

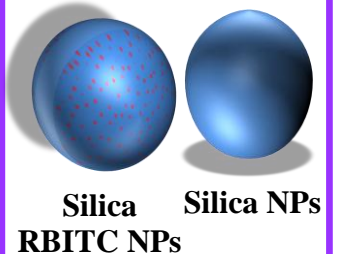
### Gas sensor



### Drug delivery



### Biocompatibility



# **Chapter 1**

## **Introduction**

# 1. INTRODUCTION

## 1.1. Nanotechnology

Nanotechnology is the assembly of materials under control conditions to manipulate the dimensions in the nanoscale range (0.1-100 nm) [1]. The widely held description of nanoparticles (NPs) has been scrutinised for not having a set definition, thus resulting in the continuous improved definitions where currently particles with a surface area less than  $60 \text{ m}^2/\text{cm}^3$  is used for the description instead of diameter [2]. From its original notion, nanotechnology, refers to nanomaterials fabricated from the bottom-up technique [3, 4]. Furthermore this technology that lies within the atomic and molecular level dates back to 1959 as it was envisioned by Richard Feynman's speech; '*There is plenty of room at the bottom*' [3]. The continuous exploitation of nanoscale material has led to interdisciplinary research where chemistry, biology and physics have been combined to manufacture enhanced tools for intended purposes. Nanomaterials offer a great alternative to the bulk materials for use in various fields. Refined synthesis techniques that manipulate dimensions and properties of materials has escalated research for numerous applications, including electronic [5], pharmaceutical [6], environmental [7], imaging diagnostics [8] and drug therapy [9] in biomedical applications. Nanomaterials encompass a wide variety of structures, including NPs, nanoparticulate films as well as complex, often bio-inspired, nanostructures. Dimensions are a key indicator in defining the material. NPs particularly refer to particle between 1-100 nm [10]. Decreasing the particle size from micron to nano-size drastically increases the surface area of the material and changes its properties. NPs are particularly useful for the construction of two-dimensional and three-dimensional nanostructures for various applications. In addition, the surface of the NPs can be functionalized to further tailor the properties of the final product.

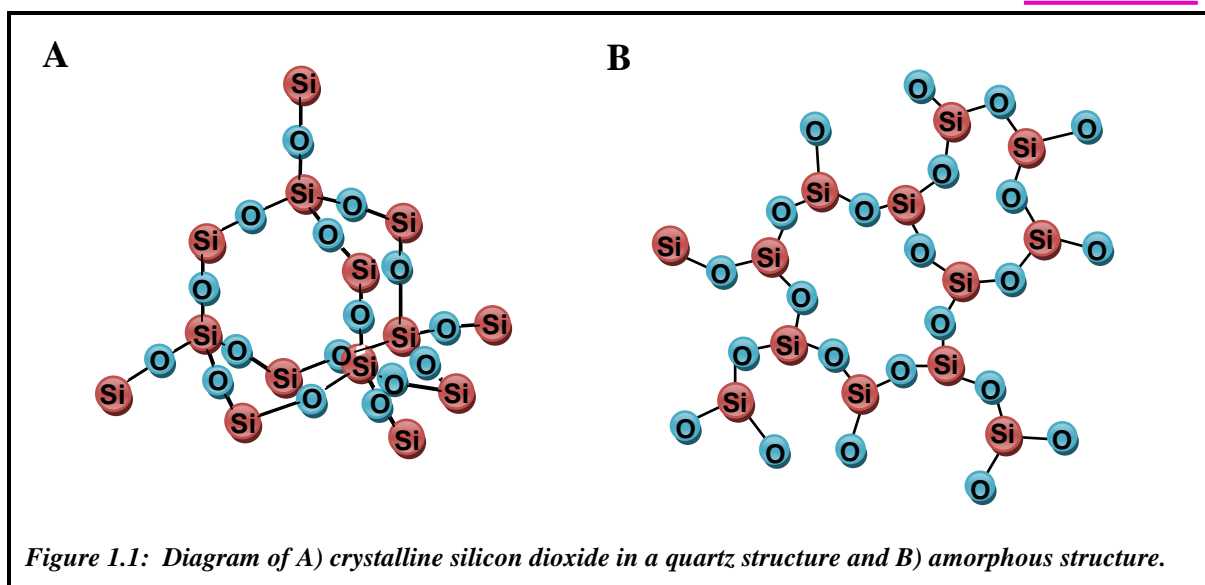
The production of nanomaterials is dependent on factors such as growth media, the temperature, the concentration of reactants and the reaction time. NPs can be classified as carbon-based (carbon nanotubes and fullerenes), inorganic (zinc oxide and cerium oxide), metal (gold and silver) and quantum dots (zinc sulphide) [11]. The uses of NPs in industrial applications require production of material at a nanoscale maintaining the size distribution and the morphology of the nanomaterial. Furthermore, most applications

require both the crystal structure and the chemical composition of the product to be the same. Finally there should be no aggregation of the nanomaterial [11].

Research development has resulted in the fabrication of new types of devices using nanomaterials. NPs may have enhanced capabilities, such as luminescence molecules encapsulated in silica shell to reduce photo-degradation of dye molecules. Roche *et al.* [12] used luminescence molecules incorporated within organically modified sol-gel film to detect oxygen gas. However, the introduction of silica shell would prolong the luminescent intensity of the luminescence molecules. The material has the ability to quantify the amount of gas via the gas quenching the molecules' luminescence. There are also profound advantages of the use of nanomaterials in biomedicine. Generally for these applications, the NPs have to be biocompatible. Silica NPs (SiNPs) are of particular interest for bioapplications due to their biocompatibility, easy synthesis and possible manipulations to obtain the desired sizes and porosities. Additionally, the external surface can be modified with biomolecules to target specific sites. The versatility for fabricating purpose-built NPs have resulted in silica being the material of choice for application in the area of medical imaging [13] and drug delivery [14].

## 1.2. Synthesis Methods of Silica Nanoparticles

Silica materials contain a molecular formula of silicon dioxide. Its structure can either be crystalline, where the atoms or molecules are arranged in an ordered array in liquid or solid, or amorphous containing a non-crystalline structure (Figure 1.1). Furthermore, the versatility of this material allows silica to be either porous or non-porous.



### 1.2.1. The Sol-gel method

The conventional precipitation method used for synthesis of NPs by the preparation of a solution that contains relevant inorganic precursors is referred to as the sol-gel method. This method is favoured over other synthetic routes as it allows particle size control by altering the *pH*, temperature, dispersants and precursor concentrations. It also allows production of porous materials using surfactants, mixed metal oxides and metals and the addition of surface functional groups all within a single synthetic step. The inorganic precursors used normally are metal salts, metal halides and alkoxides ( $M(OR)_x$ ). The inorganic alkoxide is firstly hydrolysed followed by condensation to synthesize the metal oxide. The reaction rate and in turn growth rate can be manipulated by the use of mineralizers (acids or bases) to affect the hydrolysis or condensation rate.

The sol-gel method has been used for the fabrication of colloidal systems. In colloidal silica, the synthesis entails the production of siloxane polymer from organosilica compounds. The term sol-gel refers to the production of either gel or monodispersed solution of particles. Reaction conditions with low *pH* result in fast hydrolysis and in turn slow condensation to form a gel. High *pH* conditions result in slow hydrolysis and fast condensation forming a monodispersed solution [15]. The well known sol-gel method for the fabrication of monodispersed silica colloid was first published by Stöber *et al.* in 1968 [16]. In this work, the influence of the solution concentration on the size and monodispersity of SiNPs, which ranged from 50 nm to 2  $\mu\text{m}$  was studied. Furthermore, the

effect of the temperature on the rate of nucleation was studied. This method entailed the hydrolysis of a silica precursor, such as tetraethyl orthosilicate (TEOS), in alcohol solution, which is catalysed by ammonia as shown in Figure 1.2, followed by a condensation reaction which may either occur by alcohol or water molecules [17].

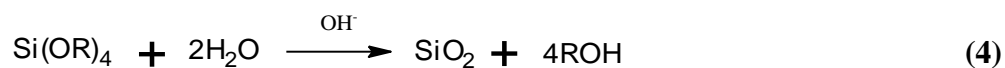
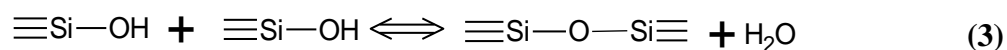
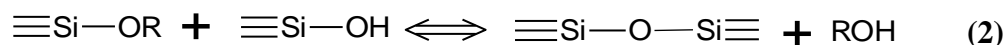
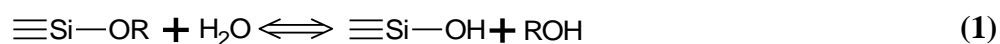
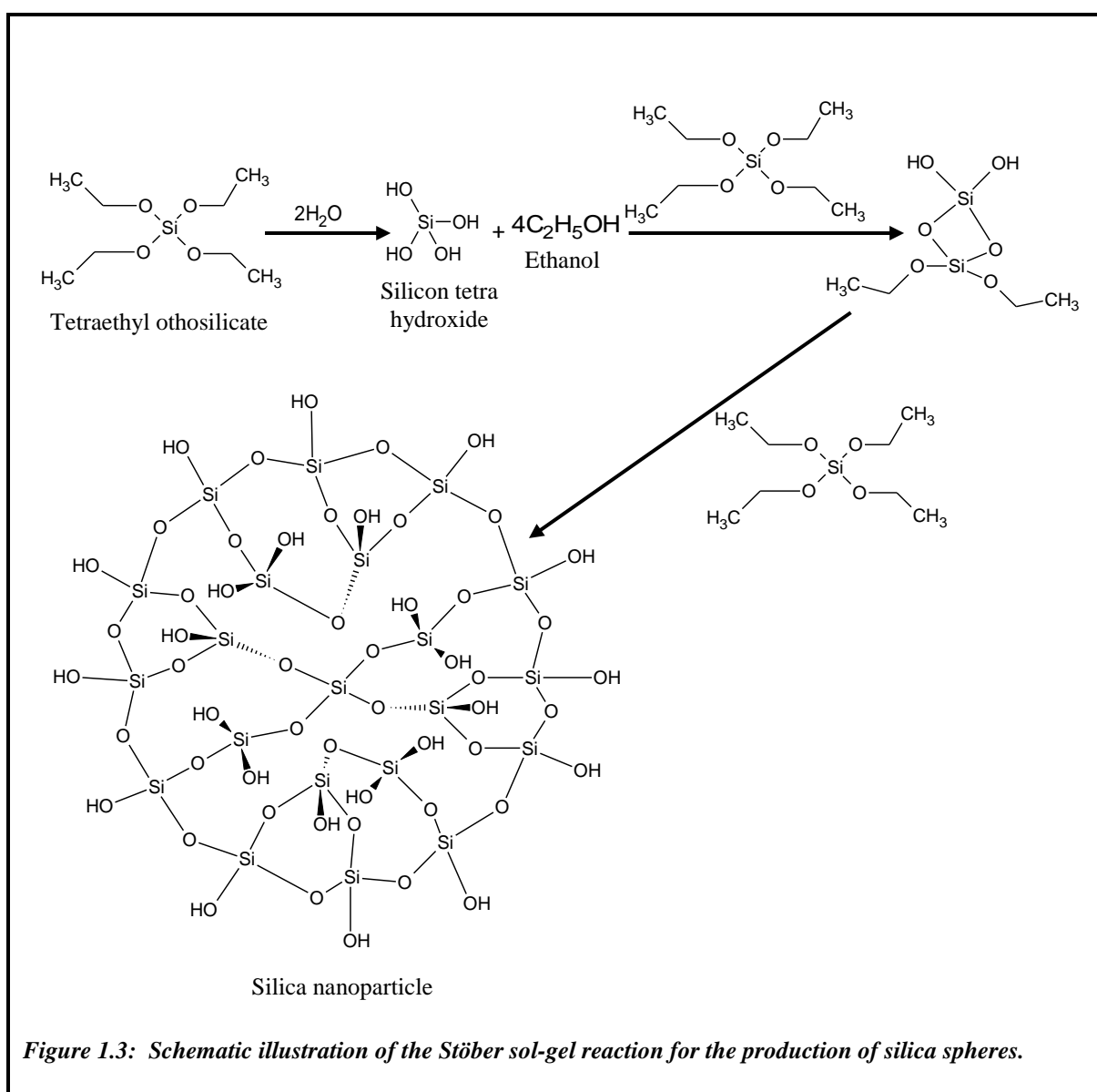


*Figure 1.2: The reaction scheme for the fabrication of silica nanoparticle; where (1) is the initial hydrolysis reaction step, (2) is the alcohol condensation reaction step and (3) is the water condensation reaction step. The overall reaction is given in step (4), where R denotes C<sub>2</sub>H<sub>5</sub>.*

Initially, there is a hydrolysis followed by condensation of the alkoxide silica ( $\text{Si}(\text{OR})_4$ ) to fabricate monodispersed silica spheres, as shown in Figure 1.3.



### 1.2.1.1. Controlled growth of silica nanoparticles

The Stober *et al.* method has been extensively studied to further minimize the size of the silica particles produced [18, 19]. Production of monodispersive silica particles below 100 nm is desirable for bioapplications. The desired silica particle size can be obtained by altering the reagent concentration (such as TEOS, water and  $\text{NH}_3$ ) along with changing the temperature. Stober *et al.* constructed a graphical representation of the relationship between particle diameter and reactant (water and ammonia) concentration, when

tetraethyl silicate concentration is  $0.28 \text{ mol dm}^{-3}$  and the reaction occurs at room temperature. However, using the Stöber method to fabricate larger particles (1-2  $\mu\text{m}$ ) tends to yield a poor size distribution.

Bogush *et al.* has expressed the relationship between reactant concentration and particle diameter through a simplified Equation 1.1, which was derived through the fabrication of over 100 samples at  $25 \text{ }^\circ\text{C}$  [18].

$$d = A [\text{H}_2\text{O}]^2 \exp(-B[\text{H}_2\text{O}]^{1/2}) \quad (1.1)$$

Where,  $d$  is the average particle diameter with units of nanometer (nm) and the reactant concentrations has units of  $\text{mol dm}^{-3}$ . The term  $A$  is specified in Equation 1.2, which was corrected by Razink *et al.* [20].

$$A = [\text{TEOS}]^{1/2} (82 + 151[\text{NH}_3] + 1200[\text{NH}_3]^2 - 366[\text{NH}_3]^3) \quad (1.2)$$

Where, the term  $B$  within Equation 1.1 is expressed in Equation 1.3.

$$B = 1.05 + 0.523[\text{NH}_3] - 0.128[\text{NH}_3]^2 \quad (1.3)$$

Bogush *et al.* have succeeded in enhancing the monodispersity by initially synthesizing small core SiNPs, known as seeds, and then coating them with TEOS. It was found that as particle size increased, the aggregation between particles of the same size was reduced [21]. Alternatively to the “aggregation-only” model, the “growth-only” model, suggests that an initial nucleation occurs followed by a diffusion-limited growth [21, 22]. Once the initial seeds have formed and the starting materials have fully reacted, the seeding growth may be conducted. The molar ratio for the addition of TEOS to water is 1:2 in order for the seeded growth. Thus, the relationship between the particle size and the total volume of TEOS added during the seeded growth was derived (Equation 1.4) [18].

$$d = d_0 \left( \frac{V}{V_0} \right)^{1/3} \quad (1.4)$$

Where,  $d$  is the average particle diameter in nm,  $d_0$  is the average diameter of the seeds,  $V_0$  is the moles of TEOS used to synthesise the seed,  $V$  is the total moles of TEOS used for the fabrication of the particles.

Achieving smooth monodispersive silica particles within the size range from 10-100 nm is difficult, the particles tend to be granular in appearance, a far more successful method has been developed involving the production of a microemulsion.

### **1.2.2. Microemulsion method**

Microemulsions are a type of colloidal system where there are two phases, an oily substance and a water-based substance. The two are not miscible but with the aid of a surfactant they may become miscible. The oil and water mixture of microemulsion are known to be thermodynamically stabilised when a surfactant is present. A surfactant molecule has a long chain with a hydrophobic tail and a hydrophilic head, its structure allows it to dissolve in both water and in organic solvents. Surfactant molecules form micelles or reverse-micelles, which have spherical structure. There is an interfacial tension between the water and the oil that is lowered by the surfactant because the surfactants hydrophilic head will adsorb in the water and the hydrophobic tail will adsorb in the oil. Above certain surfactant concentrations, micelles are formed in the water phase where the tails are in the core and the heads are facing outwards. Reverse-micelles are formed in the oil phase with the tails facing outwards and the heads in the core, as illustrated by Figure 1.4.

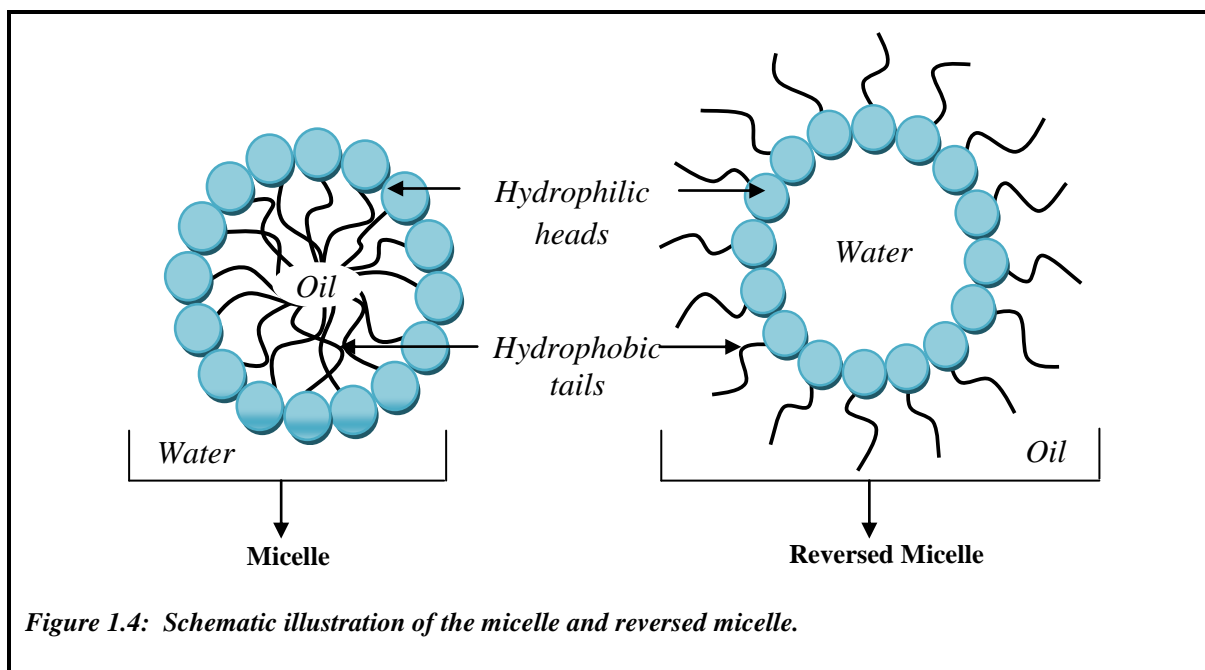


*Figure 1.4: Schematic illustration of the micelle and reversed micelle.*

The difference between a microemulsion and emulsion is the transparency, the thermodynamic stability and the heterogeneity. Due to the microemulsion being optically isotropic, it is transparent. Also, unlike microemulsion, emulsions are thermodynamically unstable.

The characteristics of the microemulsion medium has caused researchers to use this technique to synthesise various materials, such as metals, metal halides, chalcogenides, carbonates, organic polymers and SiNPs [23, 24]. When this technique is used to form NPs the reactants maybe contained in separate aqueous microemulsion. The two are mixed and due to Brownian motion they react to form small NPs.

In order to fabricate SiNPs via microemulsion, the preparation involves alkoxide hydrolysis of a silica precursor, such as TEOS, in water-in-oil microemulsion (Figure 1.5) [24]. The reversed micelles consist of water nanodroplets in an organic medium in order to be utilised as nanoreactors for the fabrication of NPs. The particle size may be adjusted by altering the ratio of water to oil [25]. The water-to-surfactant molar ratio ( $R$ ) and ammonia concentration has been shown to have an effect on the particle size [23, 24]. The early stage of the reaction is a first order with respect to TEOS concentration and as  $R$  increases the first order kinetics decrease. Initially, the reaction entails a hydrolysis of TEOS in

alcohol, such as ethanol, which is catalysed by ammonium hydroxide-base in water solution. This follows a first order kinetics reaction with respect to ammonia and TEOS concentrations [24]. In the work of Kay *et al.* it has been concluded that independently of the catalyst used for TEOS hydrolysis, acid or base the reaction will still remain first order with respect to the water concentration (1:2 molar ratio of TEOS:H<sub>2</sub>O) [26]. The water concentration has been found to play an important role in the base-catalysed hydrolysis rate [22]. The type of solvent mixed with TEOS also has an effect on the rate of hydrolysis [22, 27-30]. If the solvent has long alkyl chains, then the rate of hydrolysis decreases due to steric stabilisation. The rate of hydrolysis also decreases if the solvent has a tendency to form hydrogen bonds with water [22, 28, 29].

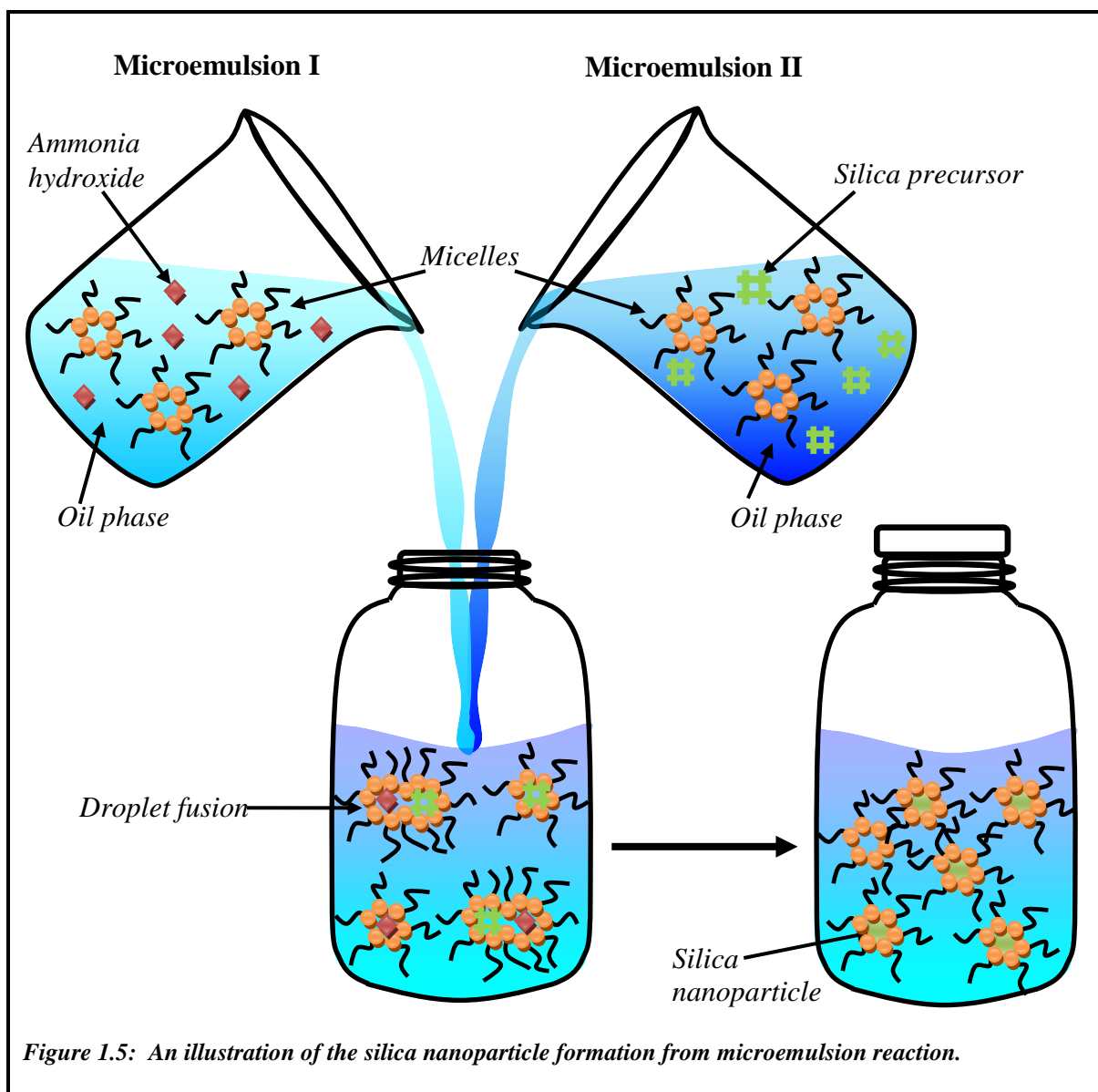
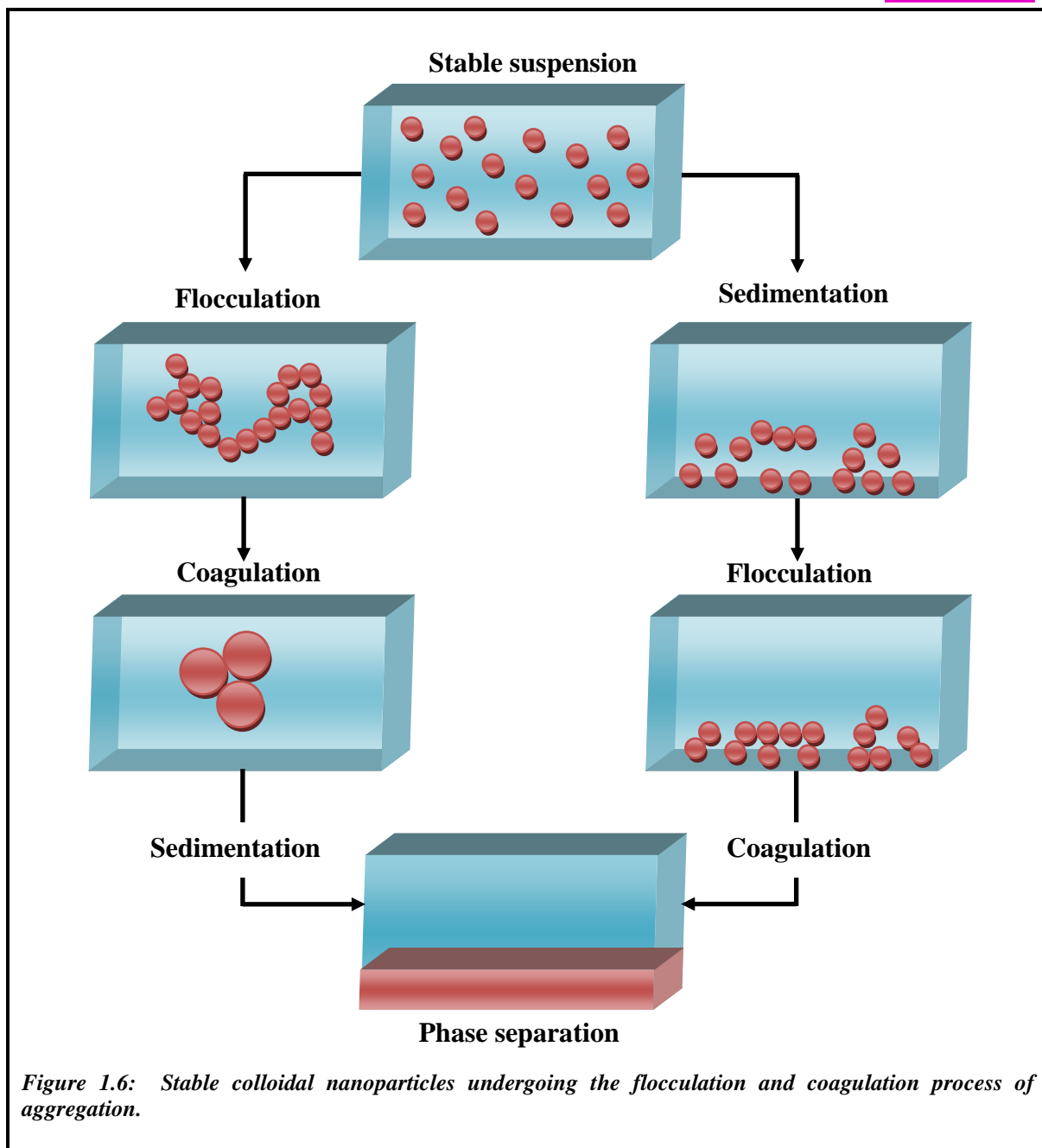


Figure 1.5: An illustration of the silica nanoparticle formation from microemulsion reaction.

### **1.3. Stability of Colloidal Silica**

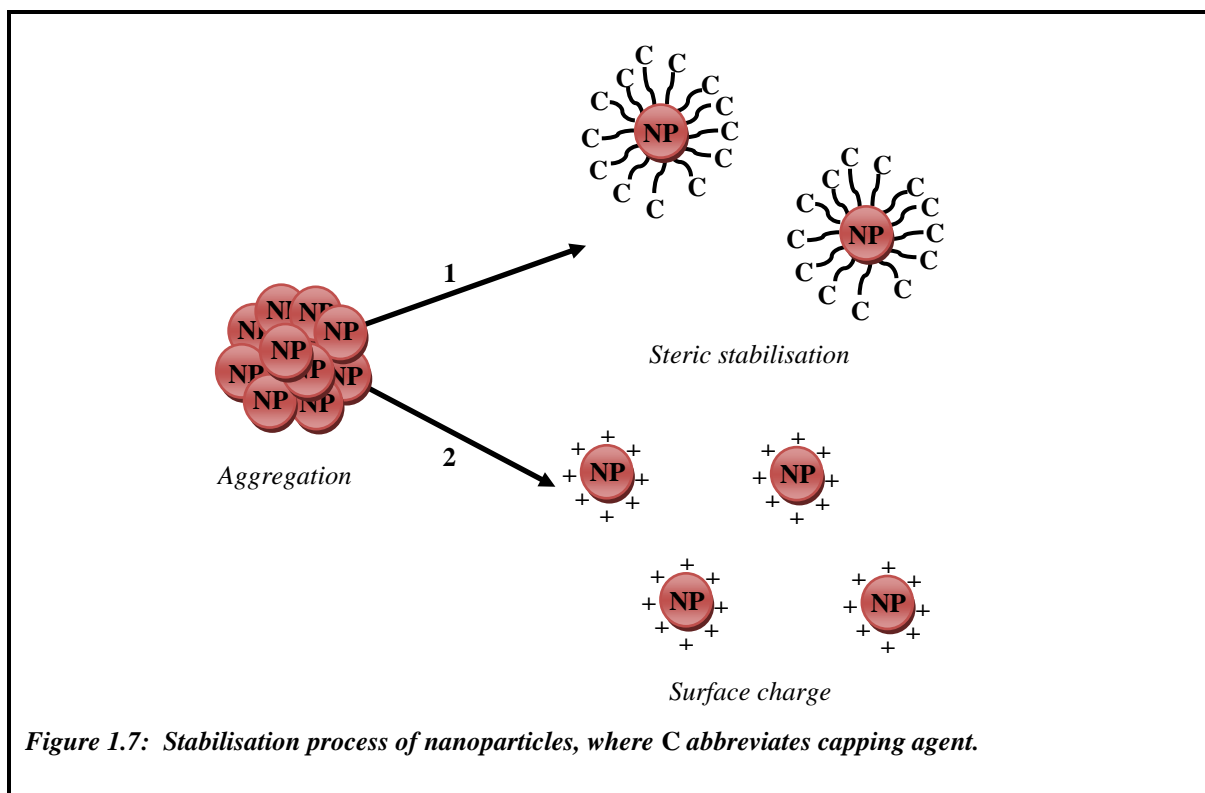
The term colloidal dispersion refers to a system that contains immiscible particles which are suspended in a continuous medium. The silica suspensions are known as lyophobic colloid, in which the dispersed phase is solvent hating, thus leading to minimal interaction between the particles and continuous phase [31]. Furthermore, in order for the system to be termed colloidal the particle size should range between 1-1000 nm [32]. The random movement of particles within a solution is due to the natural kinetic energy known as Brownian motion. Thus, causing particle collision and depending on the forces between them they can either attract or repel [33]. A silica solution is considered stable if the particles remain disperse and do not rapidly settle or aggregate. Theoretically, when only taking into account the gravity and viscous drag force, smaller particles are better dispersed in solution and will take longer to settle. In a stable colloidal suspension the electrostatic repulsive forces should be greater than the attractive forces (van der Waals forces) in order to prevent the particles from aggregating. Furthermore, the *pH* and ionic strength of the solution in which the particles are held influence particle stability [34]. Depending on the application, it can be desirable for the particles to be well dispersed or aggregated. For instance, in bioapplications where the initialisation of the nanoparticle (NP) into cells is vital then a stable colloidal suspension is preferred [35], while in water treatment the problem encountered is that these NPs can be very stable in natural water and with aid of coagulant polymers the NPs aggregates and sediments so they can be easily removed via the purification process [36]. The different types of aggregation are conservation, gelation, coagulation and flocculation (Figure 1.6). Conservation is the process where concentrated liquid phase is formed which is immiscible in the aqueous phase, as the absorption of material on the particle surface leads to its reduced hydrophilicity. Gelation is the formation of a three-dimensional network in which particles are linked into branches. This results in an increased viscosity followed by the formation of a solidified network that retains the liquid. In coagulation the particles form closely packed clumps with each another, while in flocculation the particles form bridges together that links them [37, 38].



*Figure 1.6: Stable colloidal nanoparticles undergoing the flocculation and coagulation process of aggregation.*

### 1.3.1. Stabilisation

NPs may be stabilised via steric stabilisation or by creating a surface charge on the NPs (Figure 1.7).

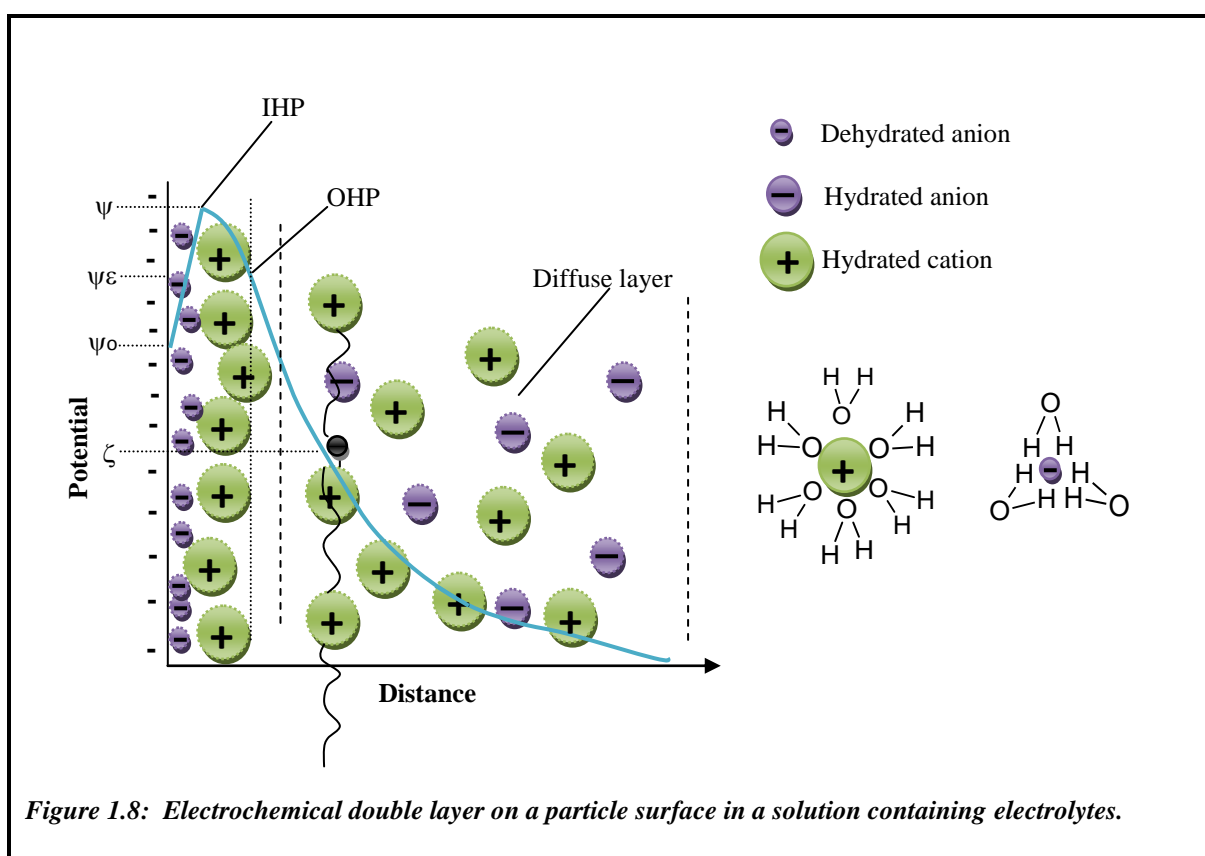


Capping agents can be a very valuable tool for the production of monodispersed NPs; however they themselves have properties which in turn make it difficult to distinguish between the properties of the NPs and capping agent.

#### 1.3.1.1. Surface charge

A major factor determining the surface properties is the overall surface charge of the NPs. The surface charge gives an insight into the interaction between particles; so gaining greater understanding of the dispersion characteristics, for example dispersive stability, the viscosity, flocculation and film forming abilities. Alternatively, by creating a surface charge on the NPs one can overcome this problem of aggregation [11]. The stability of lyophobic colloids has been described by the well-known Debye Landau Verwey Overbeek (DLVO) theory. The electrochemical double layer (EDL) is a term used to describe the structure that coats an object when it is placed in a solution. The interface

between two phases, whether it is solid/ liquid, liquid/ liquid or liquid/ gas, is different in comparison to properties in the bulk phase. This can be explained by the phase boundary having different distribution of electrical charges, therefore producing an electrical double layer which has a potential that is different to both phases. This electrochemical double layer can be described by the Stern model. This model is illustrated in Figure 1.8, showing the charge distribution of particles in electrolyte solutions. A monolayer of the electrolyte is adsorbed onto the particle surface causing it to become negatively charged. This is known as dehydrated ions and the area of the monolayer of ions is known as the inner Helmholtz plane (IHP). This adsorb monolayer may be anions or cations, depending on if they are “indifferent” or “specifically adsorbed” ions. There is a chemical interaction between the particle surfaces when the ions are specifically adsorbed, such as proton interacting with particle surface containing carboxylic groups. Charge reversal can occur because the interaction of ions with surface is very strong. However, if the surface and ions have the same charge it will lead to a higher overall potential.



If specifically adsorbed ions were not present then there would be partially or fully dehydrated counter-ions in the inner layer. If the particles with a negative surface were in a solution of NaCl, it would be the Na ions that lead to a potential ( $\psi_i$ ).

The second layer of ions is known as the outer Helmholtz plane (OHP); it consists of hydrated rigidly bound counter-ions that cause the potential to decrease ( $\psi\delta$ ). These two planes (IHP and OHP) with a thickness ( $\delta$ ) are called the Stern layer.

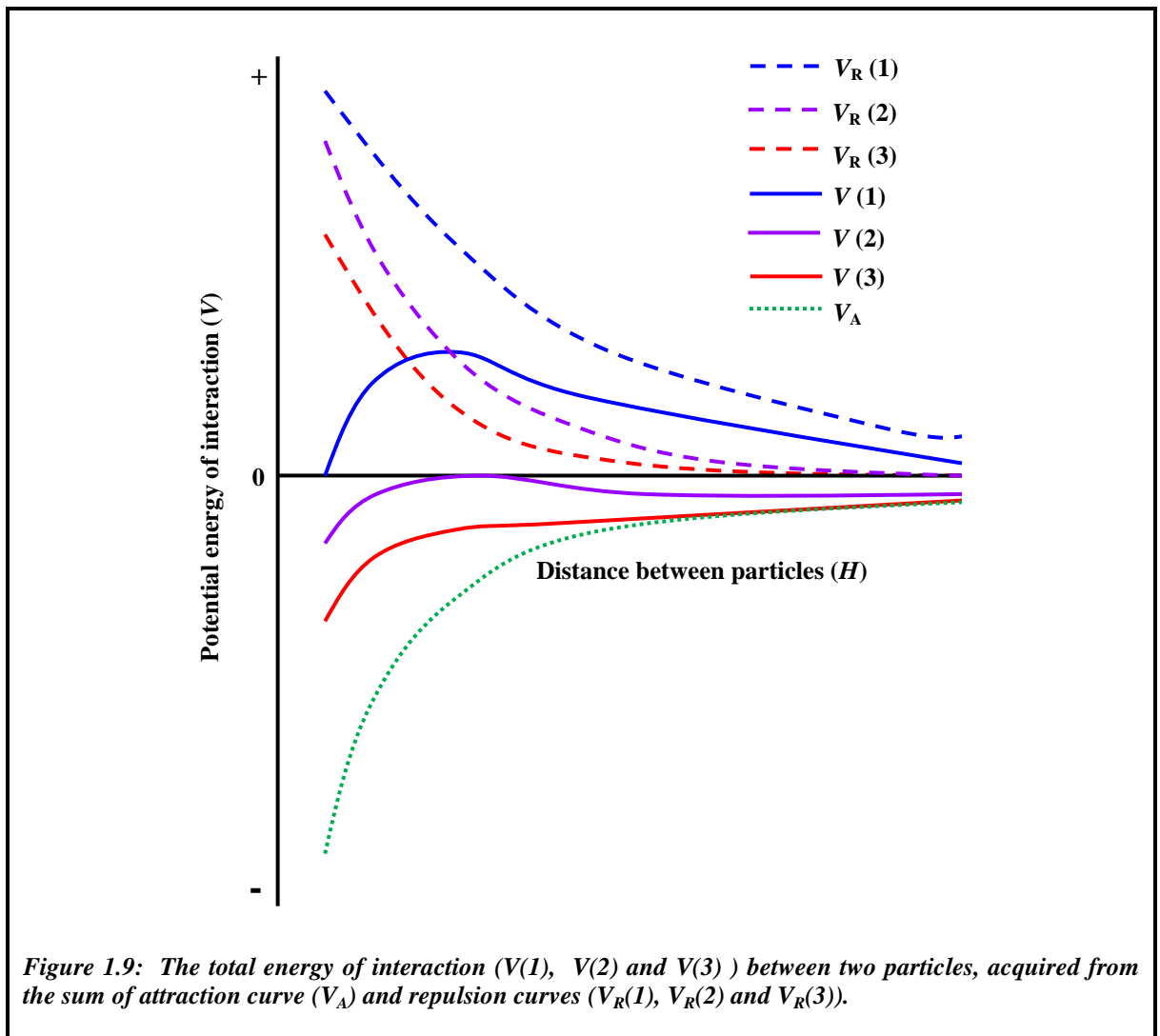
The sol-gel method is the favoured precipitation method as there are various ways of controlling the properties of the NPs, although in mass production it is often difficult to control the kinetics of the crystal growth resulting in particle aggregation along with poly-distribution [39, 40]. The discovery of developing an organised array of monodispersed SiNPs has caused substantial impact in research, leading researchers to refine Stöber method in order to obtain small NPs [19], dye incorporated silica [41] and coating them with inorganic groups.

#### ***1.3.1.1.1. Debye Landau Verwey Overbeek theory***

The DLVO theory is the basis for the understanding of colloid and interface science. Originally Derjaguin and Landau in 1941 developed the theory of stability of colloidal solutions, which was dependent on van der Waals attraction and electrostatic repulsion. The colloidal stability theory was further confirmed by Verwey and Overbeek. An advantage of working in the nano-scale is the higher surface area per unit mass in comparison to bulk materials. So when reducing the particle size or volume it in turn increases the surface area. This generally leads to high surface energy which can cause the NPs to react with each other resulting in aggregation [11]. The DLVO theory determines the interaction between charged surfaces in a liquid environment. A basic explanation of the DLVO theory is the sum of attractive and repulsive forces because of double layer of counterions, where the attractive forces ( $V_{Total}$ ) are the van der Waals attraction ( $V_A$ ) and the repulsive forces are original electrostatic forces ( $V_R$ ) (Equation 1.5) [42, 43].

$$V_{Total} = V_R + V_A \tag{1.5}$$

In colloidal suspension, the charged particle surface forms a rich surrounding diffuse layer of oppositely charged ions. Both the charged particle surface and the diffuse layer result in an electro-neutral entity. When two charged surfaces come close to each another the diffuse layer overlaps forming an osmotic pressure between the surfaces, this result in an electrostatic repulsive force that keeps the particles apart. Increasing the electrolyte concentration within a colloidal suspension leads to the compression of the diffused layer, causing the particle surface potential to decrease and hence the repulsive forces to reduce. The reduction in the repulsive forces may result in the particles being able ot overcome the electrostatic energy barrier thus leading to aggregation, as illustrated in the potential energy curves (Figure 1.9).



Where,  $V(1)$  corresponds to the total potential energy curve for a lyophobic colloid that has repulsive energy maxima ( $V_R(1)$ ) and therefore the colloidal solution is well dispersed.

The addition of electrolytes into the colloidal solution, total potential energy curve  $V(2)$ , results in the van der Waals attraction predominating the repulsive energy ( $V_R(2)$ ) as the energy barrier has just been removed. As this is the minimal amount of reduction in repulsive force to remove the energy barrier it is therefore also referred to as the critical coagulation concentration. On addition of higher concentration of electrolytes the energy barrier is further reduced resulting in a faster aggregation, the total potential energy curve  $V(3)$  [31].

### ***1.3.1.1.2. Non-DLVO Interactions***

The well-known DLVO theory, which is used to describe the stability of particles within numerous colloidal systems [44-48], fails to recognize additional interactions within some colloidal systems such as silica solutions [49-51]. Firstly, the solvent is considered to be a dielectric continuum and any interaction between the surfaces to solvent and solvent to solvent is disregarded. Therefore, any additional repulsion ( $V_{Solv}$ ) caused by a highly structured hydration layer surrounding the particle surface is ignored. The steric repulsion ( $V_{Ster}$ ) is also ignored, such as when surfaces containing grafted polymers come close to each other. Furthermore, ionic species are considered as point charges. Point charge is the dimensions of the charge become smaller according to the distance of the charge or at any distance point from the charge, thus this is an inaccurate estimation of any interaction between the ions to surface, solvent or ion. The DLVO theory considers ions to be infinitely interacting with particle surfaces and at an equal concentration and equal charged ions should have identical influences on the systems. Furthermore, not only the charge but also the type of electrolyte influences the system (known as ion specificity).

This theory is valid for silica particles in the presence of alkali and for larger particles. According to the DLVO theory silica particles at  $pH 2$ , which have no charge, should be in the least stable region. However, this is contrary to previous studies due to the possibility of steric stabilisation as the water molecules produce a monolayer via hydrogen bonding to the particle surface attached hydroxyl groups [37, 38, 52].

In order to produce well dispersed NPs it is important to understand the surface properties, which in turn affect the dispersion characteristics.

### ***1.3.1.1.3. Ion specificity***

In colloidal systems the ion specific adsorption influences the stability of the dispersion. Ions that are closer to the particle surface have a greater screening efficiency and thus lower concentrations of electrolyte are capable of destabilising the dispersion [53]. The Stern model describes the ion adsorbability; where the size and charge influence the ions adsorption. For instance, highly charged ions have greater adsorbability and in the case of equally charged ions the smaller sized [54, 55]. Ions can be categorised depending on how they interact with the solvent [56, 57]. Structure-marker ions, such as  $\text{Li}^+$  and  $\text{Na}^+$ , are referred to as ions that cause structure water forming in their presence. While in structure-breaker ions the ion cause the solvent to become less structured compared to the bulk phase. Therefore, the particle surface can be referred to as structure-marker and structure-breaker surface as they can promote or destroy water structures [58, 59]. The adsorption due to numerous oxides can be described as like seeks like. Oxides that have a high isoelectric point (IEP), such as aluminium, are structure-marker surface and thus the structure-marker ions will adsorb on their surface, while structure-breaker surfaces have low IEP such as silica [58, 60].

The ion to ion interaction in the double layer may result in an attractive electrostatic pressure between two surfaces [53, 61]. If this attractive electrostatic pressure is more dominant than ion to ion correlation interaction occurs. This is a result of charge fluctuations in the system, which is similar to dispersion interactions; however the attraction is stronger than the van der Waals attractive forces [61, 62]. When two approaching surfaces containing high ion density results in a double layer interaction it is repulsion. Although, when the ions are adsorbed close to the surface than this results in lower ion density at the midplane and thus the attractive force predominate.

### ***1.3.1.2. Surface stabilisation***

To prevent sedimentation, to maintain the NPs in dispersed form the surface may be modified with molecules. These molecules that surround the NP are known as capping agents. Capping agents can be categorised as polymers, biological or organic molecules.

### ***1.3.1.2.1. Hairy model theory***

A previous study, conducted by Kobayashi *et al.* [52] confirms that larger SiNPs follow the DLVO theory. At low ionic strengths and increasing *pH* the rate constant decreases, while at high ionic strength the aggregation becomes fast. Also, at low *pH* and high ionic strength the aggregation rate is slower and in these conditions the 30 nm and 50 nm SiNPs are well dispersed. Furthermore, it was observed that at higher *pH* the smaller SiNPs remained completely stable. Therefore, this concludes that smaller SiNPs, less than 80 nm, contain additional repulsive forces. These forces are described as postulating hairy layers comprising of poly (silicic acid) chains surrounding the particle surface [52].

## **1.4. Mesoporous nanoparticles**

Porous materials are predominately synthesised via sol-gel precipitation method contain surfactant molecules that behave as a template for the growth of material around them. Porous materials may be macroporous if the pore sizes are greater than 50 nm. If the pore sizes are between 2 to 50 nm then the materials is mesoporous, while pore sizes smaller than 2 nm are known as microporous.

In 1992 Beck *et al.* discovered that these mesoporous materials consisted of ordered porous structures. This allows mesoporous nanoparticles (MNP) to be used in sensing and drug delivery applications. However, the precipitations of these porous NPs alone do not make them a sufficient vehicle for drug delivery systems. In order for these particles to be effective in these systems the internal channel must be surfactant free to produce a porous network [63]. The main focus of investigation for MNP is silica based, this is because they are inexpensive, chemically inert, thermally stable and known for having no toxicological side effects [64].

### **1.4.1. M41S family**

The synthesis of mesoporous silica materials of various morphologies have been reported, the two main families are M41S (Figure 1.10) and SBA.

Mobil Research and Development Corporation in 1990's were the first to report the synthesis of the MCM-41, which is the most common of the M41S family and is produced

with aid of a cationic surfactant [64, 65]. The extensive use of these MNP in various applications, such as catalytic sieves, is due to the regular arrangement of pores within the NPs, thermal stability and large surface area [65].

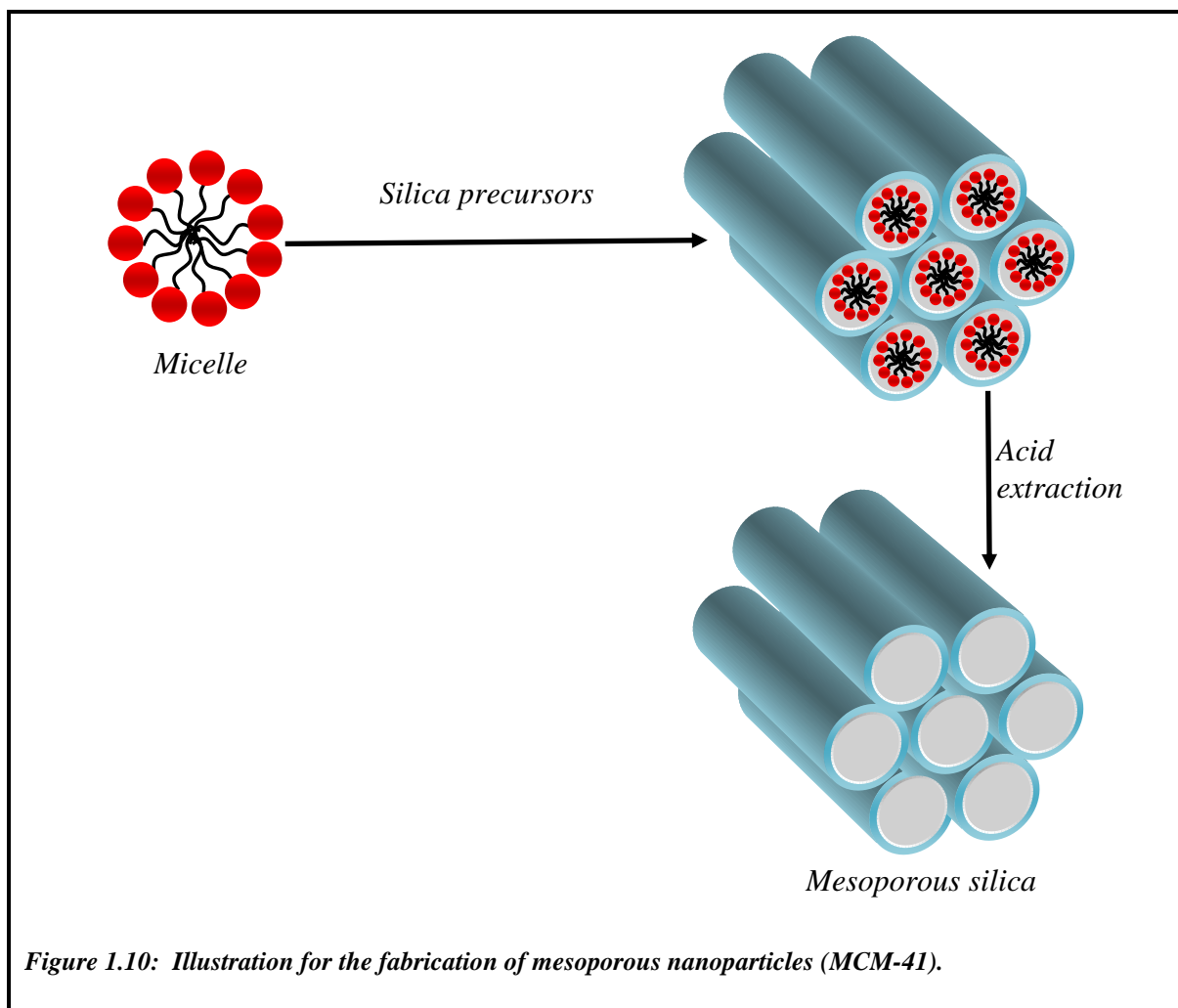


**Figure 1.10:** Illustration for the fabrication of mesoporous nanoparticles (MCM-41).

The discovery of this series has caused researchers to alter the structure directing agent (surfactant) and see how it affects the pore channels, such as the use of anionic surfactant like quaternary ammonium salts or non-ionic polyethylene oxide surfactant [66]. The SBA-15 MNP has uniform hexagonal pores that range between 5-15 nm. The SBA-15 are synthesised with aid of copolymer Pluronic 123 ( $\text{EO}_{20}\text{PO}_{70}\text{EO}_{20}$ ) acting as the template under acidic conditions in the presence of silica precursor (such as TEOS) [67]. The pore sizes for this MCM-41 are hexagonal and normally smaller than 5 nm. These synthetic reactions commonly require the aid of an organic template (such as hexadecyltrimethylammonium bromide). Depending on the molecules that are placed into the pores, for its diffusivity application, the pore diameter may be tuned. Nandiyanto *et al.*

fabricated spherical silica MNP with pore sizes between 4-15 nm by changing the styrene (template) and hydrophobic molecule concentration [64].

## 1.5. Characterisation

A variety of different techniques were used to characterise the NPs as described in the following section. The NPs sizes were determined by electron microscopy. The hydrodynamic size and stability were tested based on their Brownian motion in suspension. Furthermore, porous NPs were analysed by nitrogen ( $N_2$ ) sorption and diffuse reflectance infra-red Fourier transform spectroscopy (DRIFTS). It is important to fully characterise NPs before utilising them in their particular application as it allows for a greater understanding of the underlying factors which may affect potential applications.

### 1.5.1. Electron Microscopy

High magnified images of specimens are produced with electron microscopy. Depending on the instrumentation, the electron beam may either travel through or on the surface of the specimen as shown Figure 1.11. The two types of electron microscopes are scanning and transmission electron microscope.

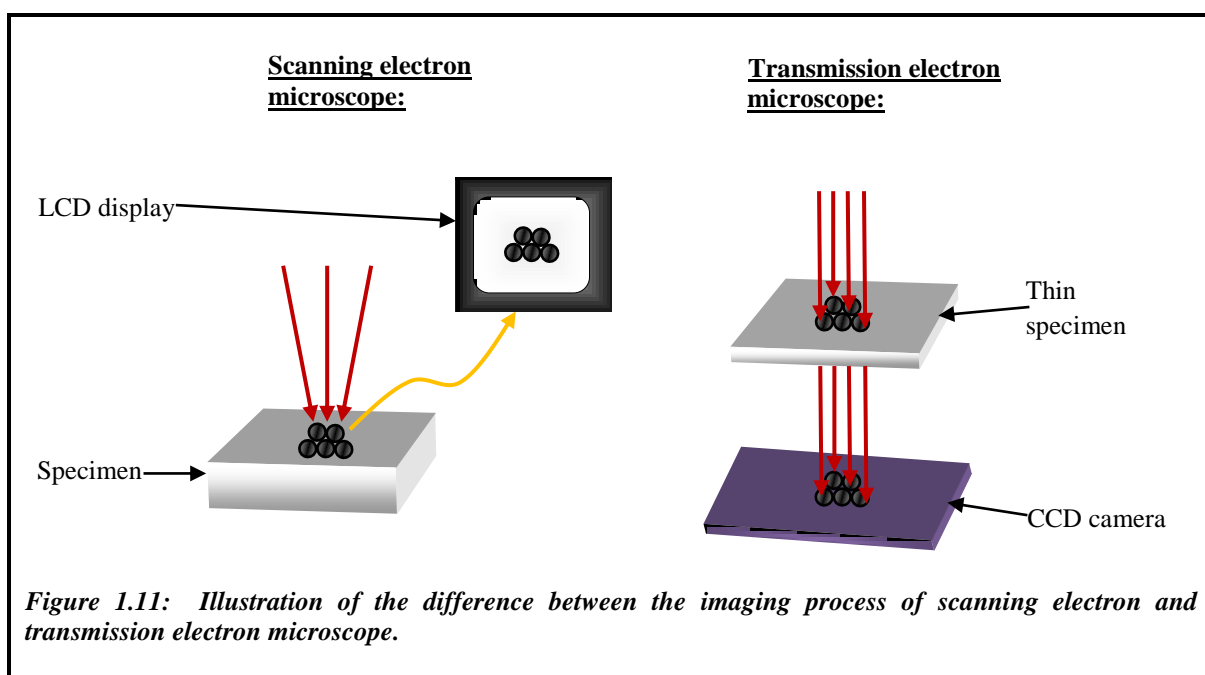


*Figure 1.11: Illustration of the difference between the imaging process of scanning electron and transmission electron microscope.*

### ***1.5.1.1. Scanning electron microscopy***

The JEOL 5600LV scanning electron microscope (SEM) was used for measuring the particle sizes (Figure 1.12). This instrument produces images of both conductive and non-conductive materials. Samples which are non-conductive are usually coated with metal to prevent the material from charging under the microscope. As this SEM had low vacuum capabilities it is able to image samples which are non-conductive and contain either moisture or oily residues. The acceleration voltage of the instrument is between 0.5 to 30 kV and has a resolution of 3.5 nm when optimum conditions are achieved.

The SEM contains a tungsten filament which produces high energy electron beam that images the sample in a raster fashion. The electrons produce signal of the surface topography by interacting with the atoms in the sample. The two types of signals produced by this SEM are secondary electron and back-scattered electrons (BSE). The most common detection is secondary electron imaging where electrons produced by the ionisation of the atoms in the sample. The term ‘secondary’ refers to the electrons not being generated by the primary source of radiation. For instance the primary source of radiation is from the electron beam generated by the tungsten filament and it ionises the surface atoms on the sample to produce secondary electrons. BSE are detected by reflection of electron wave into the direction they commenced from. As the electrons are scattered the reflection is diffused [68].



***Figure 1.12: Image of a scanning electron microscope (JEOL 5600LV).***

***1.5.1.2. Transmission electron microscopy***

Transmission electron microscopy (TEM) was used to measure particles diameter along with observing particle morphology (Figure 1.13). Unlike SEM where the electrons interact on the surface or near surface of the specimen, TEM detects the electrons which are transmitted through the specimen. The interaction of the electron beam as it passes through the specimen generates an image [68].

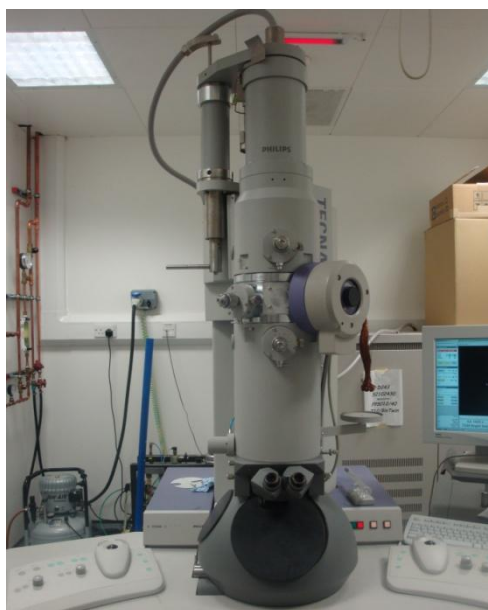


***Figure 1.13: Image of a transmission electron microscope (Philips Technai 12 Biotwin TEM).***

### **1.5.2. Photon correlation spectroscopy**

Photon correlation spectroscopy (PCS) measurements were carried out using Malvern Zetasizer Nano ZS (Figure 1.14). PCS is also known as dynamic light scattering and quasi elastic light scattering.

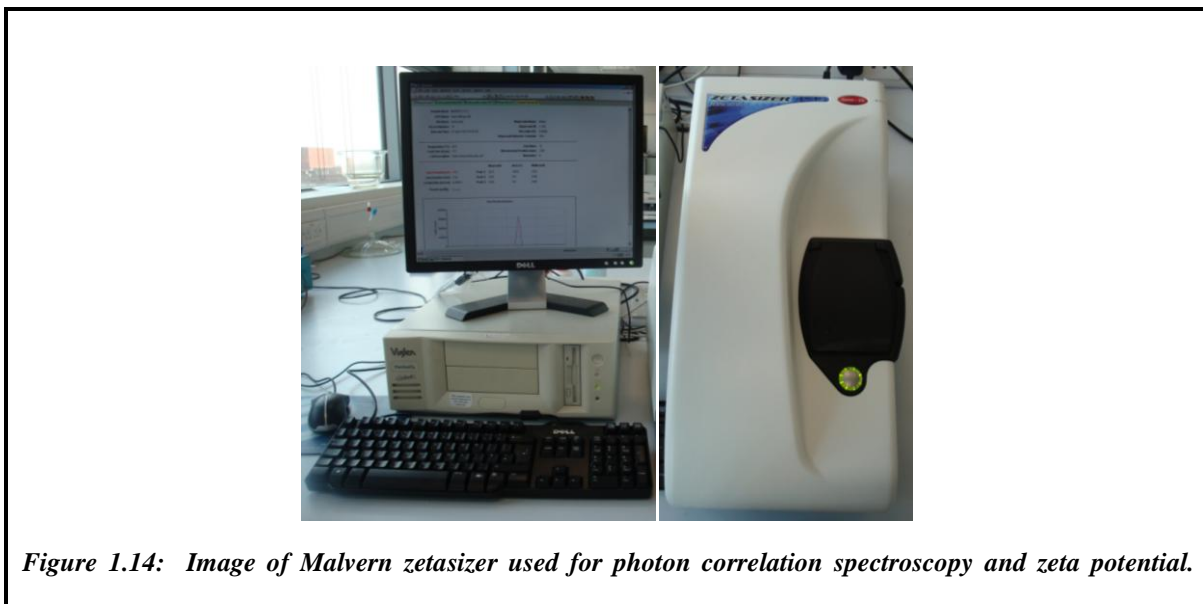


*Figure 1.14: Image of Malvern zetasizer used for photon correlation spectroscopy and zeta potential.*

The instrument measures the Brownian motion and relates this to the particle size. This is conducted by a laser illuminating the sample and analysing the intensity fluctuation of scattered light. For instance, when particles are illuminated with the light it results in the scattering of light in all directions. Furthermore, if there were a screen near the particle it would be illuminated by the scattered light. As there are thousands of particles in the solution, instead of a single particle illuminating the screen there will be thousand producing a speckle pattern. The bright areas in the speckle pattern are the illuminated light and the dark areas are where no light has been detected. The propagation waves of the light being scattered by the particle are illustrated in Figure 1.15. The bright area is of the scattered light from the particle being displayed on the screen as the same phase is constructively forms the bright light, while the dark areas occur as the phase addition is destructive and they cancel out [31].

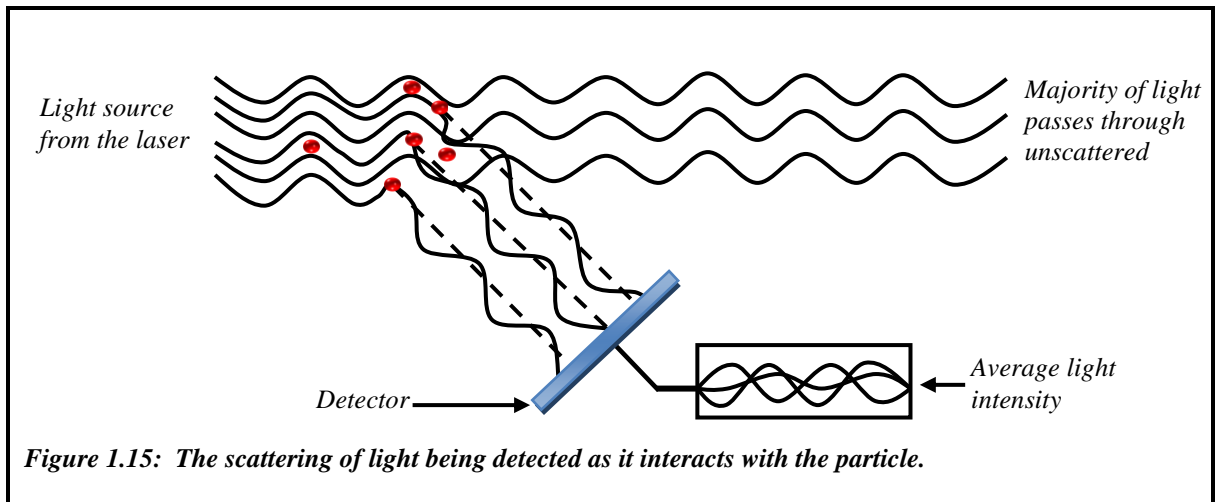


*Figure 1.15: The scattering of light being detected as it interacts with the particle.*

However, a suspension of particles will never be stationary and constantly move due to the Brownian motion. Furthermore, in accordance with the Brownian motion the smaller particles will move faster in the solution in comparison to larger ones. The relationship between particle size and motion is known as the Stokes-Einstein equation. The movement of the particles will result in the speckle pattern to move, and thus the constructive and destructive phase will result in the dark and light areas to increase and diminish. In simple terms the light intensity seems to fluctuate and the Zetasizer measures the rate of intensity fluctuation and converts this into particle size [31].

### **1.5.3. Laser Doppler velocimetry**

The Zeta potentials of dispersed colloidal nanoparticles were obtained using Malvern Zetasizer Nano ZS. The Zeta potential is a measurement of the magnitude of forces between particles and is determined by electrophoretic mobility. The sample undergoes electrophoresis and using laser Doppler velocimetry (LDV) and the velocity is measured. For well dispersed suspension of nanoparticles it is necessary for there to be relevant amount repulsive forces between them. Alternatively, there may be attractive forces between the NPs leading to aggregation [31].

#### ***1.5.3.1. Electrical double layer***

The net charge of the particle influences the ions which will surround the interfacial region, and thus causes concentrated counter ions surrounding the surface. This is known as the electrical double layer which surrounds each particle. As previously describe (Chapter 1; Section 1.3.1.1), the ions which are closely attached to the particle surface are referred to as the Stern layer. In the outer region the ions are less firmly attached and this is referred to as the diffused region. There is a natural boundary which exists within the diffused layer, and as the particle moves so do the ions that are within this boundary. However, ions that are beyond this boundary do not move with the particle. This boundary is called the surface of hydrodynamic shear or the slipping plane and the potential which exist at this boundary is referred to as the zeta potential (Figure 1.16). In order for particle to be well dispersed in solution the zeta potential must be largely negative or positive, as particles will repel each another. The zeta potential value for dividing stable particles from unstable is +30 mV or -30 mV. Therefore, particle with a greater zeta potential than +30 mV or more negative value than -30 mV is considered stable [31].

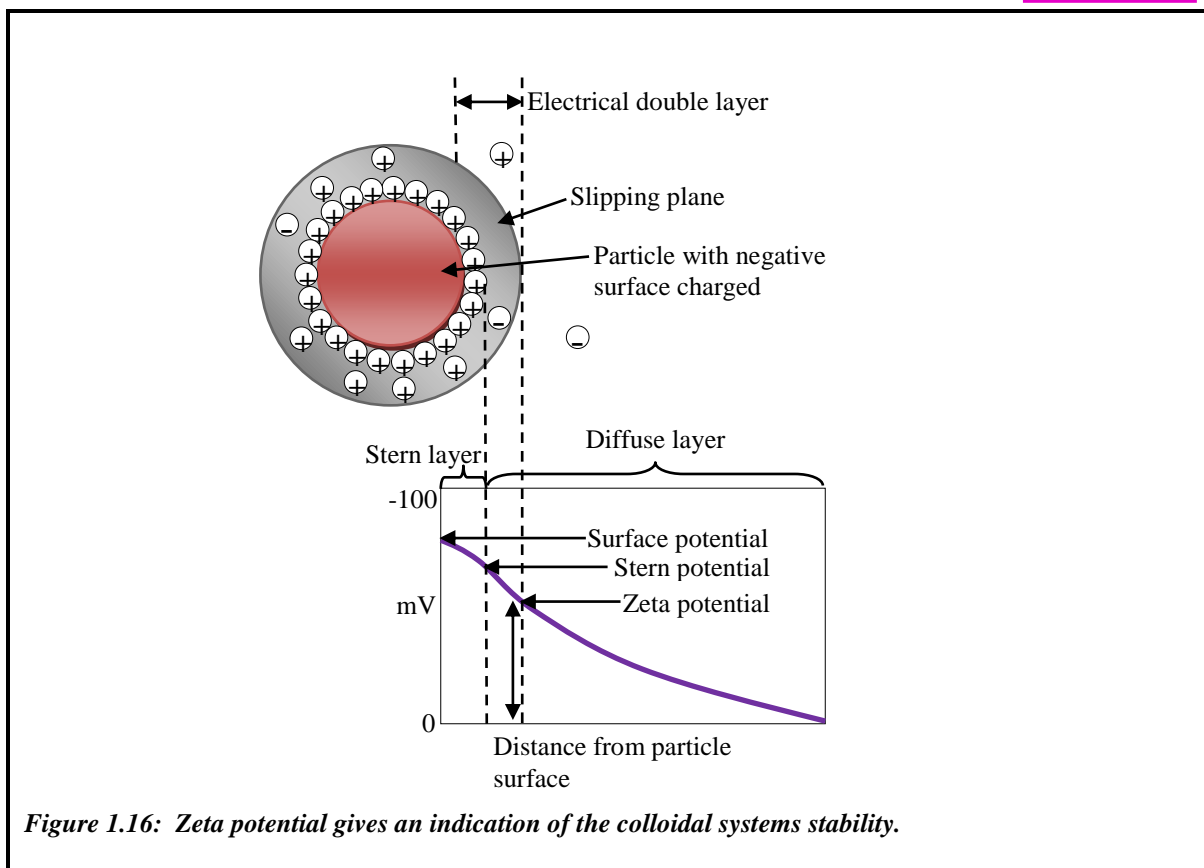


Figure 1.16: Zeta potential gives an indication of the colloidal systems stability.

The zeta potential is calculated from the measurement of the solutions electrophoretic mobility (Figure 1.17). This is conducted by placing the sample in a cell with electrodes at each side in order to apply the potential. The particle will move towards the electrode of opposite charge and measure its velocity, which will be converted into unit field strength of mobility [31].

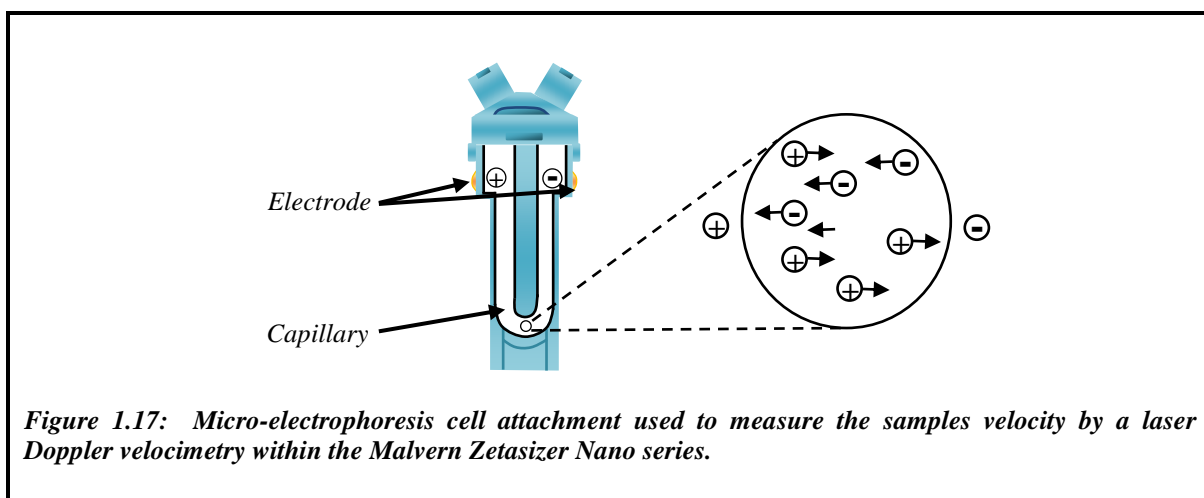


Figure 1.17: Micro-electrophoresis cell attachment used to measure the samples velocity by a laser Doppler velocimetry within the Malvern Zetasizer Nano series.

### 1.5.4. Diffuse reflectance infra-red Fourier transform spectroscopy

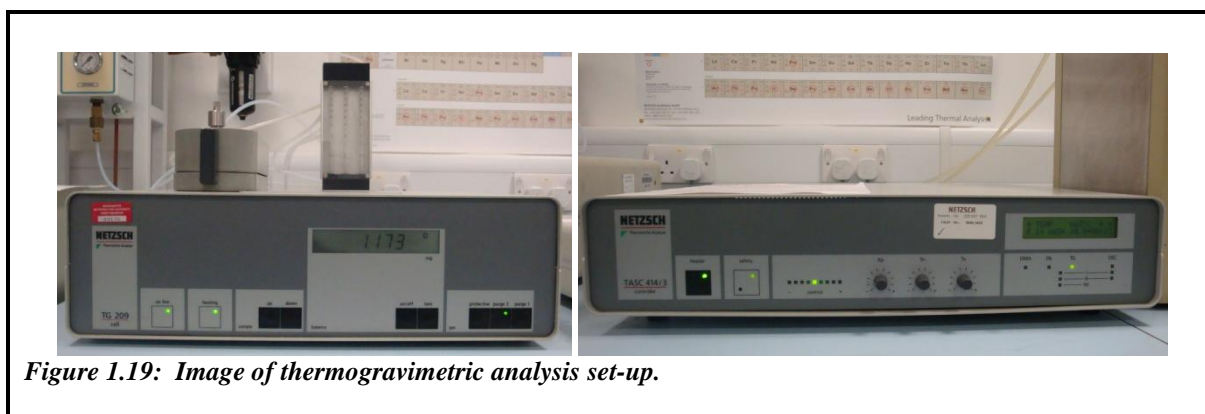
DRIFTS analysis was conducted using a Thermo Nicolet NEXUS 670 FTIR spectrometer (Figure 1.18). Infra-red spectroscopy is a vital analytical tool for acquiring the specific chemical functional groups present within the sample. The instrument detects vibrations caused by the infra-red beam interacting with the matter. Different chemical functional groups result in the infra-red light being adsorbed at a specific wavenumber which causes vibrations. The vibration corresponds to stretching, bending or contraction of the specific groups within the sample. The wavenumber band identifies the relevant functional groups present and is not altered by the other chemical groups within the molecules, temperature or pressure. DRIFTS is a infra-red technique where data collection is conducted with ease as no sample preparation is required because the powder sample is directly analysed. The infra-red beam is reflected and transmitted at various intensities from the sample depending on the chemical groups within the molecule. The term diffuse reflectance refers to the infra-red light being reflected from the roughness of the sample's surface and collected by either an ellipsoid or paraboloid mirror [69].



*Figure 1.18: Image of diffuse reflectance infra-red Fourier transform spectroscopy.*

### 1.5.5. Thermogravimetric analysis

The thermogravimetric analysis (TGA) is a thermal method use for the determination of mass loss as function of temperature (Figure 1.19). The thermogravimetric (TG) curve is mass change against temperature, where the temperature increases uniformly or is kept constant. This is an important analytical technique for determining the purity of the sample and its specific modes of transformation, which is dependent on the temperature range. A TG curve with a sample that has single stage decomposition will contain two characteristic temperatures,  $T_i$  and  $T_f$ .  $T_i$  is the lowest temperature at which the mass change is detectable by the thermobalance under the selected settings, while  $T_f$  is the temperature when the decomposition has been completed. The difference between these two parameters,  $T_i$  and  $T_f$ , is known as the reaction interval. The mass change of a sample due to the increase in temperature, normally linear with time, is known as dynamic thermogravimetry. Alternatively, when temperature is kept constant and the change of mass is measured it is known as isothermal or static thermogravimetry [69].



The TG instrumentation normally consists of four components; the furnace, sample holder, the sensors which detects the sample properties dependent on temperature and the data acquisition system (Figure 1.20). Commonly, the furnace is operated electrically and upon sample analysis it is purged with appropriate gases to allow the sample to decompose as it reacts and/ or burns. The temperature is either measured by a thermocouple or resistance sensor, while mass is measured by a thermobalance. The thermobalance is a highly sensitive electrical device which is capable of measuring small changes in mass (1  $\mu\text{g}$ ). The sample is placed in an inert crucible, such as aluminium, platinum or ceramic [69].

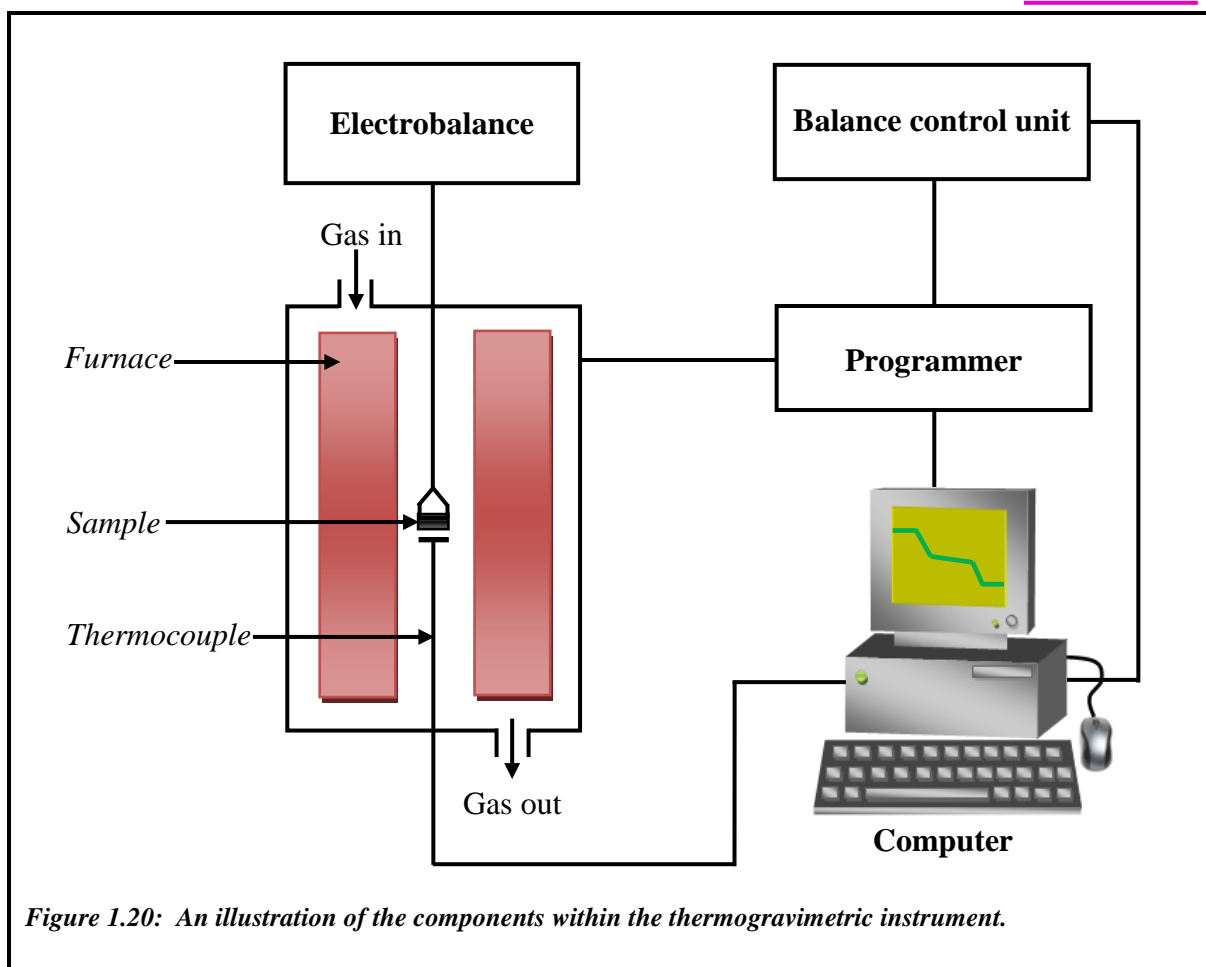
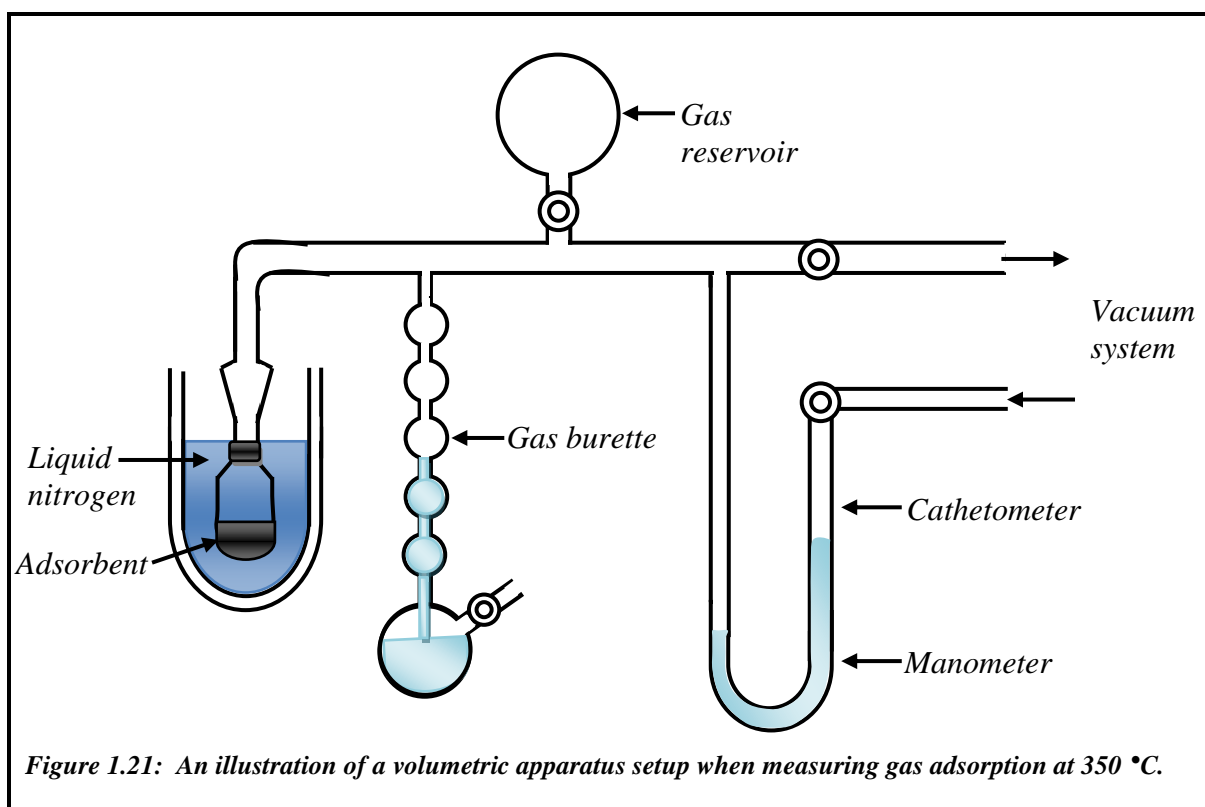


*Figure 1.20: An illustration of the components within the thermogravimetric instrument.*

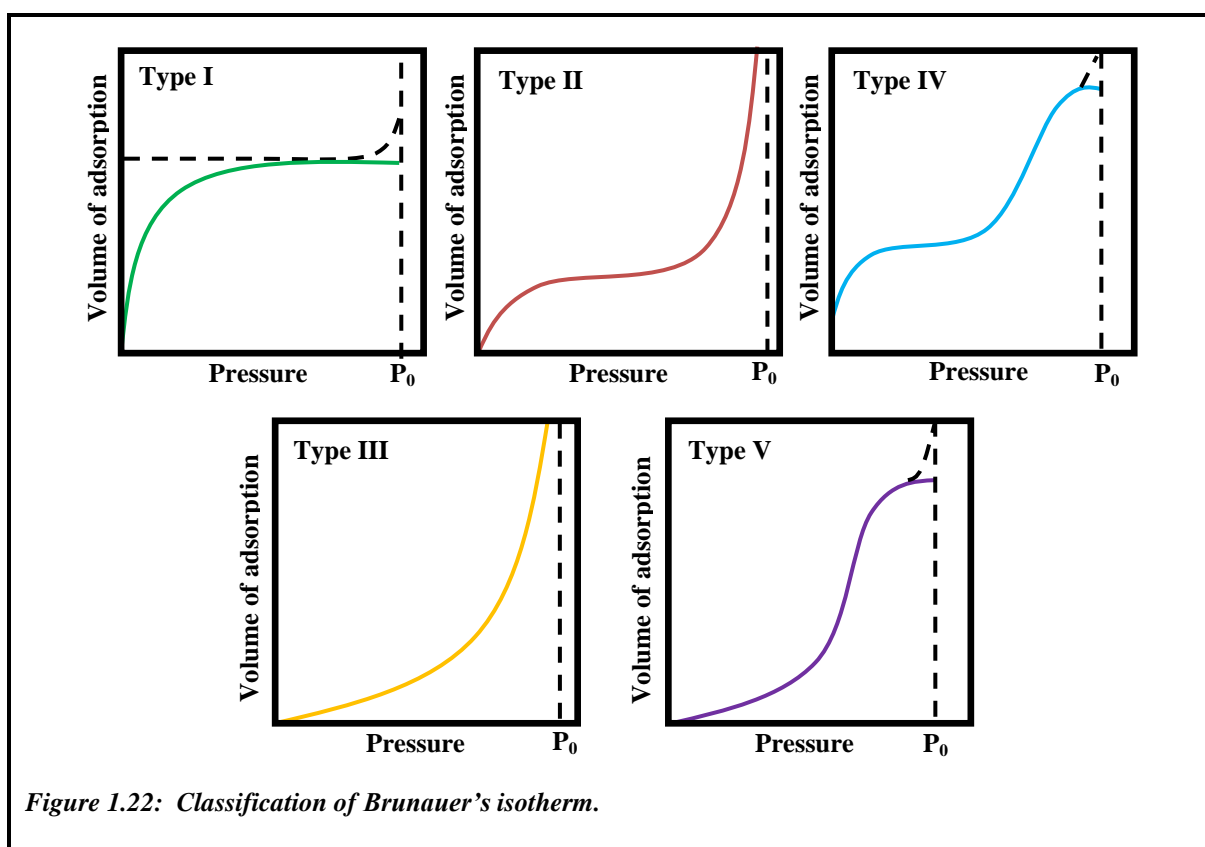
### 1.5.6. Nitrogen sorption

Commonly, for gas adsorption measurements of solid materials they must initially undergo a process whereby majority of previously adsorbed gases and vapours are removed. This process is referred to evacuation where the solid is outgassed to  $c. 10^{-4}$  Torr for several hours in order to remove the physical adsorbed gas and majority of the chemisorbed gas. It is possible to completely remove the total chemisorbed gasses from the solid material by heating the sample to high temperature (100-400 °C), however this may cause the solid to become sintered and thus altering the sorption capacity [31].

The adsorption of gas or vapour onto the sample is measured by introducing a known volume of adsorbate, which is then determined using volumetric or gravimetric analysis. The gas is held within a burette and the pressure is measured using a manometer (Figure 1.21). The volumes within the apparatus are calibrated in order for the amount of gas adsorbed by the absorbent sample to be determined via the pressure at equilibrium. The adsorption isotherm is calculated from a progression of readings obtained at different pressures.



Physical adsorption may involve three phenomena; which are monomolecular adsorption, multimolecular adsorption and condensation in pores or capillaries. Adsorption isotherms have been categorised into five different types (Figure 1.22). Type I isotherm also known as the Langmuir-type isotherm; as pressure increases the adsorption rapidly rise until the limiting pressure is reached. Furthermore, for this isotherm there is a monolayer during adsorption. Previously shown, the physical adsorption on solids that contain fine porous structure, such as adsorption of nitrogen on microporous carbon at 350 °C, have type I isotherm trend. Type II isotherm also known as the sigmoid isotherm; is the multilayer physical adsorption onto a non-porous solid. For instance, the adsorption of nitrogen onto silica gel at 350 °C, have type II isotherm trend. Type IV isotherm undergo a condensation within the capillaries of porous solid samples, followed by the saturation vapour pressure levels off towards the end of the isotherm. The isotherms for these adsorbent have an effective pore diameter in the range of 2-20 nm. The upper limit of the isotherm trend indicates the adsorption is caused by the total pore volume. Type III and V isotherm are similar are both rare, initially there is an initial slow uptake of gas. These isotherms occur when there is a relatively weak adsorption forces within the first monolayer [31].



The surface area analyses of solid materials are commonly measured by the Brunauer-Emmett-Teller (BET) isotherm via volumetric analysis. The porous sample is degassed and exposed to known volume of a particular gas. The amount of gas absorbed by the sample can be quantified by subtracting the volume of gas once the pressure is equilibrated from the initial volume of gas injected within the system. The N<sub>2</sub> sorption analysis was conducted with BET surface area and porosity instrumentation (Figure 1.23) [31].



*Figure 1.23: Image of the Brunauer-Emmett-Teller nitrogen sorption instrumentation.*

### 1.5.7. Atomic absorption spectroscopy

The atomic absorption spectroscopy is a technique used for the determination of metal concentrations. This is conducted by the light at a particular wavelength passing through a cloud of atoms. The light source is from a hollow cathode lamp and is absorbed by unexcited atoms. Therefore, the amount of light absorbed is proportional to the amount of unexcited atoms, the relationship is described as the Beer-Lambert law (Equation 1.6).

$$\text{Absorbance} = \log \left( \frac{I_0}{I} \right) \quad (1.6)$$

Where,  $I_0$  is the incident intensity and  $I$  represents the transmitted intensity. Absorbance can also be expressed as Equation 1.7.

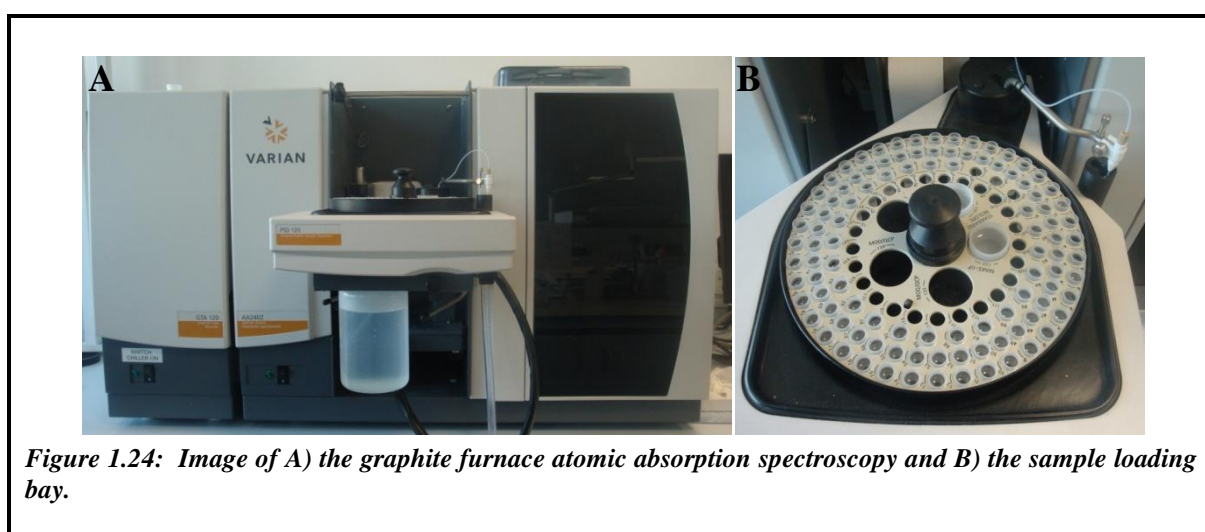
$$\text{Absorbance} = \epsilon c L \quad (1.7)$$

Where,  $\epsilon$  is the absorption coefficient,  $L$  is the length of the absorption path and  $c$  represents the concentration of absorbing atoms. Equation 1.7, shows that if the terms  $\epsilon$  and  $L$  are kept constant than absorbance is directly proportional to the concentration of absorbing atoms. Furthermore, as the terms  $\epsilon$  and  $L$  are constant then measurement of the absorbance should give the atom concentration [69]. Atomic absorption spectroscopy may be analysed using various techniques, such as flame atomic absorption spectroscopy (FAAS) and graphite furnace atomic absorption spectroscopy (GFAAS). Alternative technique commonly used to determine metal concentration within samples is inductively coupled plasma emission spectroscopy (ICP-ES), for instance inductively coupled plasma optical emission spectroscopy (ICP-OES) and inductively coupled plasma mass spectroscopy (ICP-MS). The difference between the two techniques is that one is dependent on atomic absorption while the latter is on atomic/ ionic emission spectroscopic technique. Furthermore, they differ by the way the atomic or ionic species is produced, where atomic absorption uses a combustion flame or graphite furnace and ICP-ES requires plasma.

**Table 1.1:** The limit of detection for Fe using different atomic absorption techniques, values obtained from the Perkin Elmer guide for selecting the appropriate techniques and systems.

Element	Atomic absorption Spectroscopy ( $\mu\text{g L}^{-1}$ )			
	FAAS	GFAAS	ICP-OES	ICP-MS
Fe	5	0.06	0.1	0.0003

From the limit of detection values [70] the methods used to analyse the samples was GFAAS (Figure 1.24), this is due to the high limit of detection along with the low volume of unknown sample required.



The sample is placed into the graphite tube and heated in a series of steps to up to 3000 °C in order to remove components such as the solvent and atomize the sample. The analyte is atomized and retained inside the tube for certain period of time at which light path passes through the sample to produce an absorption spectra (Figure 1.25).

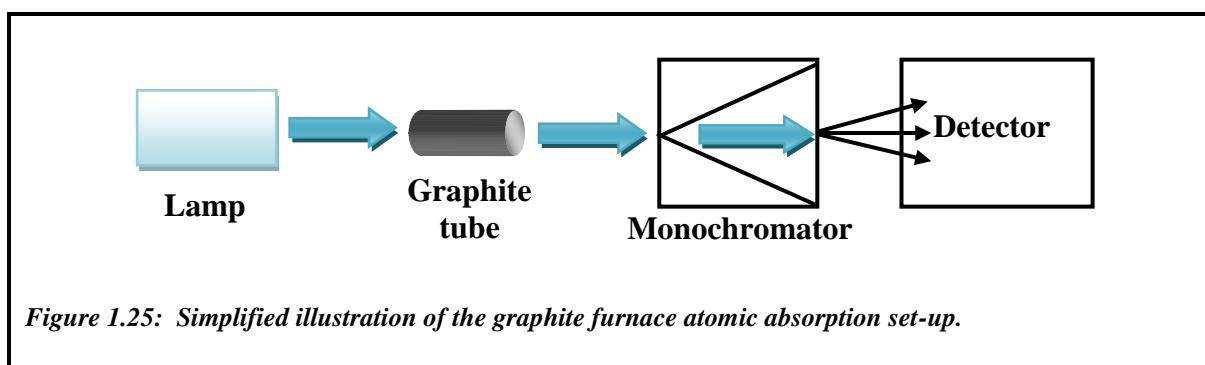
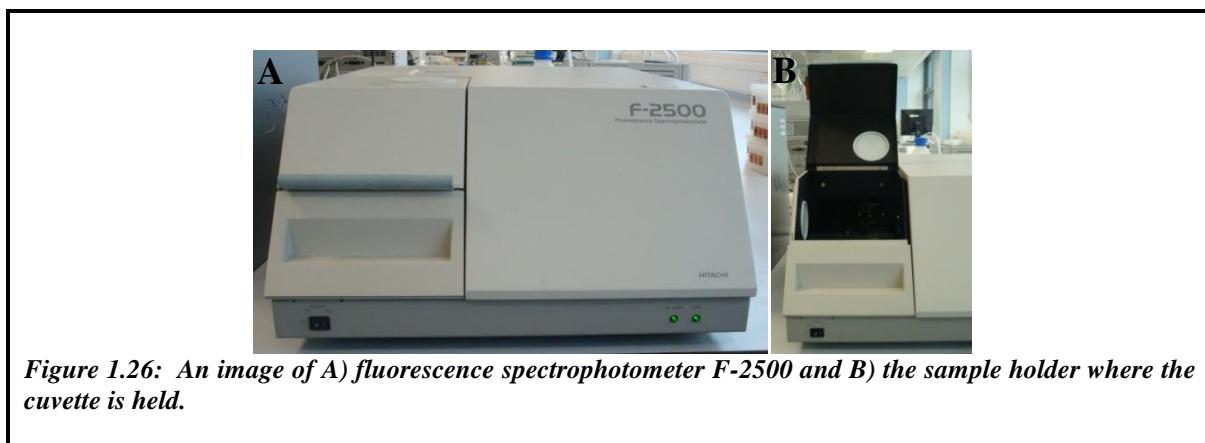


*Figure 1.25: Simplified illustration of the graphite furnace atomic absorption set-up.*

### 1.5.8. Fluorescence spectroscopy

The excitation of fluorescent molecules leads to the energy being lost as heat or emitted through fluorescence. The wavelength of the light (emission wavelength) is longer than the wavelength for the excited molecule, due to the loss of vibrational energy as heat. The fluorescence of samples was measured using a Hitachi fluorescence spectrophotometer F-2500 (Figure 1.26).



Simplified schematic of the fluorescence spectrophotometer is illustrated in Figure 1.27. The light produces a high energy radiation which passes through a monochromator, at which the excitation wavelength of the beam may be selected and it passes through the cuvette containing the sample. Upon excitation the sample fluorescence radiation occurs in all directions. The radiation passes through a second monochromator which is held at right angles to the sample, which allows the fluorescence emitted light to enter the detector [69, 71].

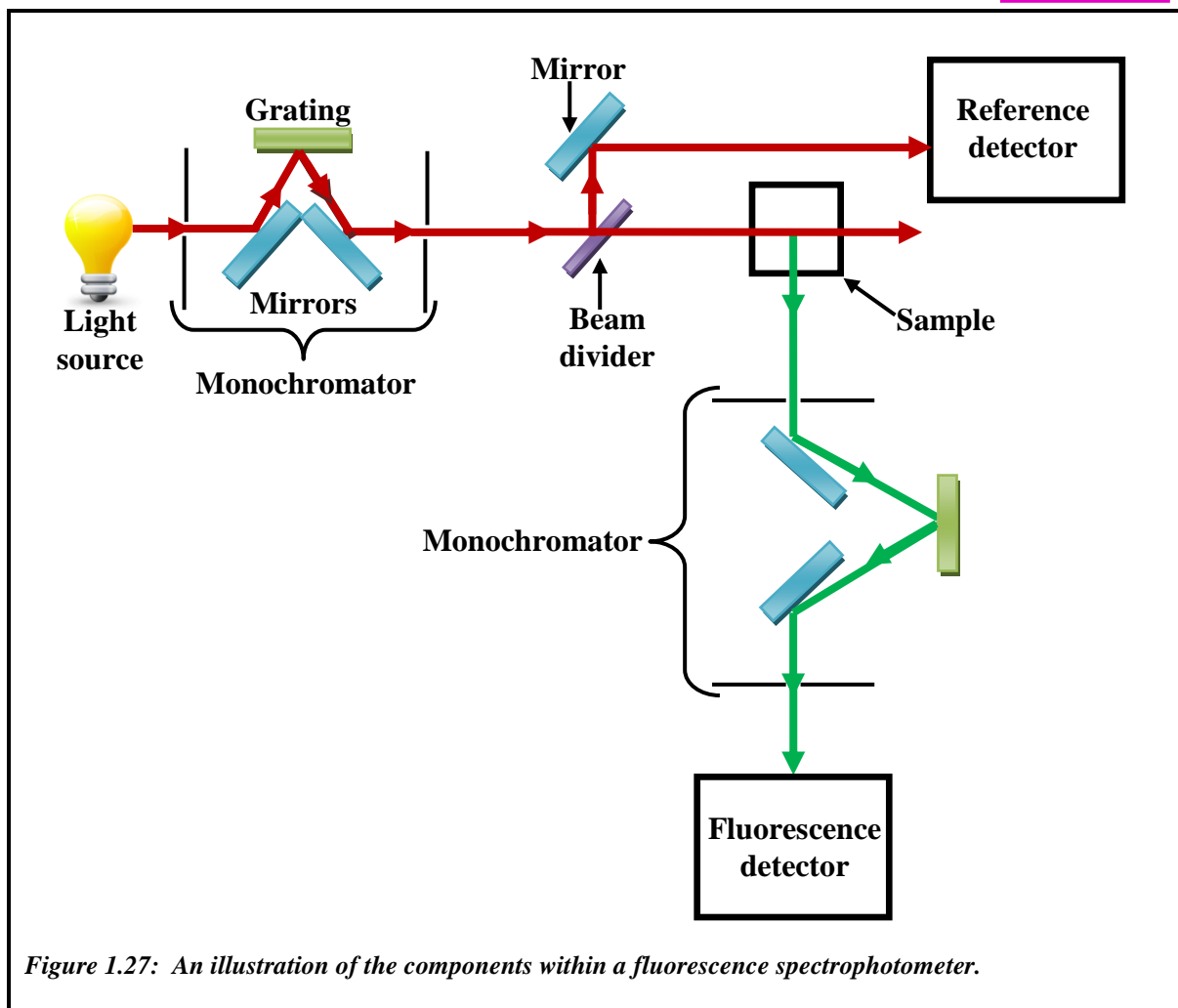


Figure 1.27: An illustration of the components within a fluorescence spectrophotometer.

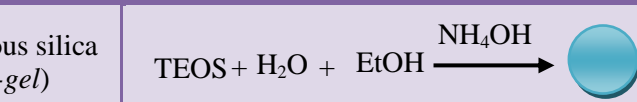
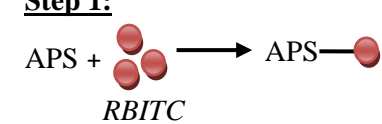
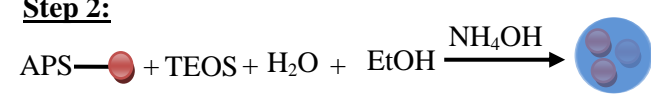
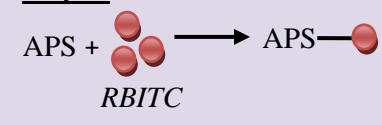
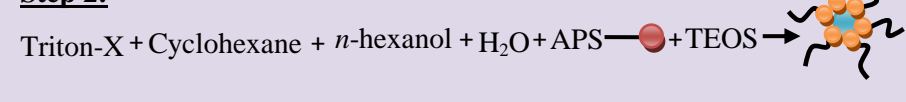
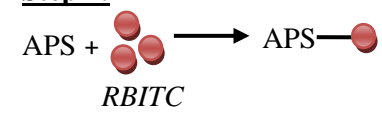
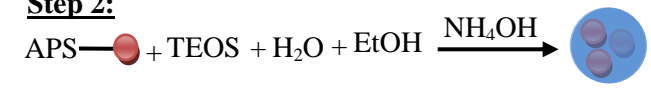
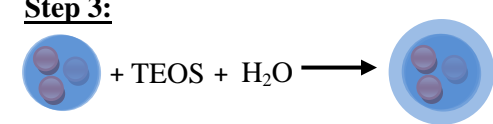
# **Chapter 2**

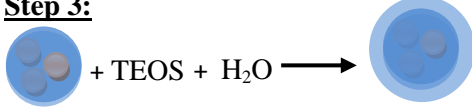
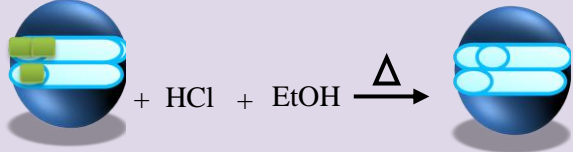
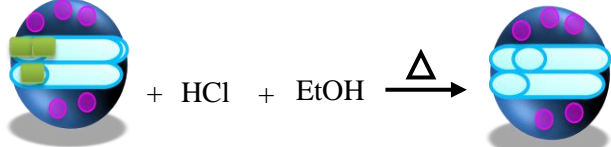
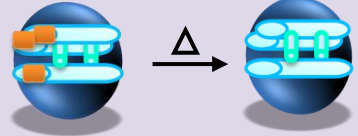
## **Nanoparticle Preparation**

## 2. NANOPARTICLE PREPARATION

The nanoparticles synthesised and characterised in the following chapter is summarised below (Table 2.1).

**Table 2.1: Overview of the types of nanoparticles fabricated in this Chapter.**

Nanoparticle type	Nanoparticle reaction scheme
Amorphous silica ( <i>Sol-gel</i> )	$\text{TEOS} + \text{H}_2\text{O} + \text{EtOH} \xrightarrow{\text{NH}_4\text{OH}} \text{Silica Nanoparticle}$ 
RBITC encapsulate silica ( <i>Sol-gel</i> )	<p><b>Step 1:</b></p> $\text{APS} + \text{RBITC} \rightarrow \text{APS-RBITC}$  <p><b>Step 2:</b></p> $\text{APS-RBITC} + \text{TEOS} + \text{H}_2\text{O} + \text{EtOH} \xrightarrow{\text{NH}_4\text{OH}} \text{Encapsulated Silica}$ 
Silica ( <i>Microemulsion</i> )	<p><b>Step 1:</b></p> $\text{APS} + \text{RBITC} \rightarrow \text{APS-RBITC}$  <p><b>Step 2:</b></p> $\text{Triton-X} + \text{Cyclohexane} + n\text{-hexanol} + \text{H}_2\text{O} + \text{APS-RBITC} + \text{TEOS} \rightarrow \text{Microemulsion}$  <p><b>Step 3:</b></p> $\text{Microemulsion} \xrightarrow{\text{Acetone}} \text{Silica Nanoparticle}$ 
SiRBITC encapsulate silica with silica shell ( <i>Sol-gel</i> )	<p><b>Step 1:</b></p> $\text{APS} + \text{RBITC} \rightarrow \text{APS-RBITC}$  <p><b>Step 2:</b></p> $\text{APS-RBITC} + \text{TEOS} + \text{H}_2\text{O} + \text{EtOH} \xrightarrow{\text{NH}_4\text{OH}} \text{Encapsulated Silica}$  <p><b>Step 3:</b></p> $\text{Encapsulated Silica} + \text{TEOS} + \text{H}_2\text{O} \rightarrow \text{Silica Shell Nanoparticle}$ 

Nanoparticle type	Nanoparticle reaction
<p>SiRu(dpp)<sub>3</sub> encapsulate silica with silica shell (Sol-gel)</p>	<p><b>Step 1:</b>  <math display="block">\text{APS} + \begin{matrix} \bullet \\ \bullet \\ \bullet \end{matrix} \longrightarrow \text{APS}-\bullet</math> <i>Ru(dpp)<sub>3</sub></i></p> <p><b>Step 2:</b>  <math display="block">\text{APS}-\bullet + \text{TEOS} + \text{H}_2\text{O} + \text{EtOH} \xrightarrow{\text{NH}_4\text{OH}}</math> </p> <p><b>Step 3:</b>   <math display="block">+ \text{TEOS} + \text{H}_2\text{O} \longrightarrow</math></p>
<p>MNP (Sol-gel)</p>	<p><b>Step 1:</b>  <math display="block">\text{H}_2\text{O} + \begin{matrix} \blacksquare \\ \blacksquare \end{matrix} + \text{NaOH} + \text{TEOS} \xrightarrow{\Delta}</math> <i>CTAB</i> </p> <p><b>Step 2:</b>   <math display="block">+ \text{HCl} + \text{EtOH} \xrightarrow{\Delta}</math></p>
<p>Fluorescent MNP (Sol-gel)</p>	<p><b>Step 1:</b>  <math display="block">\text{APS} + \begin{matrix} \bullet \\ \bullet \\ \bullet \end{matrix} \longrightarrow \text{APS}-\bullet</math> <i>RBTC</i></p> <p><b>Step 2:</b>  <math display="block">\text{H}_2\text{O} + \begin{matrix} \blacksquare \\ \blacksquare \end{matrix} + \text{NaOH} + \text{TEOS} + \text{APS}-\bullet \xrightarrow{\Delta}</math> <i>CTAB</i> </p> <p><b>Step 3:</b>   <math display="block">+ \text{HCl} + \text{EtOH} \xrightarrow{\Delta}</math></p>
<p>Silicate-1 (Sol-gel)</p>	<p><b>Step 1:</b>  <math display="block">\text{H}_2\text{O} + \begin{matrix} \blacksquare \\ \blacksquare \end{matrix} + \text{TEOS} + \text{APS} + \text{IP} \xrightarrow{\Delta}</math> <i>TPAOH</i> </p> <p><b>Step 2:</b>   <math display="block">\xrightarrow{\Delta}</math></p>

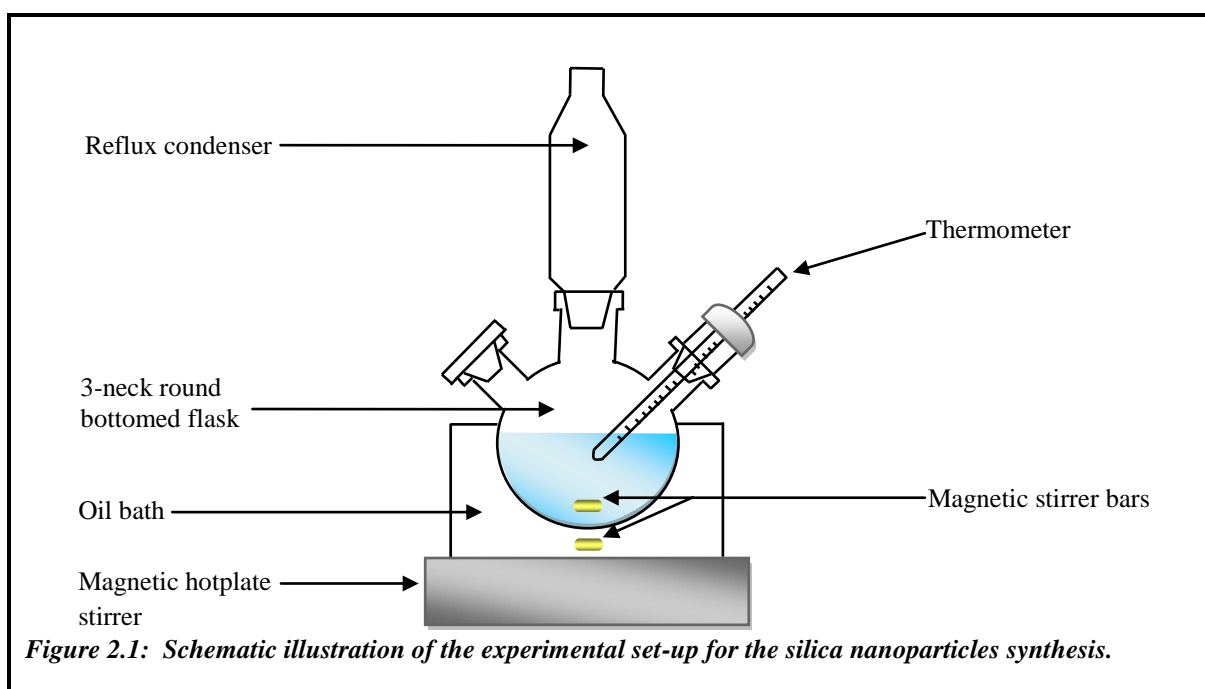
## 2.1. Amorphous Silica Nanoparticles via Sol-gel

### 2.1.1. Materials

Absolute ethanol (EtOH), ammonium hydroxide (NH<sub>4</sub>OH) and tetraethyl orthosilicate (TEOS) were purchased from Sigma-Aldrich (UK). Salt solutions were prepared using sodium chloride (NaCl), potassium chloride (KCl), magnesium sulphate heptahydrate (MgSO<sub>4</sub>·7H<sub>2</sub>O), sodium bicarbonate (NaHCO<sub>3</sub>), potassium phosphate monobasic (KH<sub>2</sub>PO<sub>4</sub>), calcium chloride (CaCl<sub>2</sub>·2H<sub>2</sub>O), ethylenediaminetetraacetic acid dipotassium salt dihydrate (K<sub>2</sub>EDTA·2H<sub>2</sub>O) were purchased from Fisher-Scientific (UK). Millipore water was used throughout the experimentation.

### 2.1.2. Methodology

Silica nanoparticles (SiNPs) were synthesised via Stöber *et al.* sol-gel precipitation method [16], as illustrated in Figure 2.1.



SiNPs of two size ranges were fabricated;  $27 \pm 7$  and  $71 \pm 6$  nm. For the synthesis of  $71 \pm 6$  nm SiNPs, 6.53 mL of NH<sub>4</sub>OH was added to a solution containing 88.3 mL of EtOH and

1.91 mL of distilled water and heated to 60 °C. Separately, a solution containing 2.27 mL of TEOS and 2.23 mL of EtOH were mixed. The resulting TEOS solution was added drop-wise to the NH<sub>4</sub>OH mixture while under vigorous stirring for 21 hours. Finally, the SiNPs were collected by centrifugation at 6000 rpm for 30 minutes and washed with EtOH and distilled water several times. The same procedure was used to synthesis small-size SiNPs, although the chemical amount and temperature differed (Table 2.2).

**Table 2.2:** The solution amounts of the reagent required to synthesise silica nanoparticles of a given composition and size.

H <sub>2</sub> O (mL)	NH <sub>4</sub> OH (mL)	EtOH (mL)	TEOS (mL)	Temperature (°C)	Particle Size (nm)	Reaction time (hours)
1.91	6.53	90.53	2.27	60	72	21
17.16	1.38	79.31	2.23	60	24	29

### 2.1.3. Physiological salt solution preparation

Physiological salt solution (PSS) was prepared using the following chemical composition [mM]: 119 NaCl, 4.7 KCl, 1.2 MgSO<sub>4</sub>.7H<sub>2</sub>O, 25 NaHCO<sub>3</sub>, 1.17 KH<sub>2</sub>PO<sub>4</sub>, 0.03 K<sub>2</sub>EDTA.2H<sub>2</sub>O, 5.5 glucose and 1.6 CaCl<sub>2</sub>.2H<sub>2</sub>O; *pH* 7.4. Potassium physiological salt solution (KPSS-60 mM) was prepared using the following chemical composition [mM]: 78.2 NaCl, 60 KCl, 1.2 MgSO<sub>4</sub>.7H<sub>2</sub>O, 25 NaHCO<sub>3</sub>, 1.17 KH<sub>2</sub>PO<sub>4</sub>, 0.03 K<sub>2</sub>EDTA.2H<sub>2</sub>O, 5.5 glucose and 1.6 CaCl<sub>2</sub>.2H<sub>2</sub>O; *pH* 7.4 [36].

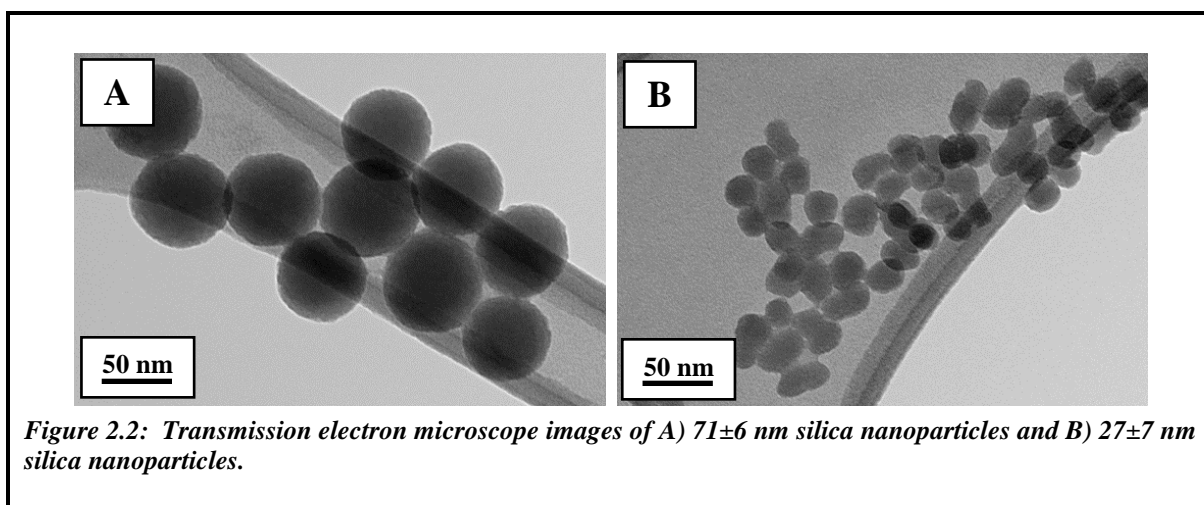
### 2.1.4. Characterisation

The SiNPs hydrodynamic size was determined by photon correlation spectroscopy (PCS, Malvern Zetasizer nano ZS instrument, UK). Briefly, the suspended nanoparticles (NPs) were placed in a polystyrene cuvette to give 0.02 % solution (1 mL). PCS of NPs were measured in distilled water and also in PSS solution. The hydrodynamic size was measured by an infra-red light passing through the sample and the resulting scattered light was detected. The SiNPs sizes were further confirmed using transmission electron microscopy (TEM, JEOL JEM-200) analysis along with obtaining the morphology of the particles. Zeta potential (zetasizer nano ZS Malvern Instrument, UK) of the SiNPs was measured by placing the suspension containing 0.02 % solution in the disposable zeta capillary cell. The zeta potential was obtained in the automatic mode by detecting the electrophoretic mobility

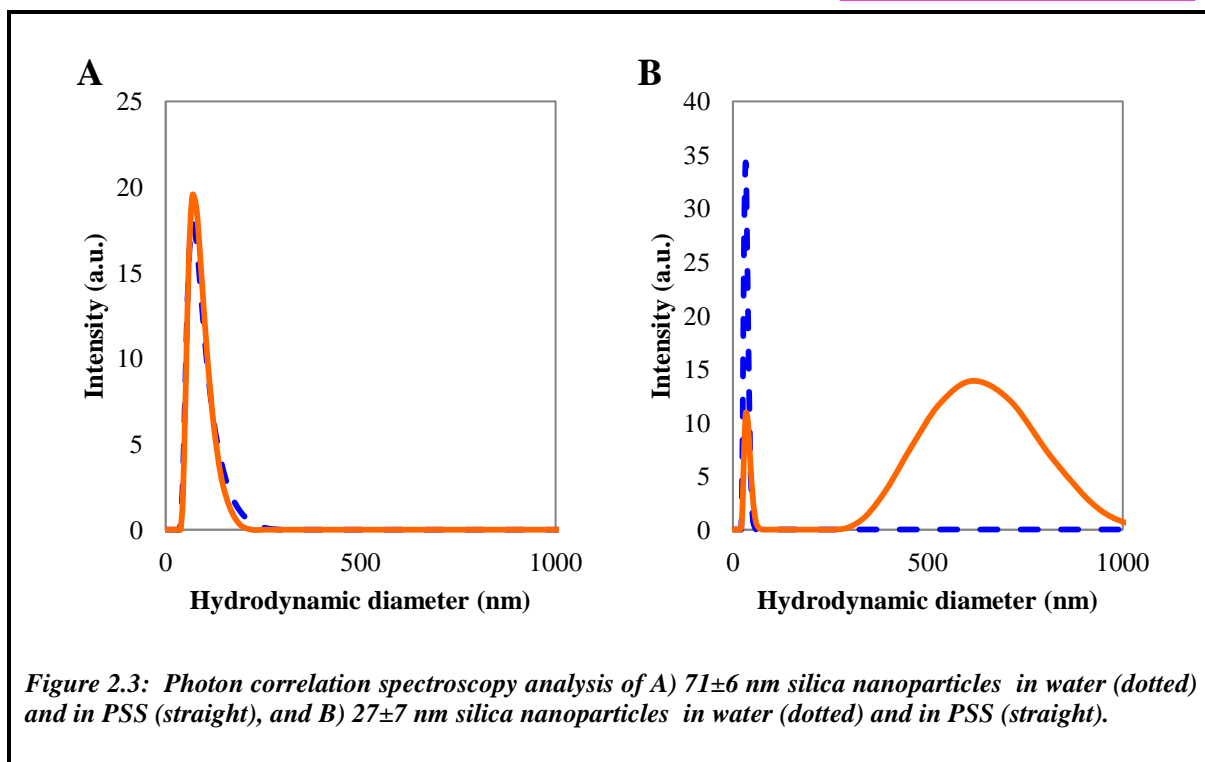
produced by the laser Doppler velocimetry. The potentials were determined for NPs in both distilled water and PSS.

### 2.1.5. Results

The TEM images of the SiNPs prepared using sol-gel methods show spherical monodispersed particles (Figure 2.2). The SiNPs sizes were identified as  $27\pm 7$  and  $71\pm 6$  nm in diameter.



The hydrodynamic sizes were in close agreement to the average diameter determined by TEM (Figure 2.3).



PCS analyses for the medium-sized NPs were approximately 30 nm greater than the actual size, while the smaller NPs were approximately 10 nm greater. SiNPs with a diameter of 71±6 and 27±7 nm had a hydrodynamic diameter of 103.8 and 34.27 nm in water respectively (Table 2.3).

**TABLE 2.3: Hydrodynamic size and stability measurements of silica nanoparticles, in water and physiological salt solution.**

Nanoparticles type	Primary diameter <sup>a</sup> (nm)	Hydrodynamic diameter <sup>b</sup> (nm)		ζ potential (mV)	
		<i>In water</i>	<i>In PSS</i>	<i>In water</i>	<i>In PSS</i>
medium-size SiNPs	71±6	103.8	96.6	-59.1	-26.8
small-size SiNPs	27±7	34.3	555	-25.1	-5.7

<sup>a</sup> Mean (±SD) diameter determined by TEM.

<sup>b</sup> Mean PCS measurement.

Medium-size SiNPs (71±6 nm) remained stable after dispersion in PSS as the hydrodynamic diameters did not significantly change; however, the smaller particles aggregated in ionic salt solution (PSS) (the hydrodynamic diameter of the small-sized SiNPs in water was 34.27 nm). Small-sized SiNPs (27±7 nm) aggregated by 91.5 % to 555 nm, in accordance with the distribution results shown by the PCS analysis (Figure 2 in the

appendix). The concentration of SiNPs placed in the solution for PCS analysis was 0.02 %, while for the organ-bath experiment the concentration was far smaller. The zeta potential values for the NPs confirm their stability in both water and PSS. Generally, the suspensions of the SiNPs in ionic salt solution (PSS) led to the slight increase in potential as compared to that in water.

#### **2.1.6. Discussion**

The SiNPs were fabricated and carefully characterised. The zeta potential values demonstrate that the SiNPs were stable in both water and PSS. When the silica nanoparticle (SiNP) suspensions were placed in PSS the potential slightly decreased, as compared to the suspension in water, due to their presence in high ionic solution (PSS). Briefly, when these SiNPs are in water, the counter ions (water molecules) surround the particle's surface and produce a structured hydration layer, known as the Stern layer. Other counter-ions that are not directly bound to the particle surface are still attracted to the negative particle, even though there is repulsion from the 'Stern layer' as well as other counter-ions attracted towards the particle, known as the diffuse layer. The electrical potential at the point where the Stern layer meets the diffused layer is known as the zeta potential. However, the introduction of ions into the solution (PSS) not only reduced the amount of water molecules but results in a competition between the ions and silica surface for the water molecules. This leads to a less structured hydration layer as the positively charged salt counter-ions and water molecules surround the SiNP, causing the short-range repulsive forces to reduce, thus lowering the zeta potential [36, 52]. The smaller SiNPs demonstrate non-Debye Landau Verwey Overbeek (DLVO) behaviour with additional forces present. It has been proposed that there is short range repulsion from a hairy layer present on the surface of small-size SiNPs. The layer is thought to consist of covalently bonded polymeric chains of silicic acid protruding from the surface [52]. The hydrodynamic diameter was approximately 7 nm above the actual size measured from the TEM image.

## 2.2. Dye Encapsulated Silica Nanoparticles via Sol-gel

### 2.2.1. Materials

Absolute ethanol (EtOH), ammonium hydroxide (NH<sub>4</sub>OH), tetraethyl orthosilicate (TEOS), 3-aminopropyl trimethoxysilane (APS), (3-aminopropyl)triethoxysilane (APTES), rhodamine B isothiocyanate (RBITC), ruthenium-tris(4, 7-diphenyl-1, 10-phenanthroline) dichloride (Ru(dpp)<sub>3</sub>), *N, N*-dimethylformamide (DMF), succinic anhydride, methyltriethoxysilane (MTEOS) and octyltriethoxysilane (OTEOS) were purchased from Sigma-Aldrich (UK). Salt solutions were prepared using sodium chloride (NaCl), potassium chloride (KCl), magnesium sulphate heptahydrate (MgSO<sub>4</sub>·7H<sub>2</sub>O), sodium bicarbonate (NaHCO<sub>3</sub>), potassium phosphate monobasic (KH<sub>2</sub>PO<sub>4</sub>), calcium chloride (CaCl<sub>2</sub>·2H<sub>2</sub>O), ethylenediaminetetraacetic acid dipotassium salt dihydrate (K<sub>2</sub>EDTA·2H<sub>2</sub>O) purchased from Fisher-Scientific (UK). Millipore water was used throughout the experimentation.

### 2.2.2. Methodology

#### 2.2.2.1. *Sol-gel precipitation of fluorophore encapsulated silica nanoparticles*

Rhodamine B isothiocyanate encapsulated silica nanoparticles (SiRBITC NPs) were prepared via a modified Stöber *et al.* [16] method, which was developed by Verhaegh *et al.* [72] (Table 2.4). The preparation of medium-size SiRBITC NPs (approximately 70 nm) was previously described by Ying *et al.* [73]. Briefly, a mixture of EtOH (0.8 mL), RBITC (5.36 mg) and APTES (13.6 µL) were stirred overnight under a nitrogen atmosphere in dark conditions. EtOH (30 mL) and NH<sub>4</sub>OH (2 mL) were added to the mixture and stirred vigorously for 20 hours, followed by addition of TEOS (558 µL) and stirring for 24 hours. A further addition of TEOS (13.8 µL) was made and stirred for 5 hours. The resulting precipitate was collected by centrifugation at 6000 rpm for 30 minutes and washed with EtOH and distilled water several times.

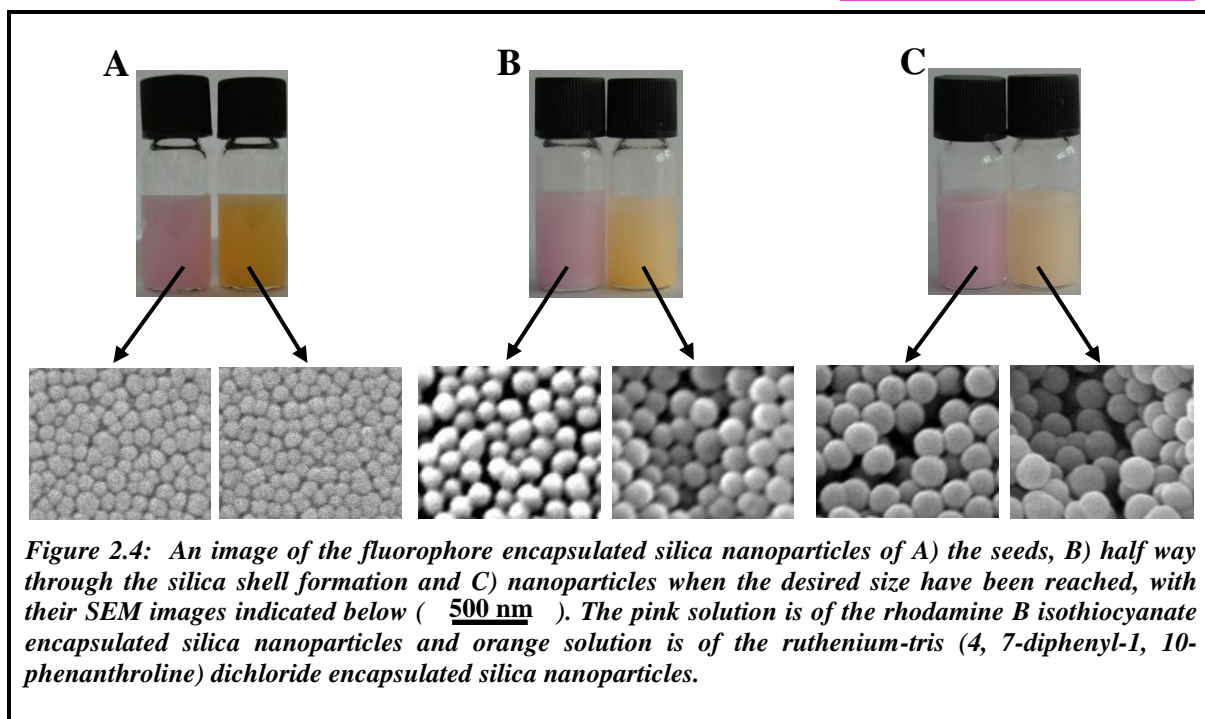
Small-size SiRBITC NPs (approximately 30 nm) were synthesised by coupling APTMS (10 µL) to the RBITC (1.2 mg) dye molecule in a nitrogen atmosphere under dark

conditions. Briefly, 1.38 ml of a  $\text{NH}_4\text{OH}$  was added to a solution containing 77.08 ml of EtOH and 17.16 ml of distilled water and was heated to 60 °C. Separately, a solution containing 2.23 ml of TEOS and 2.23 ml EtOH were mixed. The resulting TEOS solution was added drop-wise to the  $\text{NH}_4\text{OH}$  mixture while under vigorous stirring. After 15 minutes the dye mixture was added and stirred for 29 hours. Finally, the SiNPs were collected by centrifugation at 6000 rpm for 30 min and washed with EtOH and distilled water several times.

#### ***2.2.2.2. Silica coating of fluorophore encapsulated silica seeds***

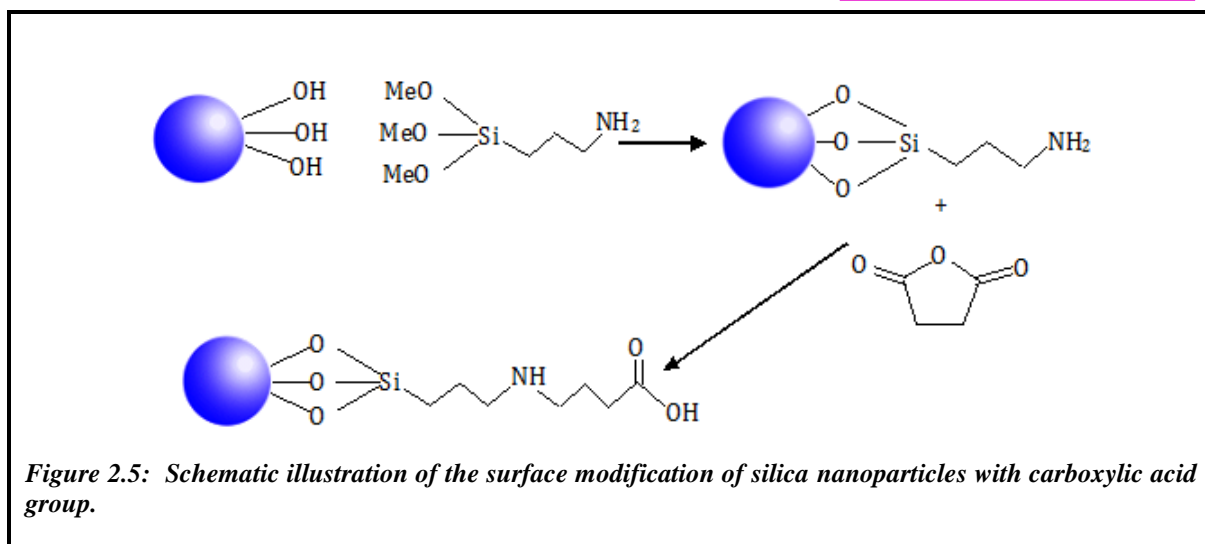
All the experiments were carried out under dark conditions due to the photosensitivity of the fluorescent dye molecules. SiNPs were synthesised using Stöber *et al.* method [16]. The reaction entailed the hydrolysis and condensation of TEOS in aqueous solution of EtOH and water. The SiRBITC NPs were synthesised using the procedure describe by Verhaegh *et al.* [72]. These were then used as seeds to coat with a silica shell in order to obtain the required size [74]. The RBITC dye (1 mg) and APS (0.01 mL) mixture, previously stirred for a few hours in  $\text{N}_2$  atmosphere, were placed in a solution of  $\text{NH}_4\text{OH}$  (2 mL) in EtOH (24 mL) and stirred. Finally, a solution of TEOS (1.5 mL) and EtOH (6 mL) was added to mixture and stirred for 24 hours, resulting in an opaque pink solution. TEOS (5.4 mL) and water (2.2 mL) were added gradually to create silica shells on the dye seeds, which produced a paler pink solution (Figure 2.4).

The ruthenium-tris(4, 7-diphenyl-1, 10-phenanthroline) dichloride encapsulated silica nanoparticles ( $\text{SiRu}(\text{dpp})_3$  NPs) were also synthesised using the sol-gel technique. Ruthenium-tris(4, 7-diphenyl-1, 10-phenanthroline) dichloride ( $\text{Ru}(\text{dpp})_3$ ) dye (0.4 mg) was dispersed in EtOH (20 mL), followed by addition of  $\text{NH}_4\text{OH}$  (2 mL) solution and the resulting mixture was stirred. Finally, a solution of TEOS (1.5 mL) and EtOH (6 mL) was added to mixture and stirred for 24 hours, resulting in an opaque orange solution. TEOS (5.4 mL) and water (2.2 mL) was added gradually to coat with a silica shell, which produced a paler orange solution (Figure 2.4).



### 2.2.2.3. Functionalising silica nanoparticles with carboxylic acid groups

The carboxylic acid functionalised SiNPs were prepared using the method described by An *et al.* [75]. APS (0.4 mL) was added to the RBITC core-shell SiNPs and stirred for 20 hours. The NPs were collected by centrifugation to remove any unreacted reagents. A solution of succinic anhydride (0.25 g) in DMF (25 mL) was prepared, to which the NPs solution was added. The solution was stirred for 24 hours and the product was collected by centrifugation. The ring opening elongation reaction with succinic anhydride is shown in Figure 2.5. The functionalisation procedure was separately carried out for the Ru(dpp)<sub>3</sub> encapsulated SiNPs.



#### 2.2.2.4. Quantifying the amount of fluorophore within the nanoparticles

The amounts of dye molecules encapsulated within the NPs were quantified using fluorescence spectroscopy (Hitachi fluorescence spectrophotometer, F-2500). Initially, a calibration graph of fluorescence intensity against fluorophore concentration was produced. The excitation of RBITC was 540 nm with an emission at 573 nm, while Ru(dpp)<sub>3</sub> excitation was 490 nm with emission at 591 nm. For the RBITC calibration graph the fluorophore concentration range was  $2.19 \times 10^{-8}$  to  $7.00 \times 10^{-7}$  mol dm<sup>-3</sup>, while for the Ru(dpp)<sub>3</sub> calibration graph the fluorophore concentration range was  $9.00 \times 10^{-7}$  to  $1.44 \times 10^{-5}$  mol dm<sup>-3</sup>.

### 2.2.3. Results

#### 2.2.3.1. Nanoparticles prepared using the sol-gel method

The TEM images of the SiNPs prepared using sol-gel methods show spherical monodispersed NPs (Figure 2.6). The medium-size SiRBITC NPs were  $61 \pm 7$  nm in diameter, while the small-size SiRBITC NPs were  $31 \pm 10$  nm in diameter.

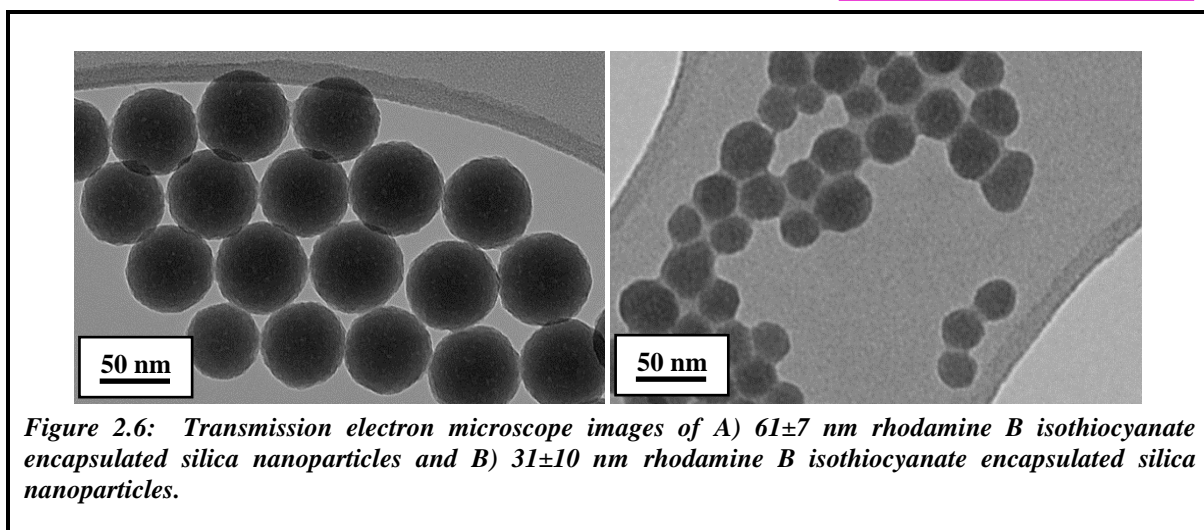


*Figure 2.6: Transmission electron microscope images of A) 61±7 nm rhodamine B isothiocyanate encapsulated silica nanoparticles and B) 31±10 nm rhodamine B isothiocyanate encapsulated silica nanoparticles.*

The hydrodynamic sizes were in close agreement to the average diameter determined by TEM (Figure 2.7).

**TABLE 2.4: Hydrodynamic size and stability measurements of rhodamine B isothiocyanate encapsulated silica nanoparticles, in water and physiological salt solution.**

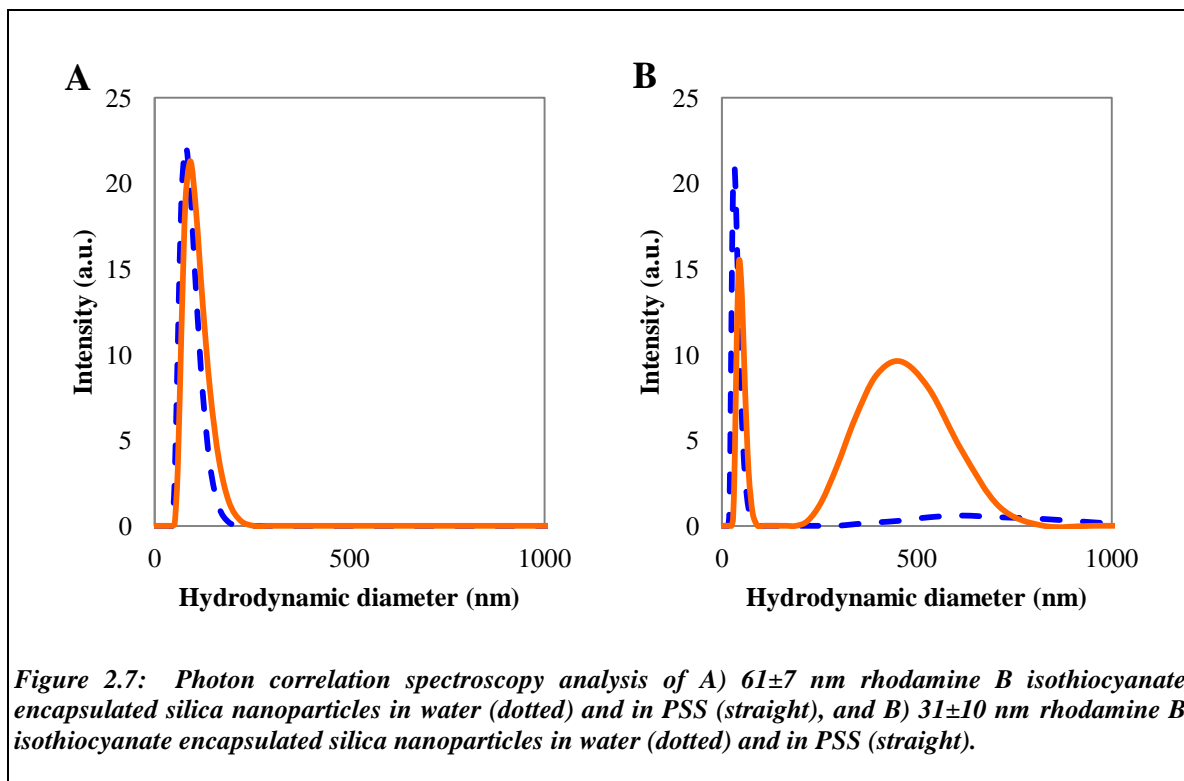
Nanoparticles type	Primary diameter <sup>a</sup> (nm)	Hydrodynamic diameter <sup>b</sup> (nm)		ζ potential (mV)	
		<i>In water</i>	<i>In PSS</i>	<i>In water</i>	<i>In PSS</i>
medium-size SiRBITC NPs	61±7	97.8	99.0	-57.7	-25.9
small-size SiRBITC NPs	31±10	42.2	410.2	-29.8	-14.5

<sup>a</sup> Mean (±SD) diameter determined by TEM.

<sup>b</sup> Mean PCS measurement.

The PCS analyses for the medium-sized SiRBITC NPs were approximately 30 nm greater than the actual size, while the small-sized SiRBITC NPs were approximately 10 nm greater. SiRBITC NPs with a diameter of 61±7 and 31±10 nm had hydrodynamic diameters of 98 and 42 nm, respectively. Medium-size SiRBITC NPs (61±7 nm) remained stable after dispersion in PSS as the hydrodynamic diameters did not significantly change; however, the smaller particles aggregated in ionic salt solution (PSS). Small SiRBITC NPs (31±10 nm) aggregated by 81.9 % to 410.2 nm, in accordance with the distribution results shown by the PCS analysis (Figure 4 in the appendix). It is noted, however, that the concentration of SiRBITC NPs placed in the solution for PCS analysis was 0.02 % solution, while for the organ-bath experiment the concentration was far smaller (refer to

Chapter 2, Section 2.1.6). The zeta potential values for the SiRBITC NPs confirm their stability in both water and PSS. Generally, suspensions of SiRBITC NPs in ionic solution (PSS) led to the slight increase in potential as compared to that in water.



### 2.2.3.2. Nanoparticle seeds coated with silica shell

The TEM, Figure 2.8, confirm the synthesis of monodispersed SiNPs. SiRu(dpp)<sub>3</sub> NPs have an average diameter of 192±8 nm (Figure 2.8A) and SiRBITC NPs have an average diameter of 208±9 nm (Figure 2.8B).

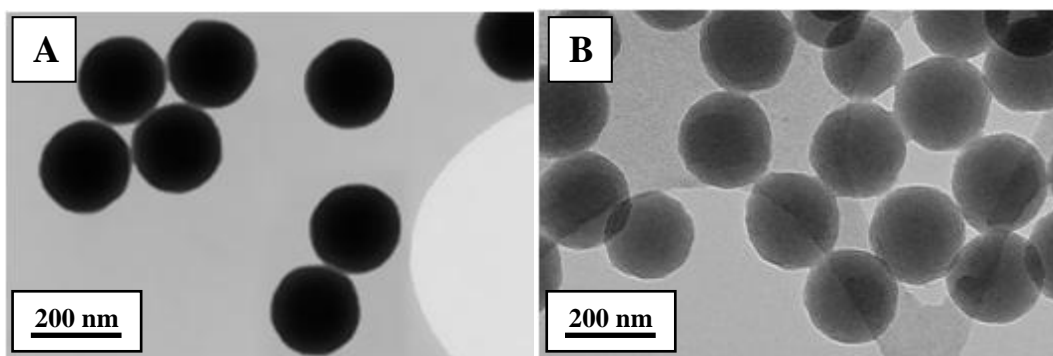


*Figure 2.8: Transmission electron microscope images of A) ruthenium-tris (4, 7-diphenyl-1, 10-phenanthroline) dichloride encapsulated silica nanoparticles and B) rhodamine B isothiocyanate encapsulated silica nanoparticles.*

The PCS analysis further confirm the average diameter of the silica dye encapsulated NPs to be approximately 200 nm, where SiRu(dpp)<sub>3</sub> NPs are 194 nm and SiRBITC NPs are 197 nm (Figure 2.9).

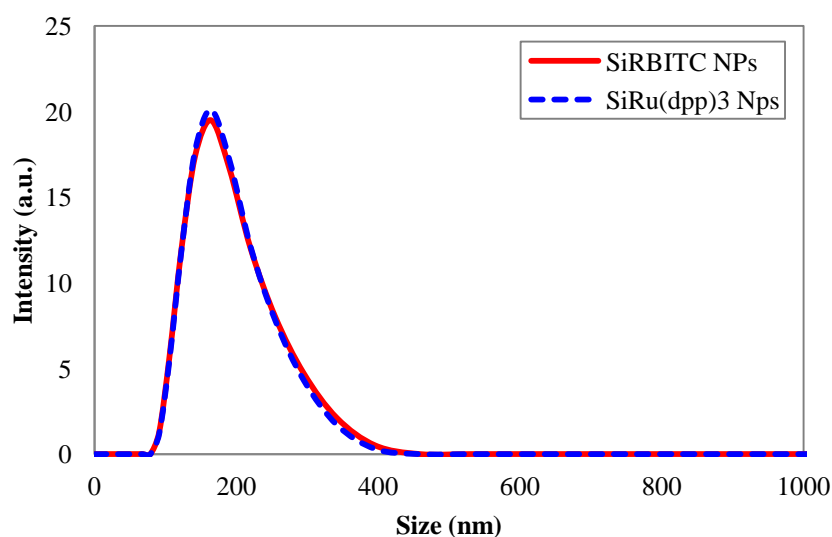


*Figure 2.9: Photon correlation spectroscopy analysis of ruthenium-tris (4, 7-diphenyl-1, 10-phenanthroline) dichloride encapsulated silica nanoparticles and rhodamine B isothiocyanate encapsulated silica nanoparticles.*

The SiNP synthesis consisted of TEOS, which has four ‘ethoxy’ groups that render it hydrophobic (Figure 2.10). These were then hydrolysed in water causing the ‘ethoxy’

groups to be substituted for hydroxyl groups. This hydrolysis reaction caused the molecule to become hydrophilic.

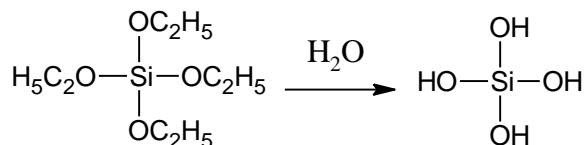


Figure 2.10: Schematic illustration of the hydrolysis of TEOS causing it to become hydrophilic.

The nanoparticle (NP) surface modification was confirmed with zeta potential measurements (Figure 2.11; Table 2.5).

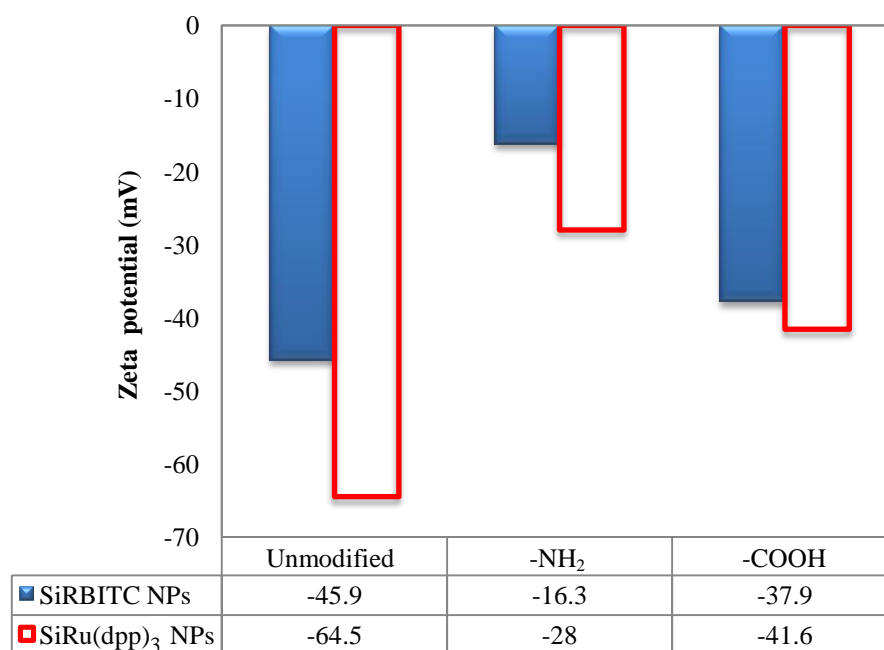


Figure 2.11: Bar chart graph illustrating the surface modification of silica dye encapsulated nanoparticles by change in zeta potential.

The addition of amine groups caused the zeta potential to become more positive while the carboxylic acid functionalisation caused the zeta potential to become more negative, as anticipated [75].

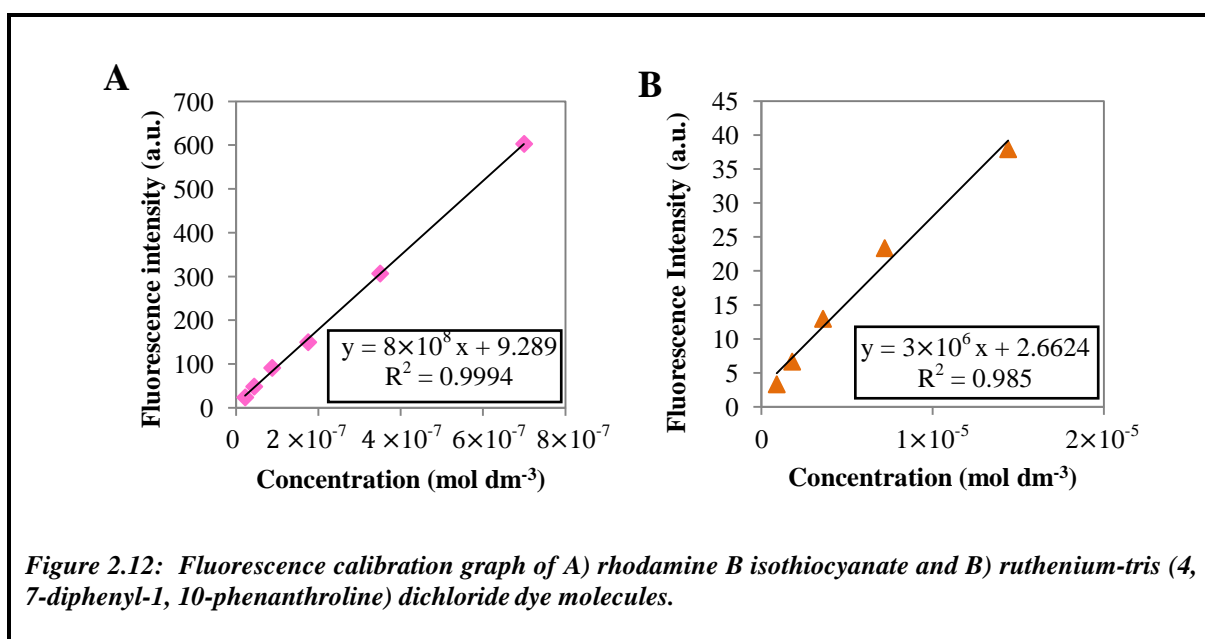
**TABLE 2.5:** Hydrodynamic size and stability measurements of silica dye encapsulated nanoparticles and their surface modification with amine and carboxylic acid groups.

Nanoparticles type	Primary diameter <sup>a</sup> (nm)	Hydrodynamic diameter <sup>b</sup> (nm)	$\zeta$ potential (mV)		
			<i>Un-modified</i>	<i>Amine functionalised</i>	<i>Carboxylic acid functionalised</i>
SiRBITC NPs	208±9	197.2	-45.9	-16.3	-37.9
SiRu(dpp) <sub>3</sub> NPs	192±8	194.9	-64.5	-28	-41.6

<sup>a</sup> Mean (±SD) diameter determined by TEM.

<sup>b</sup> Mean PCS measurement.

The amounts of dye molecules encapsulated within the NPs were quantified using fluorescence spectroscopy. Initially, the fluorescence spectra of known concentrations of fluorophores were carried out (Figure 9 and 11 in the appendix) in order to produce the calibration graphs (Figure 2.12).



These calibration graphs allow for the quantification of dye molecules within the NPs via the attainment of the fluorescence graphs of their supernatant. Thus, the dye concentration within the NPs was calculated by subtracting the concentration within the supernatant from the actual concentration of dye used (Table 2.6). The mass of RBITC dye molecules within SiRBITC NPs was 999.72  $\mu\text{g}$ , while Ru(dpp)<sub>3</sub> fluorophore within the SiRu(dpp)<sub>3</sub> NPs was 323.88  $\mu\text{g}$ .

TABLE 2.6: Quantifying the amount of dye molecules within the nanoparticles.

Dyes	Concentration of supernatant (mol dm <sup>-3</sup> )	Moles of supernatant (mol)	Mass of dye within supernatant (µg)	Mass of dye within NPs (µg)
RBITC	$1.94 \times 10^{-8}$	$5.25 \times 10^{-10}$	0.28	999.72
Ru(dpp) <sub>3</sub>	$2.96 \times 10^{-6}$	$6.51 \times 10^{-8}$	76.12	323.88

## 2.2.4. Discussion

### 2.2.4.1. Nanoparticles prepared using the sol-gel method

The medium and small-sized SiRBITC NPs were stable in both water and PSS as demonstrated by the zeta potential values. In the case of SiRBITC NPs the zeta potential in water was more negative than the non-dye encapsulated SiNPs. As previously noted for the SiNPs, when SiRBITC NPs are suspended in PSS, attraction of salt ions led to reduced negativity. Such charge attraction may have led to modification of the surface chemistry of the SiRBITC NPs, in comparison to the SiNPs. The hydrodynamic diameter of our fabricated medium-sized SiRBITC NPs was approximately 40 nm above the actual size measured from the TEM images. The zeta potentials of medium-sized SiRBITC NPs confirm it is stable in both water and PSS. The ions within the PSS media causes the SiRBITC NPs suspensions zeta potential to slightly decrease, as compared to the suspension in water, as previously explained in Chapter 2, Section 2.1.6. Briefly, a less structured hydration layer is formed around the NP, resulting in the short-range repulsive forces to reduce, thus lowering the zeta potential. However, we suggest that the small-sized SiRBITC NPs demonstrate non-DLVO behaviour with additional forces present known as the hairy layer, refer to Chapter 2, Section 2.1.6.

### 2.2.4.2. Nanoparticle seeds coated with silica shell

The TEM images confirm for the synthesis of monodispersed dye encapsulated SiNPs. The PCS analysis was in agreement with the particle size for both SiRu(dpp)<sub>3</sub> NPs and SiRBITC NPs.

Verhaegh *et al.* [72], suggested that if the RBITC dye was not functionalised with APS and used in an alcohol solution, it would not incorporate into the silica and would leach out of the NPs into the solution. APS was added to the RBITC dye in order to act as a coupling

agent, and allow the siloxyl groups to anchor to the silica core and the amine group to bind to the dye [76]. After stirring under a nitrogen atmosphere under dark conditions the colour changed from intense purple to orange as self-quenching had occurred [72]. The synthesis of SiRu(dpp)<sub>3</sub> NPs occurs as the silica is negatively charged, while the Ru(dpp)<sub>3</sub> dye is positively charged. This causes electrostatic interaction to occur between the dye and the silica and therefore leading to an ionic bond. The NPs were successfully functionalised with carboxylic acid as confirmed with the zeta potential measurements. Previous studies, have reported possible types of interaction between the aminosilane molecules and the silica surface. The amine may produce hydrogen bonds with the surface hydroxyl groups. Alternatively, the amine may abstract a proton from the silanol group resulting in the formation of an ionic bond; this is a more stable interaction as compared to the first interaction. Furthermore, it is possible for the hydrogen bonded molecules to self-catalyse the condensation reaction of the silicon groups within the silane molecule, thus forming a covalent siloxane bond [77]. The carboxylic acid group covalently bond to the NP surface via an interaction between the amine group and succinic anhydride [75]. Furthermore, the volume of dye molecules within the SiRBITC NPs is approximately twice the amount as compared to the SiRu(dpp)<sub>3</sub> NPs.

## **2.3. Silica Nanoparticles via Microemulsion**

### **2.3.1. Materials**

Triton X-100, cyclohexane, *n*-hexanol, ammonium hydroxide (NH<sub>4</sub>OH), tetraethyl orthosilicate (TEOS), rhodamine B isothiocyanate (RBITC), (3-aminopropyl)triethoxysilane (APTES) and absolute ethanol (EtOH) were purchased from Sigma-Aldrich (UK). Millipore water was used throughout the experimentation.

### **2.3.2. Methodology**

SiRBITC NPs were synthesised via a reverse microemulsion method, where reactant concentrations were altered according to Table 2.7 [78]. Initially, RBITC dye molecules were coupled with equimolar concentration of APTES by stirring the resulting solution overnight in a nitrogen atmosphere under dark conditions. Briefly, for the synthesis of sample 1, 1.77 mL of Triton X-100, 7.5 mL of cyclohexane, 1.8 mL of *n*-hexanol, 400 µL of water and 10 µL of RBITC-APTES solution were stirred for 1 hour to produce the water-in-oil microemulsion. This was followed by the addition of 200 µL of TEOS and 100 µL of NH<sub>4</sub>OH. The resulting mixture was stirred for 24 hours. The microemulsion was broken with acetone and the SiNPs were collected and washed with centrifugation (6000 rpm/ 30 minutes) using ethanol several times.

The same procedure was utilized to synthesised SiRBITC NPs of different size ranges, however for sample 4 the RBITC-APTES was added to the reaction mixture after the TEOS and catalyst addition.

**Table 2.7: The solution amounts of the reagent required to synthesise rhodamine B isothiocyanate encapsulated silica nanoparticles of a given composition and size.**

Triton-X (mL)	Cyclohexane (mL)	<i>n</i> -hexanol (mL)	Water (mL)	RBITC-APTES ( $\mu$ L)	TEOS ( $\mu$ L)	NH <sub>4</sub> OH ( $\mu$ L)	Particle Size (nm)	Sample
1.77	7.5	1.8	0.4	10	200	100	44 $\pm$ 5	1
1.77	7.5	1.8	0.4	5	200	100	53 $\pm$ 8	2
7	30	7.2	1.6	10	800	400	66 $\pm$ 3	3
7	30	7.2	1.6	10	800	400	64 $\pm$ 4	4

### 2.3.3. Characterisation

The SiRBITC NP hydrodynamic size was determined by PCS (Malvern Zetasizer nano ZS instrument, UK). Briefly, the suspended NPs were placed in a polystyrene cuvette to give 0.02 % solution (1 mL). PCS of NPs were measured in distilled water and also in PSS solution. The hydrodynamic size was measured by an infra-red light passing through the sample and the resulting scattered light was detected. The SiNPs sizes were further confirmed using TEM (JEOL JEM-200) analysis along with obtaining the morphology of the particles. Zeta potential (zetasizer nano ZS Malvern Instrument, UK) of the SiNPs was measured by placing the suspension containing 0.02 % solution in the disposable zeta capillary cell. The zeta potential was obtained in the automatic mode by detecting the electrophoretic mobility produced by the laser Doppler velocimetry.

### 2.3.4. Results

The TEM images of the SiRBITC NPs prepared via microemulsion methods show spherical monodispersed particles (Figure 2.13). The Sample 1 sizes were identified as 48 $\pm$ 4 nm in diameter, while the sample 2 were 54 $\pm$ 9 nm, sample 3 were 66 $\pm$ 4 nm and sample 4 were 65 $\pm$ 5 nm.

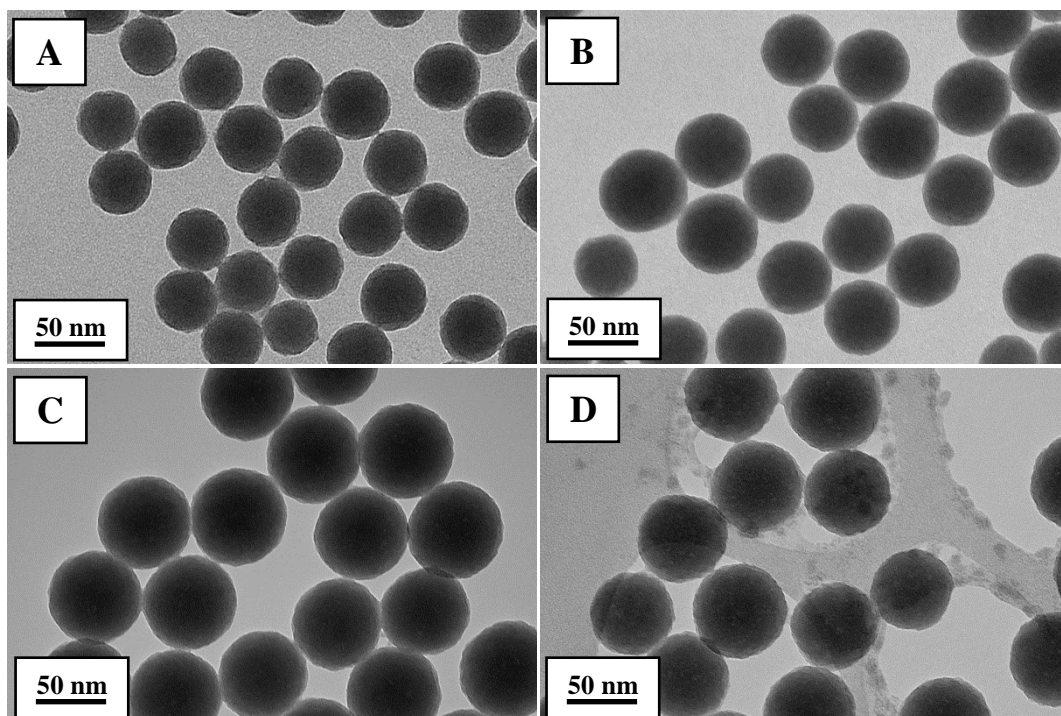


Figure 2.13: Transmission electron microscope images of rhodamine B isothiocyanate encapsulated silica nanoparticles; A) sample 1, B) sample 2, C) sample 3 and D) sample 4.

The hydrodynamic sizes were in close agreement to the average diameter determined by TEM (Figure 2.14).

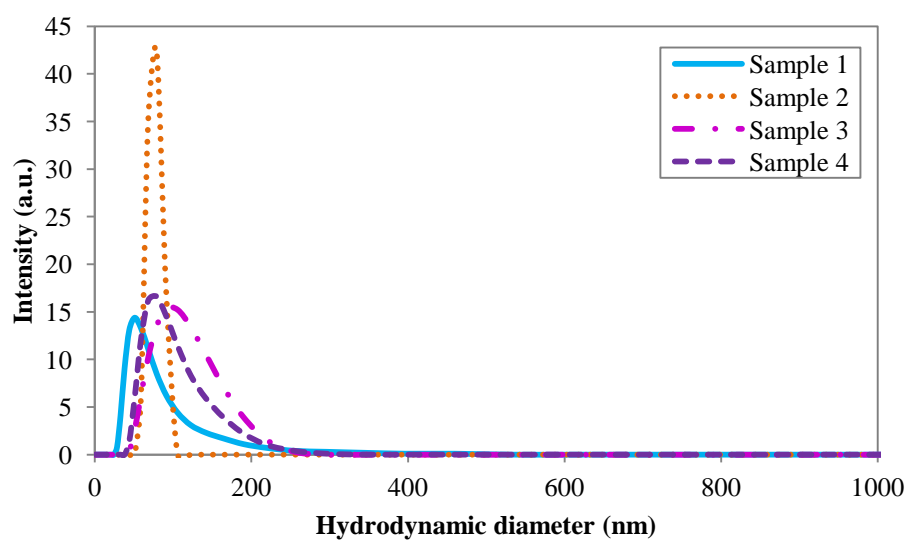


Figure 2.14: Photon correlation spectroscopy analysis of rhodamine B isothiocyanate encapsulated silica nanoparticles synthesised via microemulsion precipitation process.

PCS analyses for the SiRBITC NPs shows the hydrodynamic diameter is approximately double than the actual size. SiRBITC NPs with a diameter of  $48\pm 4$ ,  $54\pm 9$ ,  $66\pm 4$  and  $65\pm 5$  nm have a hydrodynamic diameter of 125.4, 88.08, 124.0 and 120.2 nm in water respectively (Table 2.8).

**TABLE 2.8: Hydrodynamic size and stability measurements of silica nanoparticles in water media.**

Sample	Primary diameter <sup>a</sup> (nm)	Hydrodynamic diameter <sup>b</sup> (nm)	$\zeta$ potential (mV)
1	$48\pm 4$	125.4	-36.7
2	$54\pm 9$	88.1	-30.3
3	$66\pm 4$	124.0	-46.9
4	$65\pm 5$	120.2	-40.8

<sup>a</sup> Mean ( $\pm$ SD) diameter determined by TEM.

<sup>b</sup> Mean PCS measurement.

The majority of SiRBITC NPs ( $48\pm 4$  nm) remained bimodal by 97.2 % to 125.4 nm and 2.8 % aggregated to 4038 nm, in accordance with the distribution results shown by the PCS analysis (Figure 13 in the appendix). The zeta potential values for the NPs confirm their stability in water.

### 2.3.5. Discussion

The SiRBITC NPs were synthesised using the method described by Shi *et al*, and the fabrication of the NPs were of similar size ranges to their method [78]. Interestingly, reducing the volume of dye mix added to the reaction mixture does not reduce the NP diameter. Imhof *et al*; has demonstrated that increasing the concentration dye coupled to the amino propyl groups leads to increased NP size [79], however the similar size range may be due to the amino propyl being diluted in large volume of solvent. Furthermore, when increasing the volume of reactants while the concentration remains the same increases the NP diameter. The addition of dye mixture after silica precursor addition does not alter the NP size. The PCS analysis demonstrates that these NPs synthesised by microemulsion are approximately double in size. This may be due to the NP surface containing oily residues that are attracted to each other. The zeta potentials for SiRBITC NPs confirm it is stable in water.

## 2.4. Mesoporous Nanoparticles

### 2.4.1. Materials

Rhodamine B isothiocyanate (RBITC), (3-Aminopropyl)trimethoxysilane (APTMS), fluorescein isothiocyanate (FITC), tetraethyl orthosilicate (TEOS), ammonium hydroxide solution ( $\text{NH}_4\text{OH}$ ), ammonium nitrate ( $\text{NH}_4\text{NO}_3$ ) and concentrated hydrochloric acid (HCl, 37 %) were purchased from Sigma-Aldrich (UK). Absolute ethanol (EtOH), hexadecyltrimethylammonium bromide (CTMAB), ethylene glycol (EG; 99.8 % anhydrous), dimethylformamide (DMF), sodium hydroxide (NaOH), methanol (MeOH) and isopropanol (IP) were purchased from Fisher-Scientific (UK). Millipore water was used for all the experimentation.

### 2.4.2. Methodology

#### 2.4.2.1. RBITC encapsulated mesoporous synthetic route 1 (sample 1)

The mesoporous nanoparticles (MNP) (sample 1) were prepared using Lin *et al.* [80] method, although RBITC dye was used instead of fluorescein isothiocyanate (FITC). Initially, 4.77 g of EtOH was sonicated with 1.20 g of TEOS at 50 °C. Briefly, 1 mg of RBITC was reacted under dark conditions with 10  $\mu\text{L}$  of APTMS in an  $\text{N}_2$  atmosphere by stirring the mixture overnight; leading to a colour change from pink to orange. The RBITC MNP was prepared by a co-condensation reaction where 0.65 g of hexadecyltrimethylammonium bromide (CTMAB) was dissolved in 294 mL of  $\text{H}_2\text{O}$  and 10.18 g of  $\text{NH}_4\text{OH}$  solution at 50 °C. To the resulting solution 4.88 mL of TEOS and EtOH solution was pipetted in the mixture and stirred vigorously for 5 hours. The remaining TEOS and EtOH solution was mixed with the RBITC dye and added drop wise to the mixture and allowed to stir vigorously for 1 hour. The resulting mixture was aged at 50 °C for 24 hours giving an opaque pink precipitate. The RBITC MNP was collected and washed three times by centrifugation. Initially, the mixture was centrifuged (15000 rpm/ 10 minutes) with distilled water and this was repeated at a lower speed (6000 rpm/ 30 minutes). Finally, it was centrifuged (6000 rpm/ 30 minutes) with EtOH and dried overnight at 50 °C. The surfactant template was extracted from the as-synthesised product by calcinations. The product was placed in a pre-heated furnace at 300 °C and heated to 550 °C for 3 hours at the rate of 5 °C per minute.

### 2.4.2.2. Mesoporous synthetic route 2 (sample 2-7)

MNP prepared by synthetic route 2 were synthesised using Gu *et al.* [81] method (Table 2.9).

**Table 2.9: The solution amounts of the reagent required to synthesise mesoporous nanoparticles of required composition and size.**

Sample	Size <sup>a</sup> (nm)	Water (mL)	EG (mL)	CTAB (g)	NH <sub>4</sub> OH (mL)	TEOS (mL)	APS ( $\mu$ L)	IP <sup>b</sup> (mL)	Dyes (mg)
2	100 $\pm$ 9 & 137 $\pm$ 9	180	0	1.17	7.2	1.43	265	30	0
3	182 $\pm$ 9 &140 $\pm$ 5	180	30	1.17	10	1.43	265	0	0
4	268 $\pm$ 5, 232 $\pm$ 13, 182 $\pm$ 9 & 423 $\pm$ 14	180	30	1.17	7.2	1.43	265	0	0
5	87 $\pm$ 5 & 59 $\pm$ 5	180	30	1.17	4	1.43	265	0	0
6	50 $\pm$ 5	180	30	1.17	2	1.43	265	0	0
7	73 $\pm$ 9	180	30	1.17	4	1.43	265	0	7.95

<sup>a</sup> Mean ( $\pm$ SD) diameter determined by TEM.

<sup>b</sup> Abbreviation for the solvent isopropanol.

#### 2.4.2.2.1. Amorphous mesoporous nanoparticles (samples 2-6)

Briefly, for the synthesis of 160 nm MNP, MNP was prepared by a co-condensation reaction where 1.17 g of CTMAB was dissolved in 180 mL of H<sub>2</sub>O, 30 mL of ethylene glycol (EG) and 7.2 mL of NH<sub>4</sub>OH solution at 50 °C by stirring vigorously. To the resulting solution 1430  $\mu$ L of TEOS was added followed by the addition of APTMS (265  $\mu$ L). The resulting mixture was stirred vigorously at 50 °C for 2 hours and allowed to age for 20 hours at the same temperature. The MNP were collected and washed three times by centrifugation (20,000 rpm/ 10 minutes) with distilled water and dried in an oven at 60 °C. The surfactant template was extracted from the template intact MNP by dissolving the product (1 g) and ammonium nitrate (NH<sub>4</sub>NO<sub>3</sub>) in ethanol (EtOH; 40 mL) at 60 °C for 18 hours. The template free MNP were washed several times using EtOH (14,000 rpm/ 15 minutes).

***2.4.2.2.2. Synthesis of mesoporous nanoparticles with RBITC dye (sample 7)***

Briefly, 8 mg of RBITC was reacted with 265  $\mu\text{L}$  of APTMS by stirring the mixture overnight. The RBITC MNP was prepared by a co-condensation reaction where 1.17 g of CTMAB was dissolved in 180 mL  $\text{H}_2\text{O}$ , EG (30 mL) and 4 mL of  $\text{NH}_4\text{OH}$  solution at 50  $^\circ\text{C}$ . To the resulting solution 1430  $\mu\text{L}$  of TEOS was added, followed by the addition of 265  $\mu\text{L}$  of the dye mixture. The resulting mixture was stirred vigorously at 50  $^\circ\text{C}$  for 2 hours and aged for 20 hours at the same temperature producing an opaque pink precipitate. The RBITC MNP was collected and washed three times by centrifugation (20,000 rpm/ 30 minutes) with EtOH. The surfactant template was extracted from the template intact MNP by dissolving the product (1 g) and  $\text{NH}_4\text{NO}_3$  in EtOH (40 mL) at 60  $^\circ\text{C}$  for 18 hours. The template free MNP were washed several times using EtOH (14,000 rpm/ 15 minutes).

***2.4.2.3. Mesoporous synthetic route 3 (samples 8-12)***

MNP were synthesised via the self-assembly method as previously described by Slowing *et al.* [82], where FITC dye molecules were encapsulated within MNP. In this study, different types and combinations (RBITC and FITC) of fluorophores have been encapsulated within the mesoporous matrix (Table 2.10).

**Table 2.10: Overview of the amount of reactants needed to synthesise mesoporous nanoparticles.**

Sample	Size <sup>a</sup> (nm)	Water (mL)	DMF <sup>b</sup> (μL)	CTAB (g)	NaOH (mL)	TEOS (mL)	APS (μL)	Dyes (mg)
8	104±13, 266±11, 300 & 436	480	0	1	3.5	5	50	1.5 (RBITC)
9	95±13	480	495	1	3.5	4	5	0
10	105±13	480	495	1	3.5	4	5	0.2 (RBITC)
11	109±18	480	495	1	3.5	4	5	0.2 (FITC)
12	105±13	480	495	1	3.5	4	5	0.1:0.1 (RBITC/ FITC)

<sup>a</sup> Mean (±SD) diameter determined by TEM.

<sup>b</sup> Abbreviation for the solvent dimethylformamide.

#### **2.4.2.3.1. RBITC encapsulated mesoporous nanoparticles (sample 8)**

Briefly, 1.5 mg of RBITC was reacted with 50 μL of APTMS in N<sub>2</sub> atmosphere for 3 hours. The RBITC MNP was prepared by a co-condensation reaction where 1 g of CTMAB was dissolved in 480 mL H<sub>2</sub>O and 3.5 mL of 2 M NaOH solution at 80 °C. To the resulting solution 5 mL of TEOS was added followed by the addition of 50 μL of coupled dye mixture. The resulting mixture was stirred vigorously at 80 °C for 2 hours producing an opaque pink precipitate. The RBITC MNP was collected and washed twice by centrifugation (14,000 rpm/ 15 minutes) with methanol (MeOH). The surfactant template was extracted from the as-synthesised product by dispersing the template intact MNP in MeOH (200 mL) and concentrated HCl (2 mL) at 60 °C for 18 hours. The FITC MNP was washed several times using MeOH (14,000 rpm/ 15 minutes).

#### **2.4.2.3.2. Mesoporous nanoparticles (Sample 9)**

Briefly, 5 mL of anhydrous DMF was mixed with 50 μL of APTMS. The MNP was prepared by a co-condensation reaction where 1 g of CTMAB was dissolved in 480 mL of H<sub>2</sub>O and 3.5 mL of 2 M NaOH solution at 80 °C. To the resulting solution 4 mL of TEOS was added followed by the addition of 500 μL of APTMS mixture. The resulting mixture

was stirred vigorously at 80 °C for 2 hours producing an opaque white precipitate. The MNP was collected and washed twice by centrifugation (14,000 rpm/ 15 minutes) with MeOH. The surfactant template was extracted from the as-synthesised product by dispersing the template intact MNP in MeOH (100 mL) and concentrated HCl (1mL) at 60 °C for 18 hours. The acid extraction step was repeated twice. The MNP was washed several times using MeOH (14,000 rpm/ 15 minutes) (Figure 2.15).

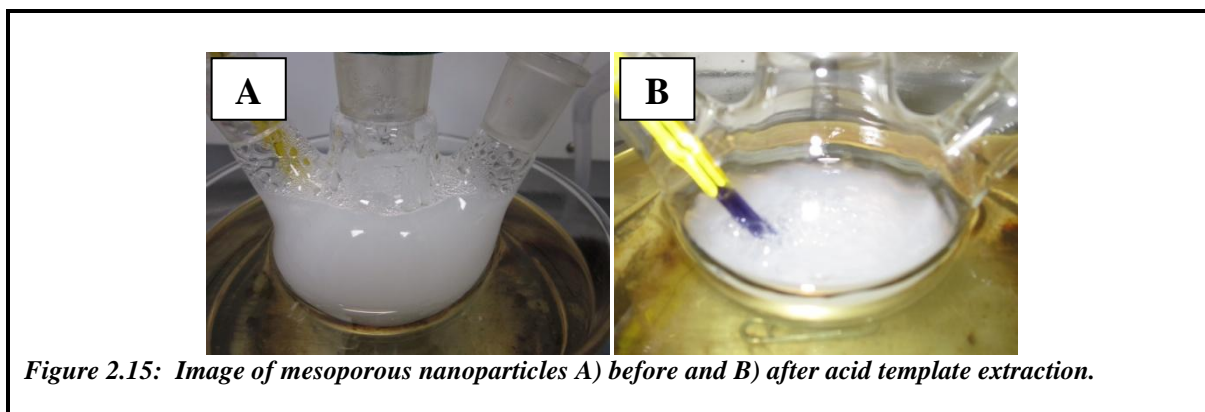


*Figure 2.15: Image of mesoporous nanoparticles A) before and B) after acid template extraction.*

#### **2.4.2.3.3. RBITC encapsulated mesoporous nanoparticles (sample 10)**

Briefly, 2 mg of RBITC was reacted with a mixture of 5 mL of anhydrous DMF and 50  $\mu$ L of APTMS for 3 hours. The RBITC MNP was prepared by a co-condensation reaction where 1 g of CTMAB was dissolved in 480 mL of H<sub>2</sub>O and 3.5 mL of 2 M NaOH solution at 80 °C. To the resulting solution 4 mL of TEOS was added followed by the addition of 500  $\mu$ L of dye mixture. The resulting mixture was stirred vigorously at 80 °C for 2 hours giving an opaque pink precipitate. The RBITC MNP was collected and washed twice by centrifugation (14,000 rpm/ 15 minutes) with MeOH. The surfactant template was extracted from the as-synthesised product by dispersing the template intact MNP in MeOH (200 mL) and concentrated HCl (2 mL) at 60 °C for 18 hours. The acid extraction step was repeated twice. The MNP was washed several times using MeOH (14,000 rpm/ 15 minutes) (Figure 2.16).

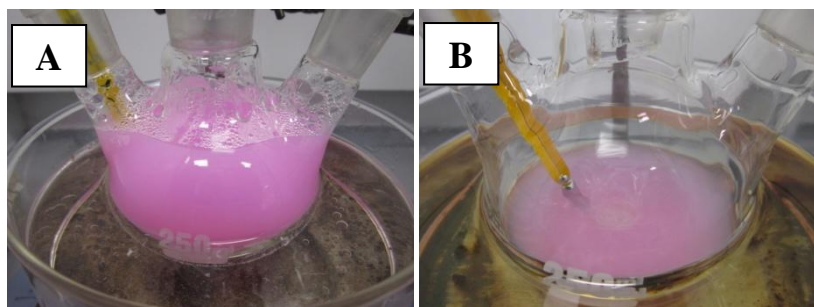


Figure 2.16: Image of rhodamine B isothiocyanate encapsulated mesoporous nanoparticles A) before and B) after acid template extraction.

#### 2.4.2.3.4. FITC encapsulated mesoporous nanoparticles (Sample 11)

Briefly, 2 mg of FITC was reacted with a mixture of 5 mL of anhydrous DMF and 50  $\mu\text{L}$  of APTMS for 3 hours. The FITC MNP was prepared by a co-condensation reaction where 1 g of CTMAB was dissolved in 480 mL of  $\text{H}_2\text{O}$  and 3.5 mL of 2 M NaOH solution at 80  $^\circ\text{C}$ . To the resulting solution 4 mL of TEOS was added followed by the addition of 500  $\mu\text{L}$  of dye mixture. The resulting mixture was stirred vigorously at 80  $^\circ\text{C}$  for 2 hours giving an opaque yellow/ orange precipitate (Figure 2.17A). The FITC MNP was collected and washed twice by centrifugation (14,000 rpm/ 15 minutes) with MeOH. The surfactant template was extracted from the as-synthesised product by dispersing the template intact MNP in MeOH (200 mL) and concentrated HCl (2 mL) at 60  $^\circ\text{C}$  for 18 hours. The acid extraction step was repeated twice resulting in a yellow solution (Figure 2.17B). The FITC MNP was washed several times using MeOH (14,000 rpm/ 15 min).

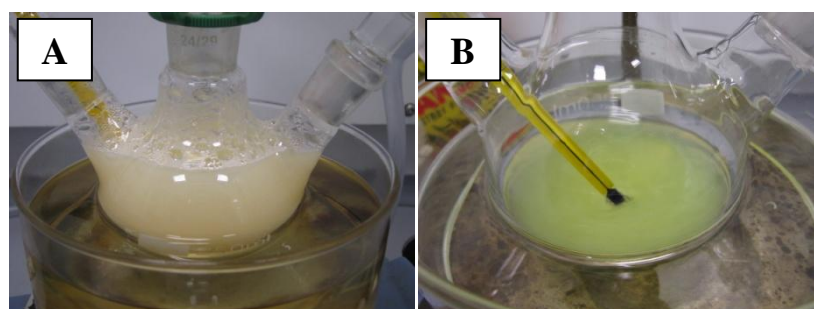
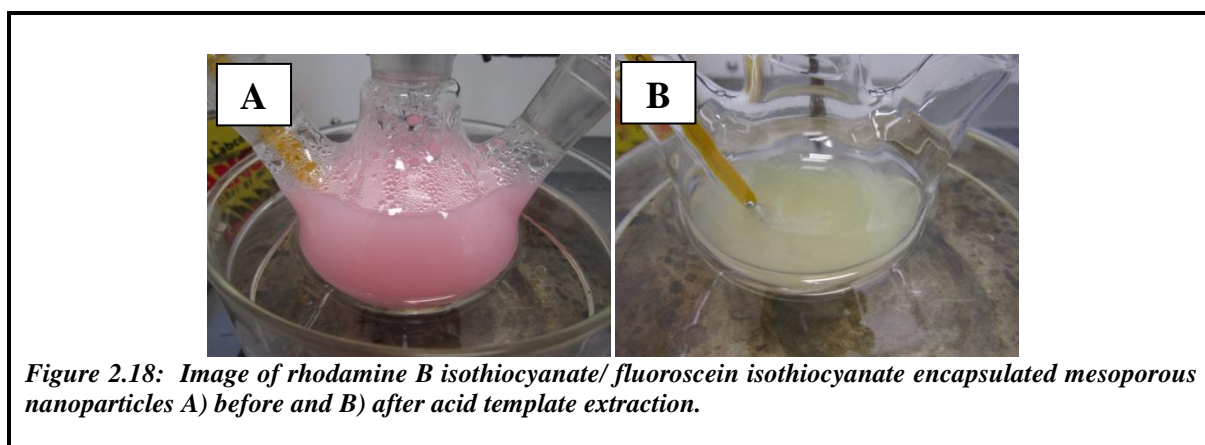


Figure 2.17: Image of fluorescein isothiocyanate encapsulated mesoporous nanoparticles A) before and B) after acid template extraction.

#### **2.4.2.3.5. RBITC/FITC encapsulated mesoporous nanoparticles (sample 12)**

Briefly, 2 mg of RBITC was reacted with a mixture of 5 mL of anhydrous DMF and 50  $\mu\text{L}$  of APTMS for 3 hours in  $\text{N}_2$  atmosphere. Separately, 2 mg of FITC was reacted with a mixture of 5 mL of anhydrous DMF and 50  $\mu\text{L}$  of APTMS for 3 hours under  $\text{N}_2$  atmosphere. RBITC/APS/DMF solution (250  $\mu\text{L}$ ) was mixed with FITC/APS/DMF solution (250  $\mu\text{L}$ ) by being stirred vigorously for the dye mixture to become homogeneous.

The RBITC/ FITC MNP were prepared by a co-condensation reaction where 1 g of CTMAB was dissolved in 480 mL of  $\text{H}_2\text{O}$  and 3.5 mL of 2 M NaOH solution at 80  $^\circ\text{C}$ . To the resulting solution 4 mL of TEOS was added followed by the addition of 500  $\mu\text{L}$  of dye mixture. The resulting mixture was stirred vigorously at 80  $^\circ\text{C}$  for 2 hours giving an opaque pinkish/ orange precipitate (Figure 2.18A). The RBITC/ FITC MNP was collected and washed twice by centrifugation (14,000 rpm/ 15 minutes) with MeOH. The surfactant template was extracted from the as-synthesised product by dispersing the template intact MNP in MeOH (200 mL) and concentrated HCl (2 mL) at 60  $^\circ\text{C}$  for 18 hours. The acid extraction step was repeated twice resulting in an orange solution (Figure 2.18B). The FITC MNP was washed several times using MeOH (14,000 rpm/ 15 minutes).



After purification of the MNP they were dispersed in a minimal amount of MeOH and dried in an oven set to 60  $^\circ\text{C}$  for several hours. The resulting powders were collected as shown in Figure 2.19. The RBITC incorporated MNP powder was used in the drug release study, refer to Chapter 3; Section 3.6.

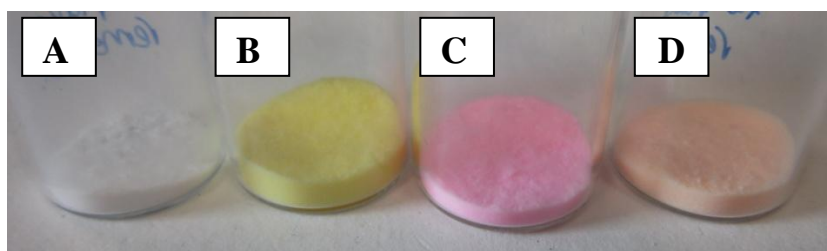


Figure 2.19: Image of A) silica mesoporous nanoparticles, B) fluorescein isothiocyanate encapsulated mesoporous nanoparticles; C) rhodamine B isothiocyanate encapsulated mesoporous nanoparticles and D) rhodamine B isothiocyanate/fluorescein isothiocyanate encapsulated mesoporous nanoparticles.

### 2.4.3. Results

Initially, MNP were prepared using Lin *et al.* method with RBITC dye molecules incorporated within the NPs [80]. They have reported the synthesis of hexagonal MNP of approximately 110 nm with FITC dye. The PCS measurements of the RBITC MNP (sample 1), shown in Figure 2.20, has a hydrodynamic size of 847.3 nm, which is much larger than the expected 110 nm diameter.

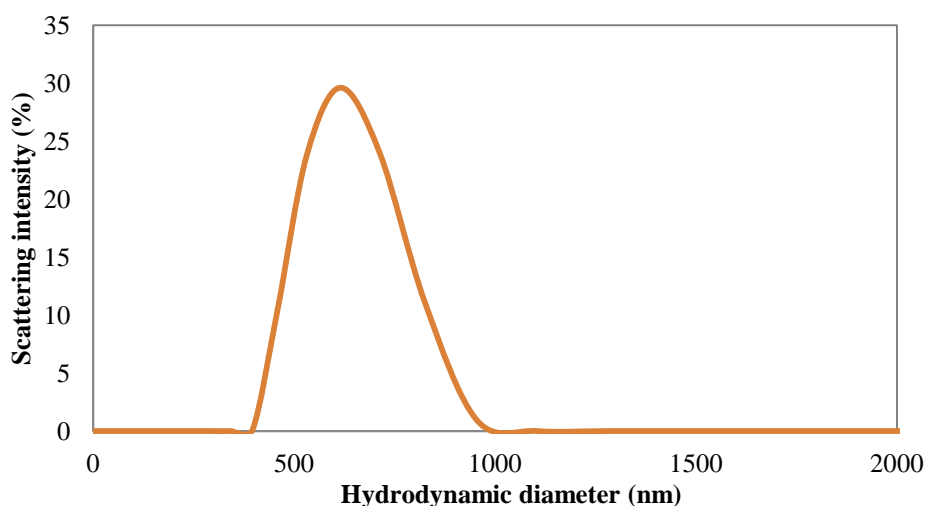
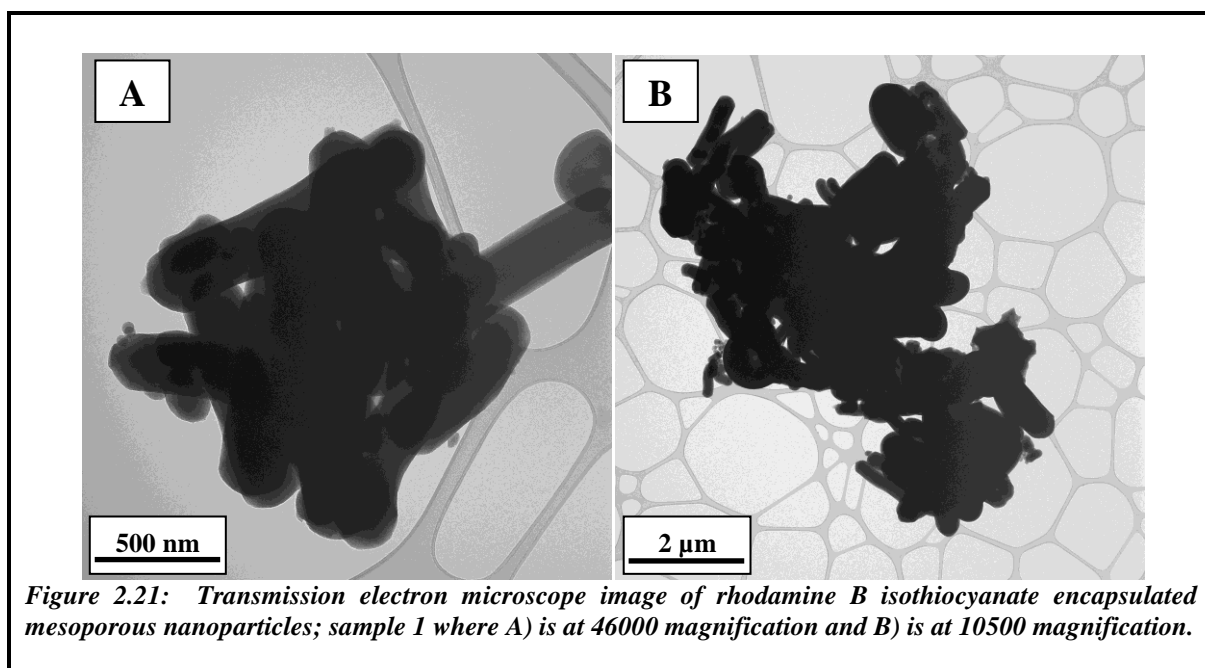
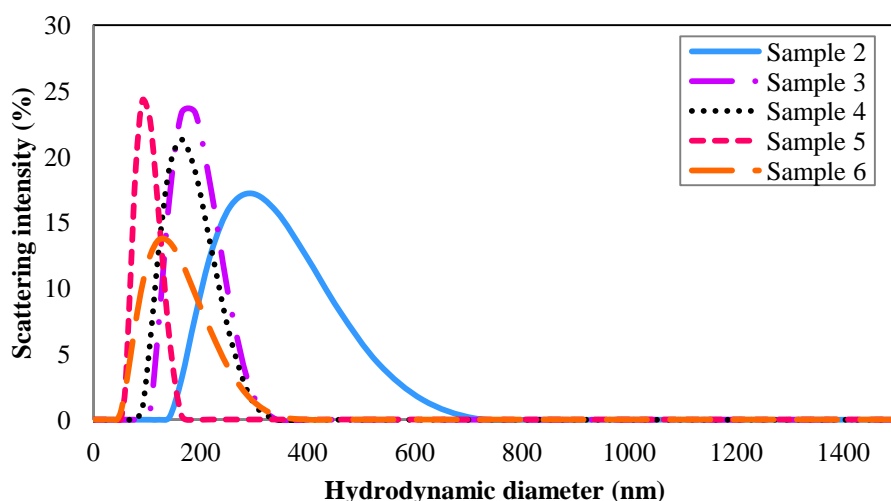


Figure 2.20: Photon correlation spectroscopy analysis of rhodamine B isothiocyanate encapsulated mesoporous nanoparticles; sample 1.

Sample 1 has a zeta potential of +42.1 mV indicating the MNP are stable as the zeta potential value is above +30 mV. Further confirmation of the MNP size was determined by TEM with an average diameter of 265, 225 and 124±15 nm; and length of 1142, 1060±6 and 494 nm (Figure 2.21).



It is of interest to synthesise smaller MNP for the biological application, as a comparison to previous *in vitro* studies [83]. Therefore an alternative experimental method was implemented, synthetic route 2, to attempt to produce smaller MNP. With the second synthetic route smaller template intact MNP were successfully synthesised, as demonstrated by the PCS (Figure 2.22).



**Figure 2.22:** Photon correlation spectroscopy analysis of mesoporous nanoparticles; sample 2 was 292.3 nm, sample 3 was 173.6 nm, sample 4 was 160.1 nm, sample 5 was 106.7 nm and sample 6 was 123.2 nm.

The hydrodynamic diameter of sample 2 was 292.3 nm, although when EG was used as the media for nucleation instead of isopropanol (IP) the MNP size dramatically decreased to 160.7 nm (sample 4). Sample 3 demonstrates that by keeping the volume of EG (30 mL) constant and increasing the amount of catalyst (10 mL) the MNP size increase by 14 nm. However, sample 6 demonstrates that as the concentration of the catalyst was decreased to 2 mL, in comparison to sample 3, then smaller MNP with an average size of 123.2 nm were produced. Sample 5 demonstrates that as the catalyst amount was double in comparison to sample 6 it further causes smaller MNP to be produced with a hydrodynamic diameter of 106.7 nm. The stability for sample 5 and 6 was determined with the zeta potential, +30.4 and +27.1 mV respectively.

Furthermore, the MNP diameters were confirmed with TEM (Figure 2.23). Sample 2 was bimodal with diameters of  $100\pm 9$  and  $137\pm 9$  nm (Figure 2.23A). Figure 2.23B (sample 3) was also bimodal and has MNP size of  $182\pm 9$  and  $140\pm 5$  nm. Sample 4 was polydispersed and has sizes of  $268\pm 5$ ,  $232\pm 13$  and  $182\pm 9$  nm, with length of  $423\pm 14$  nm (Figure 2.23C). Figure 2.23D (sample 5) was bimodal with an average size of  $87\pm 5$  and  $59\pm 5$  nm. Figure 2.23E (sample 6) have an average size of  $50\pm 5$  nm. Sample 7, has an average MNP diameter of  $73\pm 9$  nm (Figure 2.23F). The general trend suggests that as the catalyst concentration increases there is an increase in MNP sizes.

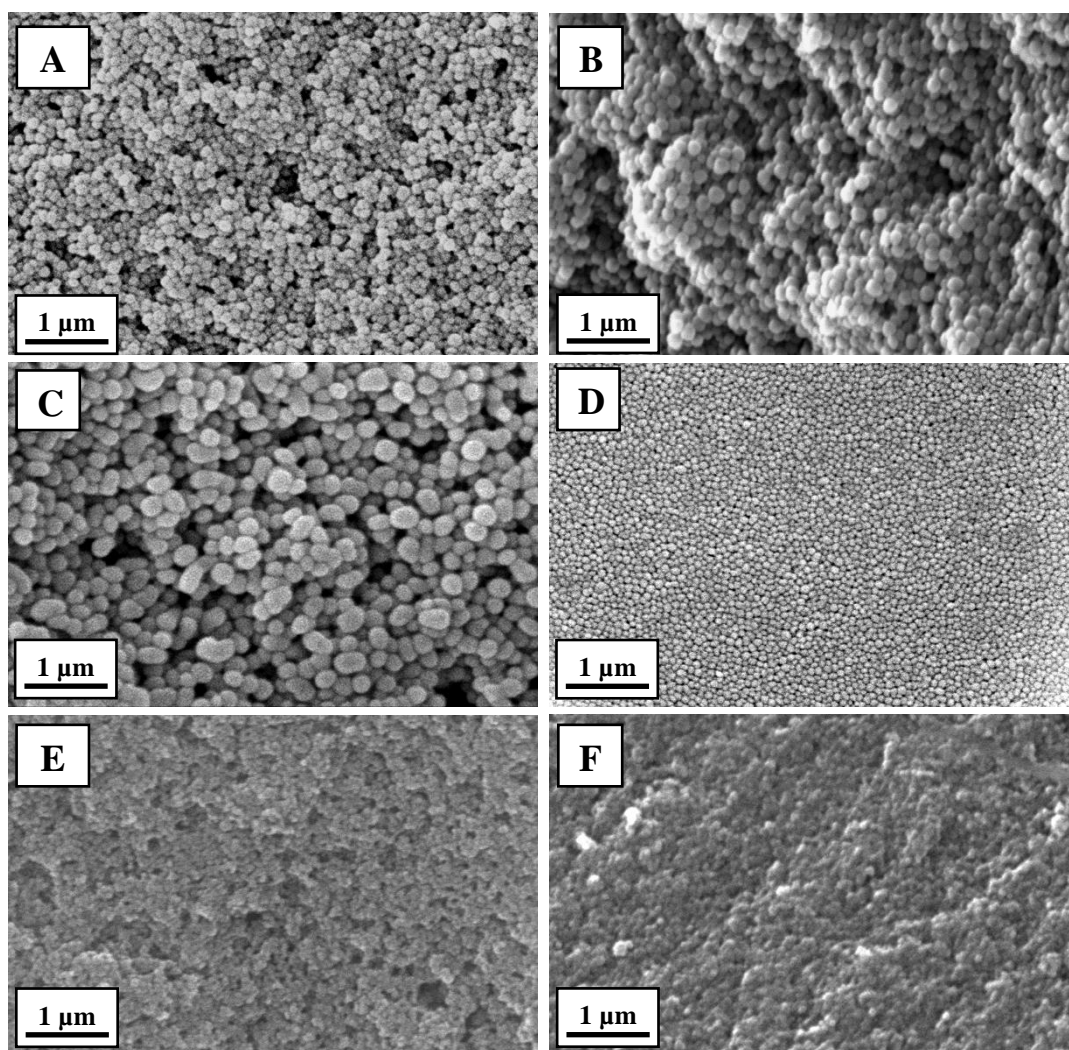


*Figure 2.23: Scanning electron microscope images of mesoporous nanoparticles of A) sample 2, B) sample 3, C) sample 4, D) sample 5, E) sample 6 and F) sample 7.*

The MNP size required for the biological application was successfully synthesised, sample 5. In order to produce a surfactant free MNP the template must be removed. There are numerous methods for template removal, such as acidic or basic template extraction in an alcoholic solution. Alternatively, the template can be removed by calcinations, which is a simple and easy method. However, when sample 5 was calcined it caused the MNP to aggregate, as demonstrated from the PCS analysis in Figure 2.24.

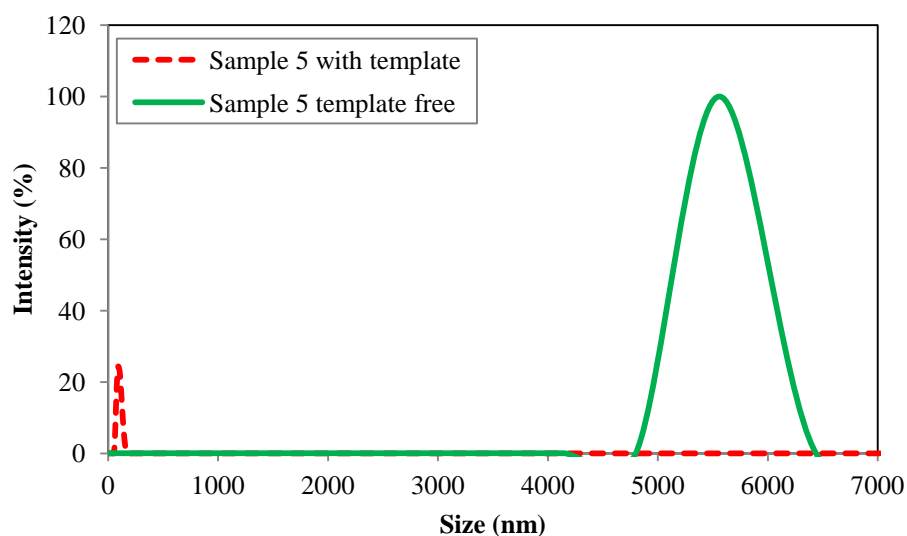


Figure 2.24: Photon correlation spectroscopy analysis of mesoporous nanoparticles, sample 5, with a hydrodynamic diameter of 106.7 nm and is increased to 8139 nm when calcined.

The zeta potential for template free sample 5 is -19.8 mV. The aggregated MNP was also confirmed by TEM image (Figure 2.25).

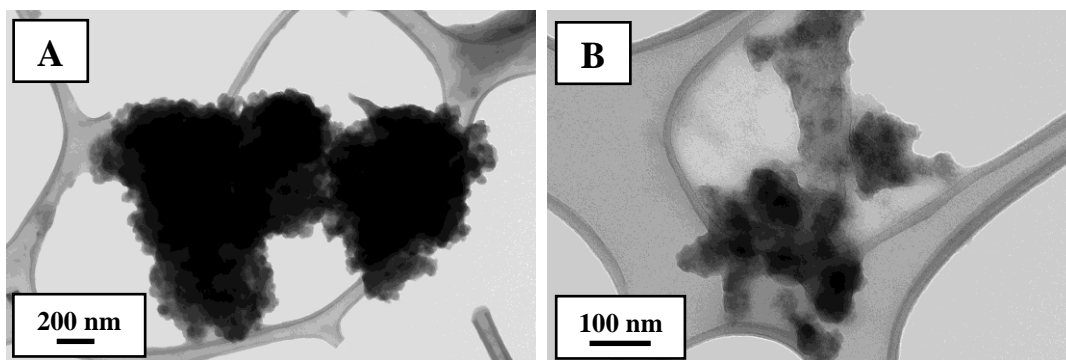


Figure 2.25: Transmission electron microscope image of template removed mesoporous nanoparticles, sample 5, at A) lower magnification and B) higher magnification.

Although, the MNP are aggregated, the N<sub>2</sub> sorption analysis was conducted to confirm the porosity of the sample (Figure 2.26).

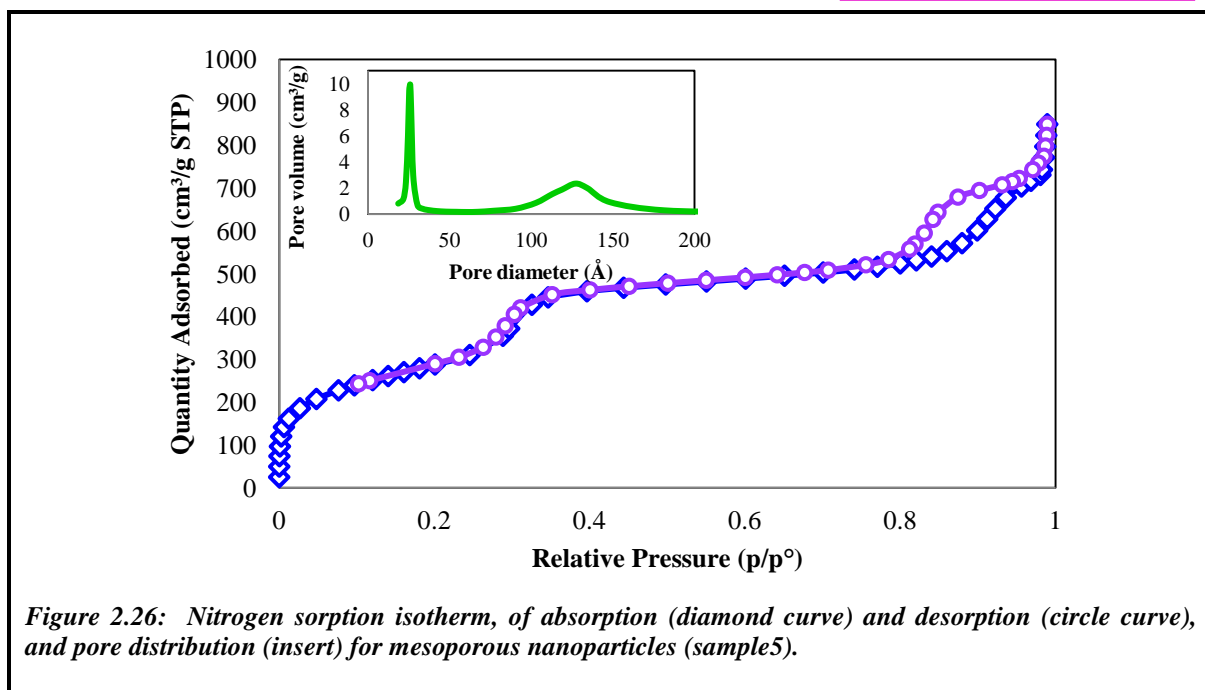
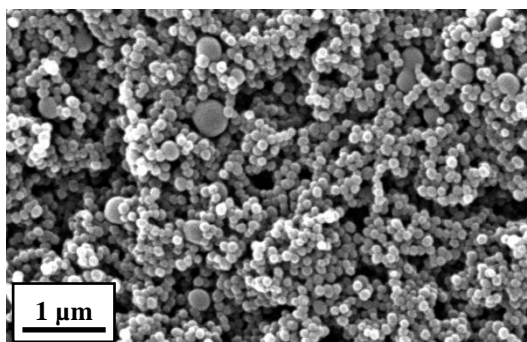


Figure 2.26: Nitrogen sorption isotherm, of absorption (diamond curve) and desorption (circle curve), and pore distribution (insert) for mesoporous nanoparticles (sample5).

Sample 5, has a large surface area of  $1222.8 \pm 63.0 \text{ m}^2/\text{g}$ . Figure 2.26 shows an initial sharp peak, representing that the majority of sample 5 has pore size of 2.6 nm, and smaller volume of 13 nm pores. The objective of synthesising porous NPs has been achieved and an advantage with this methodology is producing MNP with large surface area. However, the main objective was synthesising MNP of approximately 100 nm that are aggregation free. The biological testing will show whether the MNP have a toxicological effect on tissue via *in vitro* studies. Furthermore, the incorporating of dye molecules within the MNP can be tested for biocompatibility and would be advantageous as it would allow imaging abilities in biological systems. Therefore MNP were prepared using the procedure carried out for sample 5 but RBITC coupled with APTMS were used to synthesise sample 7 (Figure 2.23).

However, when the MNP were placed in water the sample rapidly sedimented, therefore an alternative synthetic route was examined.

The SEM, Figure 2.27, shows that RBITC MNP was polydispersed with a diameter of  $104\pm 13$ ,  $266\pm 11$ , 300 and 436 nm. The polydispersion in the sample may be due to the APS molecules reacting instantaneously with the silica seeds it comes into contact with.



*Figure 2.27: Scanning electron microscope image of rhodamine B isothiocyanate encapsulated mesoporous nanoparticles (sample 8).*

In order to overcome the polydispersity problem APTMS molecules was diluted in anhydrous DMF solution. The SEM images in Figure 2.28 confirm the synthesis of well dispersed MNP of close size distribution. The SEM images of silica MNP, Figure 2.28A, show the product is well dispersed of  $95\pm 13$  nm. Figure 2.28B, the RBITC MNP (sample 10) is well dispersed of  $105\pm 13$  nm. The FITC MNP has size distribution of  $109\pm 18$  nm (Figure 2.28C). The RBITC/ FITC MNP are well dispersed with an average diameter of  $105\pm 13$  nm (Figure 2.28D).

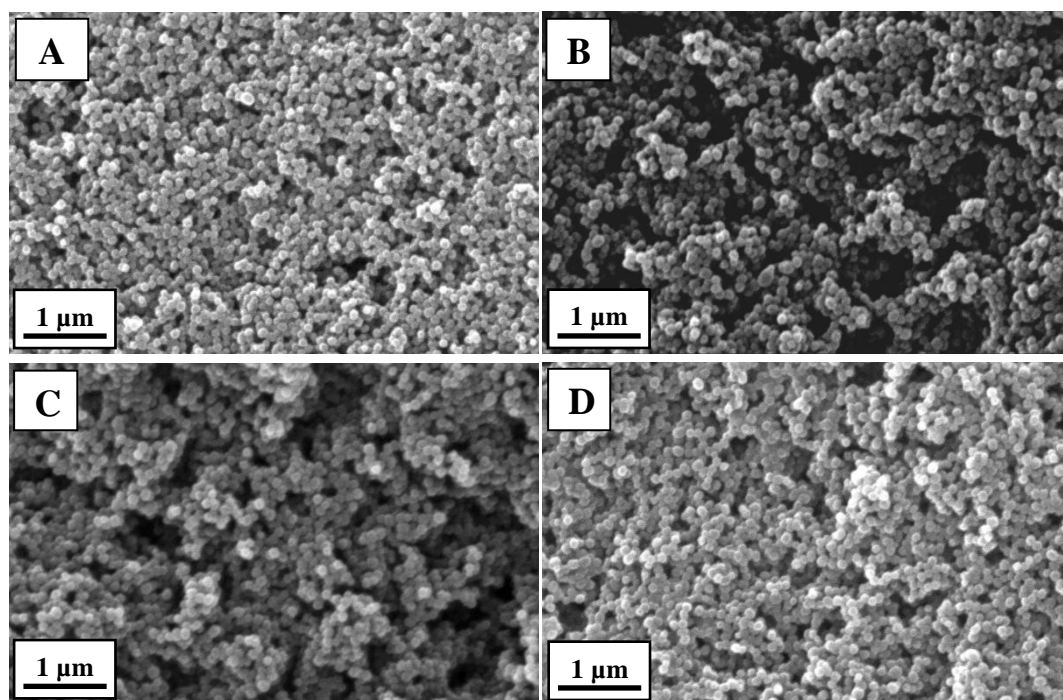
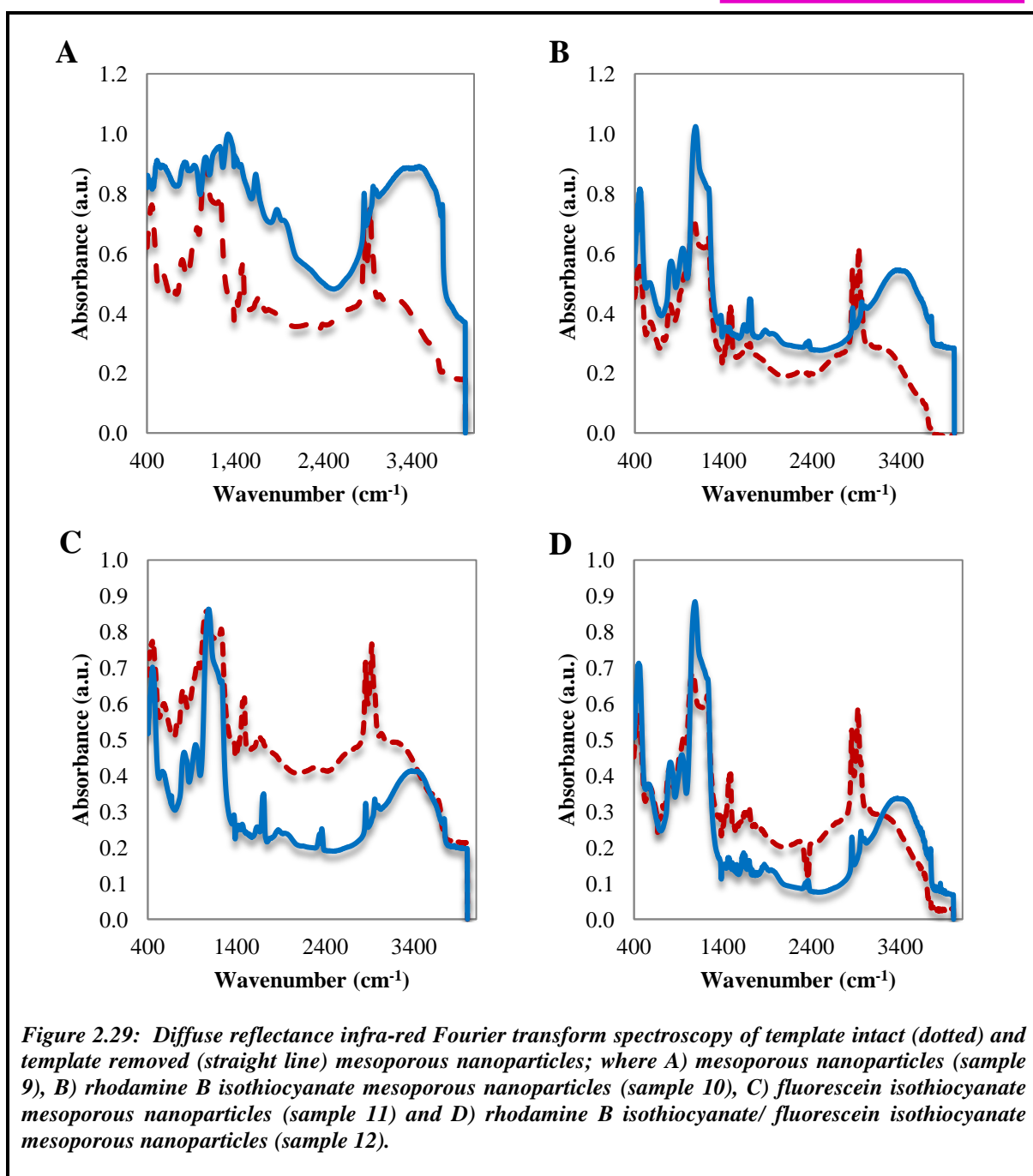


*Figure 2.28: Scanning electron microscope image of A) mesoporous nanoparticles (sample 9), B) rhodamine B isothiocyanate encapsulated mesoporous nanoparticles (sample 10), C) fluorescein isothiocyanate encapsulated mesoporous nanoparticles (sample 11) and D) rhodamine B isothiocyanate/fluorescein encapsulated isothiocyanate mesoporous nanoparticles (sample 12).*

Diffuse reflectance infra-red Fourier transform spectroscopy (DRIFTS) analysis was carried out to determine the successful removal of the CTMAB molecules from the MNP matrix (Figure 2.29).



From the DRIFTS analysis the peaks referring to groups contained within the MNP was placed in Table 2.11, where all types of MNP; A) silica MNP (sample 9), B) RBITC MNP (sample 10), C) FITC MNP (sample 11) and D) RBITC/ FITC MNP (sample 12), show similar peaks.

**TABLE 2.11: Diffuse reflectance infra-red Fourier transform spectroscopy analysis of the functional groups within the mesoporous nanoparticles.**

MNP ( <i>template intact</i> )		MNP ( <i>template removed</i> )	
Wavenumber (cm <sup>-1</sup> )	Bond	Wavenumber (cm <sup>-1</sup> )	Bond
2924	sharp C-H stretching	2957	weak C-H stretching
2854	sharp C-H stretching	2856	weak C-H stretching
1062	Si-O-Si stretching	1080	Si-O-Si stretching
		824	Si-O-H deformation

The broad band for the asymmetric Si-O-Si stretching vibration peak of the MNP with template is at 1065 cm<sup>-1</sup>. This is also observed for the template removed MNP at 1062 cm<sup>-1</sup>. The band at approximately 800 cm<sup>-1</sup> represents the symmetrical stretching vibration of Si-O bond. The band at 957 and 496 cm<sup>-1</sup> for template removed product has occurred because of the surface Si-O<sup>-</sup> groups stretching and bending vibration. These bands are also seen in the template intact MNP at 941 and 455 cm<sup>-1</sup> respectively [84]. The two sharp peaks observed at 2853 and 2923 cm<sup>-1</sup> for the MNP sample with template is due to the presence of the organic surfactant CTMAB [85]. The removal of CTMAB molecules has significantly reduced by acidic extraction as the CTMAB peaks have become very small at 2856 and 2956 cm<sup>-1</sup>.

Thermogravimetric analysis (TGA) was used to determine the presence of dye molecules by their thermal decomposition. Figure 2.30 is the TGA for A) silica MNP and B) RBITC MNP, C) FITC MNP and D) RBITC/ FITC MNP. The weight loss (4 %) from room temperature to 110 °C was due to water molecules being evaporated from the pores. The weight loss of 7 % from 110-400 °C was due to the decomposition of CTMAB molecules that are still within the MNP. The amine group of CTMAB will react to produce tertiary amine and alkene side group, known as Hoffmann elimination. The tertiary amine will react with CO<sub>2</sub> via a combustion and oxidation reaction. The weight loss above 400 °C may due to condensation of water from the silanol groups [72].

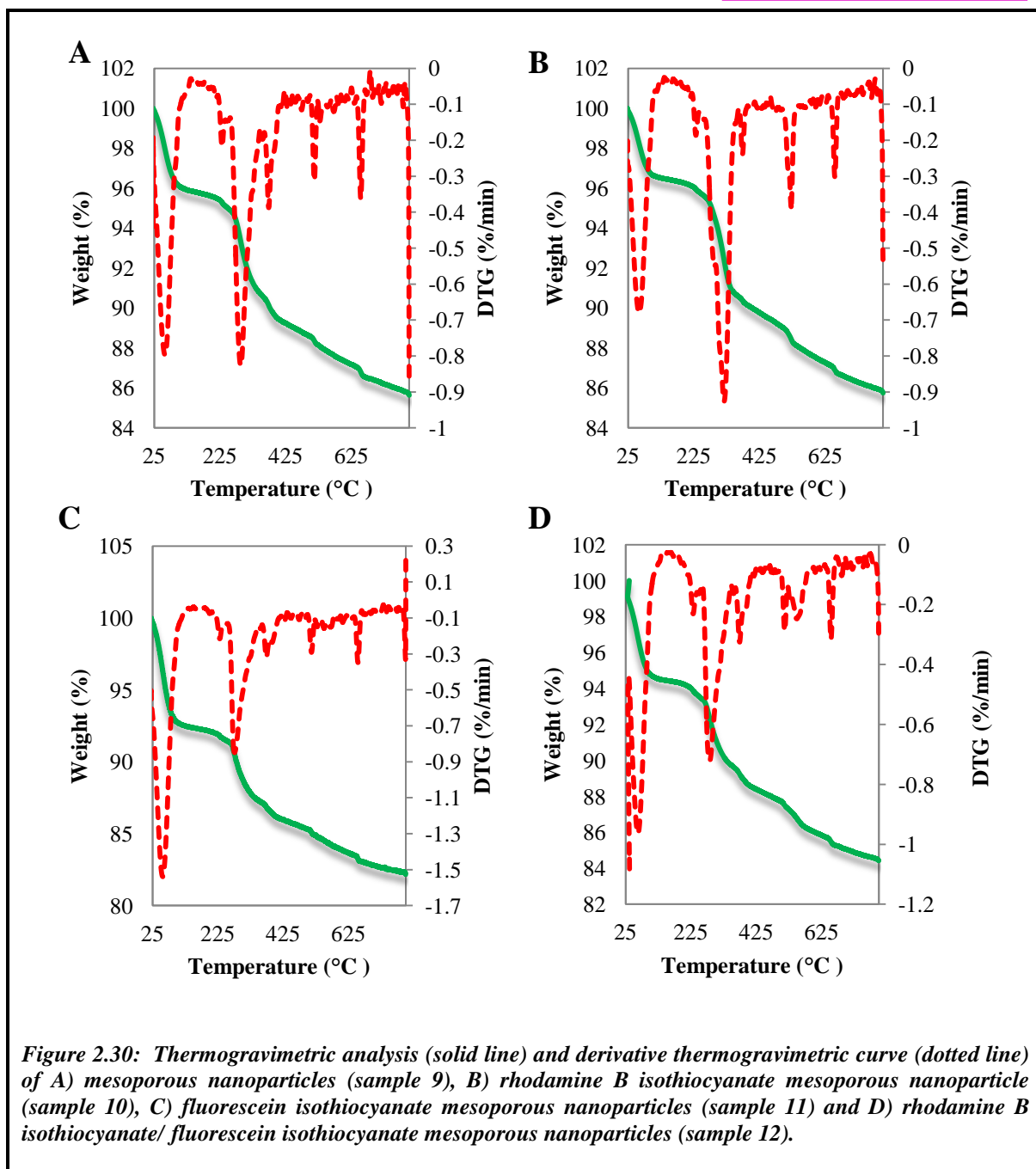
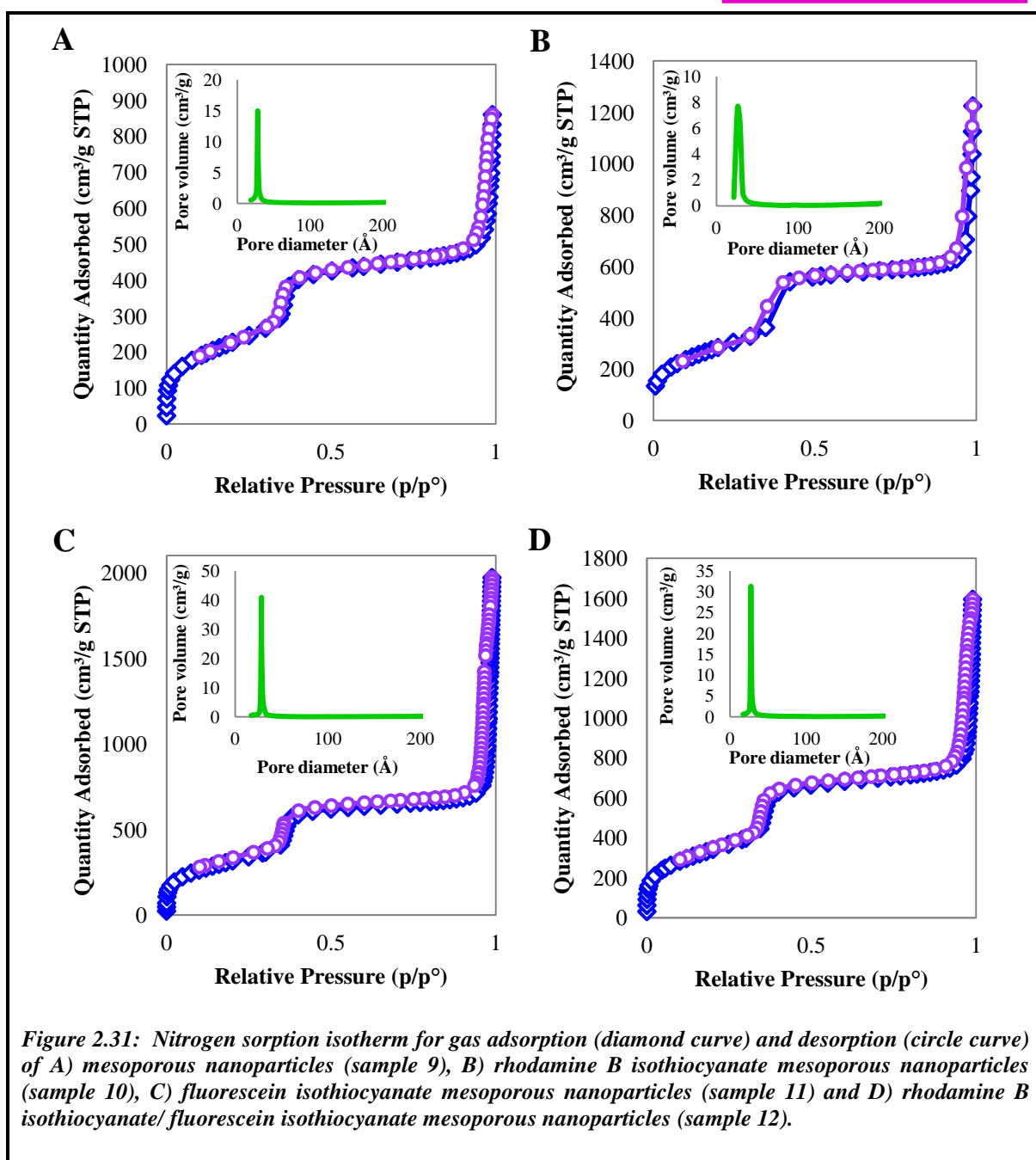


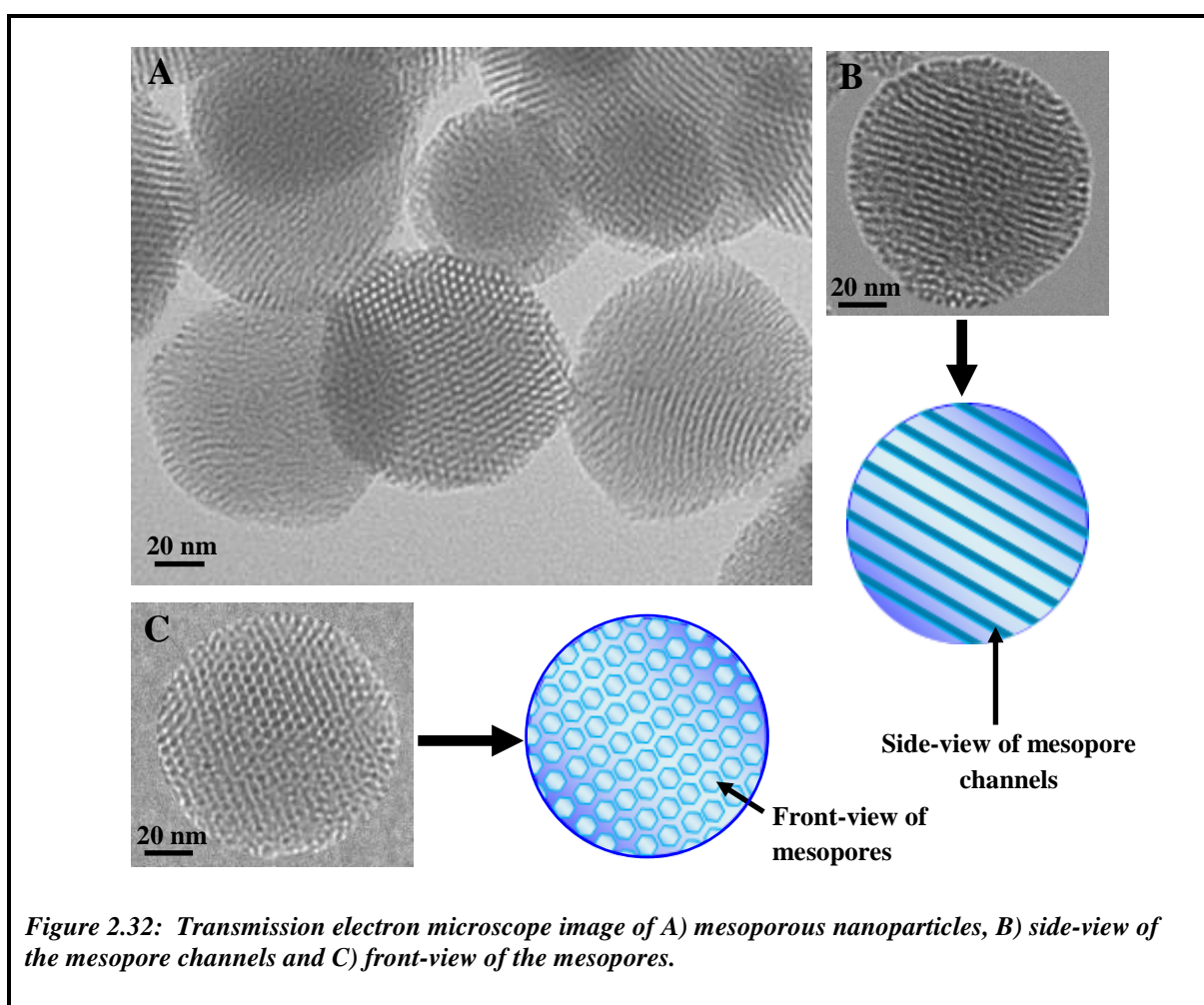
Figure 2.31 is of the N<sub>2</sub> sorption of MNP with and without dye molecules after their template was removed. The isotherm curve follows the general type-IV trend of mesoporous materials.



The silica MNP has a pore diameter of 2.9 nm as shown in the pore size distribution graph (Figure 2.31A). The sharp peak confirms the ordered mesoporous nanoparticles have a narrow size distribution. The large surface area ( $853.3 \pm 9.0 \text{ m}^2/\text{g}$ ) along with narrow pore distribution is successfully synthesised. The N<sub>2</sub> sorption analysis for RBITC MNP is shown in Figure 2.31B, with a surface area of  $1032.6 \pm 3.5 \text{ m}^2/\text{g}$  which is larger than the silica MNP. Furthermore, the insert confirms for the pore size of RBITC MNP to be 2.6 nm, smaller than the silica MNP. FITC MNP has a surface area of  $1154.5 \pm 2.1 \text{ m}^2/\text{g}$ , which is larger than the silica MNP, while the insert confirm the pore size to be 2.8 nm, similar to

the silica MNP (Figure 2.31C). RBITC/ FITC MNP have a surface area of  $1252.5 \pm 1.9$   $\text{m}^2/\text{g}$ , which is larger than the silica MNP, while the insert confirm the pore size of 2.8 nm (Figure 2.31D).

Furthermore, the TEM images confirm the synthesis of porous monodispersed MNP of narrow size distribution (Figure 2.32), where A) the silica MNP size are  $95 \pm 13$  nm and B) magnified image of silica MNP. The template removal was performed by refluxing the MNP in acidified ethanol solution.



The PCS measurements of the MNP and dye encapsulated MNP were determined in water and high salt solution (Figure 2.33).

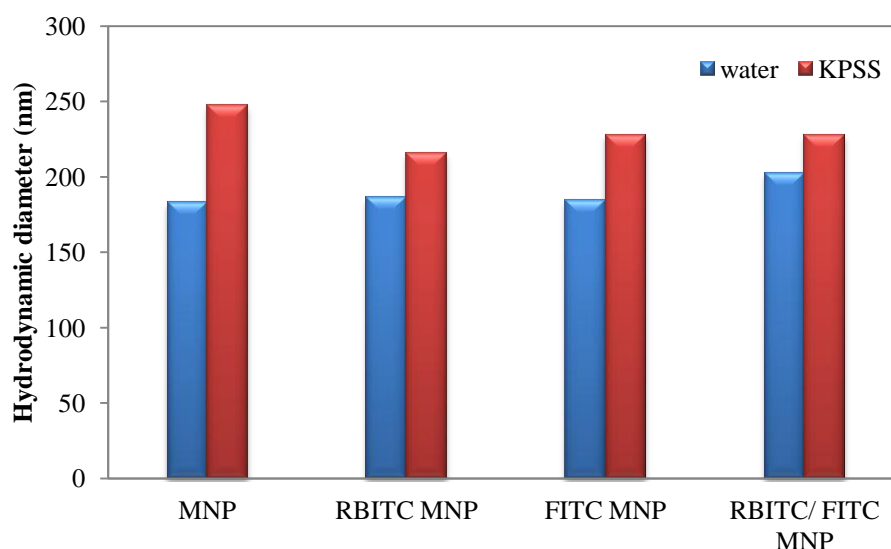


*Figure 2.33: Photon correlation spectroscopy analysis of mesoporous nanoparticles with and without dye molecules in water and potassium physiological salt solution media.*

The hydrodynamic diameter of the template intact MNP show a large aggregation as the CTMAB molecules causes the MNP to clump together, however after removal of the template they became well dispersed and are dimers with 190.7 nm. The zeta potential further confirms the stability of these MNP within their suspension when template was removed (Table 2.12). Furthermore, when MNP were placed in high potassium physiological salt solution (KPSS) the hydrodynamic diameter increased to 247.3 nm from 182.9 nm with the zeta potential values increasing to -13.8 mV from -30.0 mV, due to the high ionic salt solution (refer to Chapter 2, Section 2.1.6). RBITC MNP in KPSS media causes the hydrodynamic diameter to increase to 215.5 nm from 185.8 nm, along with the increase in the zeta potential values to -17.0 mV from -32.8 mV due to the high ionic salt solution. FITC MNP in KPSS media causes the hydrodynamic diameter to increase to 227.8 nm from 183.9 nm, along with the increase in the zeta potential values to -15.6 mV from -30.0 mV due to the high ionic salt solution. RBITC/ FITC MNP in KPSS media causes the hydrodynamic diameter to increase to 227.8 nm from 202.1 nm, along with the increase in the zeta potential values to -16.0 mV from -31.7 mV due to the high ionic salt solution.

**TABLE 2.12: Hydrodynamic size and stability measurements of mesoporous nanoparticles, in water and high potassium physiological salt solution.**

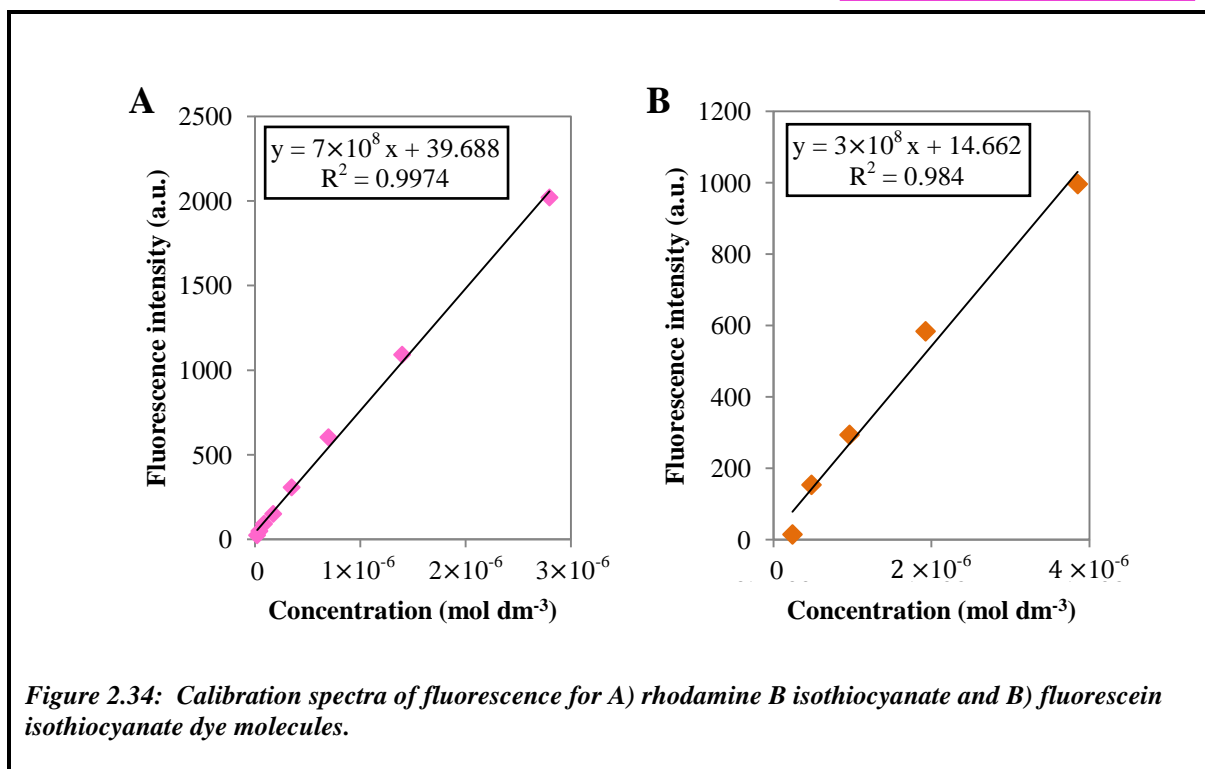
Nanoparticles type	Primary diameter <sup>a</sup> (nm)	Hydrodynamic diameter <sup>b</sup> (nm)		$\zeta$ potential (mV)	
		<i>In water</i>	<i>In KPSS</i>	<i>In water</i>	<i>In KPSS</i>
Silica MNP	95±13	182.9	247.3	-30.0	-13.8
RBITC MNP	105±13	185.8	215.5	-32.8	-17.0
FITC MNP	109±18	183.9	227.8	-30.0	-15.6
RBITC/ FITC MNP	105±13	202.1	227.8	-31.7	-16.0

<sup>a</sup> Mean ( $\pm$ SD) diameter determined by SEM.

<sup>b</sup> Mean PCS measurement.

### ***2.4.3.1. Quantification of dye molecules within mesoporous nanoparticles***

The amount of dye molecules encapsulated within the MNP was quantified with fluorescence spectroscopy. The fluorescence spectra of known concentrations of RBITC were used to produce a calibration graph (Figure 2.34). The excitation wavelength of RBITC is 540 nm with an emission at 573 nm. FITC has an excitation wavelength of 490 nm and an emission at 520 nm.



The dye molecules encapsulated within the MNP were quantified by analysing the amount of dye molecules within the supernatant (Figure 27, 28, 29 and 30 in the appendix). Thus, the dye concentration within the NPs was calculated by subtracting the concentration within the supernatant from the actual concentration of dye used (Table 2.13). The mass of RBITC dye molecules within RBITC MNP were 2.35 mg, while FITC dye molecules within FITC MNP were 5.61  $\mu$ g. The RBITC dye molecules within RBITC/ FITC MNP were 1.19 mg, while FITC dye molecules within RBITC/ FITC MNP were 90.8  $\mu$ g.

These findings demonstrate that there is a greater volume of RBITC dye molecules incorporated within the mesoporous matrix as compared to the FITC dye molecules.

TABLE 2.13: Quantification of dye molecules within the nanoparticles.

	Fluorescence intensity (a.u.)	Dye concentration in supernatant (mol dm <sup>-3</sup> )	Moles of dye in supernatant (mol)	Mass of dye in supernatant (mg)	mass of dye in the NPs (mg)
RBITC MNP 1 <sup>st</sup> supernatant	61.43	$3.11 \times 10^{-8}$	$1.45 \times 10^{-8}$	$7.76 \times 10^{-3}$	2.35
RBITC MNP 2 <sup>nd</sup> supernatant	1266	$1.75 \times 10^{-6}$	$4.33 \times 10^{-7}$	$2.32 \times 10^{-1}$	
RBITC MNP 3 <sup>rd</sup> supernatant	58.86	$2.74 \times 10^{-8}$	$1.12 \times 10^{-8}$	$6.02 \times 10^{-3}$	
FITC MNP 1 <sup>st</sup> supernatant	44.48	$9.94 \times 10^{-8}$	$4.63 \times 10^{-8}$	$1.80 \times 10^{-2}$	$5.61 \times 10^{-3}$
FITC MNP 2 <sup>nd</sup> supernatant	7866	$2.62 \times 10^{-5}$	$6.36 \times 10^{-6}$	2.48	
RBITC/ FITC MNP (RBITC dye) 2 <sup>nd</sup> supernatant	615.9	$8.23 \times 10^{-7}$	$2.02 \times 10^{-7}$	$1.09 \times 10^{-1}$	1.19
RBITC/ FITC MNP (RBITC dye) 3 <sup>rd</sup> supernatant	40.09	$5.74 \times 10^{-10}$	$1.41 \times 10^{-10}$	$7.57 \times 10^{-5}$	
RBITC/ FITC MNP (FITC dye) 1 <sup>st</sup> supernatant	34.3	$6.55 \times 10^{-8}$	$3.05 \times 10^{-8}$	$1.19 \times 10^{-2}$	$9.08 \times 10^{-2}$
RBITC/ FITC MNP (FITC dye) 2 <sup>nd</sup> supernatant	3608	$1.20 \times 10^{-5}$	$2.95 \times 10^{-6}$	1.15	

#### 2.4.4. Discussion

The fabrication of RBITC incorporated MNP of approximately 100 nm were not successfully synthesised via synthetic route 1, as the PCS analysis demonstrates the formation of much larger particles. These larger particle sizes may have resulted due to a greater concentration of catalyst, ammonia, within the reaction mixture. Previously, Lin *et al.* [63] suggested that the ammonia concentration and reaction temperature influences particle diameter. Their study suggested that as the catalyst concentration increased it in turn increased the particle diameter. Furthermore, at lower temperature and higher concentration of silica precursor the particle diameter increased.

The synthesis of template intact MNP were successfully synthesised via synthetic route 2. However, upon template removal the MNP aggregated. Previous studies, also demonstrate the influences of direct calcination of surfactant intact MNP may lead to agglomeration [86].

MNP with and without fluorophore dye molecules were successfully fabricated via synthetic route 3. Furthermore, the stability of the particles were confirmed with the laser Doppler velocimetry in both water and potassium physiological salt solution. The CTMAB template removal was conducted via acid wash method in order to make the NPs porous and remove the known cellular toxicological influence of the CTMAB molecules [87]. Interestingly, our findings demonstrate that there is a greater mass of RBITC dye molecules incorporated within the mesoporous matrix as compared to the FITC dye molecules. This may be due to the difference in the solubility of the fluorophore dye molecules. The RBITC dye molecules are readily miscible in water, however FITC require a polar solvent at *pH* greater than 6 to dissolve. Furthermore, we demonstrate that MNP without dye molecules have a greater total surface area (SA) volume as compared to dye incorporated MNP. The SA in decreasing order is as follows; MNP > FITC MNP > RBITC/FITC MNP > RBITC MNP.

The zeta potential values below +30 or -30 mV means the sample is unstable which may lead to further nucleation between NPs and growth in size.

## **2.5. Silicate-1 Nanoparticles**

### **2.5.1. Material**

Tetraethyl orthosilicate (TEOS), tetrapropylammonium hydroxide solution (TPAOH) and 3-aminopropyl trimethoxysilane (APTMS) were purchased from Sigma-Aldrich (UK). Isopropanol (IP) was purchased from Fisher-Scientific (UK). Millipore water was used for all experiments.

### **2.5.2. Methodology**

Silicate-1 NPs were synthesised via the method of Wang *et al.* [87] (Table 2.14). For synthesis of sample 1, briefly, water (5.66 mL), TEOS (19.99 g) and tetrapropylammonium hydroxide solution (TPAOH) (34.57 g) was stirred vigorously for 1 hour at room temperature until the solution becomes clear without the oil-in water consistency. The mixture was then placed in an autoclavable polypropylene bottle equipped with a condenser. The resulting mixture was aged for 20 hours in an oil bath set at 45 °C.

APTMS (12 mol% with respect to Si) solution was made by mixing APTMS (2.07 g) with isopropanol (10 mL). The APTMS solution was added to the polypropylene bottle while the mixture was stirred vigorously. When the temperature of the mixture increased to 90 °C it was allowed to heat for 6 hours. The resulting solution remained colourless. The colourless solution was placed in an autoclave and aged for 20 hours at 140 °C. This resulted in an opaque white solution which was collected by centrifugation. The template was removed by calcinations at 500 °C for 4 hours.

**Table 2.14: Overview for the fabrication of silicate-1 nanoparticles as the temperature and aging time alters.**

Sample	Hydrodynamic size <sup>a</sup> (nm)	Water (g)	TEOS (g)	TPAOH (g)	IP <sup>b</sup> (mL)	APS (mol)	Temperature (°C)	Aging time (h) <sup>c</sup>
1	181	5.65	20	34.56	10	$1.15 \times 10^{-2}$	140	20
2	153	5.65	20	34.56	10	$1.15 \times 10^{-2}$	90	96

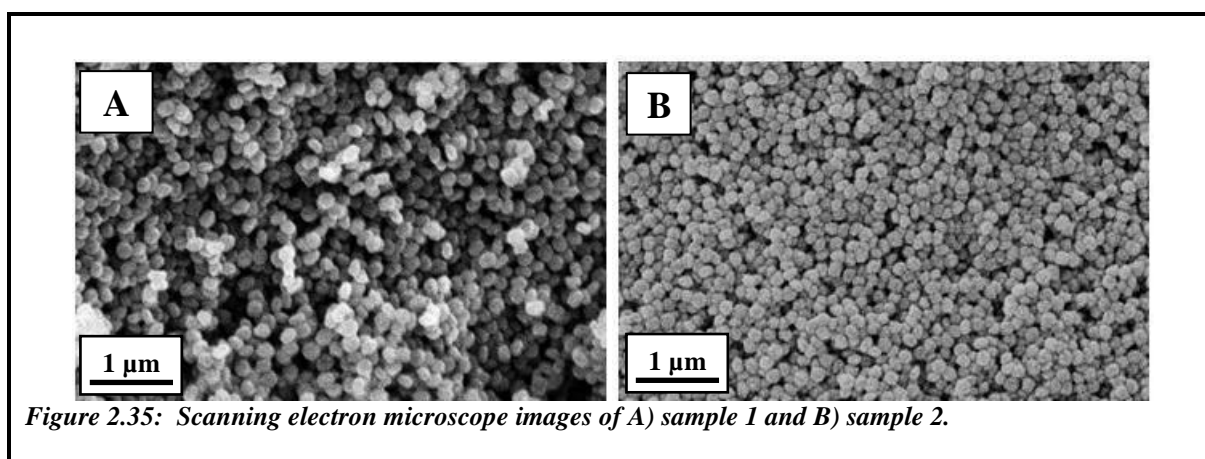
<sup>a</sup> Mean PCS measurement.

<sup>b</sup> Abbreviation for the solvent isopropanol.

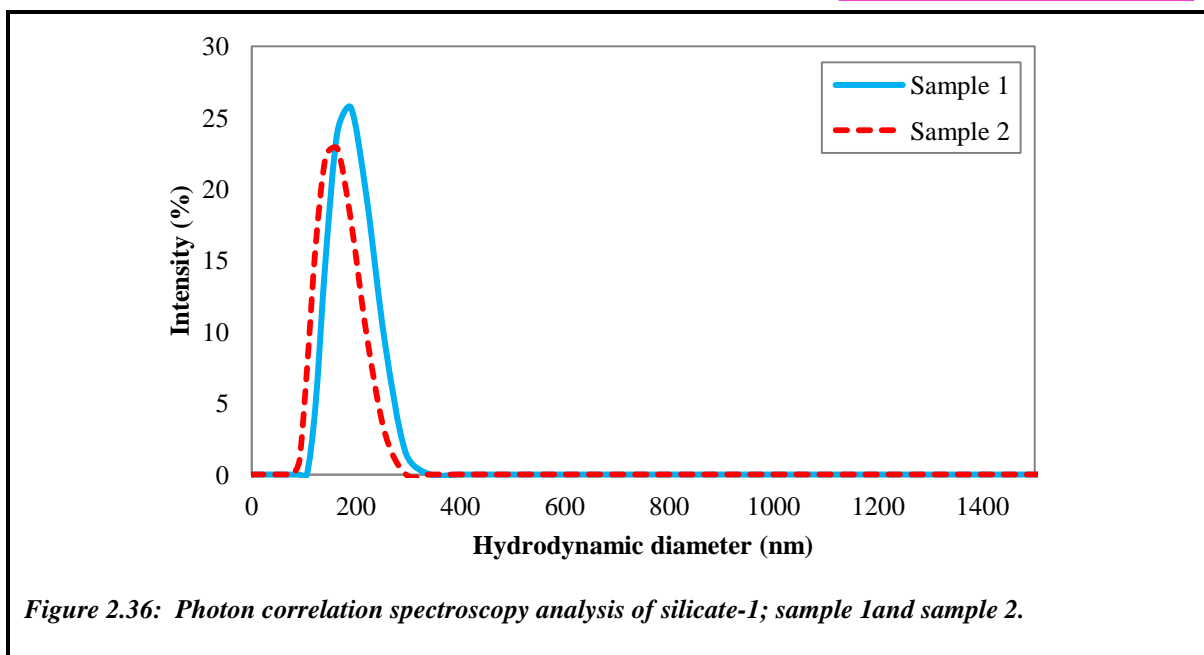
<sup>c</sup> hour.

### 2.5.3. Results

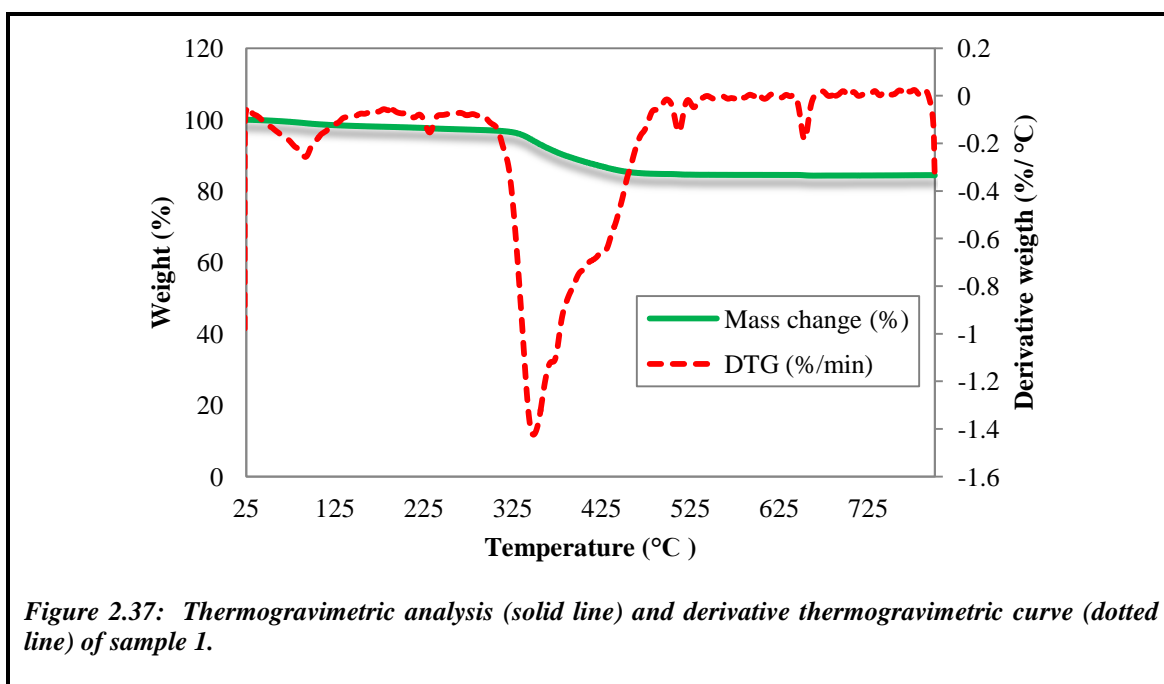
The NP morphology and sizes were determined by SEM (Figure 2.35). Sample 1 (Figure 2.35A) is bimodal with an average diameter of 146 and 164 nm and sample 2 (Figure 2.35B) is also bimodal 129±14 and 114 nm.



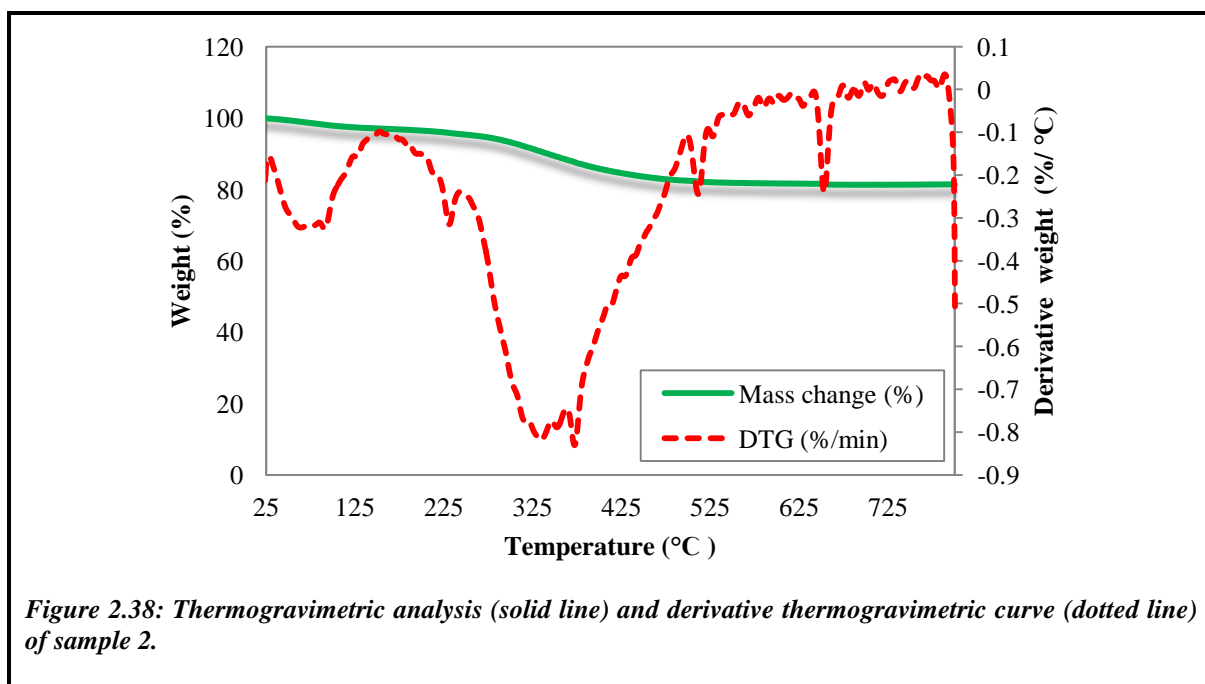
The NP dispersity along with size distribution was further confirmed with PCS analysis (Figure 2.36); the size is in close agreement with the SEM images. Both samples have a single peak at a hydrodynamic diameter of 180.6 and 152.5 nm for sample 1 and 2 respectively.



The TGA (Figure 2.37) results of sample 1 shows a small weight loss of up to 0.3 % at approximately 90 °C and weight loss of up to 1.4 % at approximately 350 °C. The initial weight loss observed can be attributed due to surface dehydration, while the latter weight loss is due to the decomposition and total loss of the aminopropyl groups (APTMS) from the material [89].



The TGA (Figure 2.38) results of sample 2 shows a small weight loss of up to 0.3 % at approximately 60 °C is due to surface dehydration, while the latter weight loss of up to 0.8 % at approximately 330 °C is due to the decomposition and total loss of the aminopropyl groups (APTMS) from the material [89]. There was a greater weight loss in sample 1, due to the decomposition of aminopropyl groups, suggesting it contained more APTMS molecules within its matrix.



The N<sub>2</sub> sorption analysis provided definite evidence of the SA and pore size distribution for the silicate-1 NPs (Figure 2.39). The pore size distributions deduced from the first condensation step clearly reflect a decrease in pore size as the amount of SA slightly increases. The SA of sample 1 is 339.3±4.5 m<sup>2</sup>/g with a maximum pore size distribution of 33.3 nm (Figure 2.40A), while sample 2 is 319.0±8.3 m<sup>2</sup>/g with a maximum pore size distribution of 53.6 nm (Figure 2.40B). It can be seen that, sample 1 has mesoporous and sample 2 is macroporous and as a consequence of the increase in the aging time and reduction in temperature the pore diameter have enlarged.

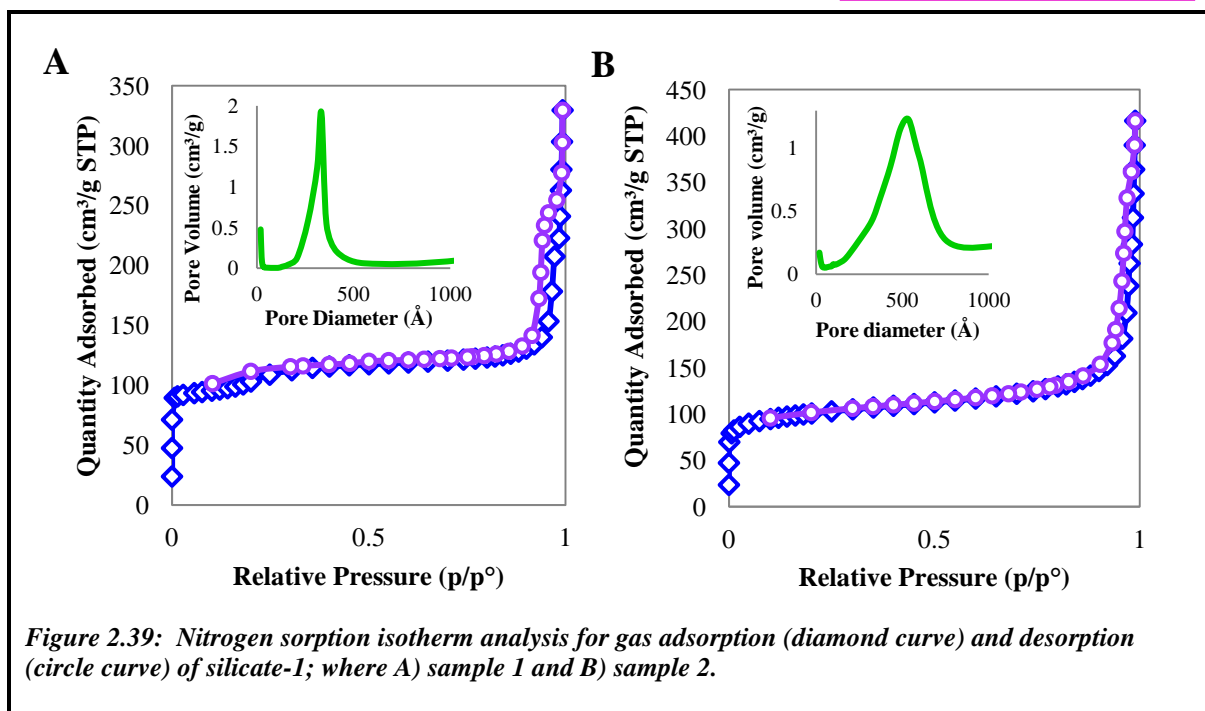


Figure 2.39: Nitrogen sorption isotherm analysis for gas adsorption (diamond curve) and desorption (circle curve) of silicate-1; where A) sample 1 and B) sample 2.

#### 2.5.4. Discussion

The fabrications of pure silicate-1 NPs were prepared via the conventional sol-gel precipitation technique, where an aqueous mixture of silica precursor in the presence of organic template was catalysed to produce these intricate porous networks. The SEM images illustrates that sample 2 is smaller than sample 1 in diameter, suggesting that increasing the aging time and reducing the reaction temperature results in the formation of smaller particles. Hence, is consistent with the SA analysis; where sample 1 is larger than 2. Interestingly, a higher aging period and lower temperature resulted in the formation of higher pore size, whereby sample 2 was macroporous and sample 1 is mesoporous. Wang *et al.* [87] suggested that the drying conditions influence the porosity, however as the same procedure for template removal was implemented; this suggest that greater aging time may increased the volume of TPAOH incorporated within the NP structure and hence upon removal leads to greater pores. Furthermore, the PCS analysis confirm for the synthesis of NPs are within the size-range determined by electron microscopy. Further characterisation using zeta potential confirms the stability of the NPs in water media. Previously, Jawor *et al.* synthesised zeolites using the conventional method and produced polydispersed NPs where the larger NPs were in close range to the PCS findings [22].

# **Chapter 3**

## **Applications**

### 3. APPLICATIONS

The nanoparticles (NPs) synthesised and characterised, in Chapter 2, were utilised for purpose built applications as sensors and in biological applications as summarised below (Table 3.1).

**Table 3.1: Overview of the types of nanoparticles used for specific applications.**

Sample type	Nanoparticle abbreviation	Size (nm)	Application	Synthesis page
2	SiRBITC NPs	208±9	Dual gas sensor	45
3	SiRu(dpp) <sub>3</sub> NPs	192±8	Dual gas sensor	45
1	SiNPs	27±7	Biocompatibility; <i>in vitro</i> studies	39
1	SiNPs	71±6	Biocompatibility; <i>in vitro</i> studies	39
2	SiRBITC NPs	31±10	Biocompatibility; <i>in vitro</i> studies	44
2	SiRBITC NPs	61±7	Biocompatibility; <i>in vitro</i> studies	44
1	SiNPs	71±6	Pressurized system; <i>in vitro</i> studies	39
4	MNP	95±13	Drug release; <i>in vitro</i> studies	62
5	RBITC MNP	105±13	Drug release; <i>in vitro</i> studies	63
6	FITC MNP	109±18	Drug release; <i>in vitro</i> studies	64
7	RBITC/ FITC MNP	105±13	Drug release; <i>in vitro</i> studies	65

## **3.1. Introduction to Fluorescence Sensing**

The engineering of devices capable of gaseous sensing has led to revolutionary development within the current technology. The most common and simplest methods of utilising such technology are via the fluorescence quenching phenomena. Previous studies, have demonstrated the capabilities of ruthenium complex for sensing oxygen. For instance, Roche *et al* fabricated an oxygen (O<sub>2</sub>) sensor consisting of a gold film coated with fluorophore encapsulated sol-gel [90]. The advancement in this field may lead to the incorporation of fluorophores within NPs to sense dissolved O<sub>2</sub>, which have great prospects within biological applications. Wang *et al*, fabricated core-shell ratiometric sensing NPs of 130±50 nm, which consist of three fluorophores encapsulated within polystyrene matrix [91]. Liewhiran *et al* developed gaseous sulphur dioxide (SO<sub>2</sub>) and hydrogen sulphide sensors via monitoring alterations in resistance when different concentrations of these gases were introduced onto a film which contains 3-20 nm tin oxide NPs [92]. Jorge *et al*, synthesised core-shell CdSe-ZnS quantum dots and placed them within a sol-gel matrix which contains ruthenium fluorophore to sense O<sub>2</sub> through the drop in fluorescence [93].

### **3.1.1. Fluorescence mechanics**

Fluorescence is described as the emission of light by an excited molecule. This occurs when an electron from its first singlet excited state is transferred to the ground state. The most simple and common method of describing the fluorescence process is the Jablonski energy level diagram (Figure 3.1).

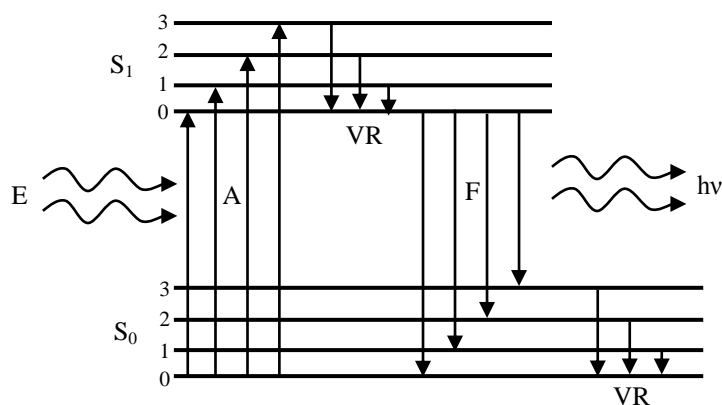


Figure 3.1: The Jablonski energy level diagram of the fluorescence mechanism.

Fluorescent molecules usually exist in the electronic ground state ( $S_0$ ), in the sub-level 0. The electrons are capable of absorbing (A) energy from an external source to an excited state (first excited singlet [ $S_1$ ] or higher vibrational energy level). The energy can either be dispersed or emitting as a photon. If the molecule has been absorbed to a higher excited state than the first singlet, sub-level 0, than the molecules energy is lowered to this level by vibrational relaxation (VR). For the electron to return to its  $S_0$  it can undergo this through fluorescence, phosphorescence or irreversible chemical reaction. The fluorescent molecule undergoes relaxation by emitting the energy in the form of light, termed as photon ( $h\nu$ ) to return to the  $S_0$  level. Once energy has reached the  $S_0$  level and is in a sub-level above 0 then the residual energy is released by VR. The total energy absorbed by the molecules is converted into different forms, vibrational and fluorescent photon. The ratio of emitted photon to absorb is termed as the fluorescent quantum yield which quantifies the fluorescence efficiency process. Thus, dye molecules that posses high quantum yield are in demand in the field of fluorescence sensing as they require low energy, or excitation source, for high emission intensity. Furthermore, the reduced excitation source in-turn reduces the photobleaching effect, where the excitation energy causes the molecules to become irreversible non-fluorescent. The term Stokes shift is used to describe the difference between the excitation and emission wavelength, while lifetime refers to the time taken for an excited electron to emit the photon [94].

### **3.1.2. Quenching modes**

There are two mechanisms of quenching; static and dynamic. Static quenching refers to when a quencher binds to the fluorescent molecule to produce a stable ground-state complex that can no longer undergo fluorescent emission. While, dynamic quenching occurs when there's a collision between the excited fluorophore and quencher, transferring energy to it, and causing it to return to the ground state without fluorescent emission. Therefore, dynamic quenching is also called collision quenching, and this is of more interest for the present study (Chapter 3; Section 3.2) as most fluorophores undergo dynamic fluorescence quenching in the presence of O<sub>2</sub> [94].

In static quenching, the quenching species complexes with the fluorophore and thus reduces the amount of molecules available for fluorescence emission. Therefore, the overall emission intensity is reduced. Furthermore, the non-fluorescent complex may not absorb photon at the same excitation wavelength as the fluorophore, thus not only reducing the emission intensity but also altering the optical absorption. Thus, changes in the optical absorption are suggestive of the possible process of static quenching occurring. Although, in dynamic quenching the fluorophore is capable of reaching the singlet excited state, however via quenching and fluorescence pathways it is returned to the ground state. Therefore, as some of the fluorophore have complexes with the quencher the overall emission intensity will reduce and also the lifetime, as the time the fluorophore exist in the excited state has also reduced. Dynamic quenching reduces both the fluorescence emission intensity and lifetime [94].

### **3.1.3. Intensity-based fluorescent sensor vs. lifetime**

There are two methods commonly used to analyse the quencher's concentration through the reduction in the fluorescence emission intensity of the fluorophore. Lifetime-based sensor is commonly used to analyse O<sub>2</sub> concentrations [12, 95]. The advantages of lifetime-based sensors are the minimal interference by noise from an external source, uninfluenced by light source and dye concentration. However, in order to improve the analysis it is preferable to use a dye that has a long lifetime (1-3 milliseconds) and hence limits the use of particular dye molecules. Therefore, this ultimately results in the reduction in the number of analytes (quenchers) that can be detected by lifetime fluorescent sensing.

Furthermore, the lifetime fluorescent sensing equipment is expensive in comparison to the fluorescence intensity spectrophotometer, which generally is simple equipment that requires a light source at a certain wavelength and a photodetection apparatus.

### 3.1.4. The Stern-Volmer relationship to dynamic quenching

The Stern-Volmer equation (Equation 3.1) describes the relationship between the fluorescence emission intensity and the concentration of the fluorophore.

$$\frac{I_0}{I} = 1 + k_q \tau_0 [Q] \quad (3.1)$$

Where,  $I$  represent the emission intensity,  $I_0$  is the emission intensity if the quencher is not present,  $k_q$  is the bimolecular quenching constant,  $\tau_0$  is the fluorescence lifetime when the quencher is not present and  $[Q]$  is the concentration of the quencher. The bimolecular quenching constant is shown below (Equation 3.2).

$$k_q = \gamma \frac{4\pi N}{1000} (R_f + R_q)(D_f + D_q) \quad (3.2)$$

Where,  $\gamma$  is the quencher efficiency,  $N$  is Avogadro's constant,  $\pi$  is equal to 3.14,  $R_f$  is the molecular radii of the fluorophore,  $R_q$  is the molecular radii of the quencher,  $D_f$  is the diffusion coefficient of the fluorophore and  $D_q$  is the diffusion coefficient of the quencher. The diffusion coefficient of a particle is described by the Stokes-Einstein equation (Equation 3.3).

$$D = \frac{kT}{6\pi\eta R} \quad (3.3)$$

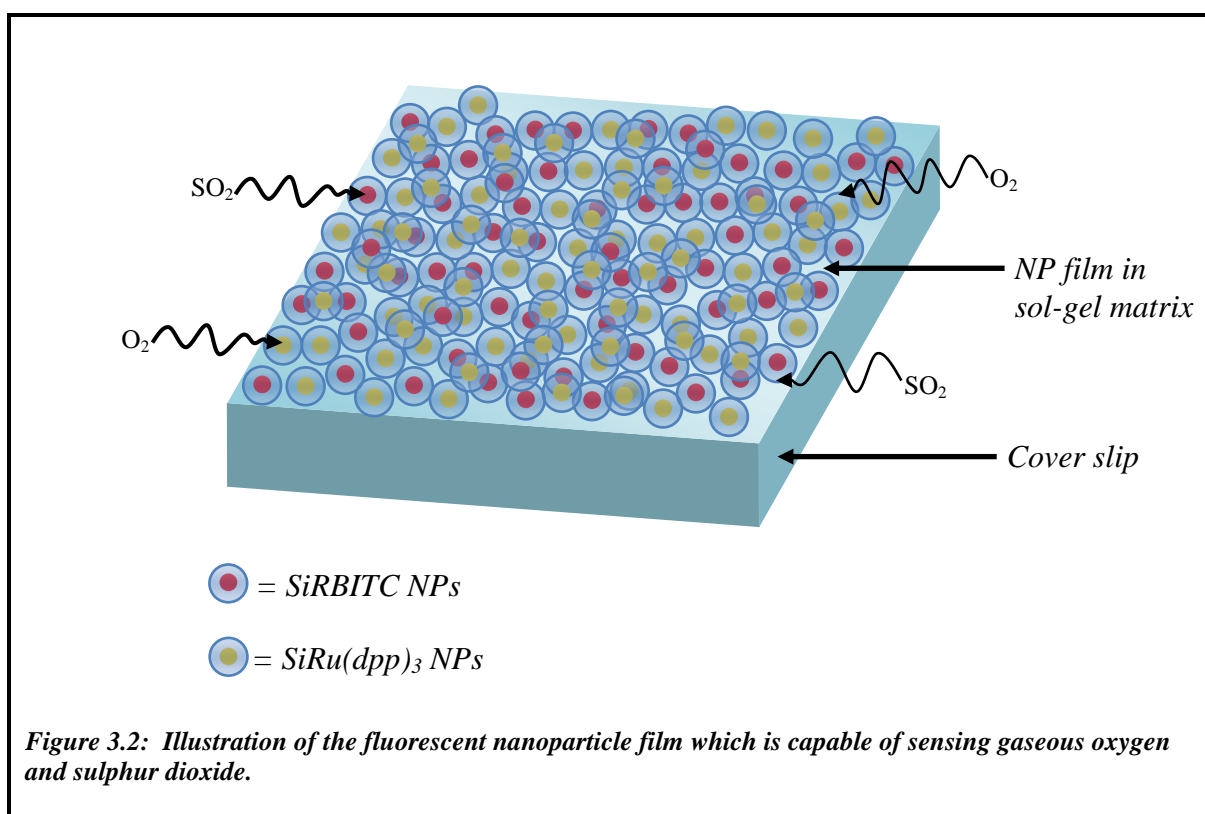
Where,  $k$  is the Boltzmann's constant,  $T$  represents the temperature,  $\pi$  is equal to 3.14,  $\eta$  is the viscosity and  $R$  is the molecules collision radius. The molecule's collision radius is commonly derived by the sum of the radius of both the fluorophore and quencher. Furthermore, as terms in Equation 3.2 and 3.3 are constants, the Stern-Volmer equation can be simplified from Equation 3.1 to Equation 3.4.

$$\frac{I_0}{I} = 1 + k_{sv}[Q] \quad (3.4)$$

Where,  $k_{sv}$  is the Stern-Volmer constant. Therefore, the inverse relationship of  $O_2$  concentration (quencher) to fluorescence emission intensity can be represented by a straight line, where the slope is the Stern-Volmer constant [94].

### 3.2. Gas Sensor

The illustration below represents a fluorescent nanoparticle (NP) film, consisting of a mixture of 2:1 ratio of ruthenium-tris (4, 7-diphenyl-1, 10-phenanthroline) dichloride encapsulated silica nanoparticles ( $\text{SiRu(dpp)}_3$  NPs) and rhodamine B isothiocyanate encapsulated silica nanoparticles ( $\text{SiRBITC}$  NPs) respectively (Figure 3.2). Gaseous  $\text{O}_2$  is able to quench the fluorescence of  $\text{SiRu(dpp)}_3$  NPs, while  $\text{SO}_2$  quenches  $\text{SiRBITC}$  NPs.

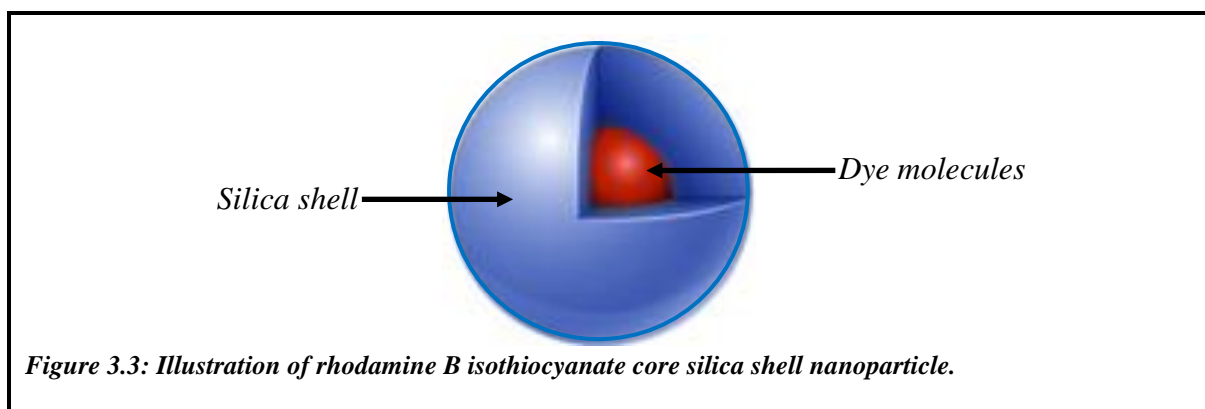


The rising air pollution problems encountered in the environment has led to the need for quantified detection of various gases. Gases such as  $\text{SO}_2$  are known for their toxicological effects where the threshold limit of human exposure to  $\text{SO}_2$  is between 5-10 parts per million (ppm) [96]. Furthermore, the detection of dissolved  $\text{O}_2$  is desirable; particularly in biological systems. For instance, the regular monitoring of  $\text{O}_2$  levels within cell culture, *in vitro*, gives vital information about the effects on metabolism [97].

The most common method of gaseous analysis is based on the principle of fluorescence quenching in real-time or via remote monitoring, whereby any reduction in intensity of the original fluorescence emission of the fluorophore can be measured. Hence, in the presence

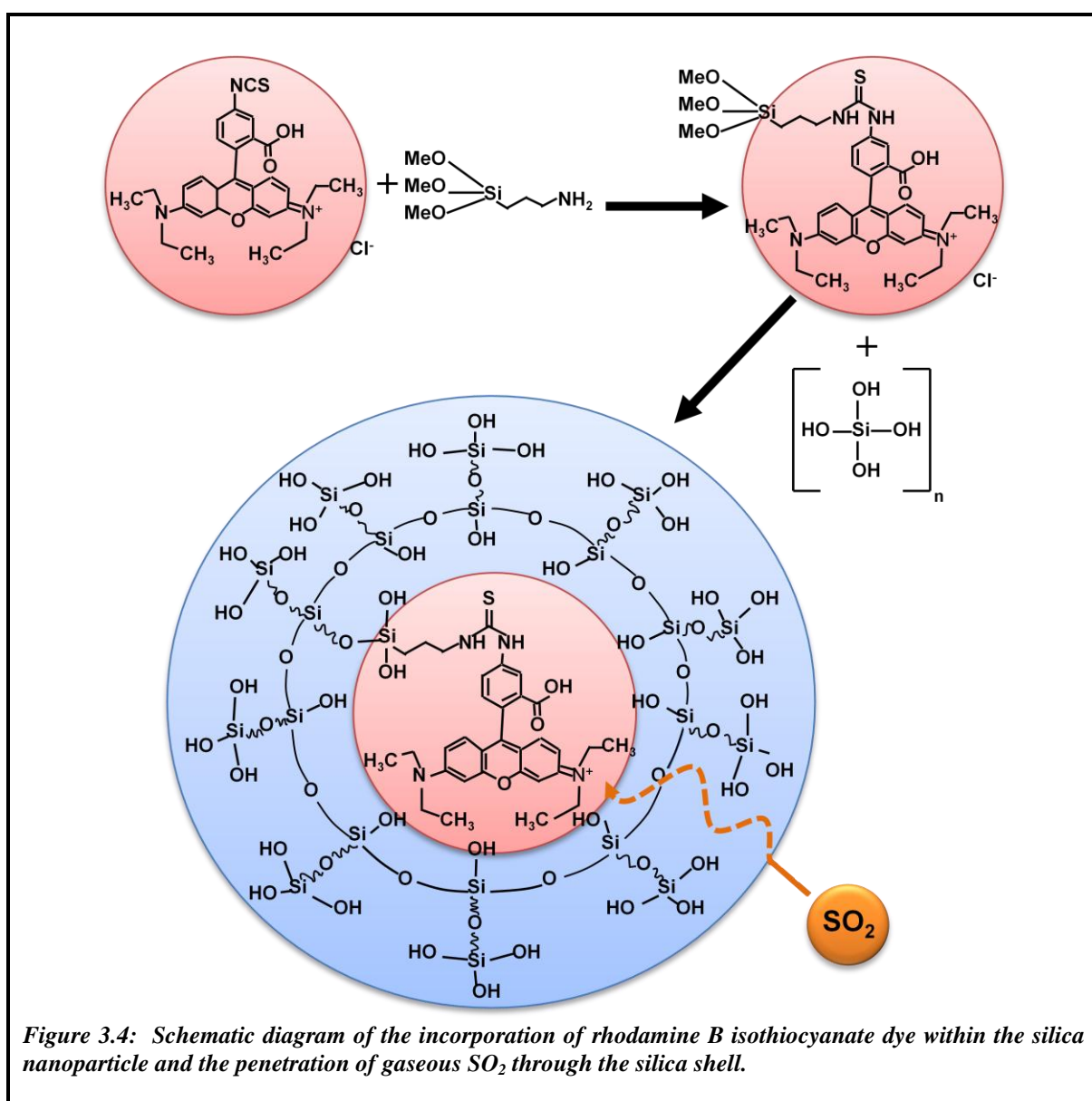
of fluorophores these gaseous molecules behave as quenchers. Furthermore, these fluorophores are known as optrodes because they behave as an optical device which measures their specific gas [98]. These fluorophores may be used as photon sources for biological imaging [99], optical computing [100], sensor technology [98] and targeted drug delivery [101]. The detection of a specific gas is dependent on the fluorophore, which can be quenched by the particular given gas. There are two mechanisms by which the fluorophore may be quenched: static or dynamic. Dynamic quenching occurs when external molecules collide with the fluorophore molecules (collisional quenching), while static quenching occurs when both molecules form a non-fluorescent complex (ground-state complex formation) [94, 102]. Metalloporphyrins and ruthenium complexes have been used for O<sub>2</sub> sensing as their fluorescence is quenched by the analyte [12, 97, 103-105], while rhodamine B isothiocyanate (RBITC) can be used to sense SO<sub>2</sub> [95, 105]. Both gases (O<sub>2</sub> and SO<sub>2</sub>) undergo dynamic quenching with their respective reagents (Ru(dpp)<sub>3</sub> and RBITC) [102].

A problem encountered by these organic dye molecules is their tendency to easily photobleach. One way to overcome this is the encapsulation of these dye molecules within core-shell NPs, which has been shown to significantly reduce the level of photo-degradation (Figure 3.3). These core-shell NPs normally consist of a molecule coated with an inorganic or polymer shell [107].

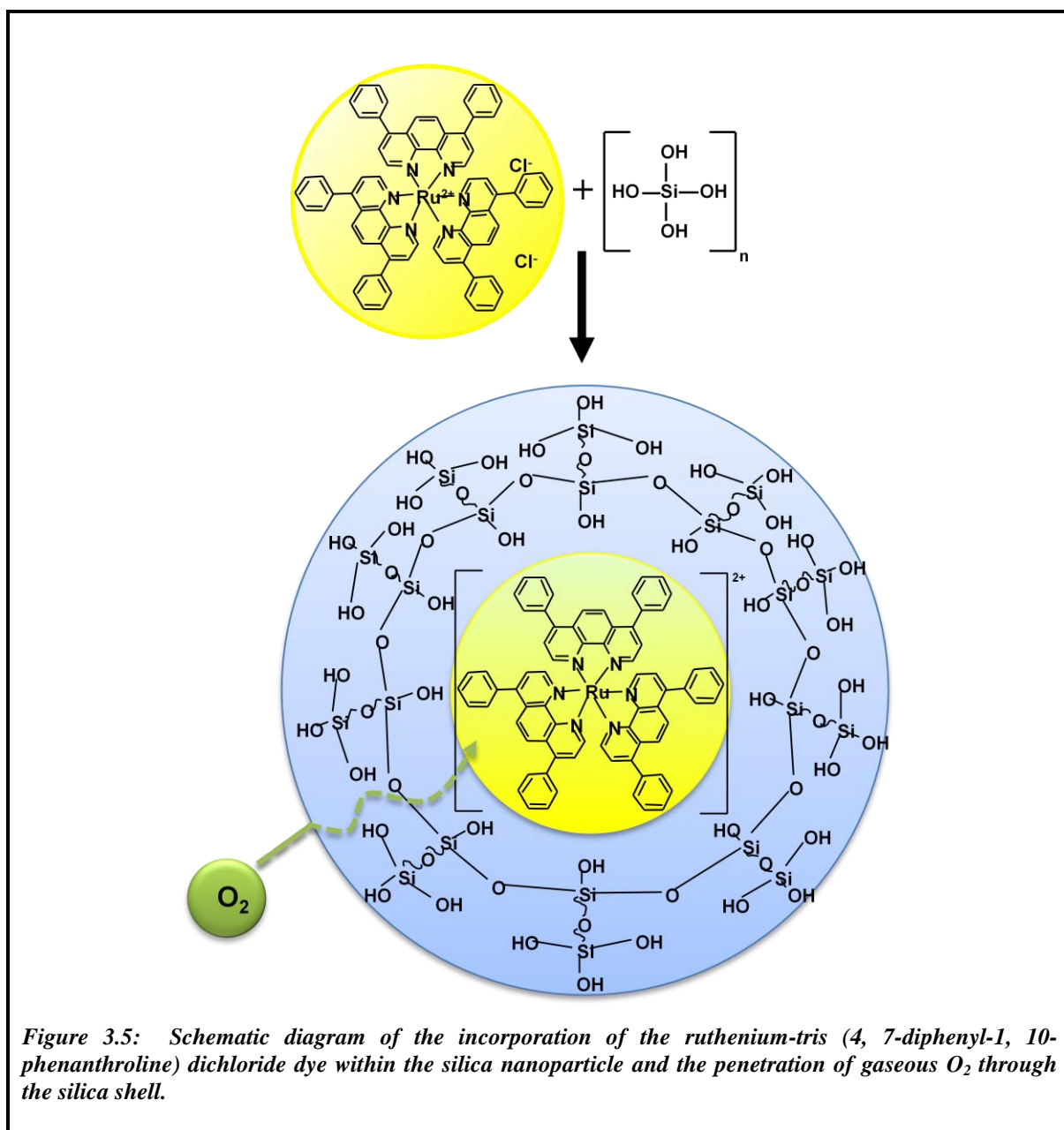


The properties of these core-shell NPs can be altered by changing the shell thickness, as well as altering its composition [108]. Encapsulating dye molecules within a silica shell leads to beneficial properties. Firstly, the fluorescence signal significantly increases as multiple dye molecules are trapped in a single shell. Secondly, it reduces the photo-

stability problem of the dye molecules. Thirdly, the surface of the silica nanoparticles (SiNPs) can easily be modified and functionalised to couple with molecules suspended in solution. Furthermore, silica is an optically transparent material allowing dye molecules to fluoresce as both the excitation and emission light can diffuse through [107]. The density of Stöber NPs are approximately  $1.9 \text{ g/cm}^3$  [109]. Molecular structure for the schematic illustration of the formation of SiRBITC NPs is illustrated in Figure 3.4. There is an initial attachment of the APTMS molecules to tetraethyl orthosilicate (TEOS), which behave as a coupling agent to bind the silica shell to the RBITC fluorophore.



The Ru(dpp)<sub>3</sub> fluorophore complex are attracted to the negatively charged hydroxyl groups of the TEOS molecule leading to the formation of dye encapsulated SiNPs (Figure 3.5).



These fluorescent sensors respond by gases quenching excited molecules and result in the latter becoming deactivated. Thus, as the concentration of the gases increases it causes the excited state lifetime and intensity of the sensor molecules to decrease. If the quenching occurs because of collisions between the fluorophore and O<sub>2</sub> molecules, then the relationship between the concentration of the quencher and lifetimes or intensities is given by the Stern-Volmer equation (Equation 3.4). The Stern-Volmer equation is normally valid

when the fluorophore is in solution or the quencher concentration is low. In most cases the Stern-Volmer fails to describe more complicated systems and other appropriate models must be employed to describe the quenching relationship [95, 102].

The  $\text{Ru}^{2+}$  ion in the dye complex is coordinated to six ligands giving it an octahedral environment, shown in Figure 3.6.

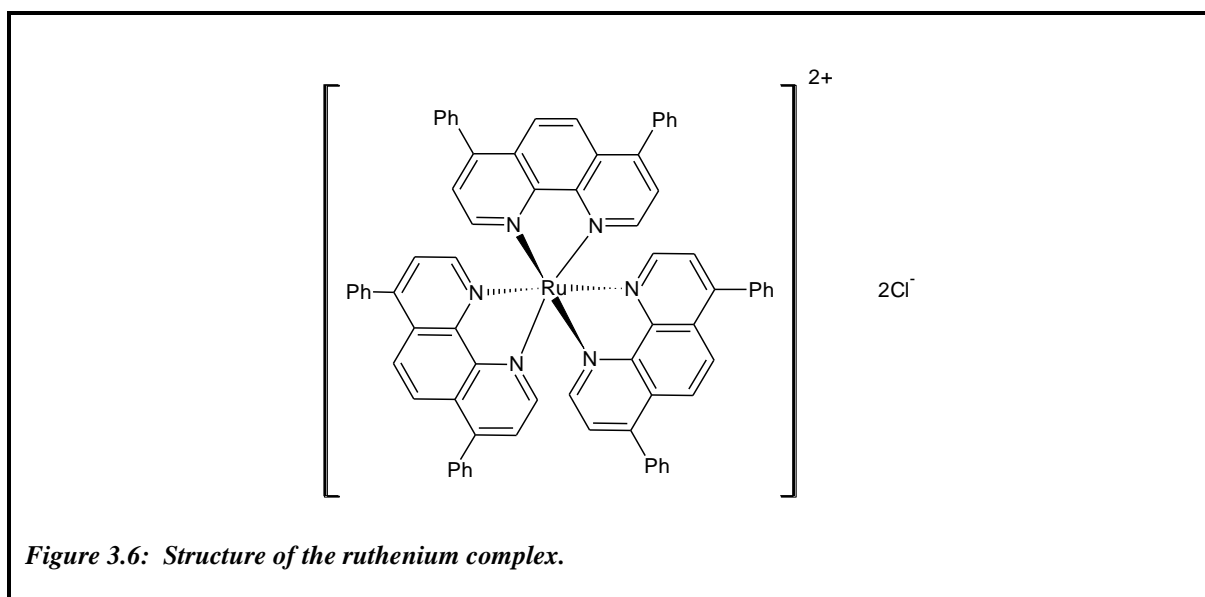


**Figure 3.6: Structure of the ruthenium complex.**

The ruthenium ion is a transition metal with  $d^6$  electron configuration. Figure 3.7 shows energy level diagram of an electron for the octahedral ruthenium complex. The dye is quenched by the gas due to a metal-to-ligand-charge-transfer (MLCT). An electron is promoted to the  $\pi^*$  orbital of the dioxygen ligand from the  $d$ -orbital of the metal [96]. An electron may be transferred from  $\pi_L$  to  $\pi_L^*$  orbital and is referred to as ligand centred electron transfer. The metal centred excited state is when an electron is promoted  $\pi_M$  to  $\sigma_M^*$  orbital. The natures of these three excited states are either singlet or triplet. However, the singlet and triplet states of MLCT and metal centered (MC) mixing due to spin-orbital mixing [110].

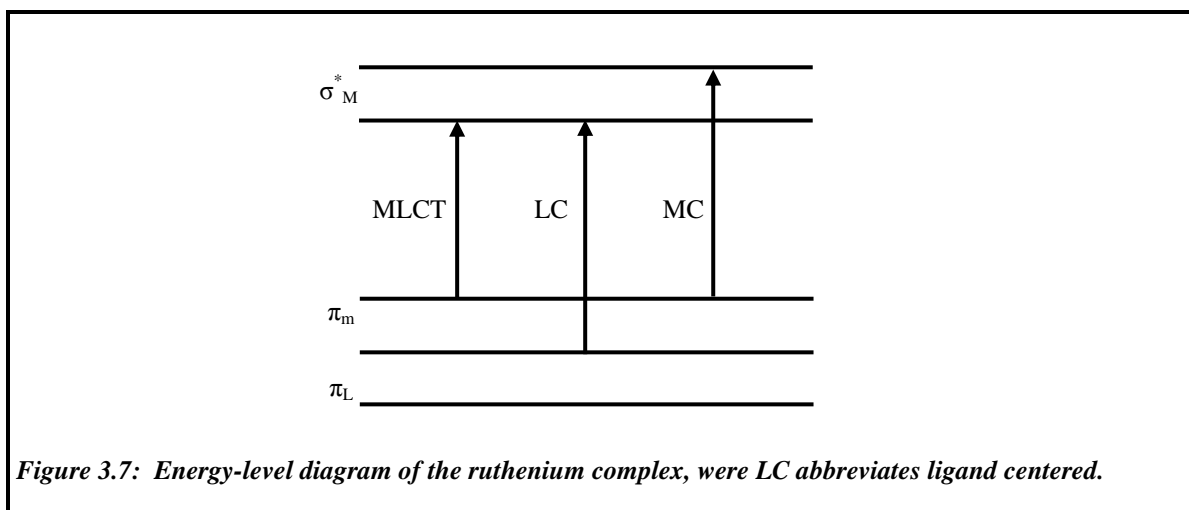
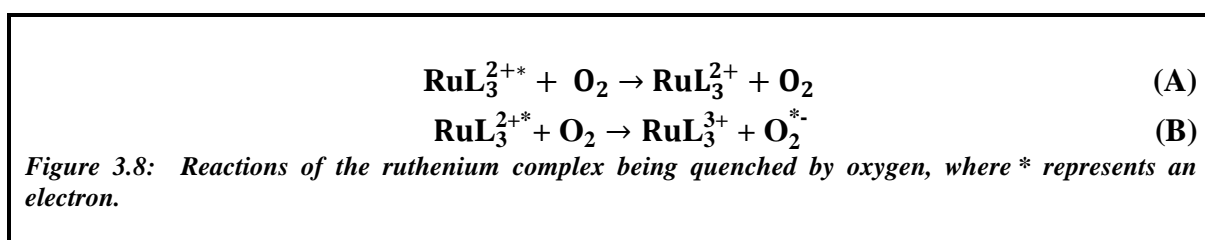


Figure 3.7: Energy-level diagram of the ruthenium complex, where LC abbreviates ligand centered.

The two reactions by which the fluorescence of  $\text{Ru}(\text{dpp})_3$  is quenched by  $\text{O}_2$  are shown in Figure 3.8. The first reaction (Figure 3.8A) shows the transfer of an electron from  $\text{Ru}(\text{dpp})_3$  complex to give singlet oxygen and ground state  $\text{Ru}(\text{dpp})_3$  complex. The second reaction (Figure 3.7B) is of the  $\text{Ru}(\text{dpp})_3$  complex being oxidised by an electron being transferred from the  $\text{Ru}(\text{dpp})_3$  complex and superoxide anion that is being produced [110].



The fluorophore alone is not the only factor that determines the sensors properties; the matrix in which it exists also plays an important role. The matrix influences the response time as the larger the porosity, the more sensitive it will be to the fluorophore. These fluorophores can be immobilised in a silicone rubber [111], polyvinylchloride [112], sol-gel [113-115] or organically modified sol-gels (ormosil) matrix [116]. Previous studies have shown that most of these sensors are placed in matrices such as sol-gel matrix. The sol-gel matrix can be prepared at room temperature unlike the silicone rubber matrix. Furthermore, it is highly sensitive to the gas phase. However, it has a tendency to crack when producing films and in the liquid phase water causes the fluorescence to quench and in turn reduce the effectiveness of the sensor. This is because the silane moiety of the sol-gel has a hydroxyl group which readily forms hydrogen bonds with water. In order to overcome this problem the matrix needs to be hydrophobic. The rubber and

polyvinylchloride matrices are hydrophobic so water molecules cannot interfere with the quenching process. However, unlike the sol-gel the porosity cannot be altered. Chen *et al.* [116] has presented a solution by using ormosil with one or more of the hydroxyl groups being replaced by an aromatic or acyl chain. Another luminescent sensor produced by Al-Jowder *et al.* [95] is the use of ruthenium-tris(4,7-diphenyl-1,10-phenanthroline) dichloride ( $\text{Ru}(\text{dpp})_3$ ) dye immobilised in ormosil to sense gaseous oxygen. Other advantages of ormosil is that it is crack resistant, has variable porosity, thermal stability, optical clarity, *pH* stability and can be prepared at room temperature. The selection of the matrix is dependent on the environment in which the sensor is to be utilised [117].

These fluorescence sensors respond when these gases quench excited molecules and results in them becoming deactivated. So as the concentration of the gases increases it causes the excited state lifetime and intensity to decrease. If the quenching occurs because of collisions between the fluorophore and oxygen molecules, diffusion, then the relationship between the concentration of the quencher and lifetimes and intensities is given by the Stern-Volmer equation [118].

In this study, we focus on producing novel nanosensors which can be used as optical sensors of atmospheric and dissolved gases. In our work the fluorescent NPs are functionalised with carboxylic acid and bound to the ormosil. Furthermore, these nanosensors may be combined to produce a dual gas sensor and even multi-sensor systems for multitude of future biological and industrial applications.

### **3.2.1. Experimentation**

#### ***3.2.1.1. Nanosensor film formation***

The ormosil composition is as previously described by Roche *et al.* [12]. Briefly, the ormosil matrix consisting of a mixture of water (1.5 mL), OTEOS (1 mL), MTEOS (1 mL), EtOH (0.5 mL), HCl (0.05 M/ 50  $\mu$ L) was stirred overnight. A 1:1.5 ratio of SiRBITC NPs ( $1.01 \times 10^{12}$  NPs) and SiRu(dpp)<sub>3</sub> NPs ( $1.52 \times 10^{12}$  NPs) were added to the mixture and further stirred for 24 hours. The film was produced by placing the mixture (250  $\mu$ L) on a cover slip and allowing it to dry over 1-2 weeks by gravity coating.

#### ***3.2.1.2. Gas sensing technique***

The real-time fluorescence quenching was analysed using a fluorescence spectrophotometer (Perkin Elmer LS55) (Figure 3.9). The excitation wavelength of Ru(dpp)<sub>3</sub> fluorophore in the ormosil matrix was 450 nm while emission was measured at 610 nm. For RBITC dye the two excitation wavelengths were 350 and 550 nm, with emission wavelength at 580 nm. Excitation using 350 nm gives less intense signal, however, it has been chosen to excite the dye because of the larger Stokes shift which will reduce or minimise light scattering.

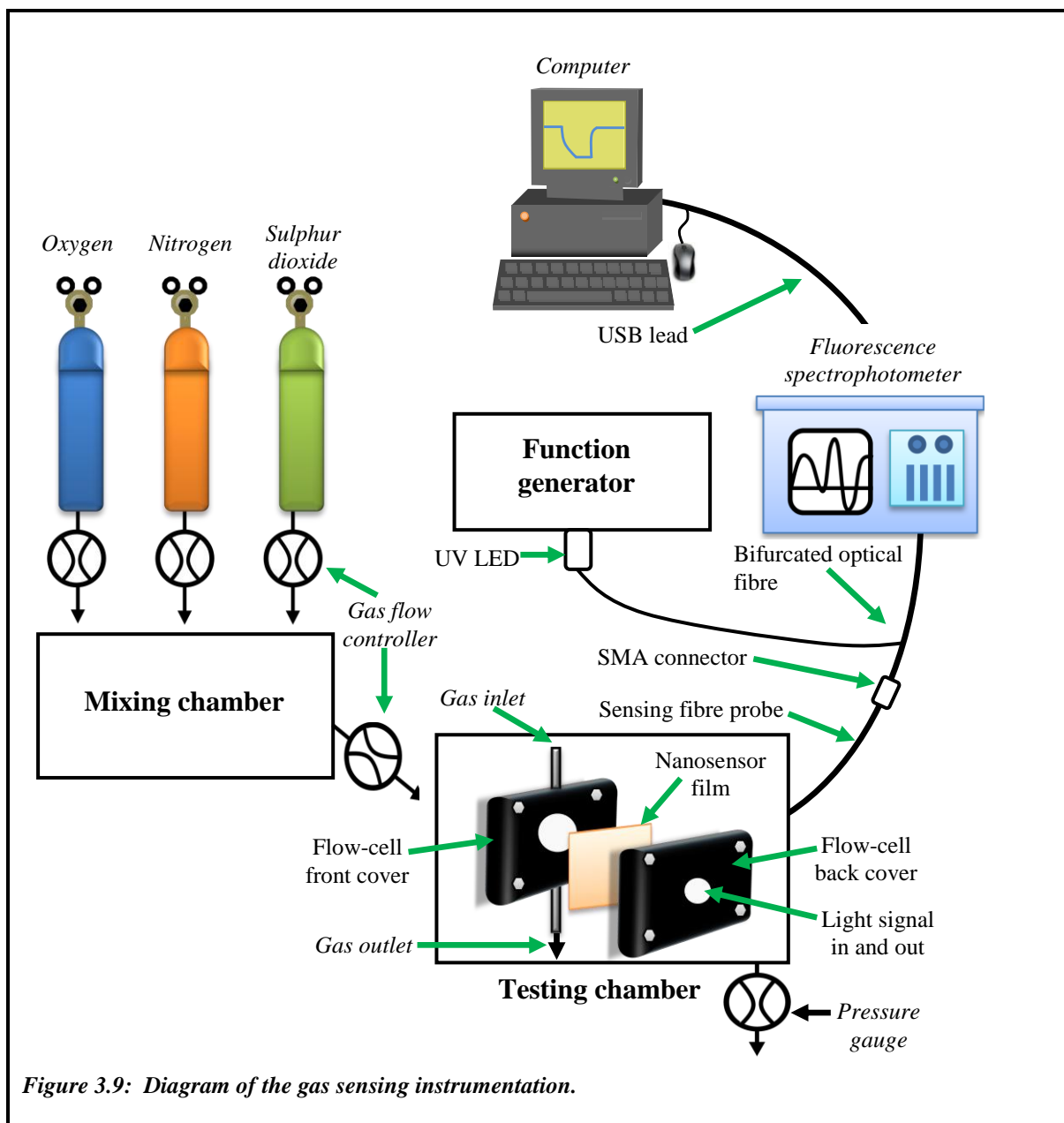


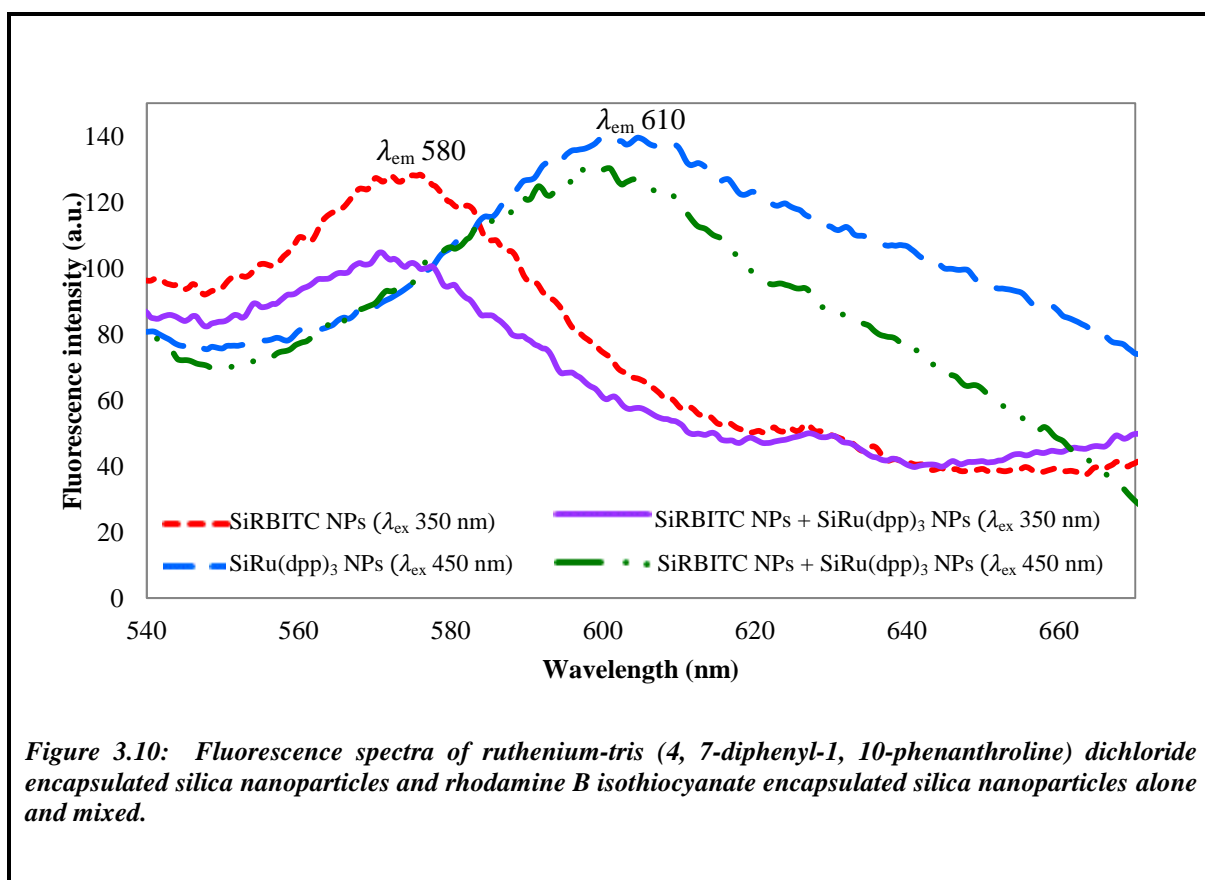
Figure 3.9: Diagram of the gas sensing instrumentation.

### 3.2.2. Results and discussion

Verhaegh *et al.* [72], suggested that if the RBITC dye was not functionalised with APS and used in an alcohol solution, it would not incorporate into the silica. APS was added to the RBITC dye in order to act as a coupling agent, and allow the siloxyl groups to bind to the silica shell and the amine group to bind to the dye [76]. After stirring for 4 hours in a nitrogen atmosphere under dark conditions the colour changed from intense purple to orange as self-quenching had occurred [72]. The synthesis of SiRu(dpp)<sub>3</sub> NPs occurs as the silica is negatively charged, while the Ru(dpp)<sub>3</sub> dye is positively charged. This causes

electrostatic interaction to occur between the dye and the silica and therefore leading to an ionic bond.

The fluorescence emission spectra of SiRBITC NPs and SiRu(dpp)<sub>3</sub> NPs alone and mixed shows there is no interference caused between the two dyes (Figure.10). The SiRBITC NPs were excited at 350 nm with an emission wavelength at 580 nm. The SiRu(dpp)<sub>3</sub> NPs were excited at 450 nm with an emission at 610 nm.



### 3.2.2.1. Dual gas sensor analysis

As described in the experimental section, SiRBITC NPs and SiRu(dpp)<sub>3</sub> NPs suspensions were added in 1:1.5 ratio to 1:1 OTEOS, MTEOS (ormosil) and the mixture was then deposited on a microscope cover glass and spread by gravity to produce a film of 2.4 mm thickness. The dry film was placed in a sealed controlled reactor environment and its sensing capabilities were measured using fluorescence spectroscopy. Recent studies have used silica matrix for optical sensing by incorporation of fluorescent dye molecules within a porous material. For instances, Wark *et al.* [119] anchored Sn-oxide into the mesopores

of siliceous molecular sieve (MCM-41) for alternative gas sensing via optical detection. Furthermore, they also loaded rhodamine B into the mesopores for detection of SO<sub>2</sub> via fluorescence quenching. Zhang *et al.* [120] covalently grafted ruthenium (II) complex within mesoporous MSU-3 silica for oxygen sensing via fluorescence quenching.

The dual NP film was subjected to gaseous O<sub>2</sub> in a N<sub>2</sub> atmosphere, and was excited at 450 nm with the emission measured at 610 nm to target the SiRu(dpp)<sub>3</sub> NPs (Figure 3.11).

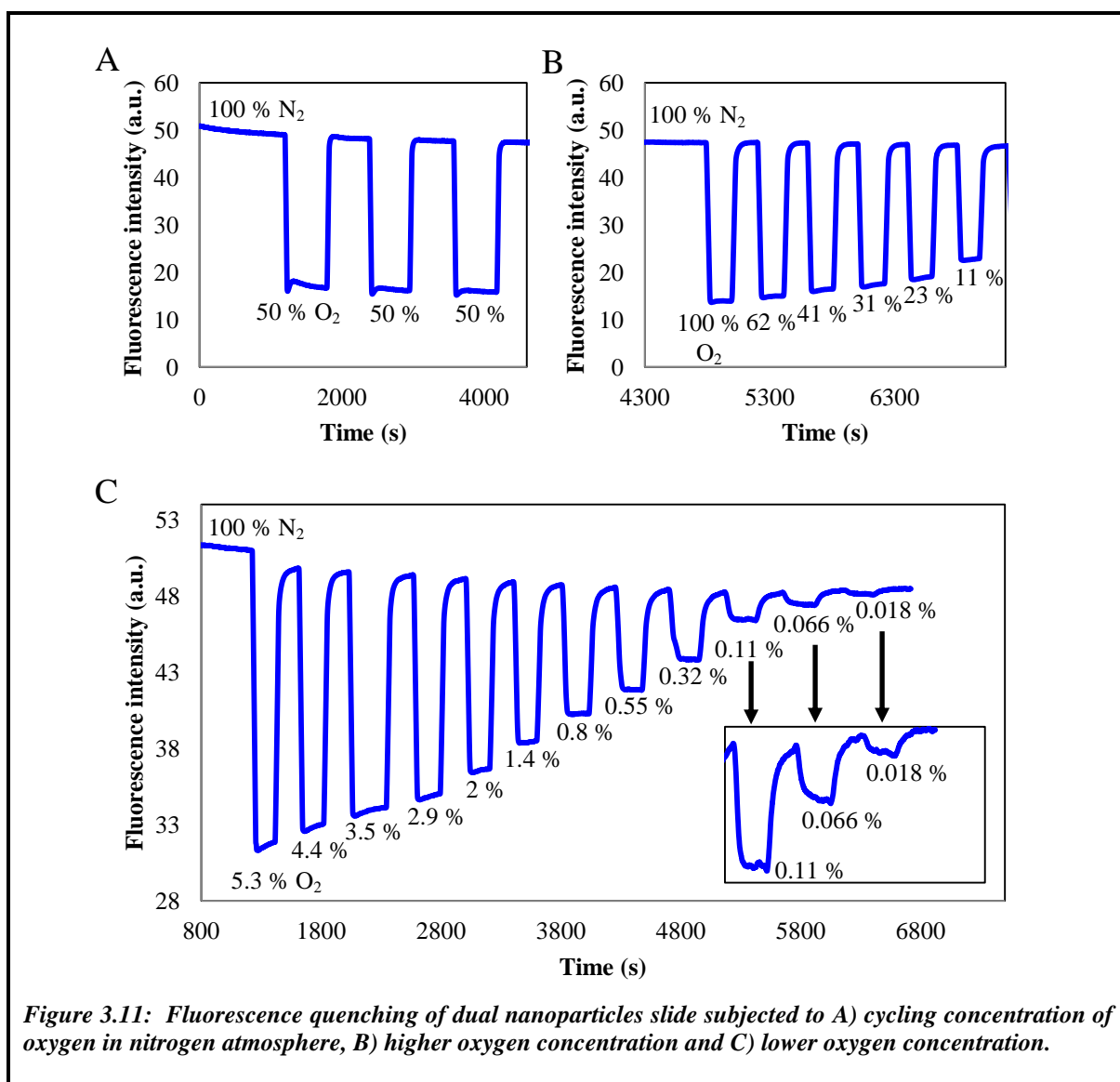
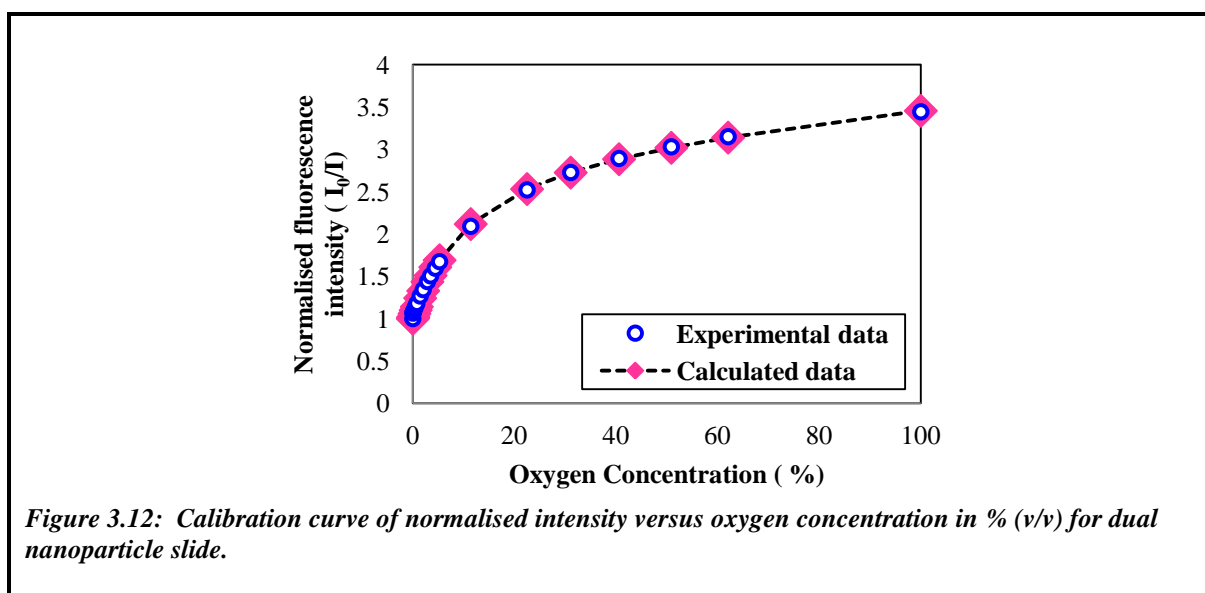


**Figure 3.11:** Fluorescence quenching of dual nanoparticles slide subjected to A) cycling concentration of oxygen in nitrogen atmosphere, B) higher oxygen concentration and C) lower oxygen concentration.

Initially, the film was subjected to cycling oxygen concentration at 50 % (v/v) (Figure 3.11A). The fluorescence quenching graph demonstrates that the SiRu(dpp)<sub>3</sub> NPs are sensitive to gaseous O<sub>2</sub> reversibly and are repeatable as the fluorescence quenched reaches

the same baseline level. Figure 3.11B shows that when the dual nanosensor slide was subjected to different concentrations of O<sub>2</sub>, which ranged from 100-5 %, the fluorescence is quenched at specific fluorescence intensity levels. The graph shows that as the O<sub>2</sub> concentration were decreased the fluorescence intensity increased. This is because reducing the quencher concentration causes less interaction with metal-ligand complexes and therefore there are more excited molecules showing fluorescence. Furthermore, the nanosensor film is also capable of detecting O<sub>2</sub> at lower levels (5-0.018 %) (Figure 3.11C). The luminescence spectra of lower O<sub>2</sub> concentrations show that the dual nanosensor is capable of detecting O<sub>2</sub> levels at very low concentrations (0.018%). The last three signals (0.1-0.018 %) are magnified in the same graph. However, the response was slower than that for dye alone in ormosil, as shown previously by Al-Jowder *et al.* [94]. This is expected as the gas will have to diffuse through the silica shell as well as the ormosil matrix. The data distribution shown by the calibration curve of normalised fluorescence intensity versus O<sub>2</sub> concentration in % (v/v) (Figure 3.12) indicates that the response of the system is of non-linear type, due to the silica shell surrounding the dye and the ormosil matrix; leading to differences in diffraction kinetics.



Also, the gravity method employed in depositing the NPs on the slide makes the film thicker, causing it to be more difficult for gases to access the dye in the NPs to quench the fluorescence. Again, the relation deviates from linear Stern-Volmer equation indicating that the system requires a non-linear modelling technique.

The dual nanosensor film was excited at 350 nm with an emission wavelength of 580 nm to detect RBITC fluorescence. SO<sub>2</sub> gas was introduced into the reactor in order to target the RBITC dye molecules. Initially, the film was subjected to 50 % cycling concentrations of SO<sub>2</sub> (Figure 3.13A). However, the steady state was not reached completely as the intensity was changing at a very slow rate (approximately 3000 seconds). Furthermore, when the film was subjected to a higher volume of SO<sub>2</sub> gas (100 and 60 %) the steady state was also not reached (Figure 3.13B).

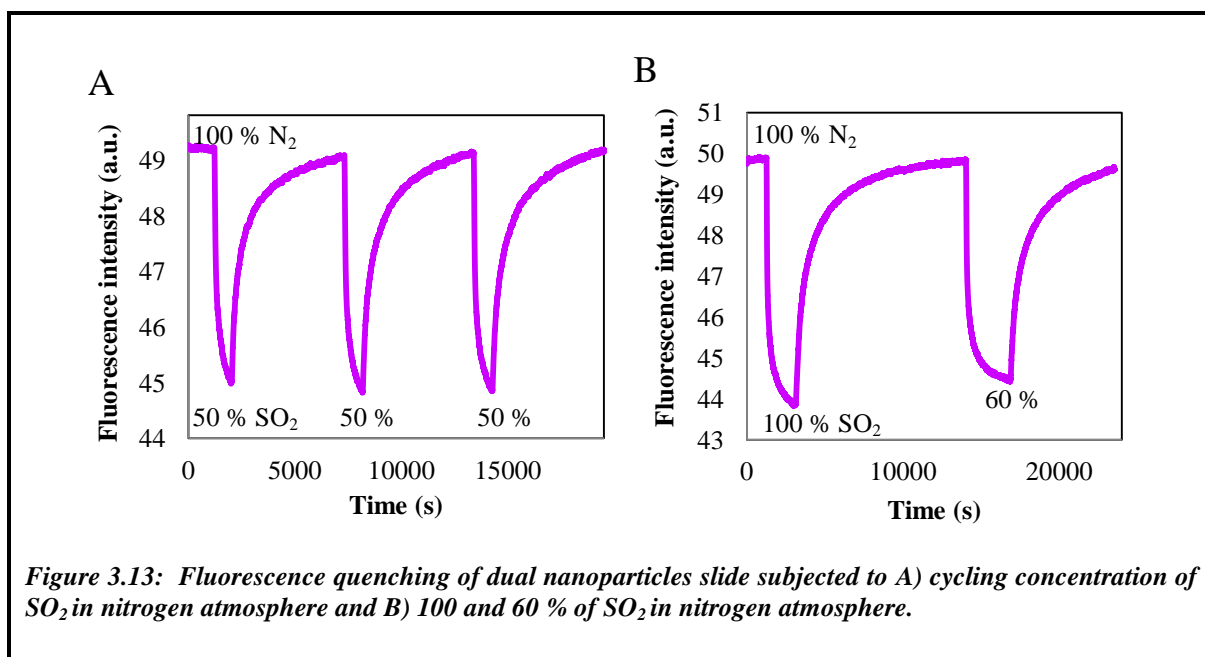


*Figure 3.13: Fluorescence quenching of dual nanoparticles slide subjected to A) cycling concentration of SO<sub>2</sub> in nitrogen atmosphere and B) 100 and 60 % of SO<sub>2</sub> in nitrogen atmosphere.*

### 3.2.3. Conclusions

The present study describes the novel synthesis of dual gas sensors incorporated within SiNPs. The carboxylic functionalized SiRBITC NPs and SiRu(dpp)<sub>3</sub> NPs nanosensor were successfully synthesized within an ormosil matrix. The nanosensor gave response to both gases by quenching fluorescence, along with fluorescence response recovery once the gases were removed. The dual nanosensor consisted of a mixture of RBITC and Ru(dpp)<sub>3</sub> core-shell NPs, which worked simultaneously without inhibiting the function of the other. Further research is required in order for the SO<sub>2</sub> gas to quench the RBITC dye sufficiently to reach steady state along with a response recovery. In comparison to previously described O<sub>2</sub> sensor, our sensor is more sensitive to lower levels of O<sub>2</sub> detection (0.018%) although the response and recover time was increased as the gas has to further travel through the silica shell. Despite this the silica shell enabled the dual nanosensor to be more resistant to photobleaching.

### **3.3. Introduction to the Bioapplications**

Progress in NP fabrication techniques has opened the door for tailoring NP properties for the development of innovatively designed biological drug delivery vehicles [121-123]. Orally and intravenously administered drugs usually have a number of systemic side effects, often leading to poor efficiency of the drug [124]. Consequently there is a drive for the development of new drug delivery systems. Thus, there is a need for the understanding of how these particles affect biological systems. For instance, Akbar *et al* tested the biocompatibility of 100 and 200 nm SiNPs on live aortic vessels *in vitro*, where they suggest surface interaction is detrimental to vasodilation function [35]. Quignard *et al* determined the size and charge influence of fluorescein isothiocyanate (FITC) encapsulated silica nanoparticles on human dermal fibroblasts. They observed that smaller NPs had greater and faster cytotoxicity as compared to larger NPs at a similar dose. Furthermore, the negatively charged small NPs are more detrimental as they induced genotoxicity compared to positively charge ones [125]. ‘Smart NPs systems’ have been developed; these are particles that are small enough to circulate around the body and so can move to targeted locations releasing the drug in a controlled manner. This approach holds great promise for revolutionising drug administration in the future. One promising material that contains many desired properties to fulfil the requirements for the design of a NP drug carrier system is mesoporous silica which was developed in 1991 as a molecular sieve [124, 126]. Mesoporous nanoparticles (MNP) were originally utilised as drug delivery system by Vallet-Regí *et al.* in 2001, whereby the release kinetics of ibuprofen was determined [127]. The ability of specific targeting delivery of therapeutics has led to the development of treatment of cancer. Gary-Bobo *et al.* employed fluorescein encapsulated mesoporous nanoparticles functionalised with galactose to target cancer cells and release camptothecin (anti-cancer drug) which leads to cell death [128]. Similarly, Lu *et al.* loaded MNP with camptothecin for cancer treatment. They observed that this drug delivery system led to suppression within mice, *in vivo* [129].

### 3.3.1. Aortic vessel structure

The aortic vessel is the largest artery in vertebrates and plays an important role in the blood transport. They allow for the uptake of large volumes of blood with small change in pressure in the arterial tree [130]. The arterial wall consists of three main structures; tunica interna, tunica media and tunica externa (Figure 3.14).

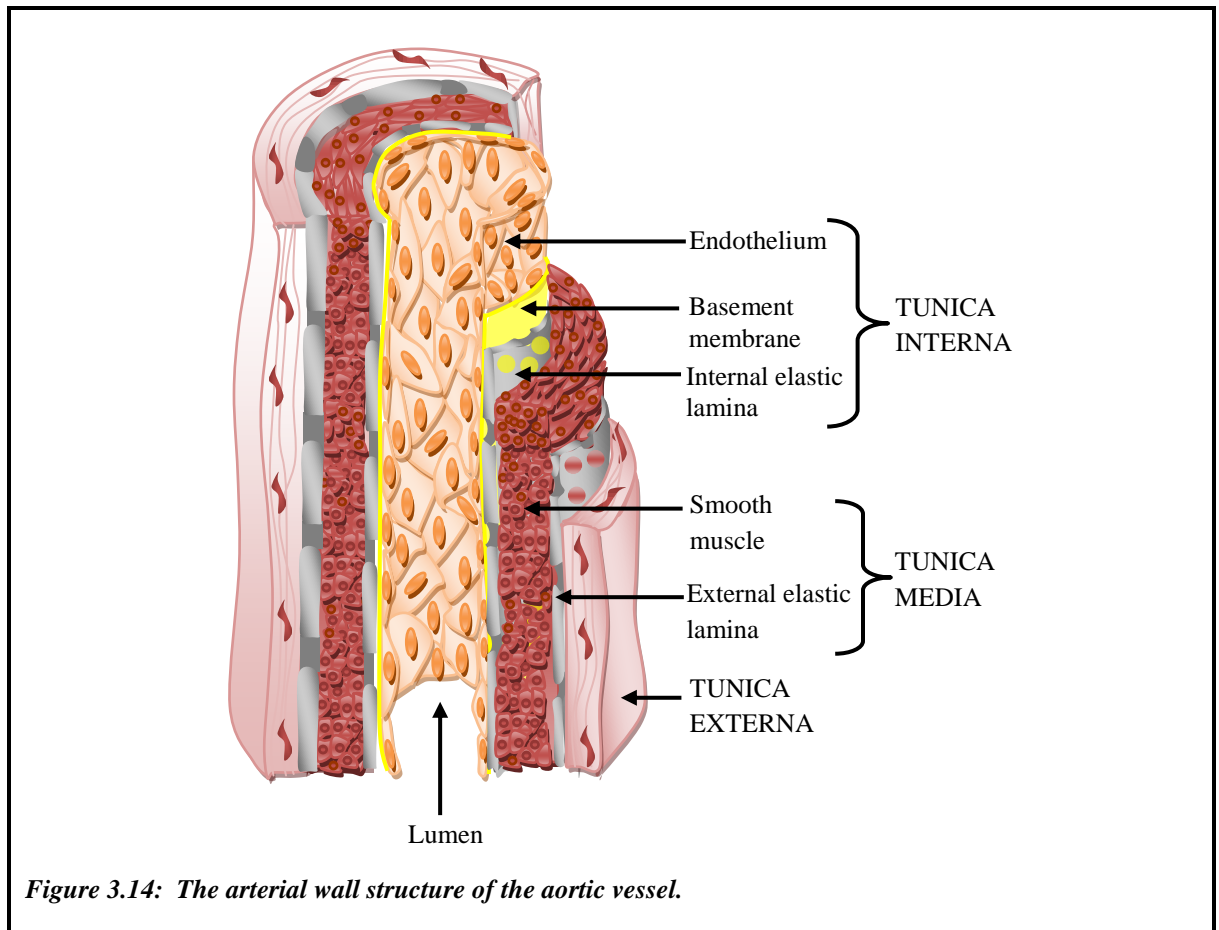


*Figure 3.14: The arterial wall structure of the aortic vessel.*

The lumen is the internal hollow area of the artery where the blood flows. The inner surface contains a lining of endothelium cells (ECs) which influences the function of smooth muscle cells (SMCs) within the vascular wall. The arrangement of ECs on the basal lamina is connected to an internal elastic lamina (IEL) layer by mixture of microfibrils and collagen known as the connecting filament. This area containing the ECs and the subendothelium part is known as the tunica interna or intima. It has been suggested that the ECs are responsible for producing IEL as they are known for producing elastin [130, 131]. The endothelium layer plays an important part in maintaining the vascular tone

due to its ability of secreting substances that are responsible for the relaxation or constriction of the vessel [132, 133].

The tunica media is normally the thickest layer as it contains SMCs and the majority of the elastin layer. The elastin layer is made up of elastin sheets, lamellae, with collagen fibres, proteoglycan-rich extracellular matrix and SMC layers positioned between them. The lamellae and fibres produce a continuous network. The elastin alone has a low tensile strength, but when incorporated in this network it allows for the even distribution of stress through the wall and collagen fibres. The static mechanical properties are believed not to be fully related to the SMCs, but the significant influence occurs due to the elastin and collagen matrix [130, 131].

The external layer of the vessel is known as tunica externa or adventitia. The tunica adventitia is connected to the tunica media layer with external elastin lamina placed between them. The myofibroblast cells lead to the formation of collagen that is within the elastin. The large volume of collagen within the adventitia prevents rupture of the vessel when the blood flow pressure is high. Current studies have suggested that the adventitia may have the ability to sense injury incurred in the vessel [130, 131].

The external surface of the vessel is covered by a layer of fat known as perivascular adipose tissue (PVAT). The PVAT is known to attenuate vascular contraction in the presence of agonists, such as phenylephrine, angiotensin II, 5-HT and U 46619. However, the actual mechanism of interaction between PVAT resulting in the attenuation of contraction is not fully explained. Löhn *et al.* has suggested that the PVAT produces adventitium derived relaxation factor (ADRF) [134]. Goa *et al.* has claimed that the relaxation is due to PVAT and not the adventitia so it would be better termed as perivascular adipose tissue-derived relaxation factor (PVRF) [135]. Recent studies have suggested that the PVRF of the vessel occurs as a result of hyperpolarisation of the SMCs membrane. For instance Verlohren *et al.* discovered that when the PVAT remains attached on rat mesenteric arteries then there was an increased amount of hyperpolarisation of SMCs [132]. Also, when the vessel is placed in high potassium salt solution (KPSS) it not only causes the potassium gradient to be lowered across the membrane, but also leads to the removal of the relaxation response caused by PVRF [135]. This suggestion is further

verified by Löhn *et al.*, where intact vessels in the presence of K<sup>+</sup> channel blockers, such as glibenclamide, have shown to significantly inhibit the action of PVAT [134]. The current studies suggest that PVRF is similar to endothelium-derived hyperpolarisation factor (EDHF). It is common knowledge that EDHF refers to the hyperpolarisation of the SMCs membrane via endothelium-dependent and endothelium-independent routes. However, further investigation of PVRF is required to distinguish whether SMCs hyperpolarisation occurs via endothelium-dependent or independent mechanisms.

Chemicals that cause constriction or relaxation of the vascular cells can be categorised as agonist, antagonist or inverse agonist. An agonist will bind to the receptor on the cell membrane and trigger a particular chemical process to occur in the cell; however, the action of the agonist can be blocked by an antagonist. An inverse agonist results in the opposite effect of the agonist.

### 3.3.2. Aortic vessel function and contractility

#### 3.3.2.1. Vasoconstrictors

Vessels viability can be tested using vasoconstrictors and high potassium salt solution (KPSS; K<sup>+</sup>). The mechanism of constriction caused by vasoconstrictors occurs via pharmacological coupling.

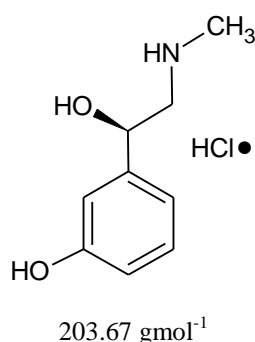
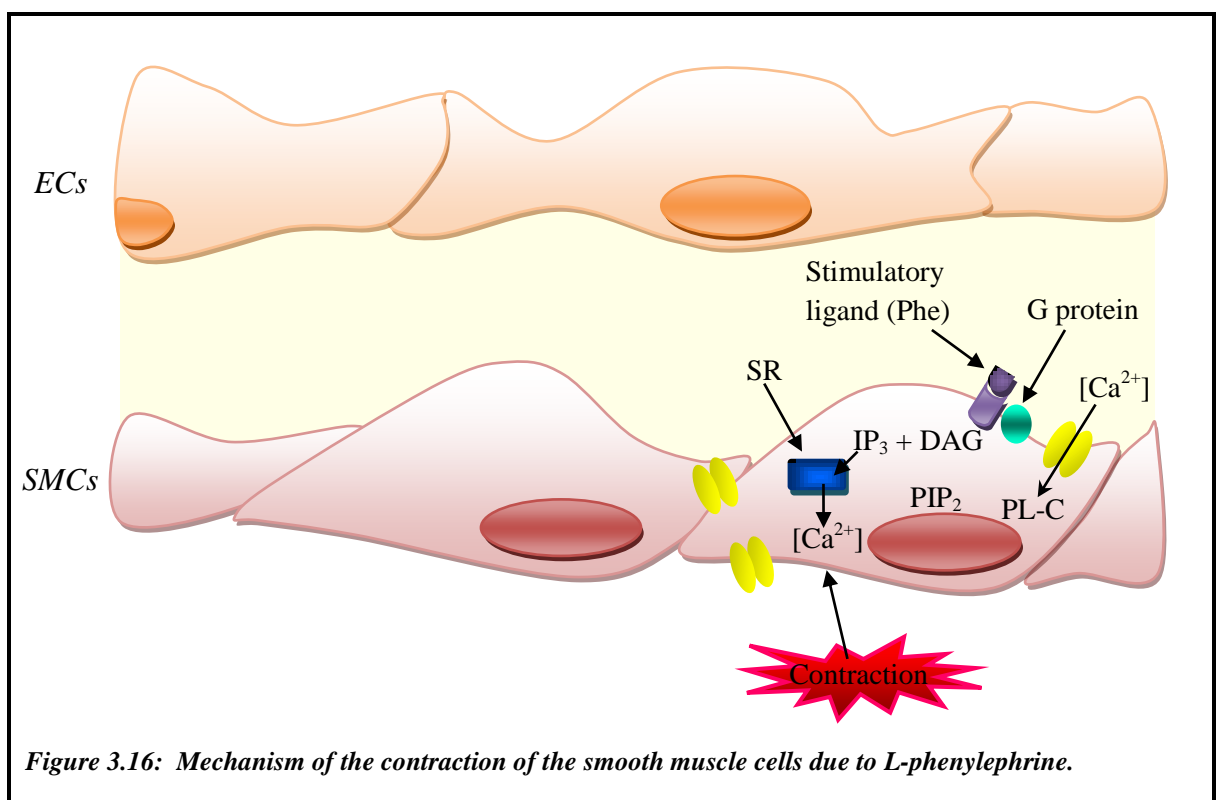


**Figure 3.15:** Molecular structure of vasoconstrictor *L*-phenylephrine.

Vasoconstrictors, such as *L*-phenylephrine (Phe) (Figure 3.15), will lead to the release of Ca<sup>2+</sup> ions from two pools (extracellular Ca<sup>2+</sup> and Ca from intracellular stores) into the cell cytosol thus resulting in the contraction of the SMCs (Figure 3.16). The exchange of ions

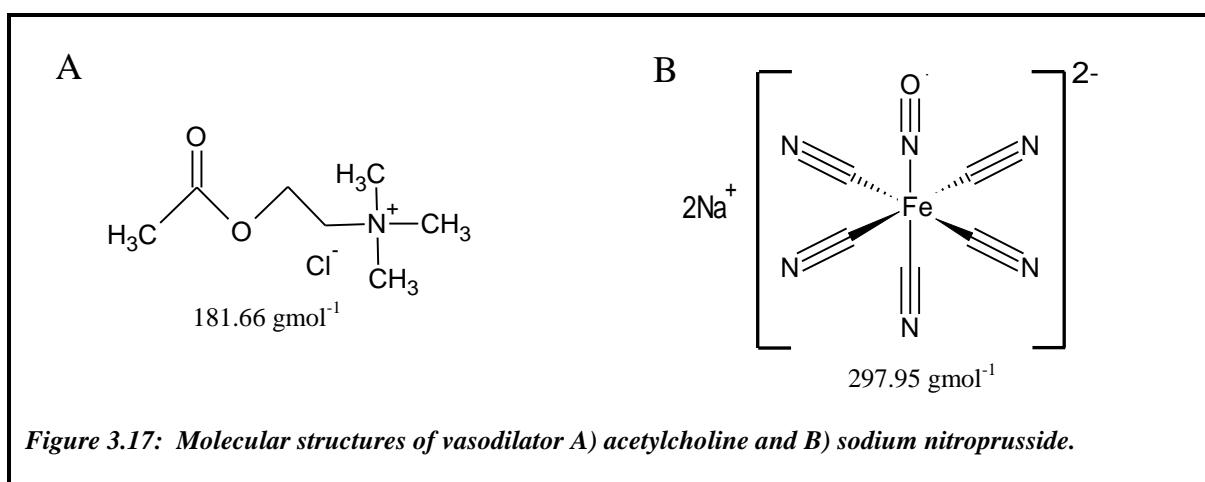
in the SMCs can occur from  $3\text{Na}^+-2\text{K}^+$  pump, delayed  $\text{K}^+$  channel, ligand activated  $\text{Ca}^{2+}$  channel, L-type voltage-dependent  $\text{Ca}^{2+}$  channel, a sarcolemmal  $\text{Ca}^{2+}$  pump and  $\text{Na}^+-\text{Ca}^{2+}$  exchanger. Phe behaves as a stimulatory ligand that binds to a receptor on the membrane ( $\alpha_1$  adrenergic receptor) which is specific for G-proteins. The predominate amount of  $\text{Ca}^{2+}$  uptake by the SMCs occurs via the ligand-gated  $\text{Ca}^{2+}$  channel (noradrenaline) and voltage-gated  $\text{Ca}^{2+}$  channel from the extracellular space. The influx of ions leads to depolarization of the membrane and therefore causing the  $\text{Ca}^{2+}$  ions to move into the cell. This depolarization further causes the voltage-gated channels to open. The binding of the stimulus to the reticular receptors leads to the activation of phospholipase C (PL-C). PL-C causes the hydrolysis of phosphatidyl inositol diphosphate ( $\text{PIP}_2$ ) to produce inositol triphosphate ( $\text{IP}_3$ ) and diacylglycerol (DAG).  $\text{IP}_3$  binds to a receptor on the sarcoplasmic reticulum which contains a pool on  $\text{Ca}^{2+}$  ions. When there is a release of Ca ions of greater concentration the  $0.1\mu\text{M}$  the contraction occurs. The  $\text{Ca}^{2+}$  ions are moved out of the cell by  $\text{Na}^+-\text{Ca}^{2+}$  exchanger (antiport) and ATP-demaning  $\text{Ca}^{2+}$  pump. The extracellular  $\text{Ca}^{2+}$  uptake is dependent on the  $\text{Na}^+$  gradient of the antiport. These  $\text{Na}^+$  and  $\text{K}^+$  pumps across the cell membrane maintain the gradient of  $\text{Na}^+$  and  $\text{K}^+$  [136, 137].



KPSS is used to assess the viability of the vessels by demonstrating their ability to contract upon its administration. The mechanism of contraction caused by KPSS is via electromechanical coupling. KPSS causes SMCs to contract via membrane depolarisation following potassium ion cellular uptake. The altered plasma membrane potential of vascular SMCs activates  $\text{Ca}^{2+}$  channels in the membrane leading to an increase in intracellular concentration of calcium. Calcium influx leads to vascular contraction. Phe can induce a further smooth muscle vascular contractile response after KPSS. This is partly due to the fact that the latter have a role in mobilising intracellular as well as extracellular  $\text{Ca}^{2+}$  [137, 138].

### 3.3.2.2. Vasodilators

Vasodilators are chemical agonists that result in the relaxation of the SMCs (Figure 3.17).



The endothelium integrity may be tested by acetylcholine (ACh) vasodilator. ACh leads to vasodilation via several mechanisms. The most predominant mechanism includes the production of nitric oxide (NO) species from ECs leading to SMCs relaxation [139]. Therefore, ACh is known as endothelial-dependent vasodilator as it triggers a cascade of reactions within the ECs for the production of NO which diffuses into the SMCs. Alternatively, vasodilation may occur by a NO donor, such as sodium nitroprusside (SNP), as it is capable of causing vasorelaxation in the SMCs without the need of ECs being intact, thus it is referred to as the endothelial-independent vasodilator (Figure 3.18).

The mechanism for endothelial derived vasorelaxation can be mediated by various stimuli, such as ACh and bradykinin (Bk). They result in the production of prostaglandin I<sub>2</sub> (PGI<sub>2</sub>), NO and EDHF. NO is a molecule synthesised by the oxidation of L-Arginine (L-Arg) forming L-citruline (L-Cit) and NO. This reaction is mediated by nitric oxide synthase (NOS), of which three isoforms exist (eNOS, nNOS and iNOS). The ECs have a basal production of NO to maintain the vascular tone at a relaxed state. Following its diffusion from ECs, NO binds to soluble guanylate cyclase (sGC) in SMCs leading to the activation of cyclic guanosine monophosphate (cGMP) by converting the binding protein (GTP) [140]. The binding protein GTP may also activate cyclic adenosine monophosphate (cAMP) which leads to the extracellular movement of Ca<sup>2+</sup> ions and thus relaxation of vascular SMCs [140, 141]. The activated cGMP in turn stimulates cGMP-dependent protein kinase G (PKG), leading to calcium (Ca<sup>2+</sup>) resequestration to the sarcoplasmic reticulum (SR), enhanced Ca<sup>2+</sup> pumping through Ca<sup>2+</sup>-ATPase and the inhibition of Ca<sup>2+</sup> influx. These effects are mediated by Ca<sup>2+</sup> channel phosphorylation. The reduction in intracellular Ca<sup>2+</sup> causes SMCs relaxation. PKG also produces its effects as a phosphatase to dephosphorylate myosin light chains of SMCs leading to vascular dilation [143].

Prostaglandins (PGs) are vasodilators derived from phospholipase A<sub>2</sub> (PLA<sub>2</sub>) converting phospholipid (PL) to arachidonic acid (20:4) [144] via the enzyme action of cyclooxygenase (COX) 1 and 2 with prostacyclin synthase (PCS) [145, 146]. PGs serve as hormone-like molecules with wide variety of effects, some of which lead to SMCs contraction, pain, fever, and inflammation. A study by Lagaud *et al.* suggests the involvement of a prostaglandin, possibly PGI<sub>2</sub>, in the ACh-induced dilation [147].

The mechanism of relaxation of blood vessels is complex and is related to the elaboration of a number of dilatory pathways that depend on the vessel size and bed. NO is the major contributor to dilation in large vessels such as the aorta [148], however in medium- and small-sized vessels such as coronary arteries and mesenteric vessels, EDHF has a predominant role in mediating relaxation [149, 150]. Furthermore, as NO leads to the increased intracellular concentration of cGMP it activates the calcium-activated potassium channels (K<sub>Ca</sub>) and the ATP-sensitive potassium channels (K<sub>ATP</sub>), which are both present in the SMCs resulting in the vascular SMCs hyperpolarization and the relaxation [130, 131]. The PGI<sub>2</sub> binds to the SMCs receptor and causes an increased concentration of intracellular

cAMP which in turn activates  $K_{ATP}$ . Both NO and  $PGI_2$  are capable of activating delayed rectifier potassium channels ( $K_{dr}$ ), which elicit hyperpolarization and relaxation of the SMCs [143, 144, 151]. EDHF, cytochrome P450 2C isoenzymes, hydrogen sulphide ( $H_2S$ ) [152], and arachidonic acid-derived epoxyeicosatrienoic acids (EETs) are produced in the vascular endothelium and act upon vascular SMCs to cause hyperpolarisation and ultimately relaxation.

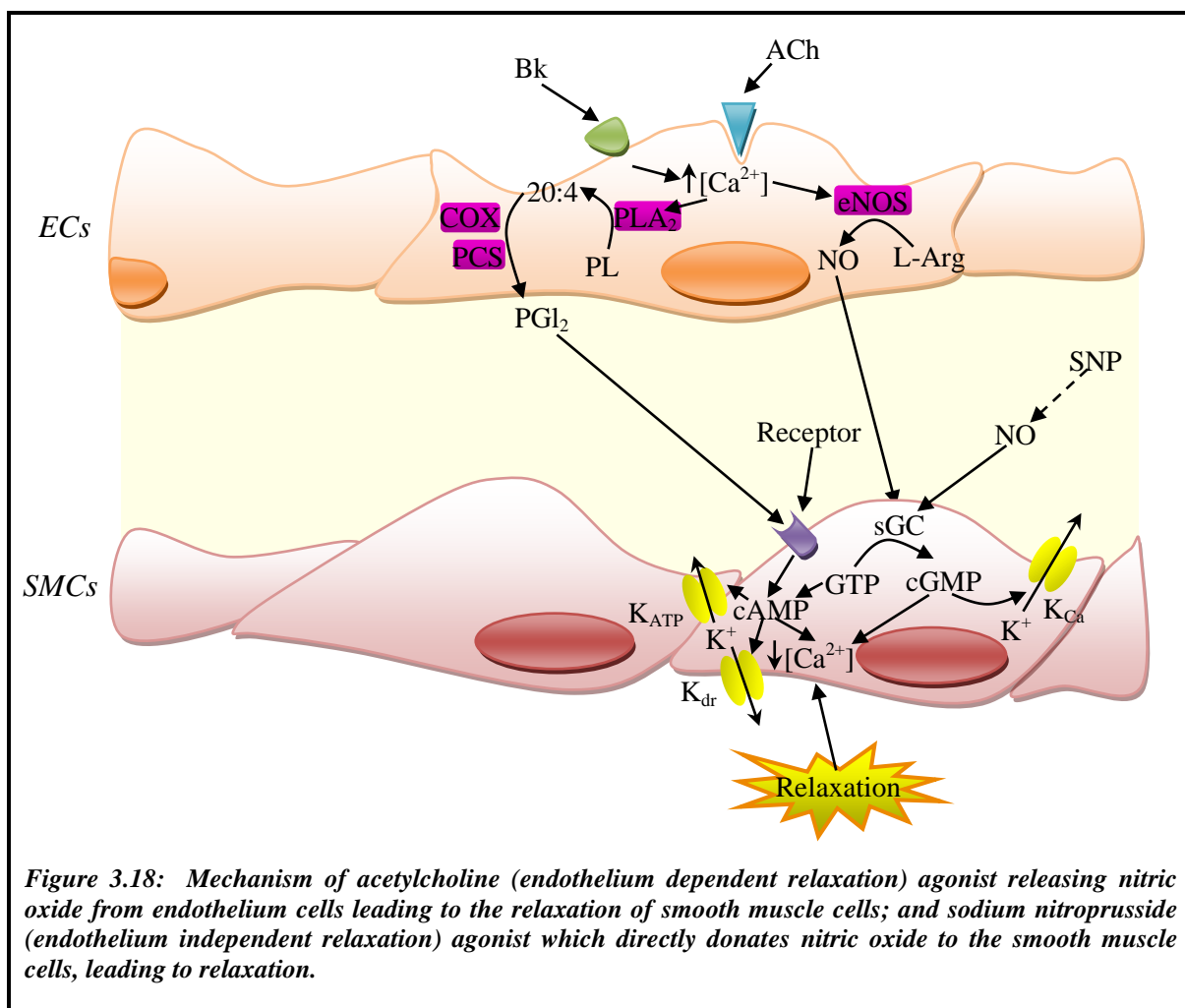


**Figure 3.18:** Mechanism of acetylcholine (endothelium dependent relaxation) agonist releasing nitric oxide from endothelium cells leading to the relaxation of smooth muscle cells; and sodium nitroprusside (endothelium independent relaxation) agonist which directly donates nitric oxide to the smooth muscle cells, leading to relaxation.

$N_{\omega}$ -Nitro-L-arginine (L-NNA) is a NOS inhibitor and therefore it can be used to investigate whether the endothelium-dependent relaxation of ACh is dependent on production of NO via the activation of NOS (Figure 3.19) [153]. Furthermore, Kellogg *et al.* suggested that relaxation of the SMCs may also be influenced by non-NO-dependent mechanisms or due to a relaxation mechanism triggered by PG [154].

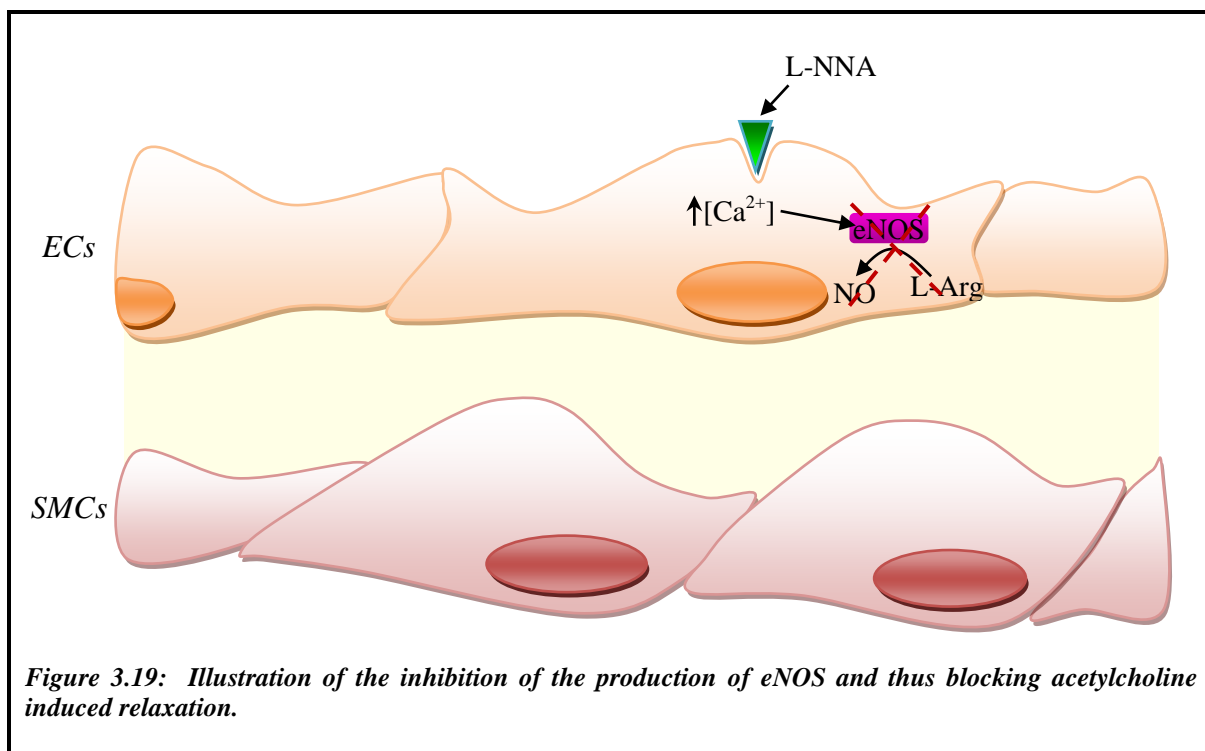
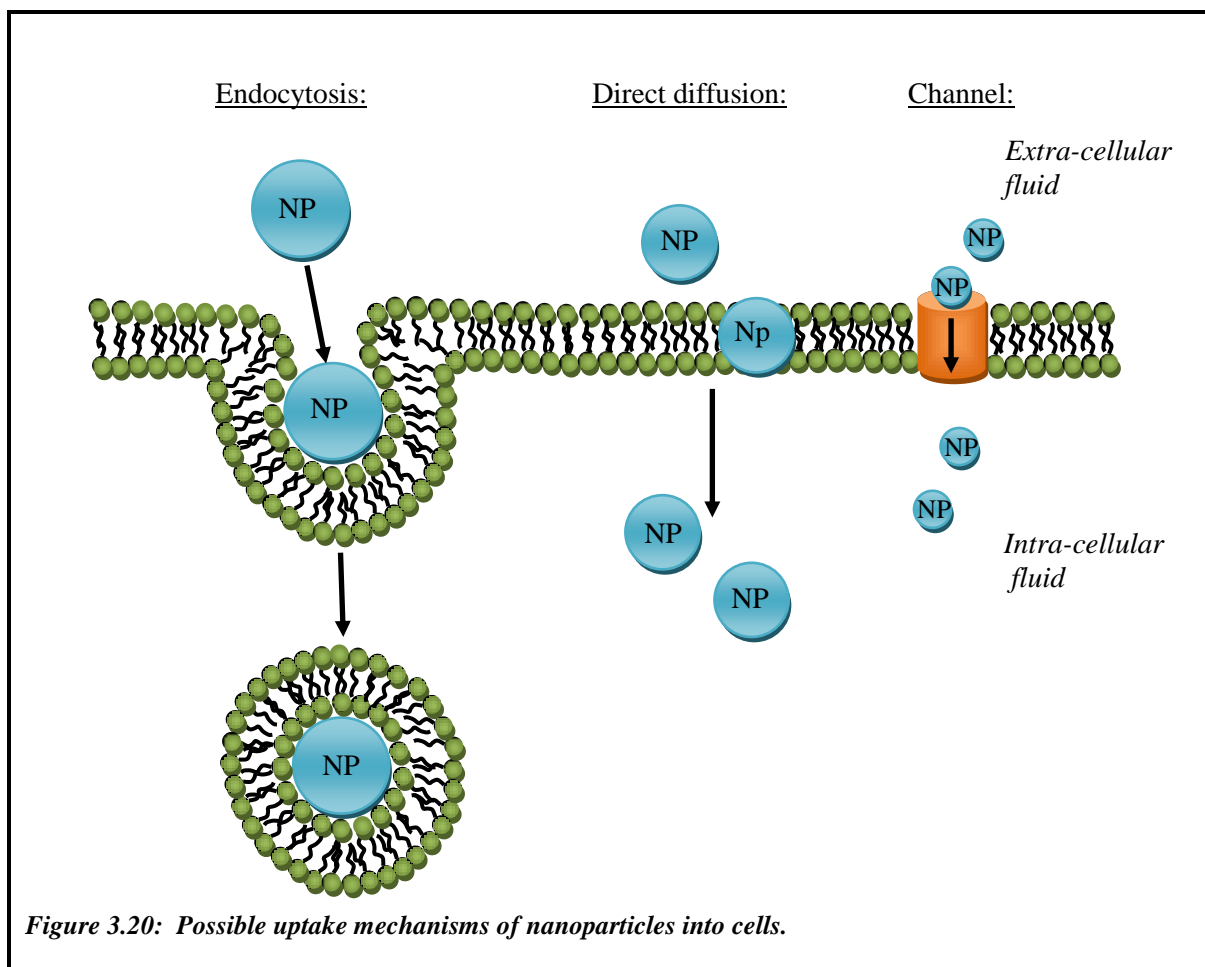


Figure 3.19: Illustration of the inhibition of the production of eNOS and thus blocking acetylcholine induced relaxation.

### 3.3.3. Cellular uptake mechanisms of nanoparticles

It is considered that for effective uptake of materials into the cell they should range in the nanometer size or even smaller. The rate of entry into the cell is not only dependent on size but also the morphology, surface charge of NPs and the actual cell type. Jin *et al.* [155] study has shown that the majority of NPs that rapidly enter the cell take place within the first 5 minutes and reaches a maximum uptake after 30 minutes incubation time [155].

The internal cellular solution and organelles are held together by an external plasma membrane that consists of a phospholipid bilayer. There are three known routes by which NPs may enter the cell; direct diffusion, endocytosis or via ion channels and transporter proteins (Figure 3.20) [66].



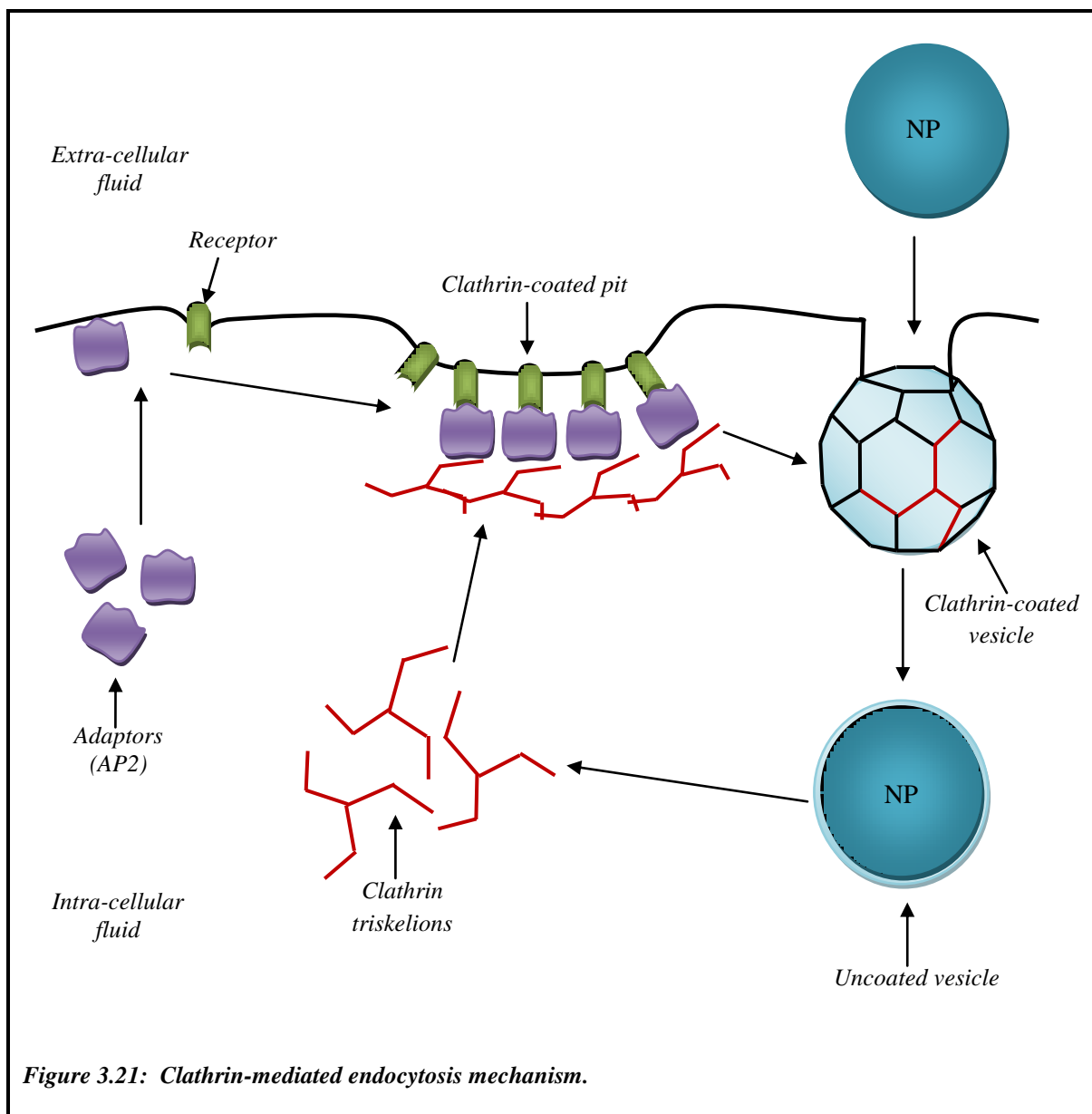
There are various types of ion channels and transporter proteins within the plasma membrane that allow for the entry and exit of specific materials through the cell. These channels are highly selective, unlikely to be open and have a very small average pore size of only a few Angstrom units [66].

NPs can directly diffuse into the cell via the plasma membrane. However, many variables have to be ascertained in order for the NPs to penetrate through the phospholipid bilayer, such as particle size, morphology, composition, charge and hydrophobicity. It is not only important to produce such purpose built NPs but also to understand how its outer surface interacts with the solid-liquid and nano-bio interface [66].

The most predominant mechanism of NP entry into the cell is via endocytosis. The general mechanism occurs by the lipid bilayer of the cell membrane wrapping around the NP. This follows a fission reaction where the NP bound lipid membrane is pinched off to produce a vesicle containing the NP. There are different pathways for endocytosis to occur. The

actual NP size greatly influences the strategic internalisation of the NPs into the cell. The pathways may occur by fluid phase or receptor mediated endocytosis. Fluid phase endocytosis occurs when a water soluble material diffuses into the cell by producing vesicle due to mass action. Receptor mediated endocytosis occurs by the material binding to a specific part of the cell surface that triggers the internalisation of the material within the cell. The receptors may be lipid, protein or carbohydrate based which is specific to the material being internalised [66].

Cellular entry of NPs may occur through clathrin (Figure 3.21) or caveolae (Figure 3.22) mediated mechanism. The clathrin-dependent endocytosis pathway entails the movement of soluble clathrin, retained within the cytoplasm, to the plasma membrane. Clathrin-binding adaptors, for instance adaptor protein-2 (AP2), will bind to the clathrin and initiate the process, followed by the assembly of clathrin triskelion to form clathrin-coated pits, which later produces a polygonal lattice at the membrane. This polygon lattice will bud and pinch off to produce the clathrin-coated vesicle. Furthermore, these coated-pits are also known to contain phospholipids, such as phosphatidylinositol-4,5-bisphosphate, which are known to facilitate the vesicle formation and the budding process [156].



Alternatively, NP entry within the cell may occur via the caveolae-mediated endocytosis (Figure 3.22). The caveolae are flask-shaped invaginations which are found on the plasma membrane of many cell types. They normally appear as rounded plasma membranes with a diameter between 50 to 80 nm. The caveolae function and composition influences its role for the specific cell types. The endothelial cell may contain components, such as the mouth or restricted diaphragm which reduces the possibility of diffusion from occurring. Previous studies have shown the initialisation of virus particles (SV40) via the clathrin-independent pathway and thus it may be possible for small NPs to enter via this process [157].

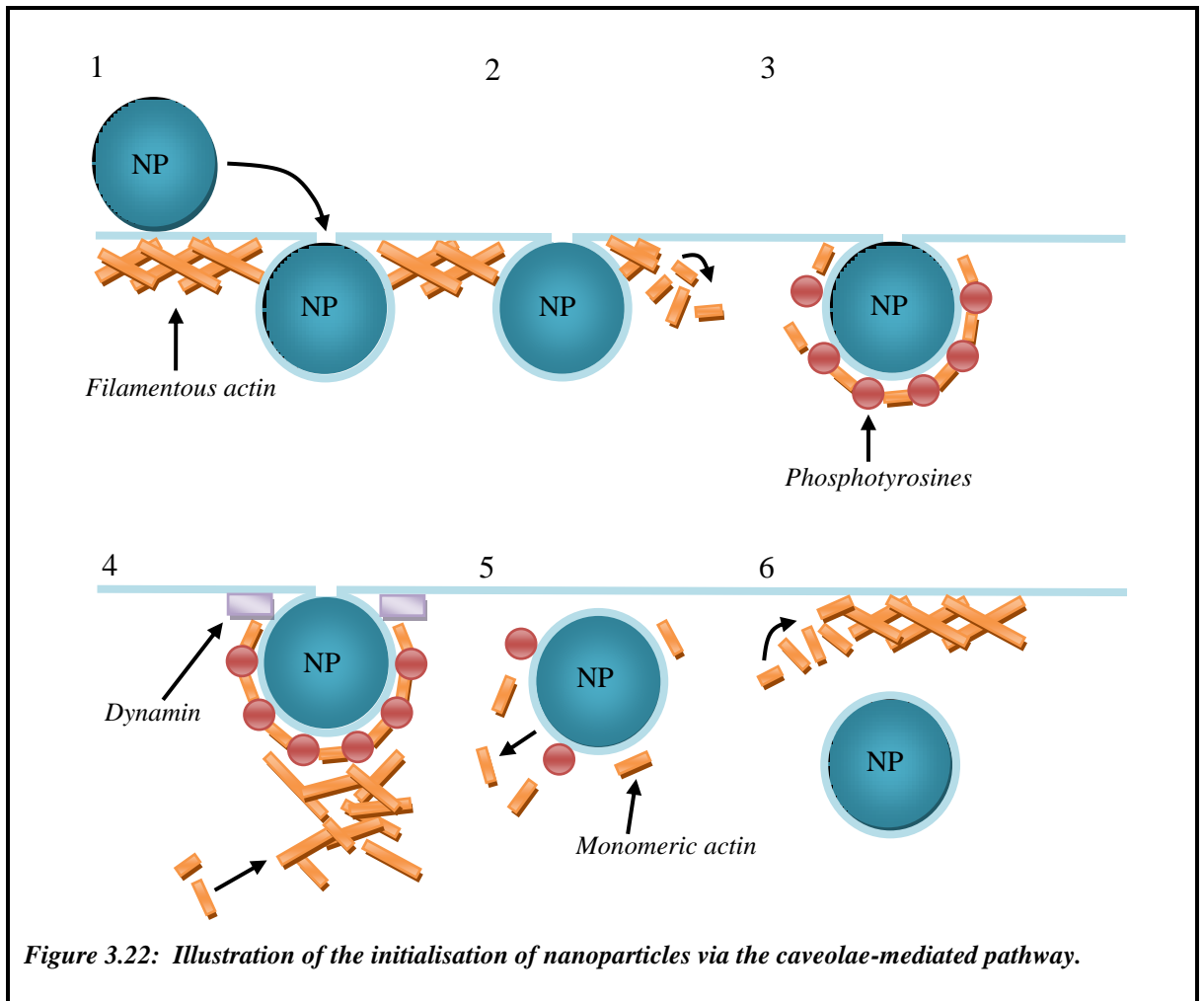
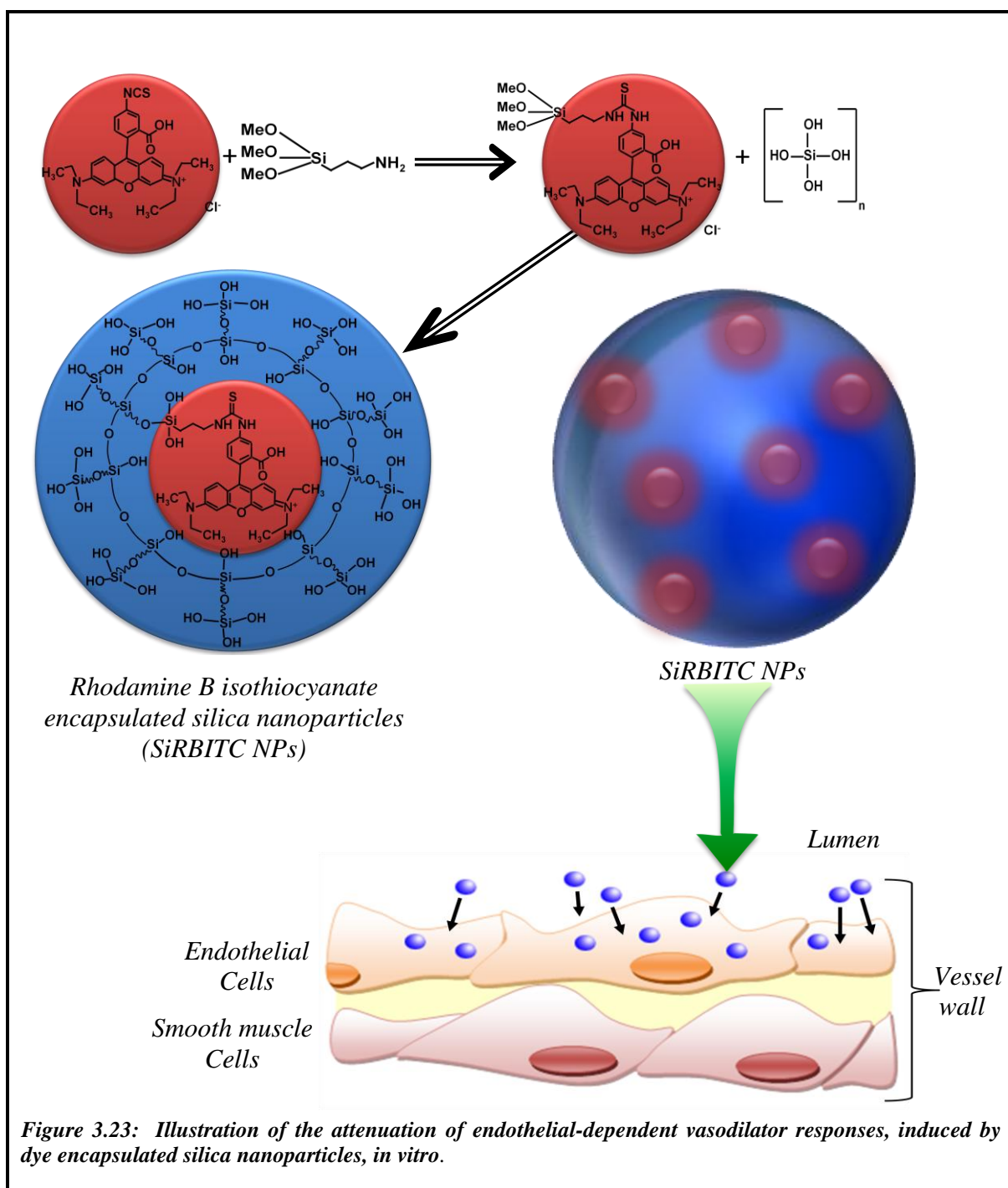


Figure 3.22: Illustration of the initialisation of nanoparticles via the caveolae-mediated pathway.

### 3.4. Biocompatibility of Silica Nanoparticles

The illustration of the incorporation of RBITC dye molecules within silica-shell followed by incubation within tissue leading to the initialisation into ECs (Figure 3.23).



NPs are useful for biotechnology engineering due to the ease of combining functional materials. The functionality is encompassed in a particle with dimensions small enough to enter into mammalian cells, while the efficiency and cellular uptake pathways can be altered depending on surface charge and material composition. One very popular material is silica, a naturally abundant compound found in glass and sand, which has been utilised in biomedicine due to its biocompatible properties. A key advantage of SiNPs is their fluorescence labelling potential. A wide range of metallo-organic and organic dyes can be encapsulated within SiNPs, including rhodamine, fluorescein, cyanine and their derivatives [73-159]. By encapsulating dye molecules in a silica shell, it is possible to overcome problems encountered by many fluorescent labelling probes, such as fluorophore, including cytotoxicity [115, 78, 160], thus leading to improved photostability and increased fluorescence signal, due to the large number of dye molecules within a single NP. SiNPs encapsulated with fluorescent trimethine indocyanine dyes have been demonstrated to display an overall three fold enhanced photoemission intensity [8]. Additionally, two-photon adsorbing fluorophores, which employ near infra-red emission, have gained particular attention for *in vivo* bio-imaging applications, as they show no cytotoxicity at low concentrations [161]. The silica surface can, furthermore, be easily modified to target specific cell surface groups, making them ideal for imaging diagnostics and targeted therapeutics [162, 163]. For example, SiRBITC NPs have been used for the imaging and detection of early stage apoptotic cells [78]. Dye encapsulated SiNPs ( $28 \pm 4$  nm), that were surface functionalised with anti-human IgG antibody, have been used for the detection of B lymphocyte subpopulations in the blood of Systemic Lupus Erythematosis patients [163].

Evidence from *in vitro* cell culture studies; however, suggest that dye encapsulated SiNPs may be toxic to cells and that their influence is dependent on their size, surface charge and particular cell type [165, 166]. While uptake of dye encapsulated SiNPs had no overall effect on the proliferation and death rate of lung epithelial cells at a concentration below 0.1 mg/ mL [155], they induced apoptosis in hepatoma cells [167] and were cytotoxic to mouse keratinocytes [168]. It remains difficult, however, to ascertain whether the dye itself within the NPs has contributed to this toxicity. Indeed, the bonding between the silica matrix and dye molecules greatly influences its properties. Dye molecules can either be covalently bonded to the silica matrix or attracted by electrostatic non-covalent bonding.

Where the attraction between the dye and silica is non-covalent, there are possibilities of dye leakage [169]. Fluorophores, such as ruthenium complex, demonstrate a unique fluorescence quenching phenomenon and have been thus utilised as ‘gas sensors’ in the detection of gaseous and dissolved gases, including O<sub>2</sub> and SO<sub>2</sub>. Additionally, we have recently demonstrated that it is possible for gaseous molecules to diffuse through silica shells and quench fluorescence of dye molecules incorporated within the dye encapsulated SiNPs (Chapter 3; Section 3.2).

Of particular relevance to imaging diagnostics, is the influence of SiNP infusion on ECs lining blood vessels. Recent studies suggest a size dependant cytotoxic affect of SiNPs. Napierska *et al.* [170] subjected human ECs in culture to SiNPs of different sizes (14-335 nm) and compared the mass concentration at which NPs cause 50 % reduction in cell viability ( $TC_{50}$ ). They concluded that smaller NPs (33-47  $\mu\text{g}/\text{mL}$ ) resulted in  $TC_{50}$  at lower mass compared to larger NPs (1087  $\mu\text{g}/\text{mL}$ ). Furthermore, Liu *et al.* [170] demonstrated that exposing 20 nm SiNPs (100-200  $\mu\text{g}/\text{mL}$ ) to human umbilical vein ECs results in the production of intracellular reactive oxygen species (ROS), such as superoxide free radicals, leading to oxidative stress and consequently dysfunction of ECs. As ECs are modulators of vascular function, it is hence unclear how intravascularly infused SiNPs are likely to modulate function. Akbar *et al.* demonstrated that 100 and 200 nm SiNPs are rapidly taken up by ECs lining of aortic vessels incubated *in vitro*, with no detrimental effect on vascular function [35]. The objective of the present study is to investigate the size dependent influence of SiNPs, smaller than 100 nm (medium [70 nm] and small [30 nm] size ranges) on aortic vessel function, *in vitro*, and whether dye encapsulation of these SiNPs alters their uptake by ECs and hence influences vascular responses. Results will inform the future fabrication of biocompatible SiNPs for use in imaging diagnostics.

### 3.4.1. Experimentation

#### 3.4.1.1. Tissue preparation

The thoracic aortic arteries of male Wistar rats were used for the *in vitro* studies ( $n=37$  animals; one vessel from each animal). The rats of approximately 150-250 g weight were humanly killed by stunning followed by cervical dislocation following institutional approval and in accordance with guidelines issued by the European Commission Directive 86/609/EEC. The PVAT was removed from the vessel while being gassed (95 % O<sub>2</sub>:5 % CO<sub>2</sub>) in cold physiological salt solution (PSS) (Figure 3.24).

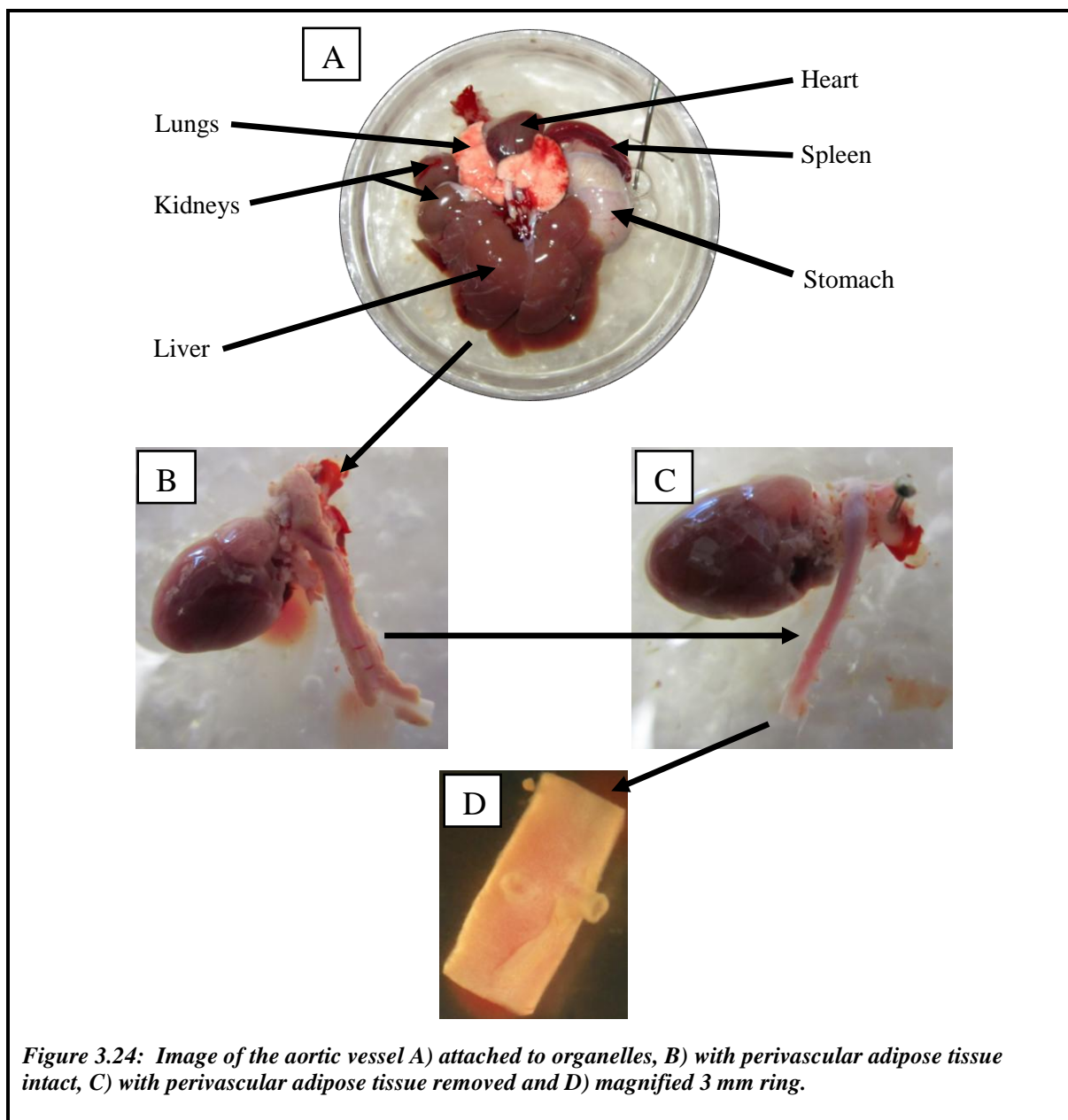


**Figure 3.24:** Image of the aortic vessel A) attached to organelles, B) with perivascular adipose tissue intact, C) with perivascular adipose tissue removed and D) magnified 3 mm ring.

### ***3.4.1.2. Organ-bath setup***

The organ-bath setup (Figure 3.25) is used for large arteries (aortic vessels) with a diameter in the range of 1-4 mm [172]. The vessels were dissected into 3-4 mm aortic rings and mounted in an organ-bath system filled with oxygenated PSS solution (37 °C) by threading the rings through a U-shaped hook, which is screwed in position via the plastic support that is attached to a micrometer, and ascending wire attached to an isometric force transducer, as previously described by Akbar *et al.* [35]. The transducer arms contain springs that when there is large distorting force on the isometric contraction, which are minimal changes in the length, allowing changes in vessel diameter to be maintained. The micrometer gives readings on the distance between the two wires from touching and the distance when the vessel is stretched. The tension between the two wires was recorded using Labchart 6 (Powerlab, AD Instruments, UK). The aortic rings were placed under a constant 2 g tension throughout the experimentation as preliminary results have determined this to be the optimal tension value. Vessels were equilibrated for approximately 1 hour, followed by pre-constriction with high K<sup>+</sup> (60 mM, KCl) to test vessel viability and achieve stable contraction. Responses to endothelium-dependent and independent dilator agonists were examined by adding cumulative doses of acetylcholine (ACh; 0.01-200 μM) and sodium nitroprusside (SNP; 0.001-10 μM), before and after incubation with SiNPs for 30 minutes. The final concentration of SiNPs placed in the organ-bath experiments were 1.31×10<sup>11</sup> NP/ mL and 1.96×10<sup>12</sup> NP/ mL.

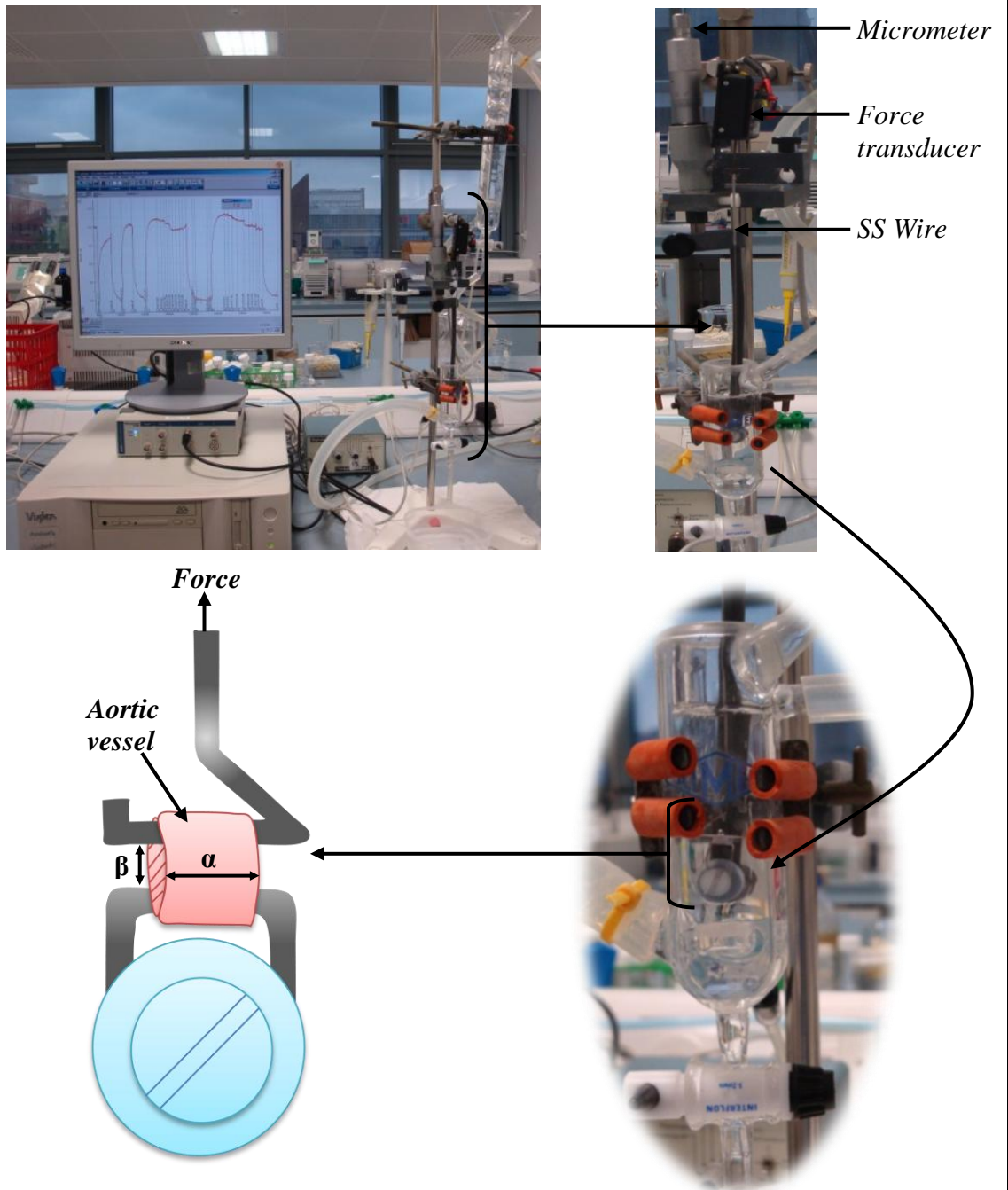
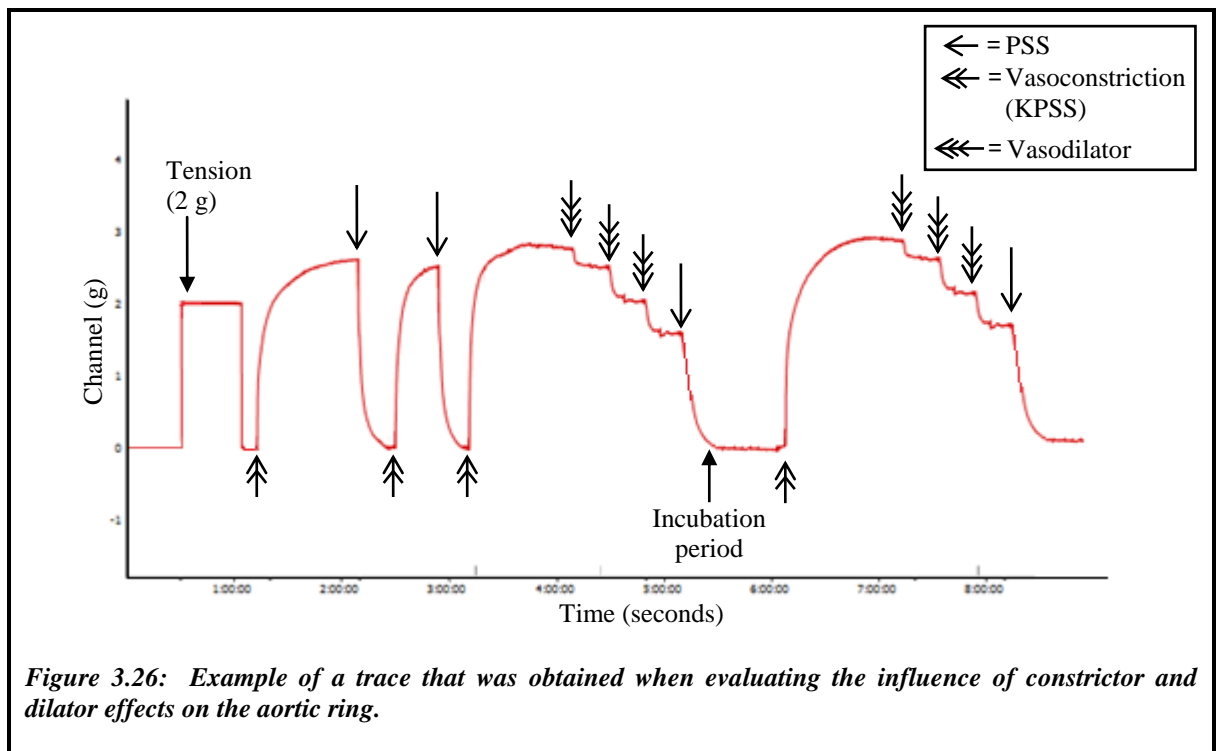


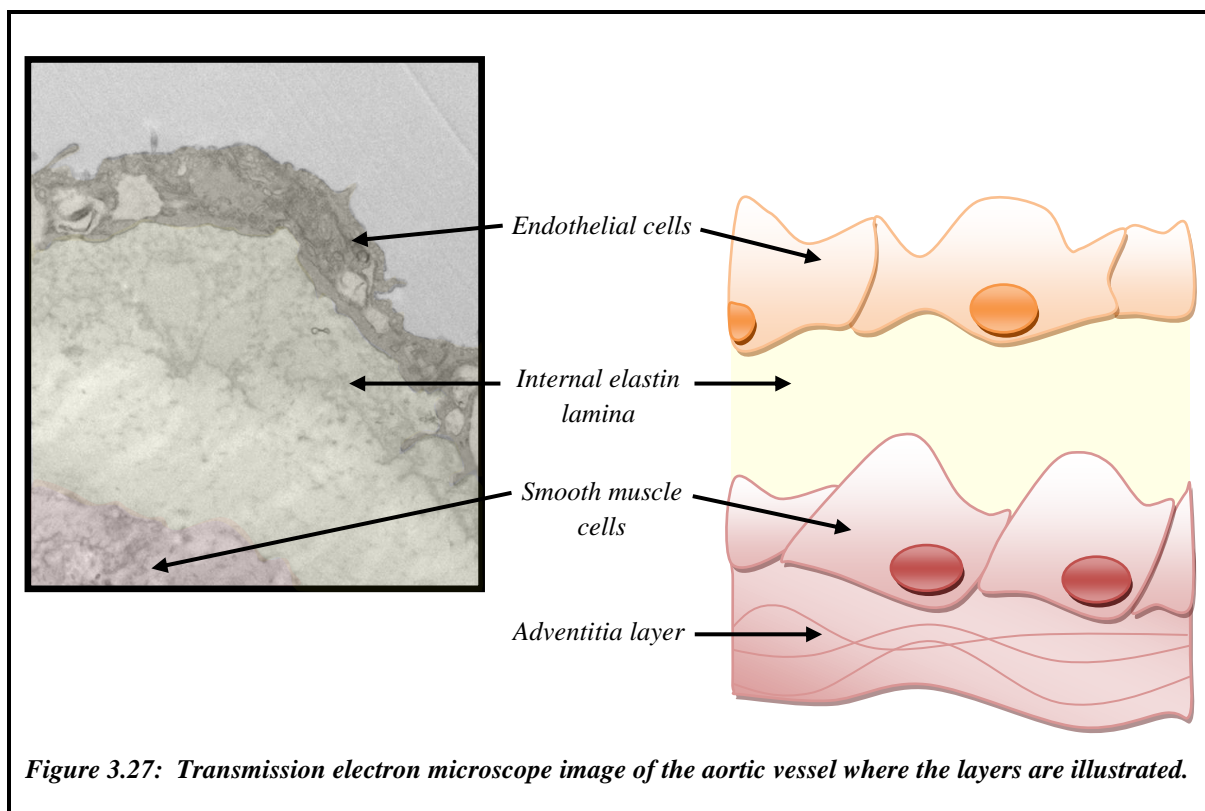
*Figure 3.25: Organ-bath system for the endothelium-dependent and independent vasodilation experimentation of aortic vessel.*

From the data acquisition system attached to the organ-bath setup, a trace will be acquired Figure 3.26.



### 3.4.1.3. Tissue fixation and processing

Vessels were fixed immediately after the functional studies. Fixation solution consisted of 2.5% glutaraldehyde in 0.1 M sodium cacodylate buffer at  $pH$  7.3. The vessels were allowed to stand in the solution for 2 hours at 22 °C. The samples were postfixated with reduced osmium ( $OsO_4$  1 % +  $K_4Fe(CN)_6$  1.5 %) for 1 hour, then dehydrated in a series of alcohols, infiltrated with TAAB LV resin and polymerized for 24 hours at 60 °C, as previously described [39]. Ultrathin 70 nm sections were cut with Leica ‘Ultracut S’ ultramicrotome and placed on copper grids. The grids were observed in Tecnai 12 Biotwin TEM at 80 kV, a cross-section of an aortic vessel is illustrated in Figure 3.27.



### 3.4.2. Results

Amorphous SiNPs ( $71\pm 6$  and  $27\pm 7$  nm) and SiRBITC NPs ( $31\pm 10$  and  $61\pm 7$  nm) (Chapter 2; Figure 2.2 and 2.6) were tested for biocompatibility via *in vitro* studies. These studies will allow for an understanding whether these NPs affect the endothelium-dependent and independent vasodilation or vasoconstriction.

#### 3.4.2.1. Detection of silica nanoparticles within vascular tissue

NP uptake was observed with TEM transverse sections through vessels following SiNP incubation. NPs of both size-ranges with and without RBITC dye molecules have entered the cytoplasm of the ECs. None were seen in the nucleus of the cells. The images of medium-size SiNP ( $71\pm 6$ ) uptake show that the NPs have acquired a transparent ring around them suggestive of the presence of a membrane due to their endocytosis into the cell (Figure 3.28).

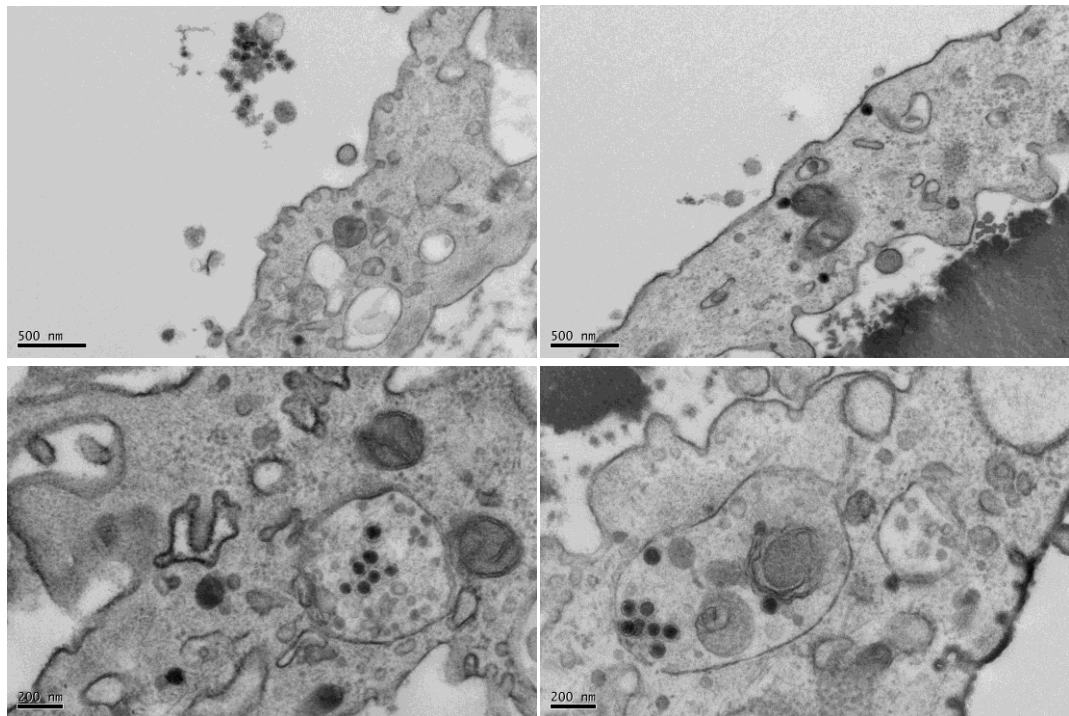


*Figure 3.28: Transmission electron microscope images of  $71\pm 6$  nm silica nanoparticles within the endothelial cell lining of the aortic vessel.*

Furthermore, medium-sized SiRBITC NPs ( $61\pm 7$  nm) were also observed to be internalised into the ECs and had also acquired a transparent ring around them (Figure 3.29).

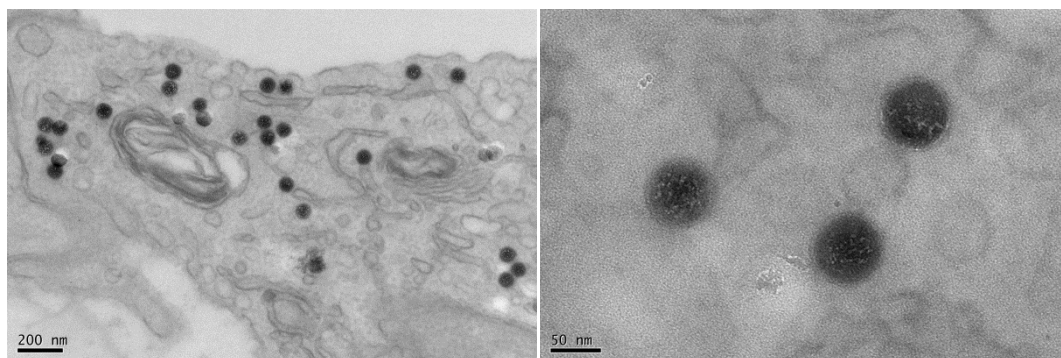


**Figure 3.29:** Transmission electron microscope image of  $61\pm 7$  nm rhodamine B isothiocyanate encapsulated silica nanoparticles within the endothelial cell lining of the aortic vessel.

The smaller SiNPs ( $27\pm 7$  nm) were also taken up by the ECs into the cytoplasm (Figure 3.30). Unlike the medium-size SiNPs, they did not seem to have a membrane coating, but seemed to accumulate within membrane invaginations suggestive of caveolae; it is thus likely that they may have entered the cell via alternative pathways. There was no evidence of NP uptake, of either size, into the adventitial or smooth muscle cell layers with no evidence of migration through the elastic lamina.

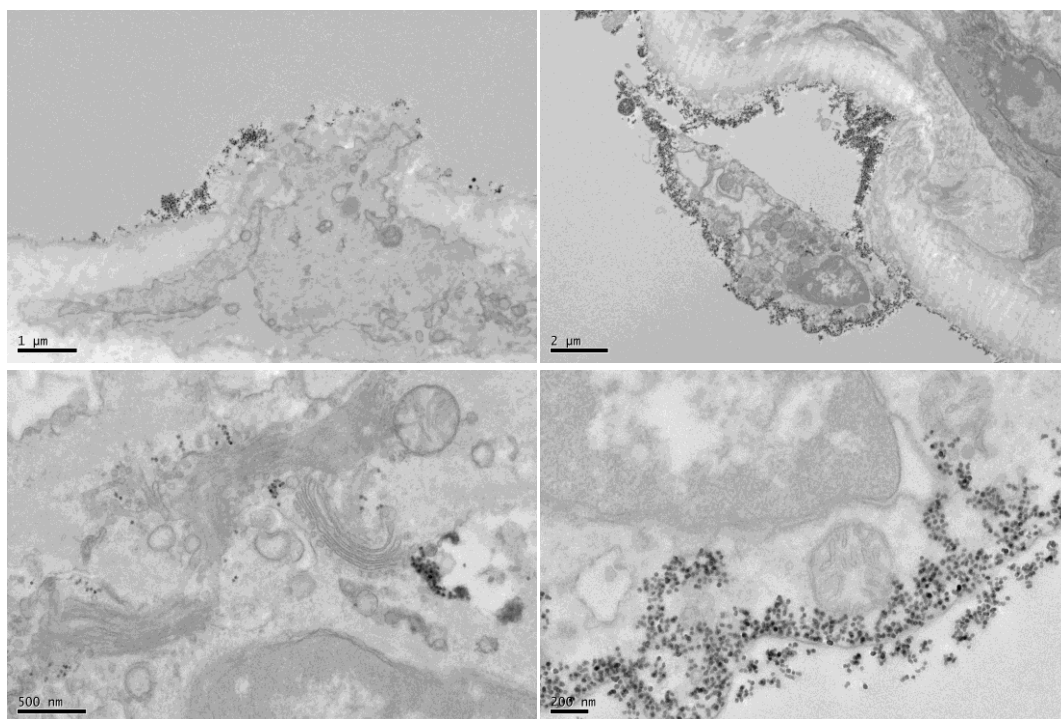


**Figure 3.30:** Transmission electron microscope images of  $27\pm 7$  silica nanoparticles within the endothelial cell lining of the aortic vessel.

The TEM images also confirm the initialisation of smaller SiRBITC NPs of  $31\pm 10$  nm (Figure 3.31).

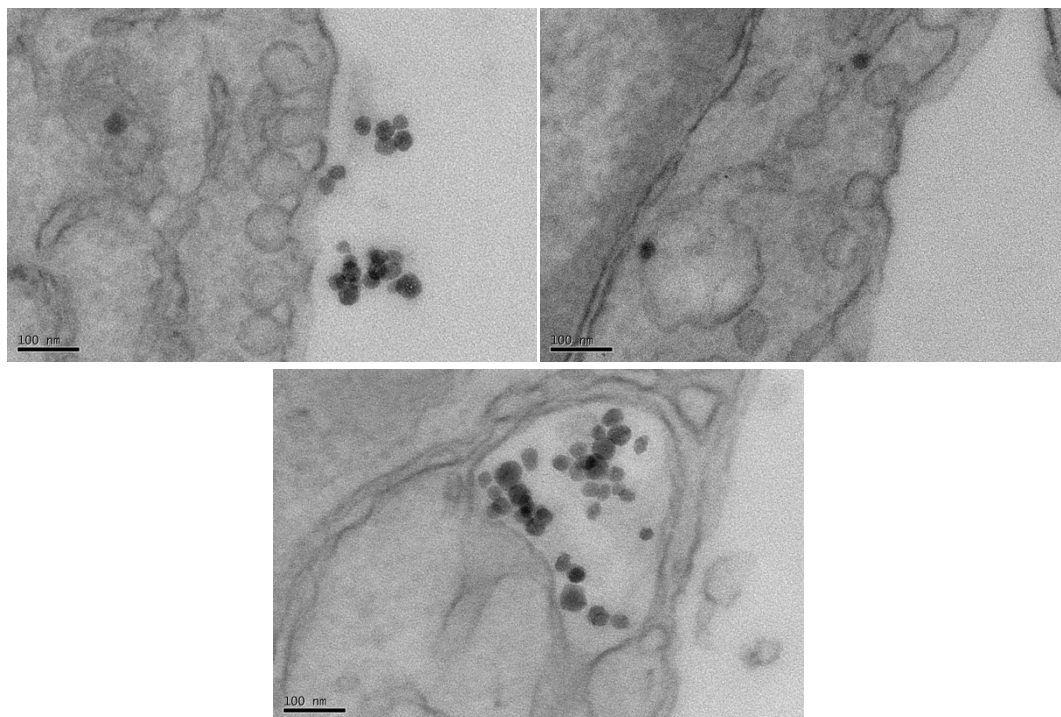


**Figure 3.31:** *Transmission electron microscope images of  $31\pm 10$  nm rhodamine B isothiocyanate encapsulated silica nanoparticles within the endothelial cell lining of the aortic vessel.*

Temperature is a pivotal factor on cellular uptake mechanism. The inhibition of one or several pathway (s) allows for a greater understanding of the mechanism by which the NPs enter the cells. A common method used for the assessment of endocytosis as the possible pathway of entry is conducted by setting the temperature of the incubation medium to 4 °C, as all the energy-dependent pathways are inhibited [173]. A non-functional study of  $71\pm 6$  nm SiNPs incubated in a vessel at 4 °C results in the inhibition of NP uptake, suggestive of endocytosis as a possible mechanism of entry (Figure 3.32).

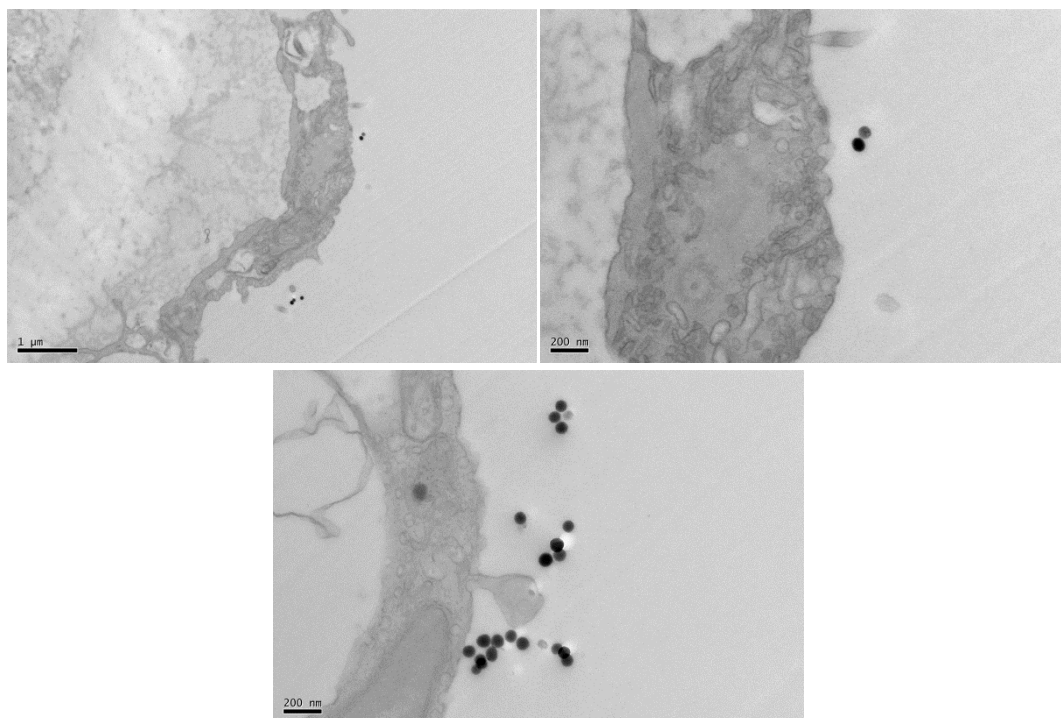
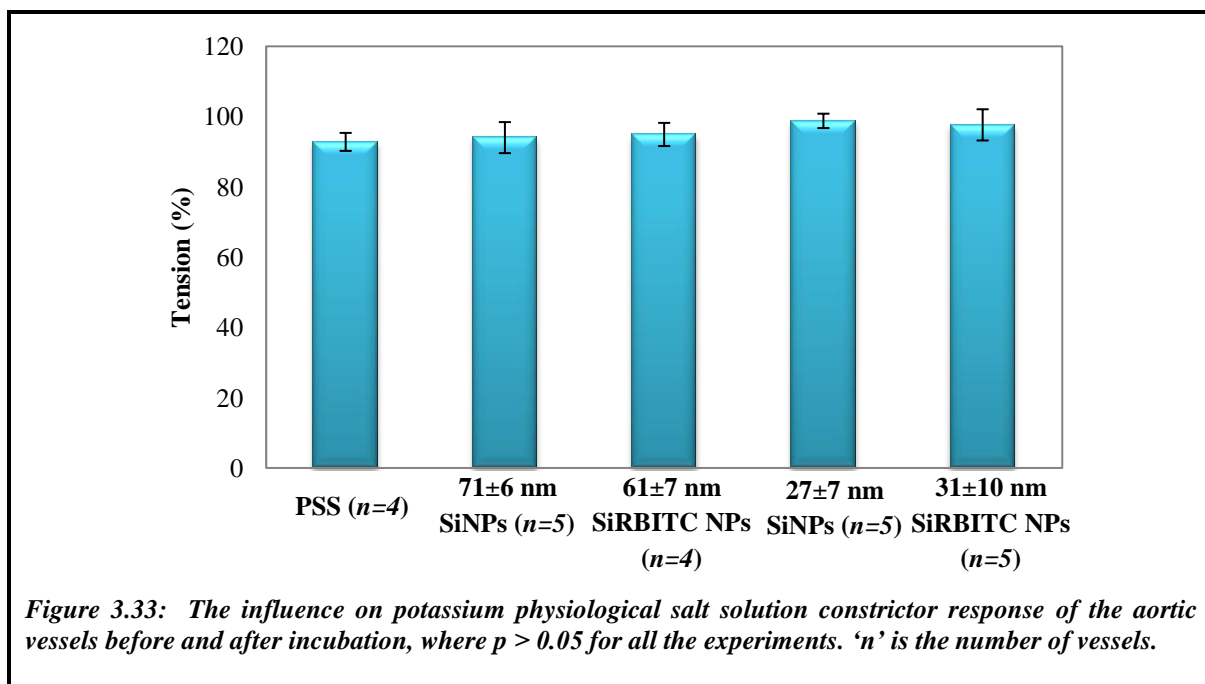


**Figure 3.32:** Transmission electron microscope images of  $71\pm 6$  nm silica nanoparticles incubated at  $4^\circ\text{C}$  in the presence of an aortic vessel.

#### ***3.4.2.2. Influence of silica nanoparticles on vasoconstrictor responses of aortic vessels***

All vessels constricted in high potassium solution (60 mM KCl). There was no significant difference in the level of constriction after the vessels were incubated in  $71\pm 6$  nm SiNPs ( $1.82 \pm 0.19$  g/tension,  $n=5$ ),  $27\pm 7$  nm SiNPs ( $2.70\pm 0.23$  g/tension,  $n=5$ ),  $61\pm 7$  nm SiRBITC NPs ( $2.67 \pm 0.37$  g/tension,  $n=4$ ) or  $31\pm 10$  nm SiRBITC NPs ( $2.35 \pm 0.21$  g/tension,  $n=5$ ) in comparison to PSS alone ( $2.32 \pm 0.26$  g/tension,  $n=4$ ).

The effects of vasoconstrictor response were investigated by observing whether there is a significant difference on constriction levels due to vasodilators and or the NPs. A histogram of the average difference in constriction before and after incubation is illustrated in Figure 3.33 in accordance to ACh traces. There is no significant difference in constriction after the vessels are incubated in PSS alone, SiNPs or SiRBITC NPs, as the p values are greater than 0.05.



### 3.4.2.3. Aortic vessel responses to vasodilation agonists

The dose dependent responses of aortic vessels to vasodilators were first investigated. The endothelium-dependent and independent vasodilation was investigated using ACh and SNP respectively. The repeatability of responses was then investigated by repeating the dose response after 30 minutes incubation in PSS, these represented the control experiments. All vessels dilated to ACh in a dose dependent manner and there was no significant difference in dilation after the incubation period (Figure 3.34). The dose response of ACh for before and after 30 minutes incubation in PSS alone shows it is repeatable.

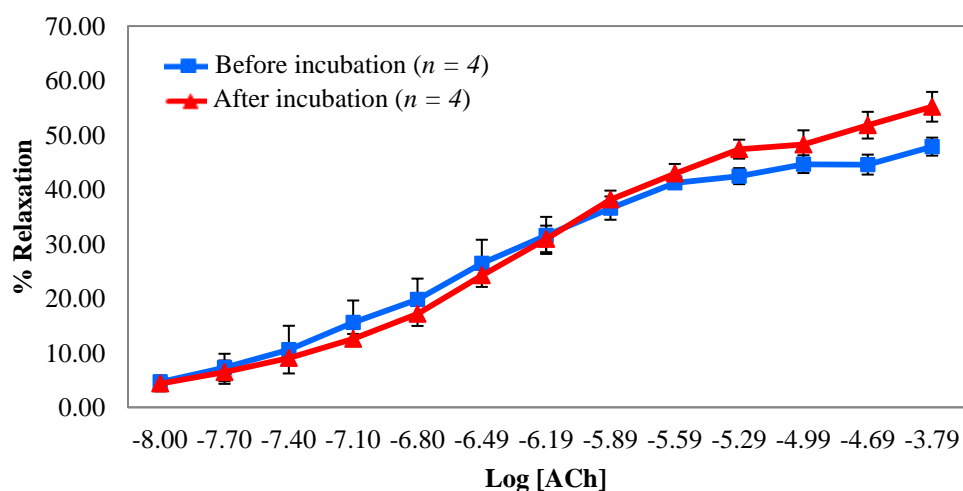


Figure 3.34: The influence on acetylcholine dilator responses of the aortic vessels before and after incubation in physiological salt solution. 'n' is the number of vessels, where  $p > 0.05$  for all the experiments.

All vessels dilated to SNP in a dose dependent manner and there was no significant difference in dilation after the incubation period (Figure 3.35). The dose response of SNP directly donating NO to the smooth muscle cells before and after 30 minute incubation in PSS alone shows it is repeatable.

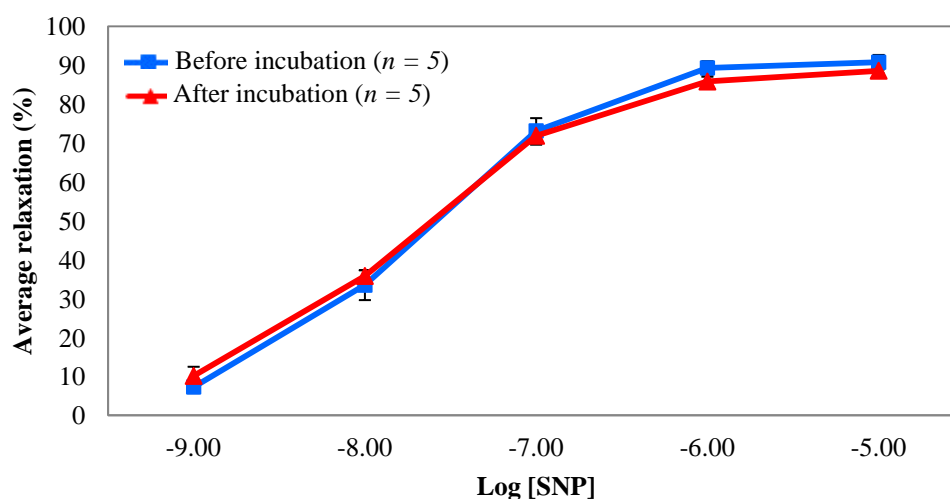
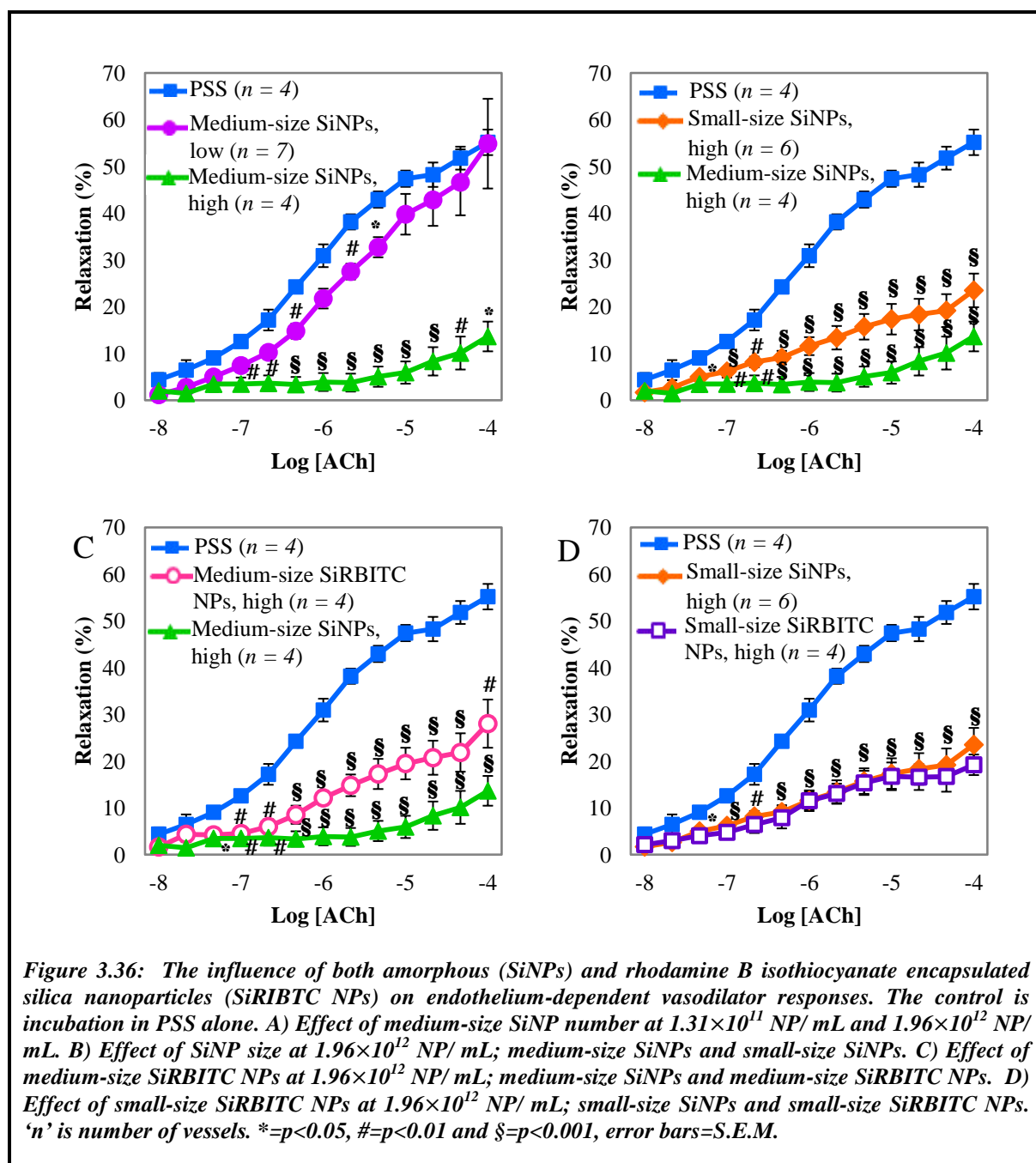


Figure 3.35: The influence on sodium nitroprusside dilator responses of the aortic vessels before and after incubation in physiological salt solution. 'n' is the number of vessels, where  $p > 0.05$  for all the experiments.

### 3.4.2.4. Influence of silica nanoparticles on endothelium-dependent and independent vasodilator responses

All pre-constricted vessels dilated to the endothelial-dependent agonist (ACh) and the endothelial-independent agonist (SNP) in a dose dependent manner. The influence of NP number and size on these dilator responses is shown in Figure 3.36.



### 3.4.2.5. Effect of nanoparticle number on vascular function

Medium-size SiNPs were firstly utilized to examine whether NP number, *per se*, influenced responses. Thus, the effect of medium-size (71±6 nm) SiNPs incubation at  $1.31 \times 10^{11}$  nanoparticle (NP)/ mL and at  $1.96 \times 10^{12}$  NP/ mL were investigated for influence on both endothelium-dependent (ACh) and independent (SNP) vasodilator responses. Generally, there was a slight attenuation in endothelium-dependent dilation after exposure to medium-sized SiNPs at  $1.31 \times 10^{11}$  NP/ mL (47 µg/ mL; at a calculated exposure surface area of  $0.0021 \text{ m}^2$ ; Table 3.2) in comparison to PSS alone.

**TABLE 3.2: Calculated surface area and mass of nanoparticles added to an experiment.**

Nanoparticle type	Total nanoparticle number (NP/ mL)	Surface area/ unit mass ( $\text{m}^2$ )	Total exposure of surface area ( $\text{m}^2$ )	Total mass of NP added ( $\mu\text{g/ mL}$ )
medium-size SiNPs	$1.31 \times 10^{11}$	$1.5837 \times 10^{-14}$	0.0021	47
medium-size SiNPs	$1.96 \times 10^{12}$	$1.5837 \times 10^{-14}$	0.0310	700
small-size SiNPs	$1.96 \times 10^{12}$	$2.2902 \times 10^{-15}$	0.0045	38
medium-size SiRBITC NPs	$1.96 \times 10^{12}$	$1.1690 \times 10^{-14}$	0.0229	443
small-size SiRBITC NPs	$1.96 \times 10^{12}$	$2.8274 \times 10^{-15}$	0.0055	53

However, incubation in higher numbers of medium-size SiNPs ( $1.96 \times 10^{12}$  NP/ mL; 700 µg/ mL;  $0.0310 \text{ m}^2$ ) led to a significant attenuation in dilator responses (Figure 36A). Furthermore, the  $\text{pD}_2$  value after incubation in medium-size SiNPs suggest that sensitivity to ACh is significantly reduced ( $p < 0.01$ ; Table 3.3).

**TABLE 3.3: The half-maximal relaxation to the endothelial-dependent vasodilator (acetylcholine).**

Incubation	$pD_2^a$	$n^b$
PSS	$-6.32 \pm 0.09$	4
Medium-size SiNPs low	$-6.08 \pm 0.18$	7
Medium-size SiNPs high	$-5.03 \pm 0.27$	4
small-size SiNPs high	$-6.15 \pm 0.16$	6
Medium-size SiRBITC NPs high	$-6.03 \pm 0.12$	4
Small-size SiRBITC NPs high	$-6.35 \pm 0.19$	4
Small-size SiNPs (high) + SOD	$-5.53 \pm 0.15$	4
Small-size SiRBITC NPs (high) + SOD	$-6.13 \pm 0.13$	6

<sup>a</sup>  $pD_2$  is the acetylcholine concentration that produces the half-maximal relaxation, expressed as negative logarithm of concentration (mol/L) with mean values  $\pm$  SEM.

<sup>b</sup>  $n$  is the number of vessels.

Vessel incubation in medium-size  $71 \pm 6$  nm SiNPs (at both  $1.31 \times 10^{11}$  NP/ mL and  $1.96 \times 10^{12}$  NP/ mL) had no overall influence on SNP dilator responses at any of the concentrations tested (Figure 3.37; Table 3.2; Table 3.4).

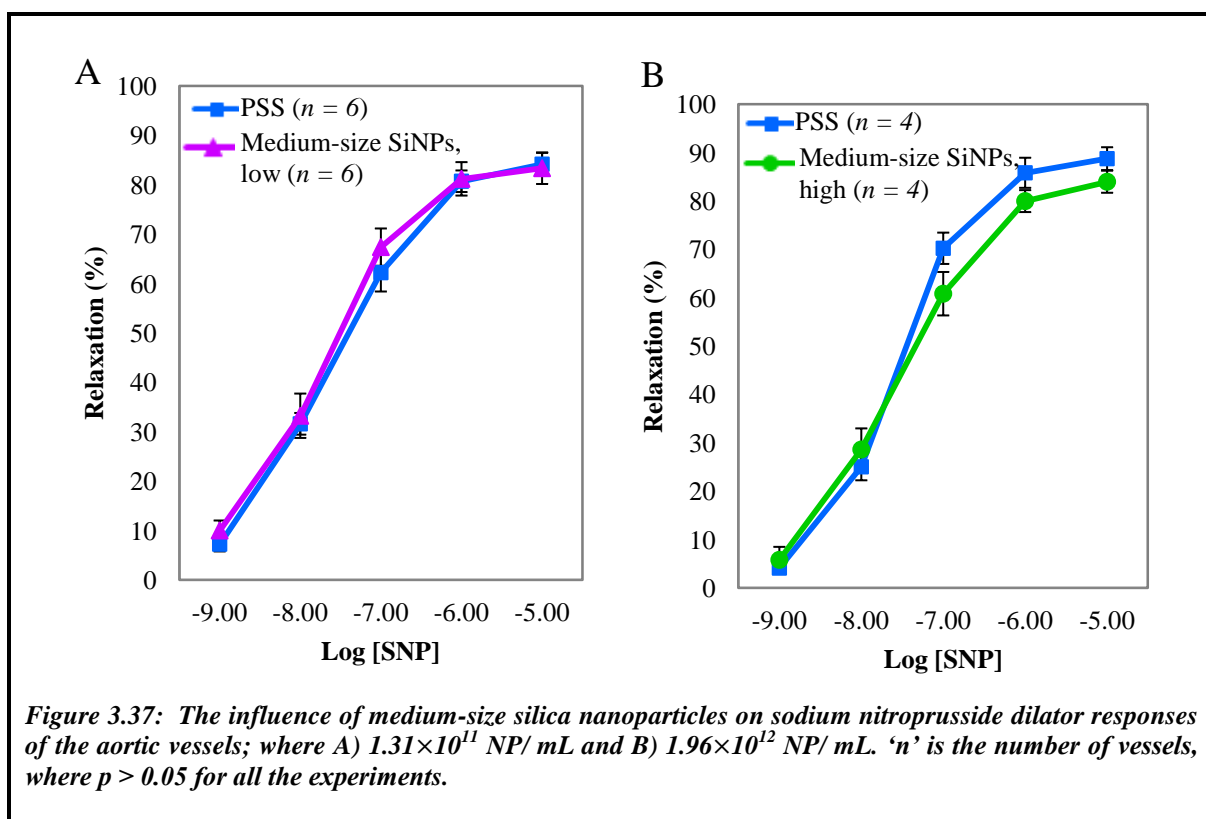


**TABLE 3.4: Half-maximal relaxation of aortic vessels due to the endothelial-independent vasodilator, sodium nitroprusside, before and after incubation with different types of nanoparticles.**

Nanoparticles		$pD_2^a$	$n^b$
Control	<i>Before incubation</i>	-7.73±0.12	4
	<i>After incubation</i>	-7.78±0.05	4
Medium SiNPs low	<i>Before incubation</i>	-7.64±0.06	6
	<i>After incubation</i>	-7.76±0.08	6
Medium SiNPs high	<i>Before incubation</i>	-7.57±0.04	4
	<i>After incubation</i>	-7.58±0.11	4
small SiNPs high	<i>Before incubation</i>	-7.55±0.21	4
	<i>After incubation</i>	-7.57±0.13	4
Medium SiRBITC NPs	<i>Before incubation</i>	-7.36±0.15	4
	<i>After incubation</i>	-7.52±0.18	4
Small SiRBITC NPs	<i>Before incubation</i>	-7.78±0.12	4
	<i>After incubation</i>	-7.85±0.10	4

<sup>a</sup>  $pD_2$  is the acetylcholine concentration that produces the half-maximal relaxation, expressed as negative logarithm of concentration (mol/ L) with mean values ± SEM.

<sup>b</sup>  $n$  is the number of vessels.

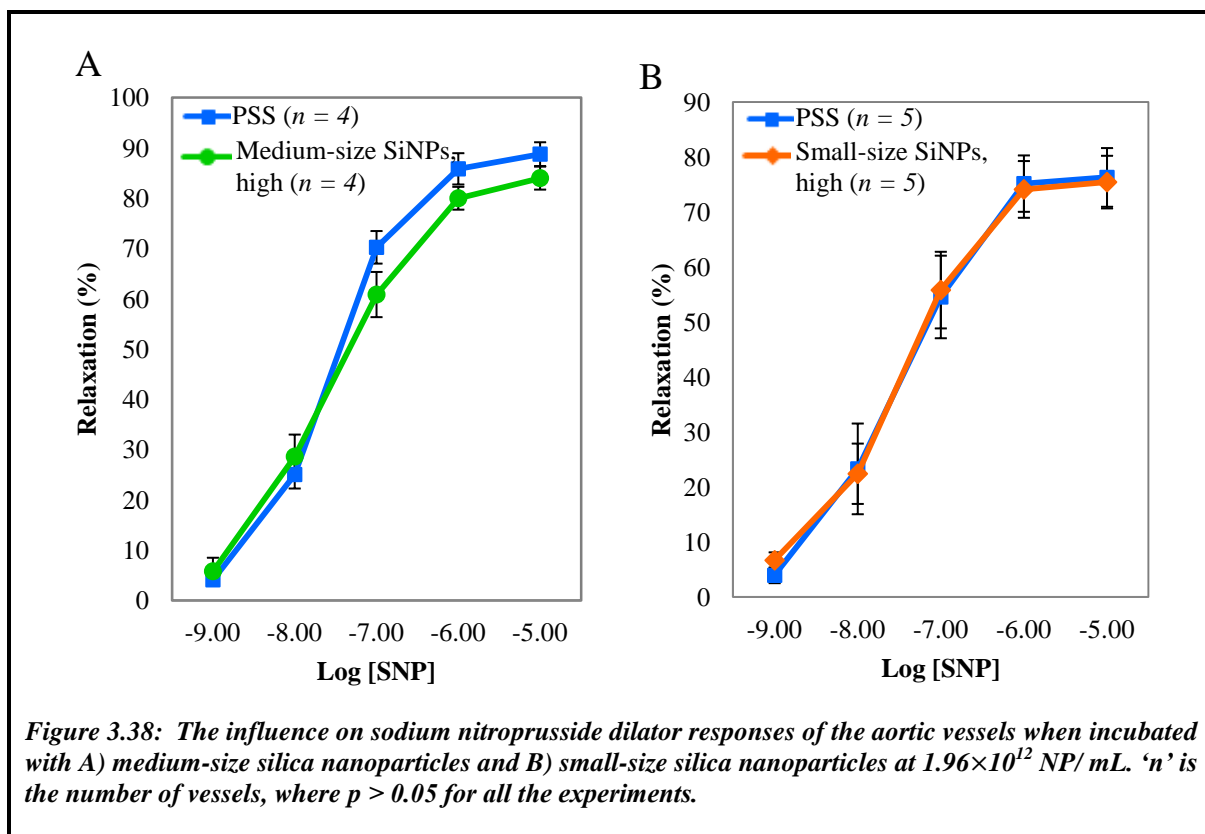
### 3.4.2.6. Effect of nanoparticle size on vascular function

NPs of two size ranges, medium and small-size NPs of 70 nm and 30 nm respectively, at  $1.96 \times 10^{12}$  NP/ mL, were utilised to examine their influence on endothelium-dependent and independent dilator responses.

Incubation in the small-size SiNPs led to a significant reduction in endothelium-dependent dilator responses, while medium-size SiNPs of the same nanoparticle number/ mL led to a further reduction in dilator response (Figure 3.36B). The mass of small-size SiNPs incubated in the vessel was 38 µg/ mL (total exposure surface area=0.0045 m<sup>2</sup>, at  $2.29 \times 10^{15}$  SA/ unit mass) and the medium-size SiNPs mass was 700 µg/ mL for the same number of NPs ( $1.96 \times 10^{12}$  NP/ mL; 0.0310 m<sup>2</sup>, at  $1.58 \times 10^{14}$  SA/ unit mass), suggesting that it is the mass and/or surface area of SiNPs that influences dilator responses, and not the individual NP size (Table 3.2). At the initial two ACh doses ( $1 \times 10^{-5}$  and  $2 \times 10^{-5}$  mM) there was no significant difference in dilation when compared to the control. However, at higher ACh concentration ( $4 \times 10^{-5}$  to  $2 \times 10^{-1}$  mM) there was significant reduction in dilation

( $p < 0.05$ ). Neither the small-size nor medium-size SiNPs altered SNP dilator responses in comparison to the control.

SNP dilator responses were unaltered after vessel incubation in either  $71 \pm 6$  nm SiNPs ( $1.96 \times 10^{12}$  NP/ mL) or  $27 \pm 7$  nm SiNPs ( $1.96 \times 10^{12}$  NP/ mL), at any of the concentrations ( $10^{-6}$  -  $10^{-2}$  mM; Figure 3.38).

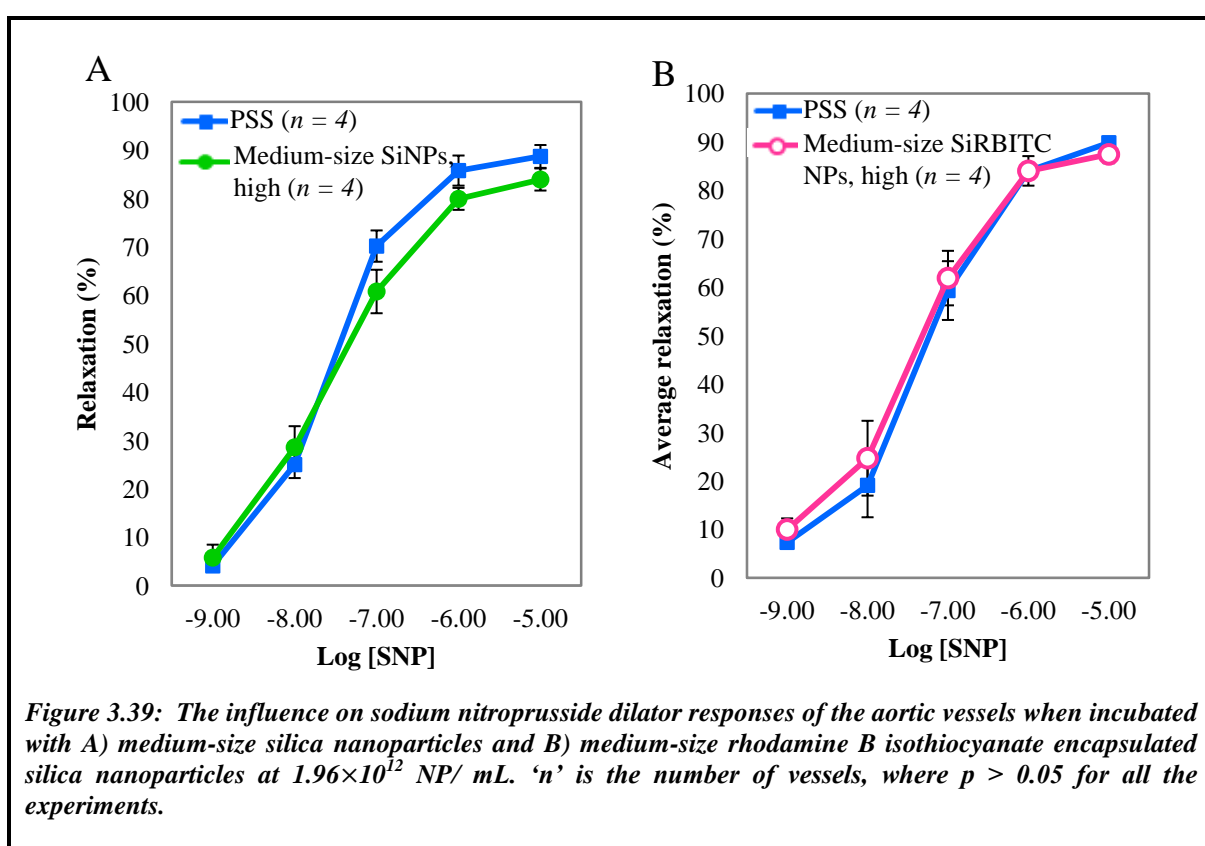


### 3.4.2.7. Effect of dye encapsulated SiNPs on vascular responses

Incubation in the medium-size SiNPs ( $700 \mu\text{g}/\text{mL}$ ;  $0.0310 \text{ m}^2$ ) led to a greater reduction in endothelium-dependent dilator responses than the medium-sized SiRBITC NPs ( $443 \mu\text{g}/\text{mL}$ ;  $0.0229 \text{ m}^2$ ) (Figure 3.36C), further supporting a role for the mass and/or surface area of SiNPs in attenuating dilation. Due to amorphous SiNPs being 10 nm larger than the dye encapsulated SiNPs, this may have led to an additional reduction in ACh vasodilator responses, being significant at higher ACh concentrations ( $4 \times 10^{-5}$  to  $2 \times 10^{-2}$  mM).

SNP dilator responses were unaltered after vessel incubation in either  $71 \pm 6$  nm SiNPs ( $1.96 \times 10^{12}$  NP/ ml) or  $61 \pm 7$  nm SiRBITC NPs ( $1.96 \times 10^{12}$  NP/ ml) at all concentrations tested ( $10^{-6}$  -  $10^{-2}$  mM; Figure 3.39).

Both amorphous SiNPs and dye encapsulated small-size SiRIBTC NPs led to a significant reduction in endothelium-dependent vasodilator response at similar levels in comparison to the control (Figure 3.35D). The small-size SiRIBTC NPs ( $53 \mu\text{g}/\text{mL}$ ;  $0.0055 \text{ m}^2$ ) led to greater reduction in dilation at higher ACh concentrations compared to the small-size SiNPs ( $38 \mu\text{g}/\text{mL}$ ;  $0.0045 \text{ m}^2$ ).



SNP dilator responses were unaltered after vessel incubation in either  $27 \pm 7$  nm SiNPs ( $1.96 \times 10^{12}$  NP/ mL) or  $31 \pm 10$  nm SiRBITC NPs ( $1.96 \times 10^{12}$  NP/ mL), at any of the concentrations tested ( $10^{-6}$  -  $10^{-2}$  mM; Figure 3.40).

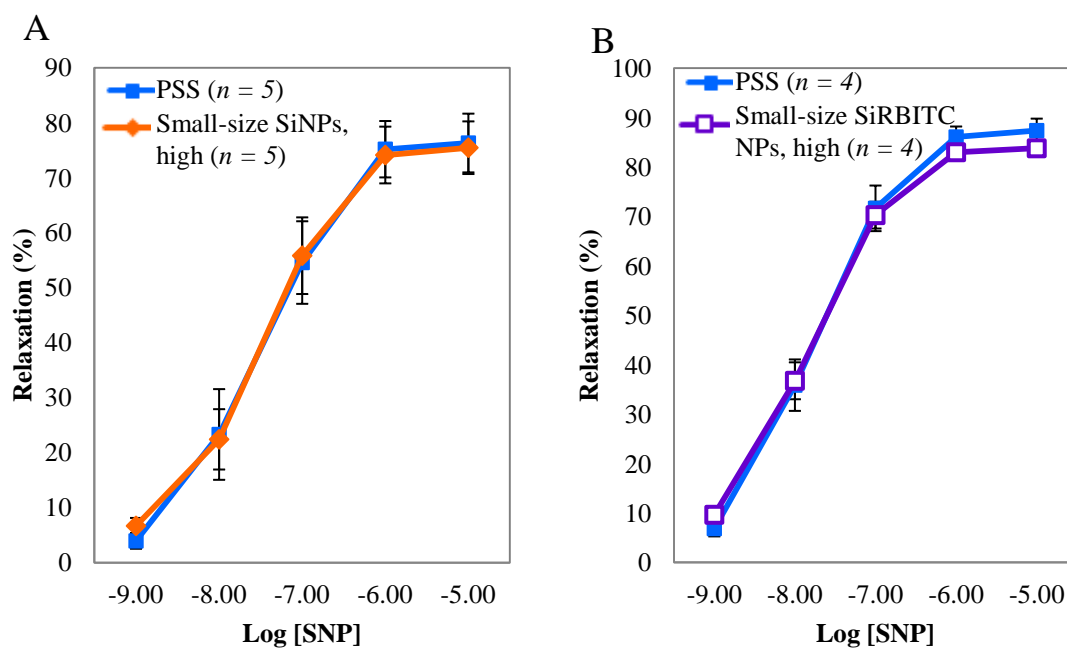
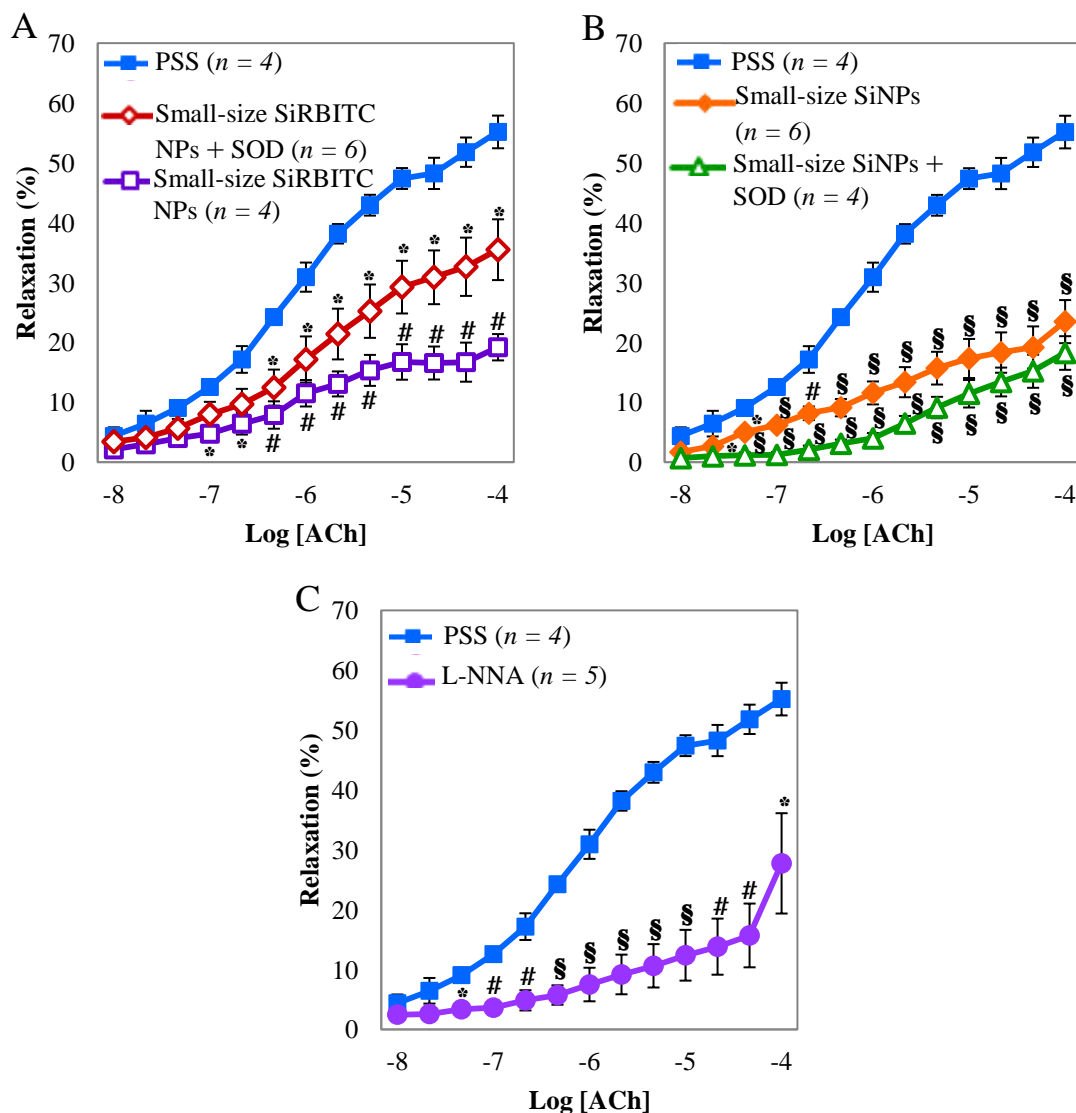


Figure 3.40: The influence on sodium nitroprusside dilator responses of the aortic vessels when incubated with A) small-size silica nanoparticles and B) small-size rhodamine B isothiocyanate encapsulated silica nanoparticles at  $1.96 \times 10^{12}$  NP/ mL. 'n' is the number of vessels, where  $p > 0.05$  for all the experiments.

### 3.4.2.8. Restoration of dilator response using SOD

To examine whether the reduction in vasodilator responses induced by SiRBITC and SiNPs is due to the generation of reactive oxygen species (ROS), vessels were co-incubated with superoxide dismutase (SOD) (300 U/ mL), which reacts with ROS to produce oxygen and hydrogen peroxide. There was a significant improvement in vasodilation when small-size SiRIBTC NPs were co-incubated with SOD (Figure 3.41A). At  $2 \times 10^{-1}$  mM dose concentration of ACh the SOD improved dilation by 16.28 %. The co-incubation of SOD (300 U/ mL) with small-size SiNPs alone did not improve vasodilator responses but caused a further reduction in dilation (Figure 3.41B); being significant at  $2 \times 10^{-5}$  to  $2 \times 10^{-1}$  mM when compared to PSS. Furthermore, the  $pD_2$  value for after incubation in small-size SiNPs co-incubated with SOD suggests that sensitivity to ACh was significantly reduced ( $p < 0.01$ ; Table 3.3).



**Figure 3.41:** The influence on acetylcholine dilator responses after: A) small-size rhodamine B isothiocyanate encapsulated silica nanoparticle co-incubation with superoxide dismutase in comparison to small-size rhodamine B isothiocyanate encapsulated silica nanoparticles alone, or PSS, B) small-size silica nanoparticle co-incubation with superoxide dismutase in comparison to small-size silica nanoparticles alone, or PSS and C)  $N_{\omega}$ -Nitro-L-arginine incubation in PSS alone. ‘n’ is number of vessels. \*= $p < 0.05$ , #= $p < 0.01$  and §= $p < 0.001$ , error bars=S.E.M.

When vessels were pre-incubated in the nitric oxide synthase (NOS) inhibitor  $N_{\omega}$ -Nitro-L-arginine (L-NNA) and the ACh dose response repeated in the continued presence of the inhibitor, dilation was significantly reduced at most concentrations examined (Figure 3.41C). Thus, suggesting that the major dilator component in rat aortic vessels is due to nitric oxide.

Detailed analysis of the data generated, using the linear mixed model, confirmed that incubation in PSS alone led to the greatest degree of relaxation, followed by medium-size SiNPs ( $1.31 \times 10^{11}$  NP/ mL) > small-size SiRBITC NPs+SOD > medium-size SiRBITC NPs > small-size SiNPs > small-size SiRBITC NPs > small-size SiNPs+SOD > medium-size SiNPs.

### **3.4.3. Discussion**

We demonstrate that silica nanoparticles (SiNPs), less than 100 nm size, attenuate endothelial-dependent (ACh), but not endothelial-independent (SNP) dilator responses in isolated viable vessels, *in vitro*. Evidence of nanoparticle uptake is shown by the lining endothelial cells but not by the smooth muscle cells or the adventitial layer. We show that the degree of attenuation is related to the surface area of the nanoparticles, rather than their size, confirming previous nanotoxicological studies using cell cultures [174]. We further demonstrate that the attenuated dilation, due to dye encapsulated silica nanoparticles (SiRIBTC NPs), but not SiNPs, can be partially restored using superoxide dismutase, suggesting that the mechanism of attenuated dilation is different for the SiNPs and SiRIBTC NPs.

The *in vitro* exposure of viable aortic vessels to the  $71 \pm 6$  nm SiNPs, resulted in their rapid uptake into the cytoplasm of endothelial cells. The small-size SiNPs ( $27 \pm 7$  nm) also seemed to accumulate in the cytoplasm of the endothelial cells. No uptake was evident when vessels were exposed to SiNPs at 4 °C, suggesting that uptake is an active process. Endocytosis is a well documented pathway by which NPs are internalised into cells. This includes clathrin-mediated endocytosis, caveolae-mediated endocytosis or clathrin-caveolae and dynamin-independent endocytosis mechanism [175]. Our TEM findings suggest that the mechanism of uptake of small-size SiNPs may be different from that of the medium-size NPs. Indeed, one recent study (using A549 cell line) suggests that at any one time, cells can use multiple pathways simultaneously, depending on the surface chemistry of the NPs [176].

The NPs were fabricated and carefully characterised within our laboratories. The zeta potential values demonstrate that the NPs were stable in both water and PSS. In the case of SiRIBTC NPs the zeta potential in water was more negative than the non dye encapsulated

SiNPs. When suspended in PSS, attraction of salt ions led to reduced negativity. Such charge attraction may have led to modification of the surface chemistry of the SiRIBTC NPs, in comparison to the SiNPs. Consequently, this may have affected the mechanism of uptake into the endothelial cells, with less SiRIBTC NPs being taken up overall. The hydrodynamic diameter of our fabricated NPs is approximately 20 nm above the actual size measured from the TEM images. Generally, the zeta potentials for amorphous SiNPs and SiRBITC NPs confirm they are stable in both water and PSS. When the NP suspensions ( $1.64 \times 10^{12}$  NP/ mL) were placed in PSS the potential slightly decreased, as compared to a suspension in water, due to their presence in high ionic solution (PSS), as follows: briefly, when these NPs are in water, the counter ions (water molecules) surround the particle's surface and produce a structured hydration layer, known as the Stern layer. Other counter-ions that are not directly bound to the particle surface are still attracted to the negative particle, even though there is repulsion from the 'Stern layer' as well as other counter-ions attracted towards the particle, known as the diffuse layer. The electrical potential at the point where the Stern layer meets the diffused layer is known as the zeta potential. However, the introduction of ions into the solution (PSS) not only reduced the amount of water molecules but resulted in competition between the ions and silica surface for the water molecules. This leads to a less structured hydration layer as the positively charged salt counter-ions and water molecules surround the NP, causing the short-range repulsive forces to reduce, thus lowering the zeta potential [35, 52]. The smaller SiNPs demonstrate non-DLVO behaviour with additional forces present. It has been proposed that there is short range repulsion from a hairy layer present on the surface of small-size SiNPs. The layer is thought to consist of covalently bonded polymeric chains of silicic acid protruding from the surface [52].

Aortic vessels were incubated in nanoparticles at  $1.31 \times 10^{11}$  NP/ mL and also at a higher concentration of  $1.96 \times 10^{12}$  NP/ mL, over a 30 minute acute exposure time period. This exposure time and concentration is representative of that utilised in pre-clinical trials. For example, Michalak *et al.* [177] estimated the circulation half life of near-infrared nanoparticles in mice to be between 3-43 minutes at an estimated relative concentration of  $4.98 \times 10^9$  NP/ mL in the blood of these mice. Although there is little information available on the number of nanoparticles expected in the blood during *in vivo* imaging, however, the study by Casciaro *et al.* [177] has provided some insight into the ideal

nanoparticle number that is necessary for successful imaging diagnostics. They investigated the acoustic behaviour of silica nanoparticles for diagnostic ultrasound identification, using a range of nanoparticles sizes (160, 330, 660 nm) and concentrations ( $10^{10} - 10^{13}$  NP/ mL). They determined that the use of 330 nm silica nanoparticles at  $1-2 \times 10^{11}$  NP/ mL were ideal for ultrasound imaging at conventional diagnostic frequencies [178].

Our findings suggest that the degree of attenuated dilation by the NPs is based on dosimetry, as the greater the number of NPs (and /or mass) the lower % relaxation of the vessels. For instance, there is a small attenuation in dilation for the medium-size SiNPs at  $1.31 \times 10^{11}$  NP/ mL ( $47 \mu\text{g/ mL}$ ;  $0.0021 \text{ m}^2$ ) while at a higher dose ( $1.96 \times 10^{12}$  NP/ mL;  $700 \mu\text{g/ mL}$ ;  $0.0310 \text{ m}^2$ ) of the same SiNPs led to a greater significant attenuation in vasodilation. Similarly, Lin *et al.* [179] have shown that a reduction in cell viability by SiNPs was both time and dose-dependent, in bronchoalveolar carcinoma-derived cells. Furthermore, when NP number were kept constant ( $1.96 \times 10^{12}$  NP/ mL), we observed that the medium-size NP ( $700 \mu\text{g/ mL}$ ;  $0.0310 \text{ m}^2$ ) had a greater attenuation effect than the small-size NPs ( $38 \mu\text{g/ mL}$ ;  $0.0045 \text{ m}^2$ ). As the mass and surface area of the medium-size SiNPs is greater compared to that of the small-size SiNPs, it suggests that both components may play an important role. The mass of small-size SiNPs ( $1.96 \times 10^{12}$  NP/ mL;  $38 \mu\text{g/ mL}$ ;  $0.0045 \text{ m}^2$ ) is lower compared to medium-size SiNPs at  $1.31 \times 10^{11}$  NP/ mL ( $47 \mu\text{g/ mL}$ ;  $0.0021 \text{ m}^2$ ); however, the small-size SiNPs have a greater attenuation effect on vasodilation, suggesting that the vital component reducing vasodilation is surface area and not mass *per se*. Previous studies have confirmed the production of ROS by amorphous SiNPs [171, 179-181]. Lin *et al.* [179] synthesised amorphous SiNPs (15 nm) which lead to the generation of ROS (hydroxyl radicals) in cultured human bronchoalveolar carcinoma-derived cells. Bhattachjee *et al.* [166] further suggest the possibility of NPs interacting with organelles, in particular the mitochondria, which lead to the production of ROS. These ROS may lead to oxidative stress in cells and possibly cell death. The mechanism of attenuated endothelial-dependent dilation by the SiNPs may thus relate to the generation of ROS at the surface of the NPs. Hence, a greater surface area/ unit mass, can lead to greater exposure of the cell to reactive oxygen species (ROS), such as hydroxyl radicals ( $\cdot\text{OH}$ ) and superoxide anions, which are able to quench NO.

The degree of attenuated endothelial-dependent vasodilation is similar for both dye encapsulated (SiRIBTC NPs) and non-dye encapsulated small-size SiNPs. The TEM images for the small-size SiNPs shows a large accumulation of NPs at the surface of the endothelial layer within caveolae structures along the cell membrane. This could lead to disruption of the caveoli and alter activity of the eNOS enzyme which is normally coupled to caveolae proteins. This may be one mechanism of attenuated dilation due to non-dye encapsulated SiNP since SOD co-incubation, did not improve dilation. In comparison, lower levels of NP uptake were observed by TEM, for the small-size SiRIBTC NPs than the SiNPs. Despite reduced uptake of the SiRIBTC NPs, the attenuation in dilation is at a similar level for both small-size SiRIBTC NPs and SiNPs, suggesting that there may be more than one factor affecting dilation of vessels incubated in the small-size SiRIBTC NPs. Numerous gases are known to quench the fluorescence of a number of fluorophores, including rhodamine. Indeed, a number of fluorescent probes have been developed that can detect NO in cellular systems, based on the principle of fluorescence quenching [181], where rhodamine chromophore has been shown to enable detection of NO release (as low as 7nM) from bovine aortic endothelial cells, *in vitro* [183]. We have demonstrated that the major component of the dilator response in aortic vessels is due to NO release (L-NNA inhibition studies), supporting previous studies [184, 185]. Consequently, incubating vessels in SiRIBTC NPs will have contributed to the reduced ACh-induced dilator responses. When vessels were co-incubated in SiRIBTC NPs and SOD, it was possible to partially restore the dilator responses, suggesting that indeed, leakage of the dye itself may quench NO. The cellular components are protected by SOD by preventing them being oxidized by ROS. However, as the dye molecules are covalently bonded to silica matrix it is more probable that the dye molecules were quenched by NO diffusing through the silica-shell, thus affecting dilation. In the case of non-dye encapsulated SiNPs, when SOD was co-incubated with SiNPs, it did not contribute to restoring dilation, as it had for SiRIBTC NPs, but it led to a further attenuation in relaxation. This may be explained by the fact that dismutation of small amounts of ROS to hydrogen peroxide, can have a small added constrictor effect on aortic vessels [186].

#### **3.4.4. Conclusions**

In conclusion, we show that uptake of silica nanoparticles of less than 100 nm in diameter can attenuate endothelial-dependent but not endothelial-independent vasodilator function

in rat aortic vessels, depending on their surface area/ unit mass. We further show that dye doping of the SiNPs, can further influence the dilator response. Our findings have implications for the future fabrication of biocompatible silica nanoparticles for use in medical therapeutics and imaging diagnostics.

### **3.5. Pressurised System for the Aortic Vessel**

Small isolated vessels under near physiological conditions may be examined using pharmacological or physiological stimuli using a pressure or perfusion myograph system. In these systems, as with the aortic vessels, the small vessels are dissected in order to remove the perivascular adipose and connective tissue surrounding the vessels. The vessel is then mounted by placing each end of the vessel through a cannula and securing it in position by tying knots at each end. The small arteries are then intravascularly pressurised to 60 mmHg [185]. Previously, such systems have been used to assess the effect of various substances including ouabain upon cerebral arteries [187]. For the organ-bath aortic vessel experiment the vessel is not pressurised and in order to mimic physiological conditions more accurately it is important for the vessels to be pressurised. Furthermore, the present study will demonstrate attempts to pressurise aortic vessels for the delivery of nanoparticles and examine its influence on structure and function.

#### **3.5.1. Experimentation**

The heart attached to the aortic vessel from a male Wistar rat was placed in an ice-cold petri dish containing oxygenated physiological salt solution in order to maintain the tissue in a viable state. The perivascular adipose tissue surrounding the vessels (4 mm length) was removed. In order to produce a pressurised system a delicate surgical procedure was required where the endothelial cell integrity was maintained. Initially, aortic vessel arch (directly connected to the heart) was dissected to allow a glass pipette to be inserted followed by tying a knot to secure it in position. The other end of the pipette was attached to a pressurised system containing mercury. The other end of the vessel was securely attached to a needle with a knot; the needle contained  $71 \pm 6$  nm silica nanoparticles (SiNPs) ( $1.31 \times 10^{11}$  nanoparticle (NP)/ mL) (Figure 3.42). Upon injection of the SiNPs (1.5 mL) the pressure rose to 60 mmHg and was maintained at that pressure for three minutes. Once the intravascular incubation period had completed a 4 mm length fragment was dissected and placed in the organ bath system containing physiological salt solution at 37 °C. The aortic ring was then mounted between two fine steel wires and passively stretched to 2 gram tension. After a one hour calibration the smooth muscle cell integrity was tested with high potassium salt solution followed by an endothelium-dependent vasodilation dose response using acetylcholine.

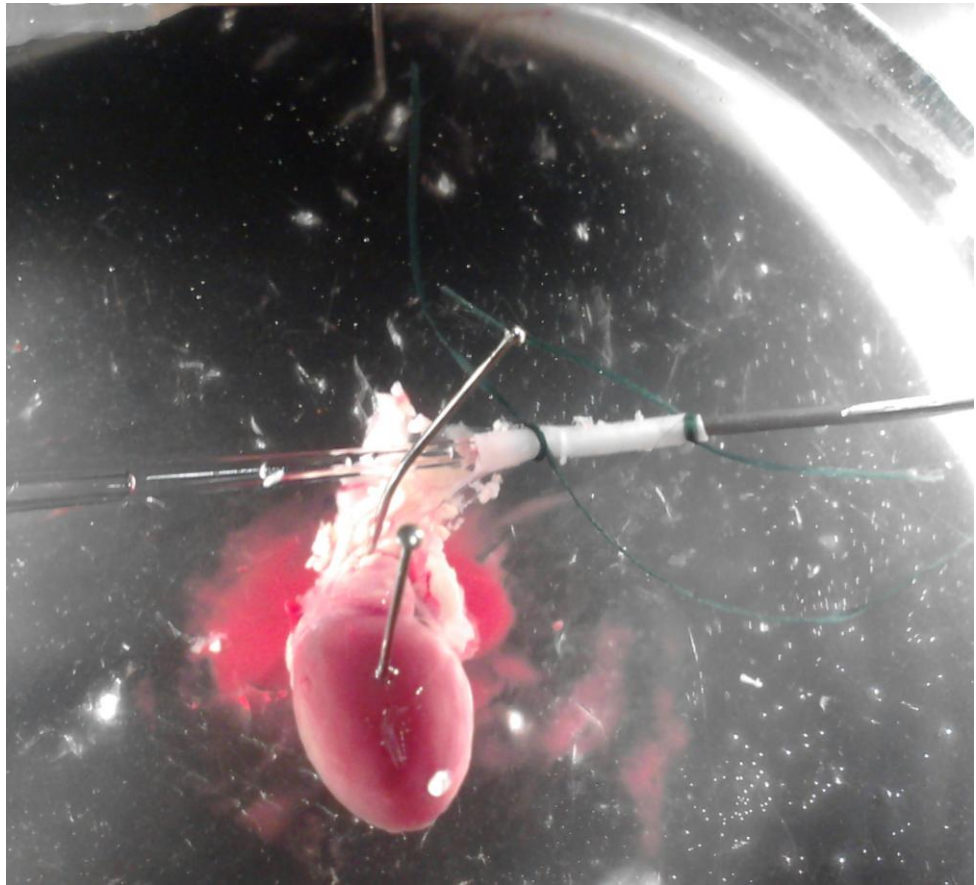
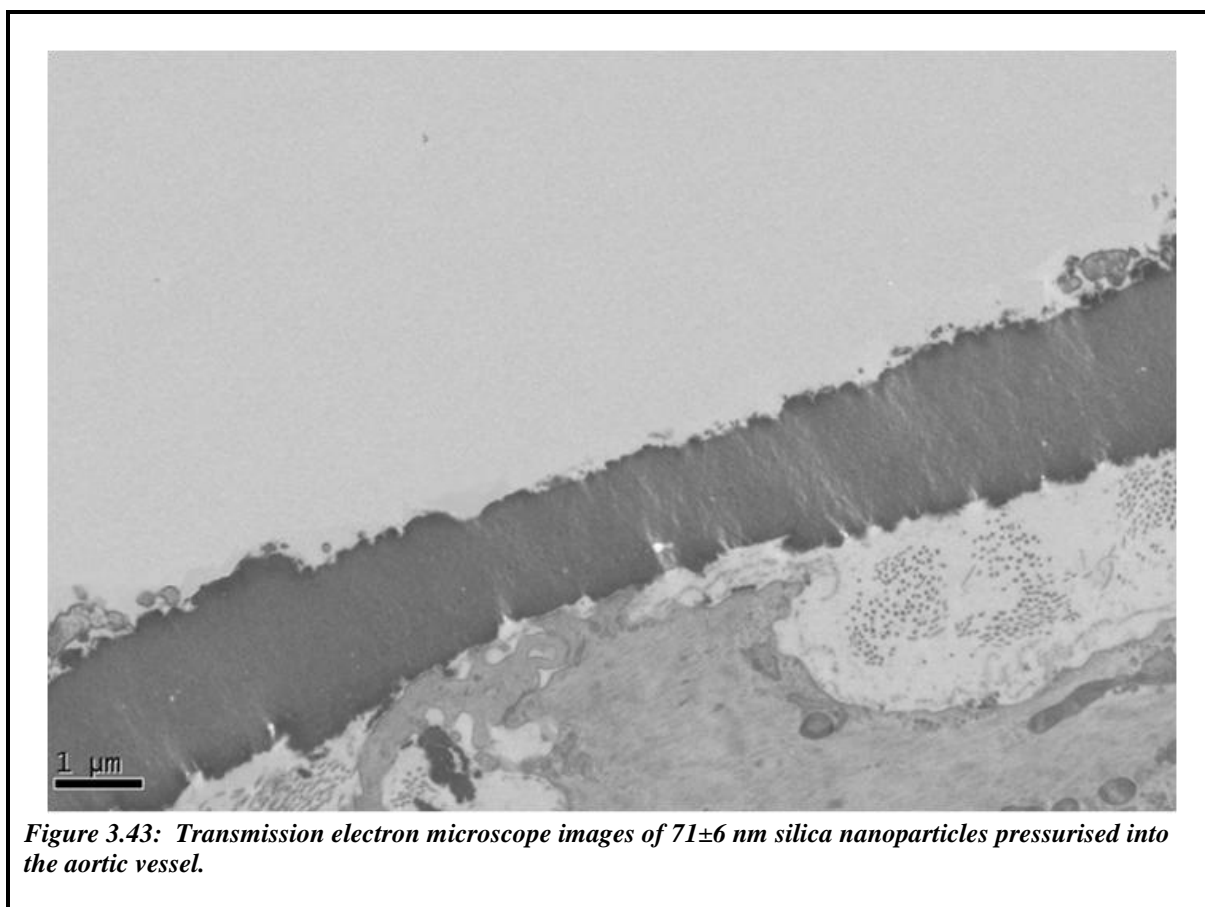


*Figure 3.42: Image of the pressurised system set-up for the large aortic vessels.*

### 3.5.2. Results

#### 3.5.2.1. *Detection of silica nanoparticles within vascular tissue*

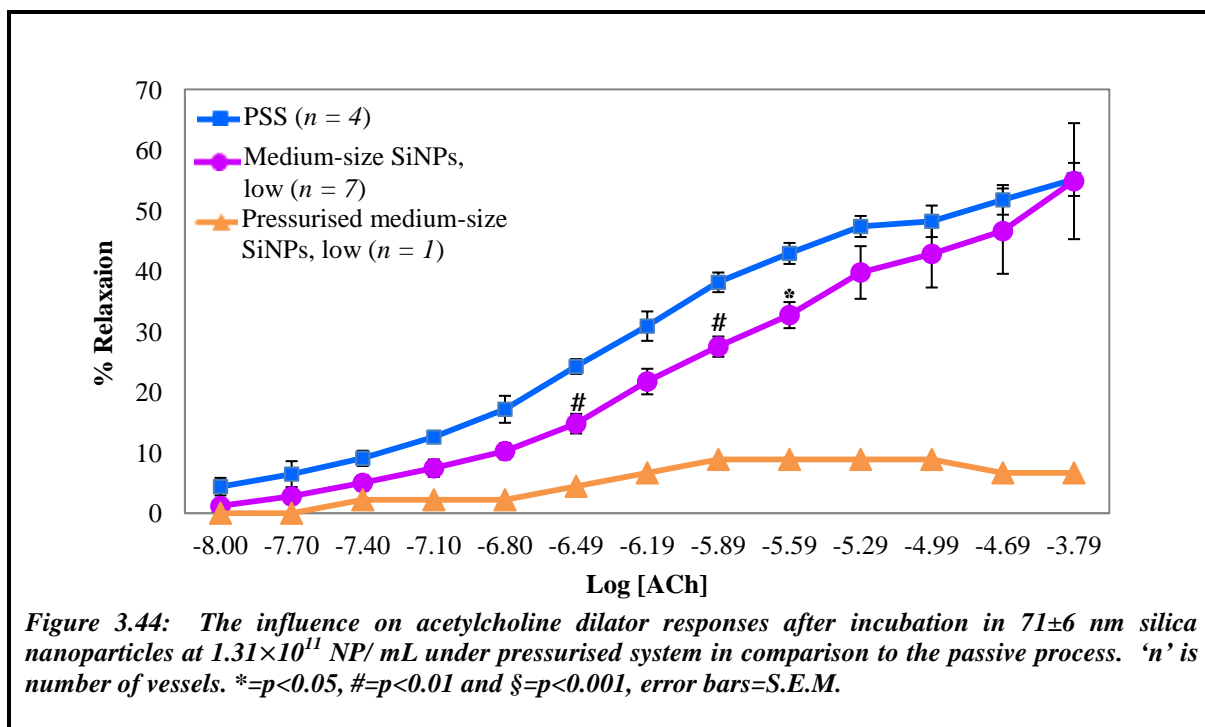
The exposure of isolated viable aortic vessel to medium-size silica nanoparticles under a pressurised system has led to the endothelial cells being sloughed (Figure 3.43). Therefore, it was not possible to examine the nanoparticle uptake by the cells. There was no evidence of nanoparticle uptake by the underlying smooth muscle cells.



#### 3.5.2.2. *Influence of silica nanoparticles on endothelium-dependent vasodilator responses*

All vessels were pre-constricted with potassium physiological salt solution (KPSS) and the influences of the pressurised system were compared to the passive process by examining the uptake of medium-size silica nanoparticles. Previously shown (Chapter 3, Section 3.4), a greater initialisation of silica nanoparticles within endothelial cells attenuated endothelial-dependent dilation. Thus, the affect of medium-size ( $71\pm 6$  nm) SiNPs

incubation at  $1.31 \times 10^{11}$  NP/ mL under a passive process were investigated in comparison to the pressurised system for influence on endothelium-dependent (ACh) vasodilator responses (Figure 3.44).



### 3.5.3. Discussion

This study investigated the influence of pressure on increased initialisation of nanoparticles within large isolated aortic vessels. The endothelium-dependent vasodilation was analysed using acetylcholine (ACh) on constricted vessels with high potassium salt solution (KPSS). Initially, the repeatability of the dose responses after the incubation period in PSS was investigated, which was used as the control. The dose responses of ACh agonist on the control vessels are repeatable after an incubation period of thirty minutes. The influence of  $71 \pm 6$  nm silica nanoparticle uptake at  $1.31 \times 10^{11}$  NP/ mL via the non-pressurised organ bath system was compared to the vessels that were initially pressurised during the intravascular injection procedure. The pressurised system led to a greater attenuation of vasodilation compared to the conventional uptake of nanoparticle in the organ bath system. However, the electron microscopy image indicates that the attenuation in vasodilation was due to the damaged endothelial cell, which may be due to the pipette when attaching the vessel. Therefore, a more controlled pressurised system whereby the pipette is controlled

by small increment mechanical movement should remove any damage caused to the endothelial layer.

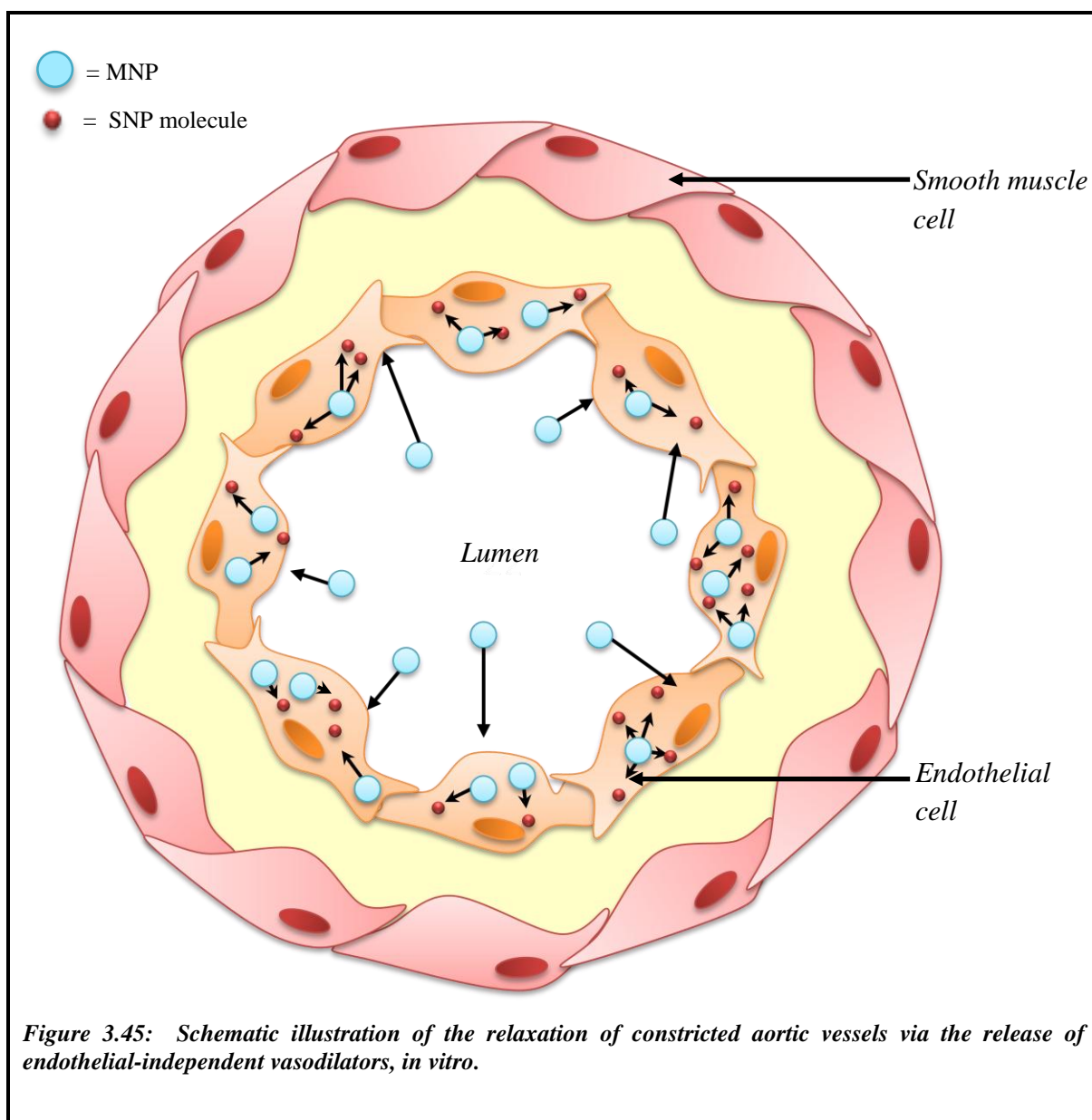
Pressure myography systems are commonly used for the study of structure and function of small vessels, in particularly for studying hypertension [188].

### **3.5.4. Conclusions**

This study represents an attempt to investigate the influence of pressure on nanoparticle uptake by aortic vessels. The system produced was capable of pressuring the vessels at 60 mmHg; however modification of the system would be necessary system where the pipettes is held in place.

### 3.6. Drug Release Study of Mesoporous Nanoparticles

The illustration below is a schematic representation of the drug release within isolated viable vessels (Figure 3.45). The mesoporous nanoparticles are initialised within the endothelial cells while sodium nitroprusside (SNP) is released into the cell.



The easy design of smart nanocarriers makes them valuable vehicles for drug delivery systems. In particular, mesoporous nanoparticles (MNP) have large surface area, ordered mesoporous structures along with their physical and chemical properties. The potential advantages of these nanocarriers within medicinal applications have given rise to the exploitation of these materials in nanotechnology. The surface functionalisation of the MNP (host) in addition to the introduction of guest molecules within these pores such as protein biomolecules or drugs allows for targeted therapy of intracellular areas [189]. The large surface area results in high pore volume and consequently allowing for uptake of large quantities of biomolecules [81]. Furthermore, unlike quantum dots and carbon nanotubes that are known to have cytotoxicological effects, MNP are well documented for their potential advantageous influence on both the environment and human health [186]. The pore size may be tuned depending on the size of the guest molecule by selecting a specific template. Previous studies have used host (such as MCM-41 and SBA-15) and guest (such as drug, enzymes, DNA and luminescent [190]) molecules to produce effective systems in which the host-guest interaction plays a vital role in their application [190]. The pore size influences the accessibility of the guest molecules adsorbed within the pores of the host material. The larger the pore size the larger the adsorption of guest molecules in the pores. However, if the interaction between the host and the guest molecules is weak, this can lead to the rapid leaching of the guest molecules [190].

Monodisperse mesoporous silica nanoparticles with diameters around 100 nm can be fabricated using colloidal methods. Regular pore structure is produced during synthesis by incorporation of surfactant molecules which self assemble into ordered arrays [191]. Once the structure is produced the surfactant template is removed by calcining or dissolution. The remaining nanoparticles comprise of an ordered silica framework with defined regular nanochannels that are aligned parallel to each other, resulting in a very high surface to volume ratio. The chain length of the surfactant molecule used as a template directs the size of the pore produced therefore careful choice allows control of particle porosity. Typical surface area measurements are around 1000 m<sup>2</sup> per gram with narrow pore size distribution that is controllable between sizes of 2-15 nm diameters [9, 192, 193]. The pore size can be tailored to allow accommodation of drug molecules of various sizes [191]. Mesoporous silica offers a mechanism for controlling the rate and period of drug delivery. The ordered pore network allows fine control of the drug loading and release kinetics,

while the large surface area afforded by the pore assemblies allows adsorption of the required dosage of drug [191]. Furthermore, there are two surfaces available for modification, the internal pore surface and the external surface of the nanoparticle. The internal surface is usually utilized for harbouring the drug, while the external surface is functionalised to direct the nanoparticles to the area for release and drug action. Once the nanoparticles have been drug loaded, the release is governed by constrained pore diffusion [9]. The drug release into cells is influenced by structural characteristics, specifically the confined diffusion of the drug to the pore entrance [126]. The diffusion rate is governed by the size of the pores and it is this property that makes this material ideally suited for allowing controlled sustained drug release. Release kinetics has been demonstrated from mesoporous silica using luminescent molecules and ibuprofen as a model drug [126, 9, 194-196]. One study showed that 80 % of ibuprofen was released after only 50 minutes from mesoporous silica with pore size 3.4nm and particle diameter of 50 microns [197]. Another study demonstrated that it took 31 hours for the release of 60 % of ibuprofen loaded into mesoporous silica (diameter 950 nm and pore size 2.5 nm) in a solution with composition similar to human body plasma. The ibuprofen loaded particles were developed for oral administration and so the release in simulated gastric fluid and simulated intestinal fluid was investigated which showed the release rate was increased to 60 % released after 11 hours [198]. It has been shown that the dynamic release rate is dependent on pore size with a more controlled sustained delivery from mesoporous silica with small pore size for up to 60 hours.

Controlled release of sodium nitroprusside from mesoporous silica nanoparticles is a promising avenue leading to the development of therapeutic intervention for treatments of diseases such as hypertension. The versatility of nanoparticles allows them to be utilised as drug loading vehicles. There are various procedures by which drugs may be attached within the nanoparticle matrix, for instance encapsulation, surface attachment or entrapment [199].

### 3.6.1. Diffusion of drug release

The release of a drug from the mesoporous matrix is influenced by factors such as the pore architecture, pore diameter, drug to pore wall interaction (s) and the physical state of the drug. The qualitative and/ or quantitative changes of the drug may not only result in changes to the release rate but also affect the *in vitro* and *in vivo* biological systems, thus this has led to the development of numerous kinetic models describing the drug release, referred to as the drug release profile. These kinetic models include the i) zero order rate where drug release is independent of the concentration of drug used, ii) first order rate where drug release is dependent of the concentration of drug used, iii) Higuchi model describes the drug release from an insoluble material, such as mesoporous silica nanoparticles, as the square root of time based on the Fickian diffusion and iv) Hixson-Crowl cube root law is for profiles where the drug release occurs by the matrix encapsulating or holding the drug changes in surface area [199].

Commonly, the release of drugs from mesoporous nanoparticles follows Fick's first law of diffusion [200], which postulates the movement of diffusive flux from high concentration gradient to low concentration gradient at a steady state.

### 3.6.2. Sodium nitroprusside

Sodium nitroprusside ( $\text{Na}_2[\text{Fe}(\text{CN})_5(\text{NO})] \cdot 2\text{H}_2\text{O}$ ) is also known by the chemical name of disodium pentacyanonitrosylferrate consists of a central transition metal in an octahedral arrangement. Its crystalline structure is orthorhombic with  $D_{2h}^{12}$ - $Pnmm$  space group. Through the extensive investigation of SNP using X-ray diffraction by Manoharan *et al.* [201] it was established that SNP has a cell constant of  $a = 6.17 \pm 0.03$ ,  $b = 11.84 \pm 0.06$  and  $c = 15.43 \pm 0.08$  Å. SNP molecules are capable to enter microporous channels due to their size, and thus will be able to enter the mesopores.

In this present study, we report the release profile of endothelium-independent vasodilator sodium nitroprusside (SNP). Follow, by the determination of the dynamics of drug-loading silica MNP on isolated live blood vessels *in vitro*.

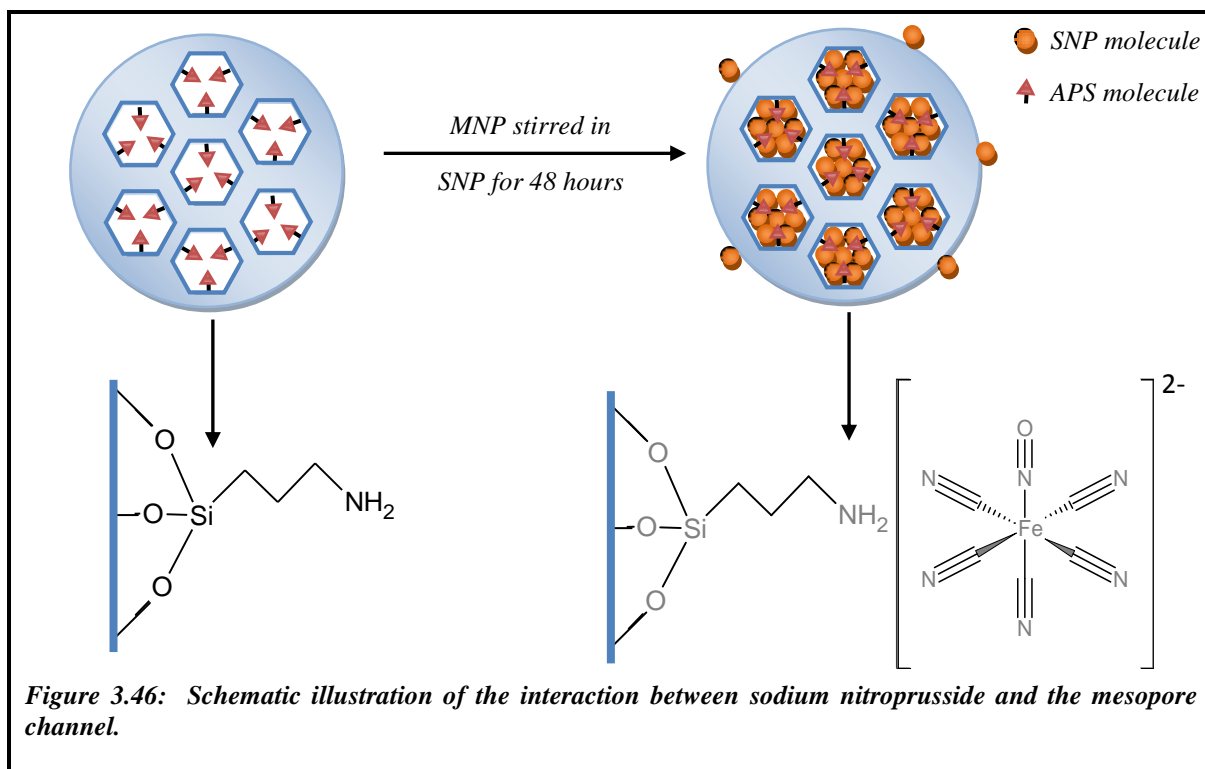
### **3.6.3. Experimentation**

#### ***3.6.3.1. Materials***

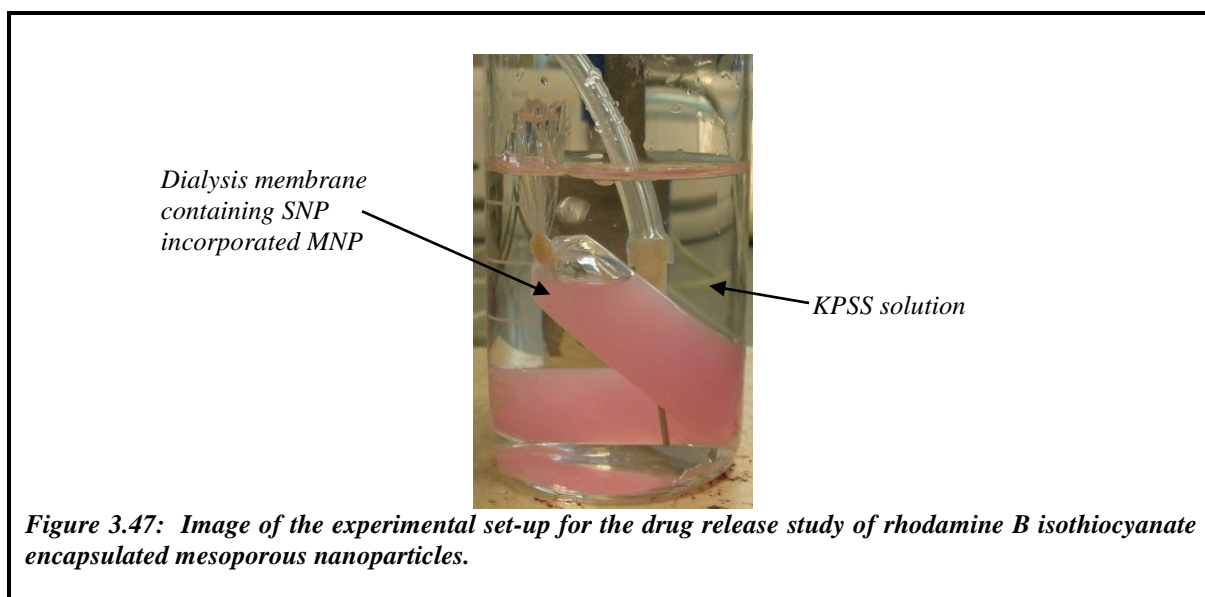
Mesoporous nanoparticles (MNP), rhodamine B isothiocyanate (RBITC) MNP, fluorescein isothiocyanate (FITC) MNP and RBITC/ FITC MNP were prepared in our laboratories (Chapter 2, Section 2.4). Salt solutions were prepared using sodium chloride (NaCl), potassium chloride (KCl), magnesium sulphate heptahydrate ( $\text{MgSO}_4 \cdot 7\text{H}_2\text{O}$ ), potassium phosphate monobasic ( $\text{KH}_2\text{PO}_4$ ), calcium chloride ( $\text{CaCl}_2 \cdot 2\text{H}_2\text{O}$ ), ethylenediaminetetraacetic acid dipotassium salt dihydrate ( $\text{K}_2\text{EDTA} \cdot 2\text{H}_2\text{O}$ ) purchased from Fisher-Scientific (UK). Sodium nitroprusside (SNP) was purchased from Sigma-Aldrich (UK). Millipore water was used for all experiments.

#### ***3.6.3.2. Release profile of sodium nitroprusside from mesoporous nanoparticles***

The drug of interest for our biological application was sodium nitroprusside (SNP). For the release profile, the drug was loaded into the mesopores by dispersing the 392 mg RBITC MNP in 25 mL of sodium nitroprusside (SNP) solution ( $1 \times 10^{-5}$  M). The mixture was stirred for 48 hours at room temperature (Figure 3.46).



The MNP-SNP solution was centrifuged at 6000 rpm for 40 minutes. The supernatant was collected and the concentration of SNP within the supernatant was measured with atomic absorption spectroscopy (AAS). The MNP-SNP pellet was dispersed in 5 mL of water and placed in dialysis tubing, as shown in Figure 3.47. The resulting dialysis membrane was placed in a beaker containing KPSS (375 mL). The solution was heated to 37 °C in order to mimic the release of SNP while in the organ bath system.



The release of SNP was examined by taking 1 mL aliquots of the solution contained within the beaker and replacing the solution with 1 mL of KPSS at regular intervals. This process was repeated for FITC MNP, RBITC/ FITC MNP and MNP. Furthermore, the release profile for different concentrations of SNP loaded within the MNP was also analysed (summarised in Table 3.5).

**Table 3.5: Summary of the reactant concentration used for the release profile.**

SNP concentration used for loading (M)	Mass of NP used for release profile (mg)				Volume of KPSS in beaker (ml)
	MNP	RBITC MNP	FITC MNP	RBITC/ FITC MNP	
$1 \times 10^{-5}$	392	392	392	392	375
$1 \times 10^{-3}$	250	300	250	250	100

The concentration of SNP within the aliquots was quantified with AAS. Initially, the method was validated by ascertained linearity of standard curves; five standard curves of known concentrations (100, 200, 400, 600, 800, 1000 ppm) of SNP in high physiological salt solutions were calibrated. The stability of the auto-sampler was established with three replicates of each sample. For the release study of the more concentrated SNP adsorption a more concentrated calibration graph was ascertained (500, 1000, 1500, 2000, 2500, 5000 ppm).

Initially, the parameters for optimal drug loading, release and decomposition under simulated biological conditions were determined. Followed by the determination of the dynamics of drug-loading MNP on isolated live blood vessels *in vitro*. Two parameters were used to calculate the efficiency of the drug loaded within MNP; the drug encapsulation efficiency (DLE; Equation 3.5) and drug loading capacity (DLC; Equation 3.6) [199].

### **3.6.3.2.1. Drug loading efficiency**

The MNP drug loading efficiency was determined with atomic absorption spectroscopy. MNP at low ( $1.31 \times 10^{11}$  NP/ mL) and high ( $1.96 \times 10^{12}$  NP/ mL) concentrations were dispersed in 2 mL of known concentrations of SNP ( $1 \times 10^{-5}$  M) and stirred for 48 hours. The mixtures were centrifuged and the concentration of SNP within the supernatant was measured using atomic absorption spectroscopy in order to determine the maximal loading

capacity of the MNP. The percentage of drug loading efficiency at each known SNP concentration was calculated as the ratio difference between the total drug concentration from the drug concentration within the supernatant over the total drug concentration.

$$\text{Encapsulation efficiency (\%)} = \frac{[\text{total drug}] - [\text{free drug}]}{[\text{total drug}]} \times 100 \quad (3.5)$$

#### **3.6.3.2.2. Drug loading capacity**

The drug loading capacity was determined based on the release profile and *in vitro* studies, where mg of MNP was stirred in 2 mL of sodium nitroprusside (SNP) solution ( $1 \times 10^{-4}$  M). The supernatant was removed from the mixture and the percentage drug loading capacity was determined as the ratio of the mass of drug in the nanoparticle over the mass of the nanoparticle.

$$\text{Drug loading capacity (\%)} = \frac{\text{mass of drug in nanoparticles}}{\text{mass of the nanoparticle}} \times 100 \quad (3.6)$$

#### **3.6.3.3. Release of sodium nitroprusside from mesoporous nanoparticles *in vitro***

Aortic vessels from male Wistar rats were incubated in drug loaded MNP for 3 hours using an organ bath set-up and a data acquisition system. Details of dissection of the tissue and organ bath system is given in Chapter 3; Section 3.4. Aortic vessel smooth muscle cells integrity was tested with high potassium salt solution (KPSS).

### 3.6.4. Results

#### 3.6.4.1. *Detection of mesoporous nanoparticles within vascular tissue*

The exposure of isolated viable aortic vessels to mesoporous nanoparticles have led to their initialisation into the cytoplasm of endothelial cells (Figure 3.48). However, they were not observed in the nucleus of the cells, elastic lamina, smooth muscle or adventitial layers.

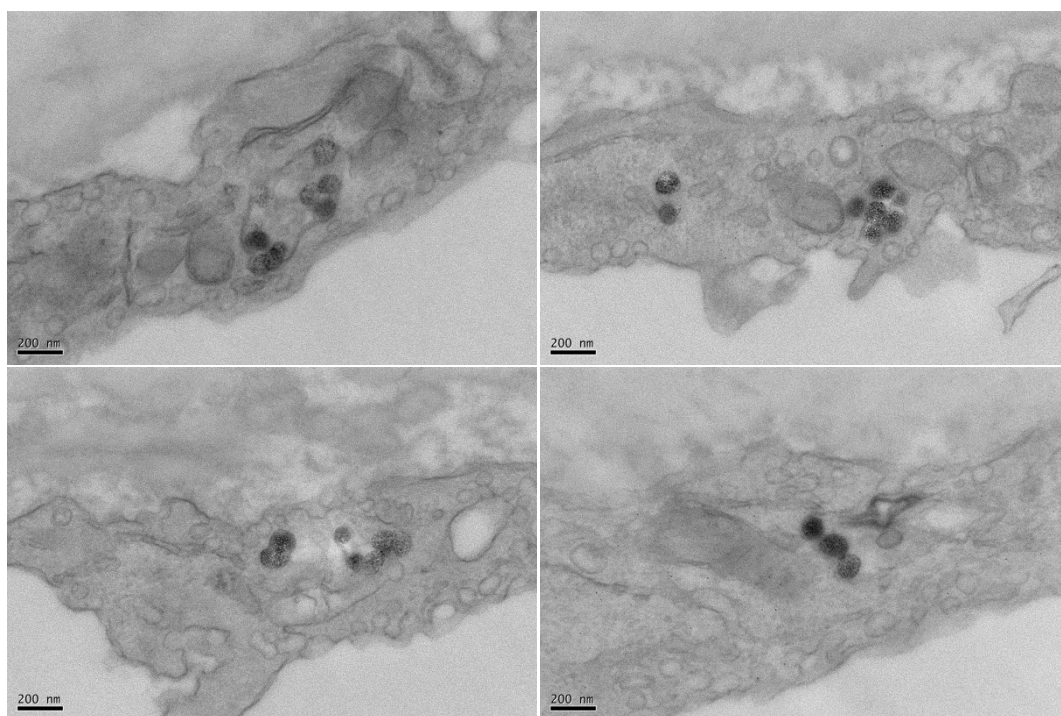
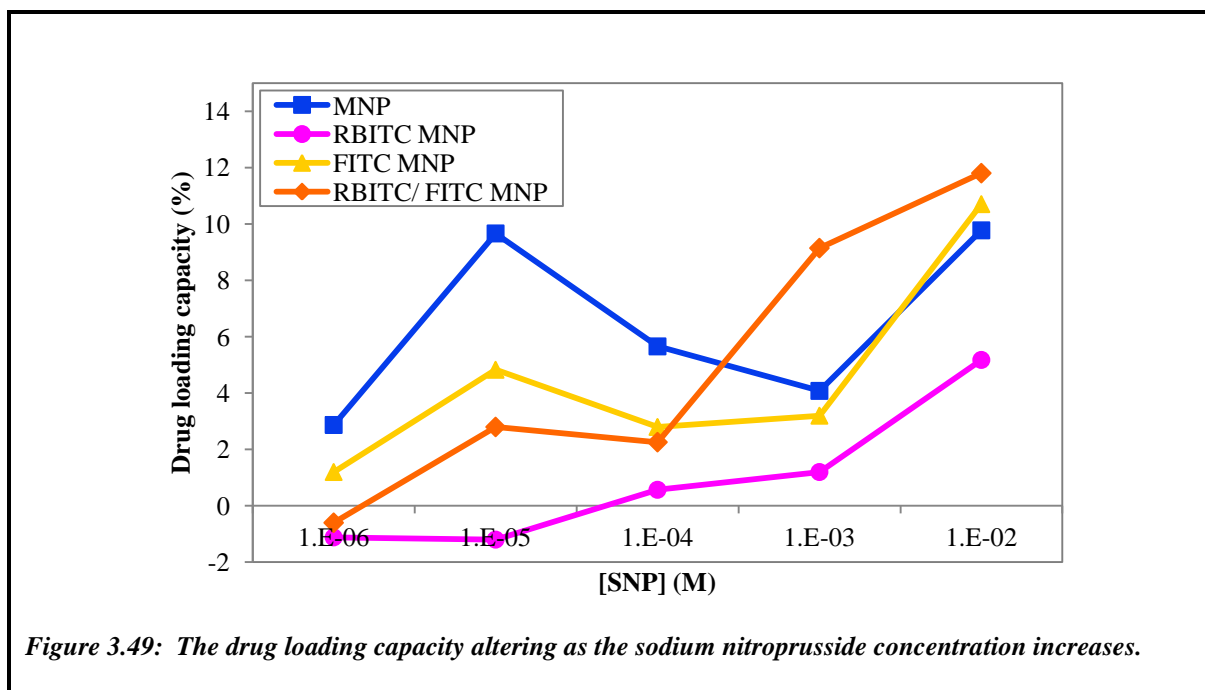


*Figure 3.48: Transmission electron microscope image of mesoporous nanoparticles within the endothelial cell lining of the aortic vessel.*

#### 3.6.4.2. *Sodium nitroprusside release from mesoporous nanoparticles*

The DLC of the different types of mesoporous nanoparticles were determined by soaking the NPs in different concentrations of SNP ( $1 \times 10^{-6}$  to  $1 \times 10^{-2}$  M), as shown in Figure 3.49.



Overall, it is observed that the introduction of dye molecules within the MNP matrix has led to a reduction in the drug loading capacity.

Mesoporous nanoparticles, without dye encapsulation, when loaded with SNP ( $1 \times 10^{-5}$  M) have a drug loading capacity of 9.66 % and an encapsulation efficiency of 93.47 % for low and 93.76 % for high dose. FITC MNP when loaded with SNP ( $1 \times 10^{-5}$  M) have a drug loading capacity of 4.82 % and an encapsulation efficiency of 92.97 % for low and 92.70 % for high dose. RBITC MNP when loaded with SNP ( $1 \times 10^{-5}$  M) have a drug loading capacity of -1.21 %. RBITC/ FITC MNP when loaded with SNP ( $1 \times 10^{-5}$  M) have a drug loading capacity of 2.79 %. However, determination of the iron concentration within the aliquots, attained from the SNP drug release profile at  $1 \times 10^{-5}$  M to mimic the *in vitro* release, was ineffective at the most sensitive wavelength (248 nm) due to the possible interference caused by the salt ions. Therefore, a release profile was achieved by the use of a more concentrated solution of SNP in the drug soaking stage.

The kinetic release of sodium nitroprusside (SNP) from MNP, FITC MNP, RBITC MNP and RBITC/ FITC MNP was investigated (Figure 3.50). The time course of SNP release demonstrates that there is a rapid initial release for approximately 400 minutes, which is similar for all types of MNP. The SNP concentration released at approximately 500 minutes was greater for the MNP as it reaches  $4.2 \times 10^{-1}$  mol dm<sup>-3</sup>, while the FITC MNP

was  $3.6 \times 10^{-1} \text{ mol dm}^{-3}$ , RBITC MNP was  $4.0 \times 10^{-1} \text{ mol dm}^{-3}$  and RBITC/ FITC MNP was  $2.8 \times 10^{-1} \text{ mol dm}^{-3}$ . This may either be due to a greater capacity of SNP loaded within the MNP or a greater release rate. For the RBITC MNP there was a greater concentration of NPs during the release study, thus overall it follows a similar trend to the bare MNP. The drug loading capacity for RBITC MNP along with the release studies of the other MNP's suggest that the SNP release would be lowest overall release. The MNP reaches a release of  $4.5 \times 10^{-1} \text{ mol dm}^{-3}$  at 895 minutes and no further release is observed until approximately 2500 minutes, where the release reaches  $5.3 \times 10^{-1} \text{ mol dm}^{-3}$ . However, for the dye encapsulated MNP there is a gradual increase in release of SNP from 520 minutes till 802 minutes for RBITC MNP and till 1040 minutes for FITC and RBITC/ FITC MNP. The release of SNP from RBITC MNP at 3692 minutes was  $4.5 \times 10^{-1} \text{ mol dm}^{-3}$ . Overall the rate of SNP release for the FITC MNP is greater than the RBITC/ FITC MNP. Furthermore, FITC MNP leads to three small jumps at 1080, 1200 and 1320 minutes followed by gradual increases. The final SNP concentration releases at 2515 minutes was  $6.0 \times 10^{-1} \text{ mol dm}^{-3}$ , where the trend suggests that further release of SNP would be observed over a longer period of time. For the RBITC/ FITC MNP from 1080 minutes there is an gradual increase in SNP release which has a small jump at 1320 minutes followed by a gradual increases to  $5.3 \times 10^{-1} \text{ mol dm}^{-3}$ , the trend also suggests that further release of SNP would be observed over a longer period of time.

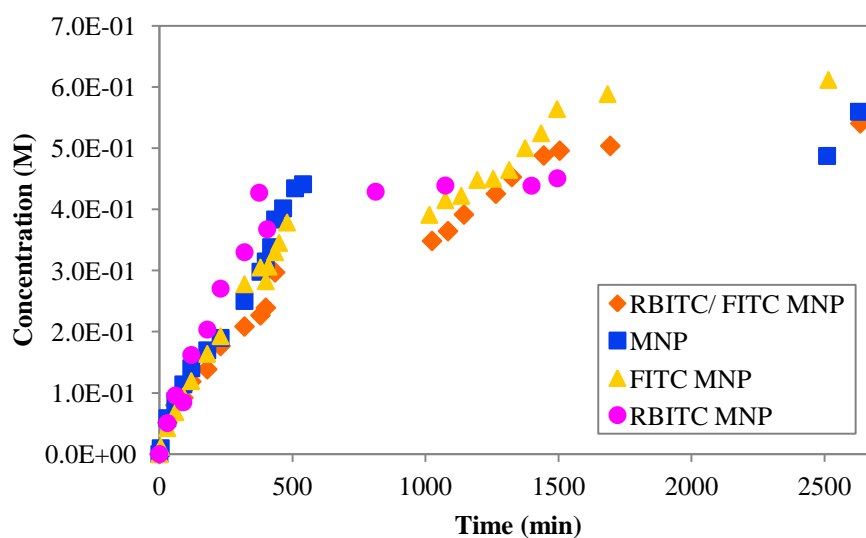


*Figure 3.50: Release profile of sodium nitroprusside from mesoporous nanoparticles using atomic absorption spectroscopy.*

### 3.6.4.3. Drug release study of sodium nitroprusside *in vitro*

Mesoporous nanoparticles (MNP) and FITC MNP at high ( $1.96 \times 10^{12}$  NP/ mL) and low ( $1.31 \times 10^{11}$  NP/ mL) concentration were placed in the organ bath system. The density of the MNP was utilised as  $0.83 \text{ g/ cm}^{-3}$  [202]. The trend observed for the vasodilation of aortic vessels when incubated in low dose of MNP loaded with SNP ( $48.81 \text{ }\mu\text{g/ mL}$ ) led to the slight reduction in vasoconstrictor levels as compared to the control (Figure 3.51; Table 2 in the appendix).

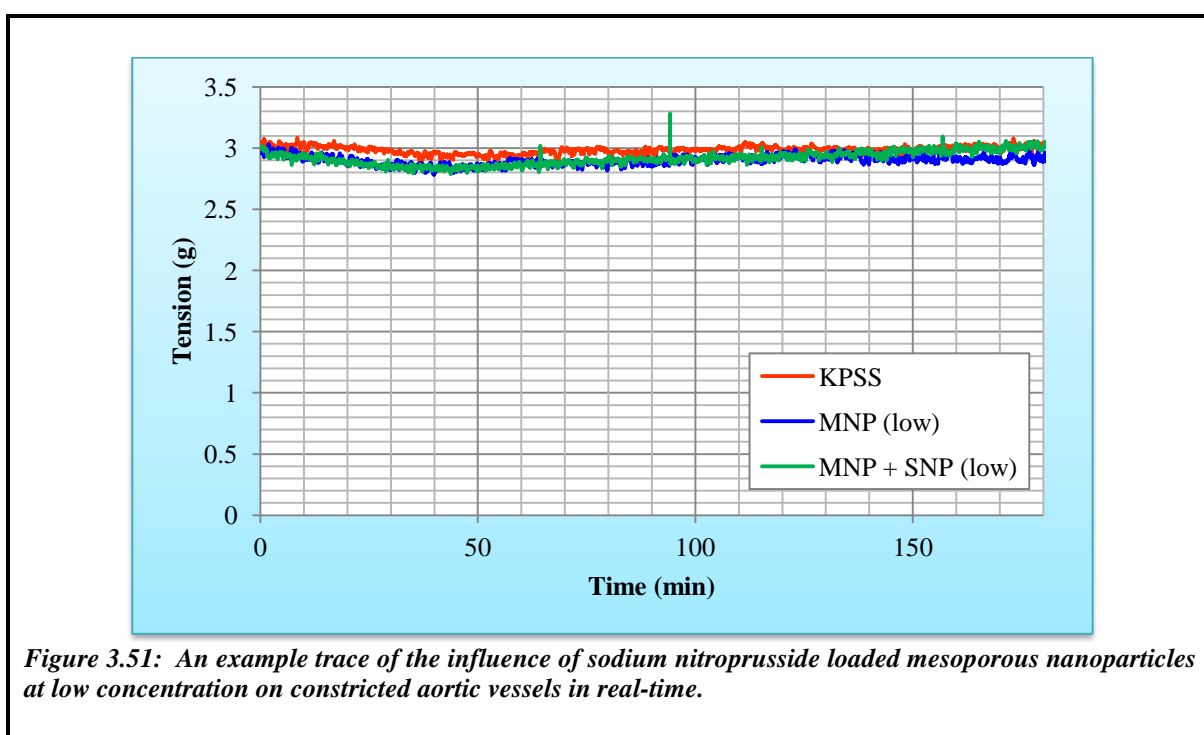


*Figure 3.51: An example trace of the influence of sodium nitroprusside loaded mesoporous nanoparticles at low concentration on constricted aortic vessels in real-time.*

However, at high dose of MNP loaded with SNP ( $730.30 \text{ }\mu\text{g/ mL}$ ) has led to a significant reduction in constriction (Figure 3.52; Table 2 in the appendix). Furthermore, the constriction level has been sustained for the control over a 3 hour period.

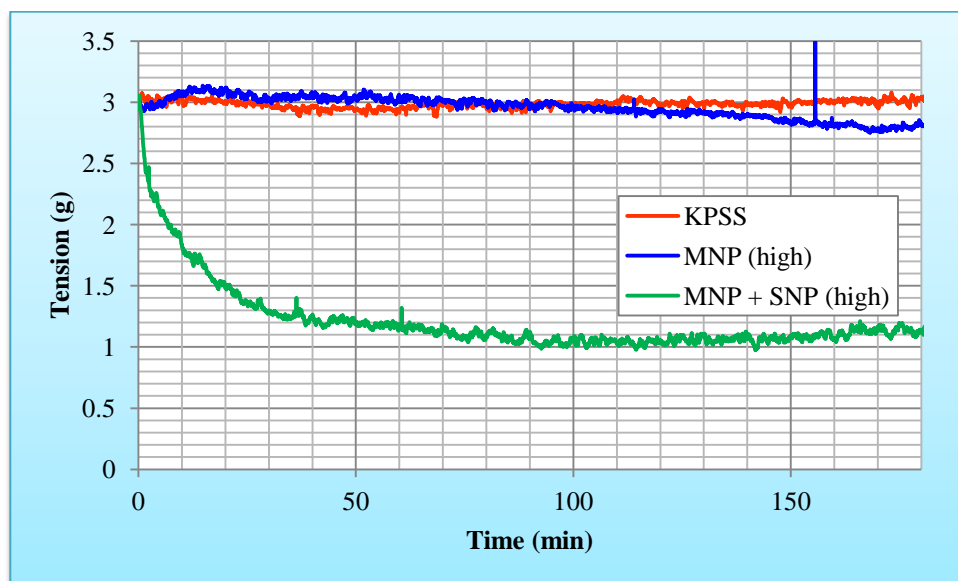
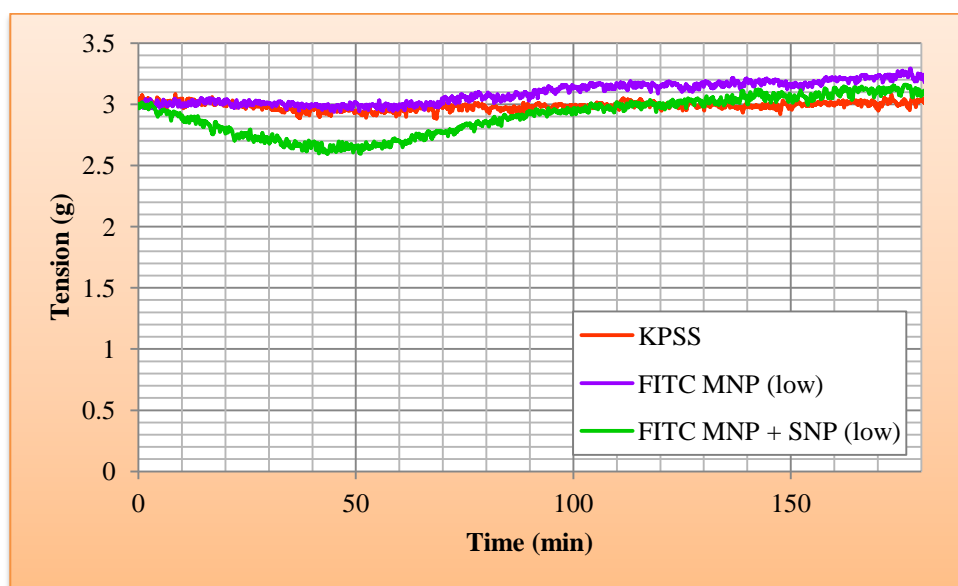


Figure 3.52: An example trace of the influence of sodium nitroprusside loaded mesoporous nanoparticles at high concentration on constricted aortic vessels in real-time.

When aortic vessels were incubated with low dose of FITC MNP loaded with SNP ( $73.73 \mu\text{g}/\text{mL}$ ) there was also a slight decline in constriction (Figure 3.53; Table 2 in the appendix); as previously observed with the dye free MNP. Furthermore, after approximately 50 minutes the vessel starts to re-constrict. Interestingly, the incubation of the vessels in  $1.31 \times 10^{11}$  NP/ mL of FITC MNP also leads to re-constriction of the aortic vessel after approximately 50 minutes. The aortic vessels are normally under a basal relaxation state, and the increased constriction levels is suggestive that the FITC MNP disrupt the basal NO production. It is possible that these FITC MNP disrupt eNOS function.



*Figure 3.53: An example trace of the influence of sodium nitroprusside loaded fluorescein isothiocyanate encapsulated mesoporous nanoparticles at low concentration on constricted aortic vessels in real-time.*

Furthermore, at high dose of FITC MNP loaded with SNP (1103.09  $\mu\text{g}/\text{mL}$ ) resulted in significant rapid relaxation of the constricted vessels (Figure 3.54; Table 2 in the appendix). However, it is observed that the relaxation was not sustained for the 3 hour period, as after approximately 120 minutes the vessel start to re-constrict.

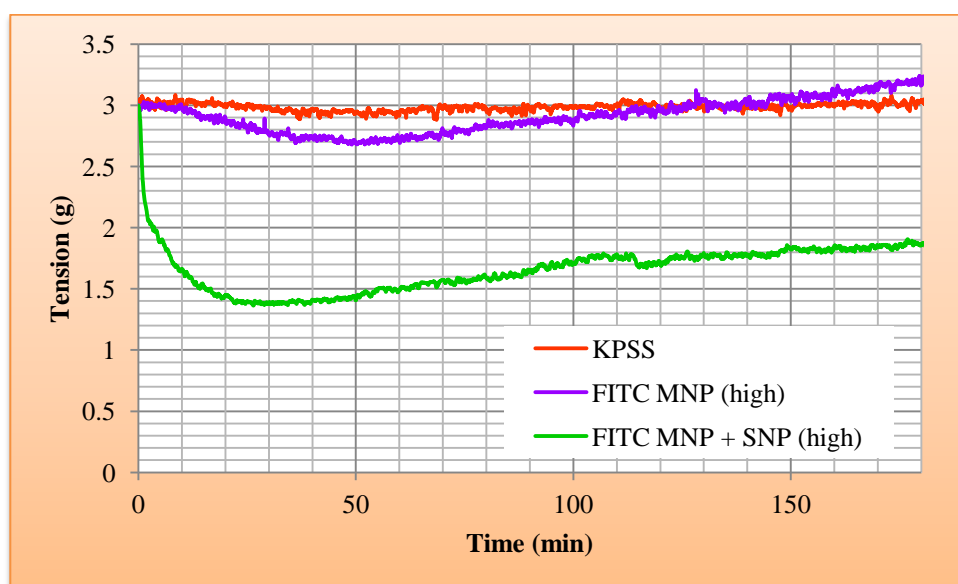
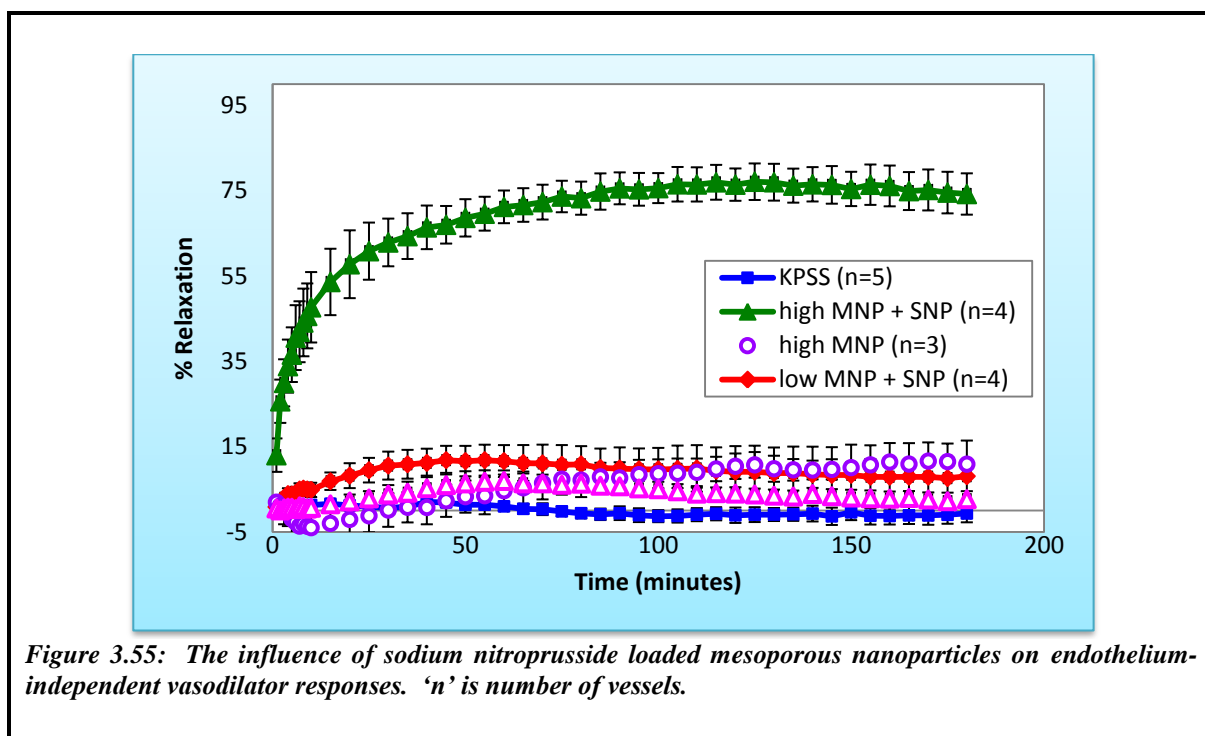


*Figure 3.54: An example trace of the influence of sodium nitroprusside loaded fluorescein isothiocyanate encapsulated mesoporous nanoparticles at high concentration on constricted aortic vessels in real-time.*

Data from the *in vitro* real-time release studies were used to construct percentage relaxation graphs in order to interpret the statistical significance. The percentage relaxation graph of the *in vitro* release of SNP from MNP is shown in Figure 3.55. There is no statistical significance over the three hour exposure time period between the KPSS control and low and high concentration of MNP (Table 2 in the appendix). Furthermore, the exposure of viable aortic vessels to low concentration of MNP loaded with SNP has no significance difference over the incubation period. However, high concentration MNP loaded with SNP has led to a rapid relaxation of the vessels. The high concentration of MNP loaded with SNP has led to an initial sharp release of SNP within the first 20 minutes leading to 57.74 % relaxation. The maximum relaxation was 77.08 % and was reached at 125 minutes.



Similarly, to the percentage relaxation graphs of MNP, there is no statistical difference over the three hour exposure time period between the KPSS control, low and high concentration of FITC MNP and low concentration of FITC MNP loaded with SNP (Figure 3.56; Table 2 in the appendix). Also, when high concentration MNP loaded with SNP, led to a rapid relaxation of the vessels. The high concentration of FITC MNP loaded with SNP has led to an initial sharp release of SNP within the first 20 minutes leading to 61.93 % relaxation. The maximum relaxation was 64.16 % and was reached at 35 minutes.

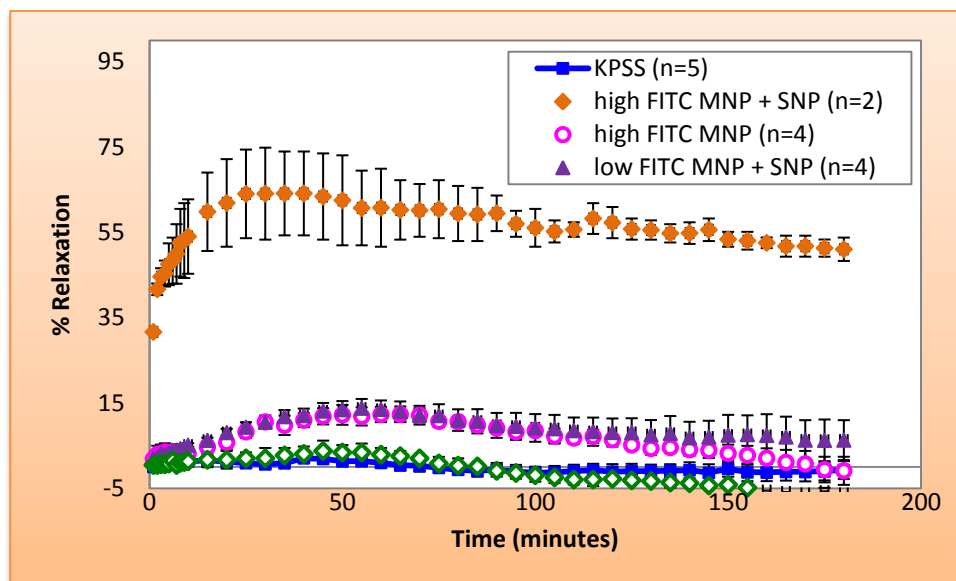


Figure 3.56: The influence of sodium nitroprusside loaded fluorescein isothiocyanate encapsulated mesoporous nanoparticles on endothelium-independent vasodilator responses. 'n' is number of vessels.

In order, to calculate the SNP release in real-time under physiological conditions a calibration plot was produced of known concentrations of SNP against % relaxation (Figure 3.57). This calibration graph was obtained from control experiments of known concentration of SNP leading to a particular relaxation of aortic vessels.

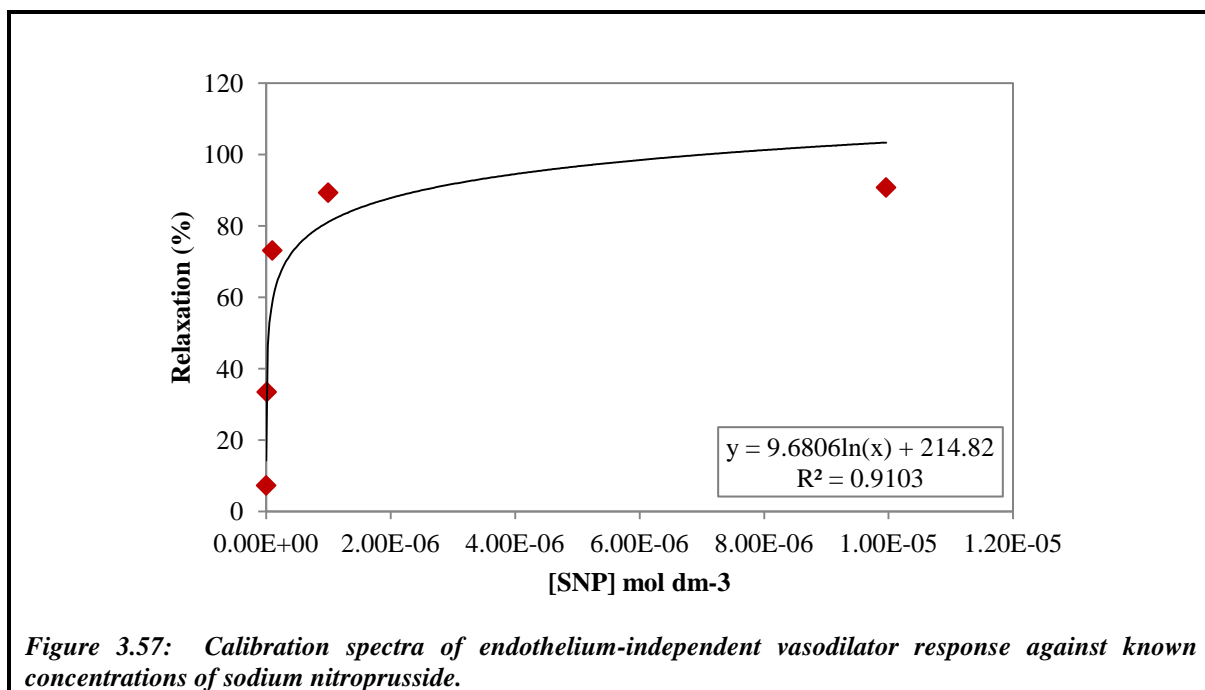


Figure 3.57: Calibration spectra of endothelium-independent vasodilator response against known concentrations of sodium nitroprusside.

The logarithm equation, determined in Figure 3.57, allows one to calculate SNP concentration released at a given time (refer to Table 1 in the appendix). The validation of the calculated SNP release using the *in vitro* studies was conducted by subtracting the total concentration of SNP released from the initial concentration of SNP used for drug loading. Thus this value was compared to the SNP concentration within the supernatant determined with atomic absorption spectroscopy. Interestingly, the SNP concentration within the supernatant was similar to the concentration calculated using the *in vitro* studies (Table 3.6).

Table 3.6: The total concentration of SNP released from the MNP matrix, *in vitro*.

	MNP	FITC MNP
Total SNP released in the <i>in vitro</i> study (mol dm <sup>-3</sup> ) <sup>a</sup>	$1.55 \times 10^{-5}$	$3.70 \times 10^{-6}$
SNP remained within the supernatant; calculated via <i>in vitro</i> study (mol dm <sup>-3</sup> ) <sup>b</sup>	$8.45 \times 10^{-5}$	$9.63 \times 10^{-5}$
SNP remained within the supernatant from MNP (mol dm <sup>-3</sup> ) <sup>c</sup>	$9.38 \times 10^{-5}$	$9.27 \times 10^{-5}$

<sup>a</sup> Calculated from the *in vitro* control studies of SNP (Chapter 3, Section 3.4.2.3).

<sup>b</sup> Calculated by subtracting the total concentration of SNP release *in vitro* from the total concentration of SNP used.

<sup>c</sup> Determined from atomic absorption spectroscopy.

### **3.6.5. Discussion**

In this current study, we demonstrate that the exposure of live aortic vessels to mesoporous nanoparticles (MNP) and fluorescein isothiocyanate encapsulated (FITC) MNP of approximately 100 nm leads to their initialisation into the cytoplasm of the endothelial cells. Furthermore, the MNP have a greater drug loading capacity as compared to the dye encapsulated MNP; where  $MNP > FITC\ MNP > RBITC/ FITC\ MNP > RBITC\ MNP$ . Thus, the dye molecules may influence the incorporation of SNP within the mesopores. The FITC MNP has a greater DLC than RBITC MNP, which further supports the influence of dye molecules as it was quantified that a greater volume of RBITC dye molecules were incorporated within the mesoporous matrix as compared to FITC dye molecules. The mesopore sizes are similar for the different types of MNP; however the total surface area reduces as higher volume of dye molecules are incorporated within the nanoparticle. The encapsulation efficiency of the MNP is slightly higher than the FITC MNP.

The initial dosage of mesoporous nanoparticles exposed to the aortic vessels was  $1.31 \times 10^{11}$  NP/ mL, as previous results from the biocompatibility study (Chapter 3, Section 3.4) of amorphous silica nanoparticles ( $71 \pm 6$  nm) confirm that at this given concentration SiNPs are biocompatible. Furthermore, Akbar *et al* also confirm that incubation of aortic vessels in  $1.1 \times 10^{11}$  NP/ mL was biocompatible for both  $97 \pm 7.6$  and  $197 \pm 7.5$  nm SiNPs, as there was no significance difference in the attenuation of vasodilation when compared to the control [35]. Furthermore, the biocompatibility testing of silica nanoparticles (Chapter 3, Section 3.4) confirms that a greater surface area will ultimately reduce biocompatibility. However, as the surface area of MNP are lower than amorphous silica nanoparticles of the same size range, thus greater concentration of MNP may lead to less detrimental effect as observed by the amorphous SiNPs. In Slowing *et al.* study, human cervical cancer cells (HeLa) were exposed to 100  $\mu$ g/ mL of FITC MNP and there was no difference between the control and the FITC MNP cell growth profile thus confirming they are not cytotoxic [82]. The Singh *et al.* *in vitro* study on the assessment of the biocompatibility of HeLa cells was performed by measuring the mitochondrial activity when incubated in  $70 \pm 8$  nm MNP, the as-synthesised MNP at 1000  $\mu$ g/ mL showed signs of cytotoxicity but not significantly [203].

To the best of our knowledge, this study is the first to compare the drug loading capacity and the kinetic release of vasodilator drug, sodium nitroprusside, from mesoporous

nanoparticles with and without incorporated fluorophore dye molecules. We further demonstrate that the incorporation of fluorophore dye molecules within the mesoporous matrix results in a lower volume of SNP released. Furthermore, to our knowledge this is the first study where live isolated aortic vessels are exposed to these SNP loaded MNP and SNP loaded FITC MNP. The *in vitro* real-time exposure of MNP loaded with and without SNP at  $1.31 \times 10^{11}$  NP/ mL shows a small observable attenuation in constriction as compared with the control over a 3 hour time period. However, at higher concentration ( $1.96 \times 10^{12}$  NP/ mL) the real-time exposure of MNP without SNP results in a small attenuation in constriction that occurs after approximately 1 hour. The MNP loaded with SNP have led to a rapid relaxation of aortic vessels along with relaxation sustained over the three hour period. The statistical analysis confirms that the relaxation is significant only for SNP loaded MNP at  $1.96 \times 10^{12}$  NP/ mL.

The exposure of FITC MNP loaded with and without SNP at  $1.31 \times 10^{11}$  NP/ mL shows that the FITC MNP constriction level is similar to the KPSS control. Furthermore, the SNP loaded FITC MNP result in a small observable relaxation as compared with the control over a 3 hour time period. At higher concentration ( $1.96 \times 10^{12}$  NP/ mL) the real-time exposure of FITC MNP without SNP has a similar observable constriction level as the control. The FITC MNP loaded with SNP leads to a rapid relaxation of aortic vessels however the relaxation was sustained for 120 minutes followed by re-constriction. The statistical analysis confirms that the relaxation is significant for the SNP loaded FITC MNP at  $1.96 \times 10^{12}$  NP/ mL.

### **3.6.6. Conclusions**

In conclusion, we have designed a drug delivery system allowing for the release of SNP agonist from mesoporous matrix. We further placed these systems in isolated aortic vessels to record the release profile, *in vitro*. It was observed that the incorporation of fluorophores within the MNP led to lower drug loading ability, and thus relaxation was not maintained for the 3 hour incubation period, while MNP without dye molecules was capable of maintaining relaxation for the duration of the incubation period. Therefore the dye molecules used within the MNP matrix plays a significant role in the release kinetics. This has therapeutic implications for the use of appropriately fabricated nanoparticles for drug loading potential.

# **Chapter 4**

## **Conclusions**

## 4. CONCLUSIONS

Well dispersed silica nanoparticles of various sizes and structure were successfully prepared. The nanoparticles were pure or dye encapsulated non-porous and mesoporous silica with sizes in the range 30-200 nm. The materials were extensively characterised with TEM, SEM, PCS, zeta potential, DRIFTS, TGA, AAS and fluorescence spectroscopy. The 200 nm dye encapsulated non-porous silica nanoparticles were incorporated within silica sol-gel matrix. Films were casted on glass cover slips and used as sensors for gaseous oxygen and sulphur dioxide molecules. These nanoparticles have great potential for the detection of pollutant gases and oxygen levels within biological systems. The biocompatibilities of non-porous silica nanoparticles with and without fluorescent dye molecules were determined. The nanoparticles at  $71\pm 6$  nm were found to be biocompatible at  $1.31\times 10^{11}$  NP/ mL. Furthermore, the dye encapsulated non-porous silica nanoparticles interact with the NO molecules contained within the endothelial cells and thus attenuate vasodilation; these findings have important implication for the therapeutic and imaging diagnostic. Finally, the influence of dye molecules contained within mesoporous nanoparticle was assessed upon different drug loadings. The results obtained provide prospects for developing fluorescent nanoparticles for diagnostics and drug delivery in biomedical applications.

### 4.1. Future work

Silica nanoparticles are utilized for therapeutic intervention for the development of therapeutic agents and for imaging diagnostics. However, our study suggests that non-porous silica nanoparticles may affect vessel function depending on the actual dosimetry and the influence of dye molecules encapsulated within non-porous silica nanoparticles. Furthermore, we have demonstrated that non-porous silica nanoparticles influences vascular function by affecting the cascade of NO production within the endothelial cells. Future investigation may involve assessing the pathways where non-porous nanoparticles with and without dye encapsulation are initialised into the cell, and their impact on cell function.

Preliminary, data acquired from the pressured study of large vessels have found that endothelial layer was damaged, thus preventing uptake of nanoparticles. Future study will

involved the development of a chamber used for mounting large isolated vessels for a pressure system in order to preserve the vessel integrity. Additionally, the influence of nanoparticle uptake delivered within the vessel structure will be assessed with pressure.

The synthesising of nanocarriers for therapeutic purposes produced via a triggered slow release mechanism. Initially, the surface of the mesoporous nanoparticles (MNP) loaded with sodium nitroprusside (SNP) may be functionalized in order to target a specific site, so the drug delivery is aimed for a precise cells and receptors. Exploring how the surface modified nanoparticles behave when the drug delivery is in circulation by carrying out *in vivo* studies. Therefore, future studies will involve:

***Cell culture studies:*** Aortic endothelial cells will be cultured in growth medium with nanoparticles using the standard cell culture techniques. The effect of pure or dye encapsulated non-porous and mesoporous silica nanoparticles uptake on cell proliferation will be determined. In addition, different concentrations of the rhodamine B isothiocyanate dye on cell proliferation will be analysed. The influence of concentration and size of silica nanoparticles in comparison to dye encapsulated silica nanoparticles will be established for use in the functional studies.

***Functional studies:*** Initialisation of nanoparticles and their influence on arterial function will be further investigated using the organ bath and pressure myography techniques, in order to determine the slow release of drug from mesoporous nanoparticles.

***Histology:*** The visualization of fluorescent dye encapsulated nanoparticles within cells will be determined using confocal microscopy.

# References

## References

---

- [1] Franks, A., '*Nanotechnology*', Journal of Physics E: Scientific Instruments, 1987, **20**, 1442-1451.
- [2] Napierska, D., Thomassen, L. C. J., Lison, D., Martens, J. A. and Hoet, P. H., '*The nanosilica hazard: another variable entity*', Particle and Fibre Toxicology, 2010, **7**, 1-32.
- [3] Ernest, H. and Shetty, R., '*Impact of nanotechnology on biomedical sciences: review of current concepts on convergence of nanote*', Journal of Nanotechnology Online, 2005, 1-15.
- [4] Bhattacharyya, D., Singh, S., Satnalika, N., Khandelwal, A. and Jeon, S. -H., '*Nanotechnology, big things from a tiny world: a review*', International Journal of u- and e- Services, Science and Technology, 2009, **2 (3)**, 29-38.
- [5] Bhattacharyya, S., Sen, T. and Patre, A., '*Host-guest energy transfer: semiconducting polymer nanoparticles and Au nanoparticles*', The Journal of Physical Chemistry C, 2010, **114 (27)**, 11787-11795.
- [6] Gordon, S., Teichmann, E., Young, K., Finnie, K., Rades, T. and Hook, S., '*In vitro and in vivo investigation of thermosensitive chitosan hydrogels containing silica nanoparticles for vaccine delivery*', European Journal of Pharmaceutical Sciences, 2010, **41 (2)**, 360-368.
- [7] Ndungu, K., '*Dissolved silver in the Baltic sea*', Environmental Research, 2011, **111 (1)**, 45-49.
- [8] Miletto, I., Gilardino, A., Zamburlin, P., Dalmazzo, S., Lovisolò, D., Caputo, G., Viscardi, G. and Martra, G., '*Highly bright and photostable cyanine dye-doped silica nanoparticles for optical imaging: photophysical characterization and cell tests*', Dyes and Pigments, 2010, **84 (1)**, 121-127.
- [9] Slowing, I. I., Vivero-Escoto, J. L., Wu, C. -W. and Lin, S. -Y., '*Mesoporous silica nanoparticles as controlled release drug delivery and gene transfection carriers*', Advanced Drug Delivery Reviews, 2008, **60 (11)**, 1278-1288.
- [10] Kim, H. R., Kim, M. J., Lee, S. Y., Oh, S. M. and Chung, K. H., '*Genotoxic effects of silver nanoparticles stimulated by oxidative stress in human normal bronchial epithelial (BEAS-2B) cells*', Mutation Research, 2011, **726 (60)**, 129-135

- [11] Ju-Nam, Y. and Lead, J. R., ‘*Manufactured nanoparticles: an overview of their chemistry, interactions and potential environmental implications*’, *Science of the Total Environment*, 2008, **400 (1-3)**, 396-414.
- [12] Roche, P., Al-Jowder, R., Narayanaswamy, R., Young, J. and Scully, P., ‘*A novel luminescent lifetime-based optrode for the detection of gaseous and dissolved oxygen utilising a mixed ormosil matrix containing ruthenium (4, 7-diphenyl-1, 10-phenanthroline)<sub>3</sub>Cl<sub>2</sub> (Ru.dpp)*’, *Analytical and Bioanalytical Chemistry*, 2006, **386 (5)**, 1245-1257.
- [13] Sharma, P., Brown, S., Walter, G. Santra, S. and Moudgil B., ‘*Nanoparticles for bioimaging*’, *Advances in Colloid and Interface Sciences*, 2006, **123-126**, 471-485.
- [14] Ferrari, M., ‘*Nanogeometry: beyond drug delivery*’, *Nature Nanotechnology*, 2008, **3**, 131-132.
- [15] Øye, G., Glomm, W. R., Vrålstad, T., Volden, S., Magnusson, H., Stöcker, M. and Sjöblom, J., ‘*Synthesis, functionalisation and characterisation of mesoporous materials and sol-gel glasses for applications in catalysis, adsorption and photonics*’, *Advances in Colloid and Interface Sciences*, 2006, **123-126**, 17-32.
- [16] Stöber, W. and Fink, A., ‘*Controlled growth of monodispersed silica spheres in the micron sized range*’, *Journal of Colloid and Interface Science*, 1968, 62-69.
- [17] Chang, C. –L. and Fogler, H. S., ‘*Controlled formation of silica particles from tetraethyl orthosilicate in nonionic water-in-oil microemulsions*’, *Langmuir*, 1997, **13**, 3295-3307.
- [18] Bogush, G. H., Tracy, M. A. and Zukoski Iv, C. F., ‘*Preparation of monodisperse silica particles: control of size and mass fraction*’, *Journal of Non-Crystalline Solids*, 1988, **104 (1)**, 95-106.
- [19] Giesche, H., ‘*Synthesis of monodispersed silica powders I. Particle properties and reaction kinetics*’, *Journal of the European Ceramic Society*, 1994, **14 (3)**, 189-204.
- [20] Razink, J. J. and Schlotter, N. E., ‘*Correction to “Preparation of monodisperse silica particles: Control of size and mass fraction” by G.H. Bogush, M.A. Tracy and C.F.*

- Zukoski IV, Journal of Non-Crystalline Solids 104 (1988) 95–106’, Journal of Non-Crystalline Solids, 2007, **353**, 2932-2933.
- [21] Bogush, G. H. and Zukoski Iv, C. F., ‘*Studies of the kinetics of the precipitation of uniform silica particles through the hydrolysis and condensation of silicon alkoxides*’, Journal of Colloid and Interface Science, 1991, **142** (1), 1-18.
- [22] Byers, C. H., Harris, M. T. and Williams, D. F., ‘*Controlled microcrystalline growth studies by dynamic laser-light-scattering methods*’, Ind. Eng. Chem. Res., 1987, **26** (9), 1916-1923.
- [23] Arriagada, F. J. and Osseo-Asare, K., ‘*Synthesis of nanosize silica in a nonionic water-in-oil microemulsion: effects of the water/surfactant molar ratio and ammonia concentration*’, Journal of Colloid and Interface Science, 1999, **211** (2), 210-220.
- [24] Osseo-Asare, K. and Arriagada, F. J., ‘*Growth kinetics of nanosize silica in a nonionic water-in-oil microemulsion: a reverse micellar pseudophase reaction model*’, Journal of Colloid and Interface Science, 1999, **218** (1), 68-76.
- [25] Gao, F., Wang, L., Tang, L. and Zhu, C., ‘*A novel nano-sensor based on rhodamine -  $\beta$ - isothiocyanate - doped silica nanoparticle for pH measurement*’, Microchimica Acta, 2005, **152**, 131-135.
- [26] Kay, B. D. and Assink, R. A., ‘*Sol-gel kinetics: II. chemical speciation modelling*’, Journal of Non-Crystalline Solids, 1988, **104** (1), 112-122.
- [27] Artaki, I., Bradley, M., Zerda, T. W. And Jonas, J., ‘*NMR and Raman study of the hydrolysis reaction in sol-gel processes*’, The Journal of Physical Chemistry, 1985, **89** (20), 4399-4404.
- [28] Chatterjee, M. and Ganguli, D., ‘*Alkoxide derived monodisperse silica microspheres: the role of solvents in synthesis*’, Transactions of the Indian Ceramic Society, 1986, **45**, 95-99.
- [29] Byers, C. H. and Harris, M. T., ‘*In ultrastructure processing of advanced ceramics*’, Edited by Mackenzie, J. D. And Ulrich, D. R., New York, Wiley, 1988, 843-853.
- [30] Brinker, C. J. and Scherer, G. W., ‘*Sol-Gel Science*’, Academic Press, San Diego, 1990, 139-142.

- [31] Shaw, D. J., *'Introduction to Colloid & Surface Chemistry'*, Fourth edition, Butterworth Heinemann, 1992, 1-306.
- [32] Baalousha, M., Kammer, F. V. D., Motelica-Heino, M., Hilal, H. S. and Le Coustumer, P., *'Size fractionation and characterization of natural colloids by flow-field flow fractionation coupled to multi-angle laser light scattering'*, Journal of Chromatography A, 2006, **1104**, 272-281.
- [33] Pashley, R. M. and Karaman, M. E., *'Applied colloid and surface chemistry'*, Wiley, Chichester, 2004, 1-188.
- [34] Birdi, K. S., *'Surface and colloid chemistry: principles and applications'*, Taylor & Francis group, Boca Raton, 2010, 1-244.
- [35] Akbar, N., Mohamed, T., Whitehead, D. and Azzawi, M., *'Biocompatibility of amorphous silica nanoparticles: Size and charge effect on vascular function, in vitro'*, Biotechnology and Applied Biochemistry, 2011, **58**, 353-362.
- [37] Koohestanian, A., Hosseini, M. and Abbasian, Z., *'The separation method for removing of colloidal particles from raw water'*, American-Eurasian Journal of Agricultural & Environmental Sciences, 2008, **4 (2)**, 266-273.
- [38] Bergna, W. E. and Roberts, W. O., *'Colloidal silica: fundamentals and applications'*, Taylor & Francis group, Boca Raton, 2006, 1-917.
- [39] Iler, R. K., *'The chemistry of silica: solubility, polymerization, colloid and surface properties, and biochemistry'*, Wiley, Hoboken, 1979, 1-866.
- [40] Andersson, N., *'Structural features and adsorption behaviour of mesoporous silica particles formed from droplets generated in a spraying chamber'*, Microporous and Mesoporous Materials, 2004, **72 (1-3)**, 175-183.
- [41] Marchisio, D. L., Rivautella, L. and Barresi, A. A., *'Design and scale-up of chemical reactors for nanoparticle precipitation'*, AIChE Journal, 2006, **52 (5)**, 1877-1887.
- [42] Burns, A., Ow, H. and Wiesner, U., *'Fluorescent core-shell silica nanoparticles: towards "Lab on a Particle" architectures for nanobiotechnology'*, Chemical Society Reviews, 2006, **35 (11)**, 1028-1042.

- [43] Churaev, N. V., '*The DLVO theory in Russian colloid science*', Advances in Colloid and Interface Science, 1999, **83**, 19-32.
- [44] Ninham, B. W., '*On progress in forces since the DLVO theory*', Advances in Colloid and Interface Science, 1999, **83**, 1-17.
- [45] Norrish, K. and Rausell-Colom, J. A., '*Low-angle X-Ray diffraction studies of the swelling of montmorillonite and vermiculite*', Clays and Clay Minerals, 1961, **10**, 123-149.
- [46] Donners, W. A. B., Rijnbout, J. B. and Vrij, A., '*Light scattering from soap films: I. Determination of double-layer repulsion forces*', Journal of Colloid and Interface Science, 1977, **61** (2), 249-260.
- [47] Israelachvili, J. N. and Adams, G. E., '*Measurement of Forces between Two Mica Surfaces in Aqueous Electrolyte Solutions in the Range 0-100 nm*', Journal of the Chemical Society, Faraday Transactions 1, 1978, **74**, 975-1001.
- [48] Pashley, R. M., McGuiggan, P. M., Ninham, B. W., Brady, J. and Evans, D. F., '*Direct measurements of surface forces between bilayers of double-chained quaternary ammonium acetate and bromide surfactants*', The Journal of Physical Chemistry, 1986, **90**, 1637-1642.
- [49] Hartley, P. G., Larson, I. and Scales, P. J., '*Electrokinetic and direct force measurements between silica and mica surfaces in dilute electrolyte solutions*', Langmuir, 1997, **13** (8), 2207-2214.
- [50] Pashley, R. M. and Kitchener, J. A., '*Surface forces in adsorbed multilayers of water on quartz*', Journal of Colloid and Interface Science, 1979, **71**, 491-500.
- [51] Pashley, R. M. J., '*DLVO and hydration forces between mica surfaces in  $Li^+$ ,  $Na^+$ ,  $K^+$  and  $Cs^+$  electrolyte solutions: A correlation of double-layer and hydration forces with surface cation exchange properties*', Journal of Colloid and Interface Science, 1981, **83**, 531-546.
- [51] Israelachvili, J. N. and Pashley, R. M., '*Molecular layering of water at surfaces and origin of repulsive hydration forces*', Nature, 1983, **306**, 249-250.

- [52] Kobayashi, M., Juillerat, F., Galletto, P., Bowen, P. and Borkovec, M., '*Aggregation and charging of colloidal silica particles: effect of particle size*', *Langmuir*, 2005, **21**, 5761-5769.
- [53] Lyklema, J., '*Lyotropic sequences in colloid stability revisited*', *Advances in Colloid and Interface Science*, 2003, **100-102**, 1-12.
- [54] Grahame, D. C., '*The role of the cation in the electrical double layer*', *Journal of The Electrochemical Society*, 1951, **98**, 343-350.
- [55] Gierst, L., Herman, P. and Fresen. J., '*On the desorption of pyridine at negative potentials in mercury-water systems*', *Analytical Chemistry*, 1966, **216**, 238-242.
- [56] Marcus, Y., '*Viscosity B-coefficients, structural entropies and heat capacities, and the effects of ions on the structure of water*', *Journal of Solution Chemistry*, 1994, **23** (7), 831-848.
- [57] Marcus, Y., '*Effect of ions on the structure of water: Structure making and breaking*', *Chemical Reviews*, 2009, **109**, 1346-1370.
- [58] Dumont, F., Warlus, J. and Watillon, A., '*Influence of the point of zero charge of titanium dioxides hydrosols on the ionic adsorption sequence*' *Journal of Colloid and Interface Science*, 1990, **138**, 543-554.
- [59] Gierst, L., Vandenberghen, L., Nicolas, E. and Fraboni, A., '*Ion pairing mechanisms in electrode processes*', *Journal of the Electrochemical Society*, 1966, **113**, 1025-1035.
- [60] Franks, G. V., '*Zeta potentials and yield stresses of silica suspensions in concentrated monovalent electrolytes: isoelectric point shift and additional attraction*', *Journal of Colloid and Interface Science*, 2002, **249**, 44-51.
- [61] Kjellander, R. and Ber. Bunsenges, '*Ion-ion correlations and effective charges in electrolyte and macroion systems*', *Physical Chemistry*, 1996, **100** (6), 894-904.
- [62] Labbez, C., Jonsson, B., Skarba, M. and Borkovec, M., '*Ion-Ion Correlation and Charge Reversal at Titrating Solid Interfaces*', *Langmuir*, 2009, **25**, 7209-7213.
- [63] Kecht, J. and Bein, T., '*Oxidative removal of template molecules and organic functionalities in mesoporous silica nanoparticles by H<sub>2</sub>O<sub>2</sub> treatment*', *Microporous and Mesoporous Materials*, 2008, **116**, 123-130.

- [64] Nandiyanto, A. B. D., Kim, S. -G., Iskandar, F. and Okuyama, K., ‘*Synthesis of spherical mesoporous silica nanoparticles with nanometer-size controllable pores and outer diameters*’, *Microporous and Mesoporous Materials*, 2009, **120**, 447-453.
- [65] Kong, Y., Jiang, S. -Y., Wang, J., Wang, S. -S., Yan, Q. -J. and Lu, Y. -N., ‘*Synthesis and characterization of Cu-Ti-MCM41*’, *Microporous and Mesoporous Materials*, 2005, **86**, 191-197.
- [66] Rappoport, J. Z., Preece, J. and Chipman, K., ‘*How do Manufactured Nanoparticles Enter Cells?*’, *Microporous and Mesoporous Materials*, 2011, **116**, 123-130.
- [67] Thielemann, J. P., Girgsdies, F., Schlögl, R. And Hess, C., ‘*Pore structure and surface area of silica SBA-15: influence of washing and scale-up*’, *Beilstein Journal of Nanotechnology*, 2011, **2**, 110-118.
- [68] Pennycook, S. J. and Nellist, P. D., ‘*Scanning transmission electron microscopy: imaging and analysis*’, Springer New York, 2011, 1-762.
- [69] Kealey, D. and Haines, P. J., ‘*Instant notes: analytical chemistry*’, BIOS Scientific Publishers Limited, 2002, **7**, 1-342.
- [70] Perkin Elmer, Atomic spectroscopy: a guide to selecting the appropriate technique and systems, accessed 27<sup>th</sup> July 2012, [http://www.perkinelmer.com/PDFs/Downloads/BRO\\_WorldLeader\\_AAICPMSICPMS.pdf](http://www.perkinelmer.com/PDFs/Downloads/BRO_WorldLeader_AAICPMSICPMS.pdf).
- [71] Glencross, H., Ahmed, N. and Wang, Q., ‘*Biomedical science practice: experimental and professional skills*’, Oxford University Press, 2011, **7**, 1-342.
- [72] Verhaegh, N. A. M., Blaaderen, Av., ‘*Dispersions of rhodamine-labeled silica spheres: synthesis, characterization, and fluorescence confocal scanning laser microscopy*’, *Langmuir*, 1994, **10**, 1427-1438.
- [73] Ying, W., ZhongHui, L., Ying, Z. W., Hui, L., DanKe, X. and Yuan, C. H., ‘*Rhodamine B doped silica nanoparticle labels for protein microarray detection*’, *Sci. China Chem.*, 2010, **53**, 747-751.
- [74] Giesche, H., ‘*Synthesis of monodispersed silica powder II. Controlled growth reaction and continuous production process*’, *Journal of the European Ceramic Society*, 1994, **14**, 205-214.

- [75] An, Y., Chen, M., Xue, Q. and Liu, W., '*Preparation and self-assembly of carboxylic acid-functionalized silica*', Journal of Colloid and Interface Science, 2007, **311**, 507-513.
- [76] A. van Blaaderen, A. Vrij, '*Synthesis and characterization of monodispersed colloidal organo-silica spheres*', Journal of Colloid and Interface Science. 156 (1993) 1-18.
- [77] K. C. Vrancken, K. Possemiers, P. Van der Voort, E. F. Vansant, '*Surface modification of silica gels with aminoorganosilanes*', Colloids and Surfaces A, 1995, **98**, 235-241.
- [78] Shi, H., He, X., Wang, K., Yuan, Y., Deng, K., Chen, J. and Tan, W., '*Rhodamine B isothiocyanate doped silica-coated fluorescent nanoparticles (RBITC-DSFNPs)-based bioprobes conjugated to annexin V for apoptosis detection and imaging*', Nanomedicine: Nanotechnology, Biology and Medicine, 2007, **3**, 266-272.
- [79] Imhof, A., Megens, M., Engelbert, J. J., de Lang, D. T. N., Sprik, R. and Vos, W. L., '*Spectroscopy of fluorescein (FITC) dyed colloidal silica spheres*' The Journal of Physical Chemistry B, 1999, **103**, 1408-1415.
- [80] Lin, Y. -S., Tsai, C. -P., Huang, H. -Y., Kuo, C. -T., Hung, Y., Huang, D. -M., Chen, Y. -C. and Mou, C. -Y., '*Well-Ordered Mesoporous Silica Nanoparticles as Cell Markers*', Chemistry of Materials, 2005, **17**, 4570-4573.
- [81] Gu, J., Fan, W., Shimojima, A. and Okubo, T., '*Organic-Inorganic Mesoporous Nanocarriers Integrated with Biogenic Ligands*', Small, 2007, **3 (10)**, 1740-1744.
- [82] Slowing, I., Trewyn, B. G. and Lin, V. S. -Y., '*Effect of surface functionalization of MCM-41-type mesoporous silica nanoparticles on the endocytosis by human cancer cells*', Journal of American Chemical Society, 2006, **128**, 14792-14793.
- [83] Hudson, S. P., Padera, R. F., Langer, R. and Kohane, D. S., '*The biocompatibility of mesoporous silicates*', Biomaterials, 2008, **29 (30)**, 4045-4055.
- [84] Liu, Y., Hou, D. and Wang, G., '*A simple wet chemical synthesis and characterization of hydroxyapatite nanorods*', Materials Chemistry and Physics, 2004, **86**, 69-73.

- [85] Lin, J., Chen, H. and Yao, L., ‘*Surface tailoring of SiO<sub>2</sub> nanoparticles by mechanochemical method based on simple milling*’, Applied Surface Science, 2010, **256**, 5978-5984.
- [86] Wang, S., Lu, W., Tovmachenko, O., Rai, U. S., Yu, H. and Ray, P. C., ‘*Challenge in understanding size and shape dependent toxicity of gold nanomaterials in human skin keratinocytes*’, Chemical Physics Letters, 2008, **463**, 145–149.
- [87] Wang, Z. B., Mitra, A., Wang, H. T., Huang, L. M. and Yan, Y., ‘*Pure Silica Zeolite Films as Low-k Dielectrics by Spin-On of Nanoparticle Suspensions*’, Advanced Materials, 2001, **13 (19)**, 1463-1466.
- [88] Luan, Z., Fournier, J. A., Wooten, J. B. and Miser, D. E., ‘*Preparation and characterization of (3-aminopropyl)triethoxysilane-modified mesoporous SBA-15 silica molecular sieves*’, Microporous and Mesoporous Materials, 2005, **83 (1-3)**, 150-158.
- [89] Jawor, A., Jeong, B. -H. and Hoek, E. M. V., ‘*Synthesis, characterization, and ion-exchange properties of colloidal zeolite nanocrystals*’, Journal of Nanoparticle Research, 2009, **11**, 1795-1803.
- [90] Roche, P. J. R., Cheung, M. C. -K., Yung, K. Y., Kirk, A. G., Chodavarpu, V. P. and Bright, F. V., ‘*Application of gold quenching of luminescence to improve oxygen sensing using a ruthenium (4, 7-diphenyl-1,10-phenanthroline)<sub>3</sub>Cl<sub>2</sub>:TEOS thin film*’, Sensors and Actuators B: Chemical, 2010, **147**, 581-586.
- [91] Wang, X. -H., Peng, H. -S., Ding, H., You, F. -T., Huang, S. -H., Teng, F., Dong, B. and Song, H. -W., ‘*Biocompatible fluorescent core-shell nanoparticles for ratiometric oxygen sensing*’, Journal of Materials Chemistry, 2012, **22 (31)**, 16066-16071.
- [92] Liewhiran, C., Tamaekong, N., Wisitsora-at, A. and Phanichphant, S., ‘*The monitoring of H<sub>2</sub>S and SO<sub>2</sub> noxious gases from industrial environment with sensors based on flame-spray-made SnO<sub>2</sub> nanoparticles*’, Engineering Journal, 2012, **16 (3)**, 123-134.

- [93] Jorge, P. A. S., Maule, C., Silva, A. J., Benrashid, R., Santos, J. L. and Farahi, F., 'Dual sensing of oxygen and temperature using quantum dots and a ruthenium complex', *Analytica Chimica Acta*, 2008, **606**, 223-229.
- [94] Lakowicz, J. R., 'Principles of Fluorescence Spectroscopy', Third edition, Springer, 2010, **1**, 1-954.
- [95] Al-Jowder, R., Roche, P. J. R. and Narayanaswamy, R., 'Use of an artificial neural network to model the quenching of a Ru.dpp: ormosil-based optrode to gaseous and dissolved oxygen', *Sensors and Actuators B: Chemical*, 2007, **127**, 383-391.
- [96] Razek, T. M. A., Miller, M. J., Hassan, S. S. M. and Arnold, M. A., 'Optical sensor for sulfur dioxide based on fluorescence quenching', *Talanta*, 1999, **50**, 491-498.
- [97] O'Neal, D. P., Meledeo, M. A., Davis, J. R., Ibey, B. L., Gant, V. A., Pishko, M. V. and Coté, G. L., 'Oxygen Sensor Based on the Fluorescence Quenching of a Ruthenium Complex Immobilized in a Biocompatible Poly(Ethylene Glycol) Hydrogel', *IEEE Sensor Journal*, 2004, **4**, 728-734.
- [98] Glazer, B. T., Marsh, A. G., Stierhoff, K. and Luther, G. W., 'The dynamic response of optical sensors and voltammetric electrodes to temporal changes in dissolved oxygen concentrations', *Analytica Chimica Acta.*, 2004, **518**, 93-100.
- [99] Kumar, R., Roy, I., Ohulchansky, T. Y., Goswami, L. N., Bonoiu, A. C., Bergey, E. J., Tramposch, K. M., Maitra, A. and Prasad, P. N., 'Covalently Dye-Linked, Surface-Controlled, and Bioconjugated Organically Modified Silica Nanoparticles as Targeted Probes for Optical Imaging', *ACSNANO.*, 2008, **2**, 449-456.
- [100] Bakker, J. W. P., Filippini, D., Lundström, I., 'Enhancing classification capabilities of computer screen photo-assisted fluorescence fingerprinting', *Sensors and Actuators B: Chemical*, 2005, **110**, 190-194.
- [101] Plajnšek, K. T., Pajk, S., Govedarica, B., Pečar, S. and Srčič, S., 'A novel fluorescent probe for more effective monitoring of nanosized drug delivery systems within the cells', *Pharmaceutical Nanotechnology*, 2011, **416**, 384-393.
- [102] Arik, M., Çelebi, N. and Onganer, Y., 'Fluorescence quenching of fluorescein with molecular oxygen in solution', *Journal of Photochemistry and Photobiology A: Chemistry*, 2005, **170**, 105-111.

- [103] Chu, C. -S., Lo, Y. -L. and Sung, T. -W., 'Review on Recent Developments of Fluorescent Oxygen and Carbon Dioxide Optical Fiber Sensors', *Photonic Sensors*, 2011, **1**, 234-250.
- [104] Jeong, Y. C., Sohn, O. -J., Rhee, J. I., Lee, S. and Kim, H. J., 'Optical Sensing Material for Dissolved Oxygen: Covalent Immobilization of Tris(4, 7-diphenyl-1, 10-phenanthroline) ruthenium (II) Complex in Sol-Gels, *Bull*', Korean Chemical Society, 2007, **28**, 883-886.
- [105] Lee, S. -K. and Okura, I., 'Photoluminescent determination of oxygen using metalloporphyrin-polymer sensing systems', *Spectrochimica Acta Part A: Molecular and Biomolecular Spectroscopy*, 1998, **54**, 91-100.
- [106] Sharma, A. and Wolfbeis, O. S., 'The quenching of the fluorescence of polycyclic aromatic hydrocarbons and rhodamine 6G by sulphur dioxide', *Spectrochimica Acta Part A: Molecular Spectroscopy*, 1987, **43**, 1417-1421.
- [107] Tallury, P., Malhotra, A., Byrne, L. M. and Santra, S., 'Nanobioimaging and sensing of infectious diseases', *Advanced Drug Delivery Reviews*, 2010, **62**, 424-437.
- [108] Wilhelm, P. and Stephan, D., 'Photodegradation of rhodamine B in aqueous solution via SiO<sub>2</sub>@TiO<sub>2</sub> nano-spheres', *Journal of Photochemistry and Photobiology A: Chemistry*, 2007, **185**, 19-25.
- [109] Wan, Q., Ramsey, C. and Baran, G., 'Thermal pretreatment of silica composite filler materials', *Journal of Thermal Analysis and Calorimetry*, 2010, **99** (1), 237-243.
- [110] Saraidarov, T., Reisfeld, R., Zigansky, E., Sashchiuk, A. and Lifshitz, E., 'Electrical conductivity of doped porous glasses as possible sensors for oxygen', *Optica Applicata*, 2008, **1**, 109-117.
- [111] Li, X. -M., Ruan, F. -C., Ng, W. -Y. and Wong, K. -Y., 'Scanning optical sensor for the measurement of dissolved oxygen and BOD', *Sensors and Actuators B: Chemical*, 1994, **21**, 143-149.
- [112] Kuratli, M. and Pretsch, E., 'Sulfur dioxide-selective optrodes', *Analytical Chemistry*, 1994, **66**, 85-91.

- [113] Grant, S. A. and Satcher, J. H., Bettencourt, K., ‘*Development of-sol-gel-based fibre optic nitrogen dioxide gas sensors*’, *Sensors and Actuators B: Chemical*, 2000, **69**, 132-137.
- [114] Lopez, S., Senz, A. and Gsponer, H. E., ‘*Luminescent Properties of Tris(2, 2'-bipyridine (ruthenium (II) in Sol-Gel-Processed Dip-Coated Thin Films*’, *Journal of Colloid and Interface Science*, 2002, **246**, 122-128.
- [115] Tsyalkovsky, V., Klep, V., Ramaratnam, K., Lupitsky, R., Minko, S. and Luzinov, I., ‘*Fluorescent Reactive Core-Shell Composite Nanoparticles with A High Surface Concentration of Epoxy Functionalities*’, *Langmuir*, 2008, **20**, 317-325.
- [116] Chen, X., Zhong, Z., Li, Z., Jiang, Y., Wang, X. and Wong, K., ‘*Characterization of ormosil film for dissolved oxygen-sensing*’, *Sensors and Actuators B: Chemical*, 2002, **87**, 233-238.
- [117] Vogel, R., Surawski, P. P. T., Littleton, B. N., Miller, C. R., Lawrie, G. A., Battersby, B. J. and Trau, M., ‘*Fluorescent organosilica micro- and nanoparticles with controllable size*’, *Journal of Colloid and Interface Science*, 2007, **310**, 144-150.
- [118] Kneas, K. A., Demas, J. N., DeGraff, B. A. and Periasamy, A., ‘*Fluorescence Microscopy Study of Heterogeneity in Polymer-supported Luminescence-based Oxygen Sensors*’, *Microscopy Microanalysis*, 2000, **6**, 551-561.
- [119] Wark, M., Rohlfing, Y., Altindag, Y. and Wellmann, H., ‘*Optical gas sensing by semiconductor nanoparticles or organic dye molecules hosted in the pores of mesoporous siliceous MCM-41*’, *Physical Chemistry Chemical Physics*, 2003, **5**, 5188-5194.
- [120] Zhang, H., Lei, B., Mai, W. and Liu, Y., ‘*Oxygen-sensing materials based on ruthenium (II) complex covalently assembled mesoporous MSU-3 silica*’, *Sensors and Actuators B: Chemical*, 2011, **160**, 677-683.
- [121] Kirkpatrick, C. J. and Bonfield, W., ‘*Nanobiointerface: a multidisciplinary challenge*’, *Journal of the Royal Society Interface*, 2010, **7**, S1-S4.
- [122] Knopp, D., Tang, D. and Niessner, R., ‘*Review: Bioanalytical applications of biomolecule-functionalized nanometer-sized doped silica particles*’, *Analytical Chimica Acta*, 2009, **647 (1)**, 14-30.

- [123] De, M., Ghosh, P. S, and Rotello, V. M., ‘*Application of nanoparticles in biology*’, *Advanced Materials*, 2008, **20**, 1-17.
- [124] Li, Z. –Z., Wen, L. –X., Shao, L. and Chen, J. –F., ‘*Fabrication of porous hollow silica nanoparticles and their applications in drug release control*’, *Journal of Controlled Release*, 2004, **98**, 245-254.
- [125] Quignard, S., Mosser, G., Boissière, M. and Coradin, T., ‘*Long-term fate of silica nanoparticles interacting with human dermal fibroblasts*’, *Biomaterials*, 2012, **33** (17), 4431-4442.
- [126] Wang, G., Otuonye, A. N., Blair, E. A., Denton, K., Tao, Z. and Asefa, T., ‘*Functionalized mesoporous materials for adsorption and release of different drug molecules: a comparative study*’, *Journal of Solid State Chemistry*, 2009, **182** (7), 1649-1660.
- [127] Vallet-Regí, M., Ramila, A., del Real, R. P. and Perez-Pariente, J., ‘*A new property of MCM-41: drug delivery system*’, *Chemistry of Materials*, 2001, **13**, 308-3011.
- [128] Gary-Bobo, M., Hocine, O., Brevet, D., Maynadier, M., Raehm, L., Richeter, S., Charasson, V., Looock, B., Morère, A., Mailard, P., Garcia, M. and Durand, J. –O., ‘*Cancer therapy improvement with mesoporous silica nanoparticles combining targeting, drug delivery and PDT*’, *International Journal of Pharmaceutics*, 2012, **423** (2), 509-515.
- [129] Lu, J., Li, Z., Zink, J. I. and Tamanoi, F., ‘*In vivo tumor suppression efficiency of mesoporous silica nanoparticles-based drug-delivery systems: enhanced efficacy by folate modification*’, *Nanomedicine: Nanotechnology, Biology and Medicine*, 2012, **8** (2), 212-220.
- [130] Wagenseil, J. E., and Mecham, R. P., ‘*Vascular Extracellular Matrix and Arterial Mechanics*’, *Physiology Review*, 2009, 89, 957-989.
- [131] Tortora, G. J. and Grabowski, S. R., ‘*Principles of Anatomy and Physiology*’, 10<sup>th</sup> edition.
- [132] Verlohren, S., Dubrovskaja, G., Tsang, S. –Y., Essin, K., Luft, F. C., Huang, Y. and Gollasch, M., ‘*Visceral Periadventitial Adipose Tissue Regulates Arterial Tone of Mesenteric Arteries*’, *Hypertension*, 2004, 44, 271-276.

- [133] Celermajer, D. S., '*Endothelial Dysfunction: Does It Matter? Is It Reversible?*', American College of Cardiology, 1997, 30 (2), 325-333.
- [134] Löhn, M., Dubrovskaja, G., Lauterbach, B., Luft, F. C., Gollasch, M. and Sharma, A. M., '*Periadventitial fat releases a vascular relaxing factor*', Federation of American Societies for Experimental Biology Journal, 2002, 16, 1057-1063.
- [135] Goa, Y. -J., Lu, C., Su, L., -Y., Sharma, A., M. and Lee, R., M., K., W., '*Modulation of vascular function by perivascular adipose tissue: the role of endothelium and hydrogen peroxide*', British Journal of Pharmacology, 2007, 151, 323-331.
- [136] van Obbergh, L., Leonard, V., Chen, H., Xu, D. and Blaise, G., '*The endothelial and non-endothelial mechanism responsible for attenuated vasoconstriction in cirrhotic rats*', Experimental Physiology, 1995, **80**, 609-617.
- [137] Clarke, C. J., Forman, S., Pritchett, J., Ohanian, V. and Ohanian, J., '*Phospholipase C $\delta_1$  modulates sustained contraction of rat mesenteric small arteries in response to noradrenaline, but not endothelin-1*', American Journal of Physiology-Heart Circulatory Physiology, 2008, **295(2)**, H826-H834.
- [138] Budzyn, K., Marley, P. D. and Sobey, C. G., '*Opposing roles of endothelial and smooth muscle phosphatidylinositol 3-Kinase in vasoconstriction: effects of rho-kinase and hypertension*', The Journal of Pharmacology and Experimental Therapeutics, 2005, **313 (3)**, 1248-1253.
- [139] Keogh, A. M., Mayer, E., Benza, R. L., Corris, P., Darteville, P. G., Frost, A. E., Kim, N. H., Lang, I. M., Pepke-Zaba, J. and Sandoval, J., '*Interventional and Surgical Modalities of Treatment in Pulmonary Hypertension*', Journal of the American College of Cardiology, 2009, **54 (1)**, 67-77.
- [140] Cardillo, C., Kilcoyne, C. M., Quyyumi, A. A., Cannon, R. O. and Panza, J. A., '*Decreased vasodilator response to isoproterenol during nitric oxide inhibition in humans*', Hypertension, 1997, **30 (4)**, 918-921.
- [141] Knox, A. J. and Tattersfield, A. E., '*Airway smooth muscle relaxation*', Thorax, 1995, **50**, 894-901.

- [142] Peters, S. L. M. and Michel, M. C., '*cAMP-independent relaxation of smooth muscle cells via G<sub>5</sub>-coupled receptors*', *Naunyn-Schmiedeberg's Archives of Pharmacology*, 2003, **368**, 329-330.
- [143] Campbell, W. B. and Fleming, I., '*Epoxyeicosatrienoic acids and endothelium-dependent responses*', *Pflügers Archiv European Journal of Physiology*, 2010, **459** (6), 881-895.
- [144] Hecker, M., '*Endothelium-derived hyperpolarizing factor-fact or fiction ?*', *News Physiology*, 2000, **15**, 1-5.
- [145] Craven, P. A., Patterson, M. C. and DeRubertis, F. R., '*Role for protein kinase C in A23187 induced glomerular arachidonate release and PGE<sub>2</sub> production*', *Biochemical and Biophysical Research Communications*, 1987, **149** (2), 658-664.
- [146] Wu, K. K., Hatzakis, H., Lo, S. S., Seong, D. C., Sanduja, S. K. and Tai, H. H., '*Stimulation of de novo synthesis of prostaglandin G/H synthase in human endothelial cells by phorbol ester*', *Journal of Biological Chemistry*, 1988, **263** (35), 19043-19047.
- [147] Lagaud, G. J., Masih-Khan, E., Kai, S., van Breemen, C. and Dubé, G. P., '*Influence of type II diabetes on arterial tone and endothelial function in murine mesenteric resistance arteries*', *Journal of Vascular Research*, 2001, **38** (6), 578-589.
- [148] Chataigneau, T., Félétou, M., Huang, P. L., Fishman, M. C., Duhault, J. and Vanhoutte, P. M., '*Acetylcholine-induced relaxation in blood vessels from endothelial nitric oxide synthase knockout mice*', *British Journal of Pharmacology*, 1999, **126** (1), 219-226.
- [149] Waldron, G. J., Ding, H., Lovren, F., Kubes, P. and Triggle, C. R., '*Acetylcholine-induced relaxation of peripheral arteries isolated from mice lacking endothelial nitric oxide synthase*', *British Journal of Pharmacology*, 1999, **128** (3), 653-658.
- [150] Hinton, J. M. and Langton, P. D., '*Inhibition of EDHF by two new combinations of K<sup>+</sup>-channel inhibitors in rat isolated mesenteric arteries*', *British Journal of Pharmacology*, 2003, **138** (6), 1031-1035.
- [151] Ko, E. A., Park, W. S., Firth, A. L., Kim, N., Yuan, J. X. -J. and Han, J., '*Pathophysiology of voltage-gated K<sup>+</sup> channels in vascular smooth muscle cells:*

- modulation by protein kinase*', Progress in Biophysics and Molecular Biology, 2009, **103**, 95-101.
- [152] Coletta, C., Papapetropoulos, A., Erdelyi, K., Olah, G., Módis, K., Panopoulos, P., Asimakopoulou, A., Gerö, D., Sharina, I., Martin, E. and Szabo, C., '*Hydrogen sulfide and nitric oxide are mutually dependent in the regulation of angiogenesis and endothelium-dependent vasorelaxation*', PNAS, 2012, **109**, 9161-9166.
- [153] Lund, D. D., Faraci, F. M., Miller, F. J. and Heistad, D. D., '*Gene transfer of endothelial nitric oxide synthase improves relaxation of carotid arteries from diabetic rabbits*', Circulation, 2000, **101**, 1027-1033.
- [154] Kellogg, D. L., Zhao, Jr. J. L., Coey, U. and Green, J. V., '*Acetylcholine-induced vasodilation is mediated by nitric oxide and prostaglandins in human skin*', Journal of Applied Physiology, 2005, **98**, 629-632.
- [155] Jin, Y., Kannan, S., Wu, M. and Zhao, J., X., '*Toxicity of Luminescent Silica Nanoparticles to Living Cells*', Chemical Research in Toxicology, 2007, **20**, 1126-1133.
- [156] Roy, C. L. and Wrana, J. L., '*+Clathrin- and non-clathrin-mediated endocytic regulation of cell signalling*', Nature, 2005, **6**, 112-126.
- [157] Pelkmans, L. and Helenius, A., '*Endocytosis via Caveolae*', Traffic, 2002, **3**, 311-320.
- [158] Bae, S. W., Tan, W. and Hong, J. -I., '*Fluorescent dye doped silica nanoparticles: new tools for bioapplications*', Chemical Communications, 2012, **48**, 2270-2282.
- [159] Zhang, N., Ding, E., Feng, X., Xu, Y. and Cai, H., '*Synthesis, characterisation of dye doped silica nanoparticles and their application in labeling cells*', Colloids and surfaces B: Biointerfaces, 2012, **89**, 133-138.
- [160] Scutaru, A. M., Krüger, M., Wenzel, M., Richter, J. and Gust, R., '*Investigations on the Use of Fluorescence Dyes for Labeling Dendrimers: Cytotoxicity, Accumulation Kinetics, and Intracellular Distribution*', Bioconjugate Chemistry, 2010, **21**, 2222-2226.

- [161] Bertazza, L., Celotti, L., Fabbrini, G., Loi, M. A., Maggini, M., Mancin, F., Marcuz, S., Menna, E., Muccini, M. and Tonellato, U., '*Cell penetrating silica nanoparticles doped with 2-photon absorbing fluorophores*', Tetrahedron, 2006, **62**, 10434-10440.
- [162] Kim, J., Cao, L., Shvartsman, D., Silva, E. A. and Mooney, D. J., '*Targeted delivery of nanoparticles to ischemic muscle for imaging and therapeutic angiogenesis*', Nano Letters, 2011, **11**, 694-700.
- [163] Rampazzo, E., Boschi, F., Bonacchi, S., Juris, R., Montalti, M., Zaccheroni, N., Prodi, L., Calderan, L., Rossi, B., Becchi, S. and Sbarbati, A., '*Multicolor core/shell silica nanoparticles for in vivo and ex vivo imaging*', Nanoscale, 2012, **4**, 824-830.
- [164] Wang, X., Morales, A. R., Urakami, T., Zhang, L., Bondar, M. V., Komatsu, M. and Belfield, K. D., '*Folate Receptor-Targetted Aggregation-Enhanced Near-IR Emitting Silica Nanoprobe for One-Photon in Vivo and Two-Photon ex Vivo Fluorescence*', Bioconjugate Chemistry, 2011, **22**, 1438-1450.
- [165] Jiang, W., Kim, B. Y. S., Rutka, J. T. and Chan, W. C. W., '*Nanoparticle-mediated cellular response is size-dependent*', Nature Nanotechnology, 2008, **3**, 145-150.
- [166] Bhattacharjee, S., de Haan, L. H. J., Evers, N. M., Jiang, X., Marcelis, A. T. M., Zuilhof, H., Rietjens, I. M. C. M. and Alink, G. M., '*Role of surface charge and oxidative stress in cytotoxicity of organic monolayer-coated silicon nanoparticles towards macrophage NR8383 cells*', Particle and Fibre Toxicology, 2010, **7**, 1-12.
- [167] Lu, X., Qian, J., Zhou, H., Gan, Q., Tang, W., Lu, J., Yuan, Y. and Liu, C., '*In vitro cytotoxicity and induction of apoptosis by silica nanoparticles in human HepG2 hepatoma cells*', International Journal of Nanomedicine, 2011, **6**, 1889-1901.
- [168] Yu, O. K., Grabinski, M., Schrand, M., Murdock, C., Wang, W., Gu, B. and Hussain, M. S., '*Toxicity of amorphous silica nanoparticles on mouse keratinocytes*', Journal of Nanoparticle Research, 2009, **11**, 15-24.
- [169] Santra, S., Liesenfeld, B., Bertolino, C., Dutta, D., Cao, Z., Tan, W., Moudgil, B. M. and Mericle, R. A., '*Fluorescence lifetime measurements to determine the core-shell nanostructure of FITC-doped silica nanoparticles: an optical approach to evaluate nanoparticle photostability*', Journal of Luminescence, 2006, **117**, 75-82.
- [170] Napierska, D., Thomassen, L. C. J., Rabolli, V., Lison, D., Gonzalez, L., Kirch-

- Volders, M., Marten, J. A. and Hoet, P. H., '*Size-dependent cytotoxicity of monodispersed silica nanoparticles in human endothelium cells*', *Small*, 2009, **5**, 846-853.
- [171] Liu, X. and Sun, J., '*Endothelial cells dysfunction induced by silica nanoparticles through oxidative stress via JNK/ P53 and NF- $\kappa$ B pathways*', *Biomaterials*, 2010, **31**, 8198-8209.
- [172] Angus, J. A. and Wright, C. E., '*Techniques to study the pharmacodynamics of isolated large and small blood vessels*', *Journal of Pharmacological and Toxicological Methods*, 2000, **44**, 395-407.
- [173] Lu, J., Liong, M., Sherman, S., Xia, T., Kovichich, M., Nel, A. E., Zink, J. I. and Tamanoi, F., '*Mesoporous Silica Nanoparticles for Cancer Therapy: Energy-Dependent Cellular Uptake and Delivery of Paclitaxel to Cancer Cells*', *Nanobiotechnology*, 2007, **3 (2)**, 89-98.
- [174] Monteiller, C., Tran, L., MacNee, W., Faux, S., Jones, A., Miller, B. and Donaldson, K., '*The pro-inflammatory effects of low-toxicity low-solubility particles, nanoparticles and fine particles, on epithelial cells in vitro: the role of surface area*', *Occupational and Environmental Medicine*, 2007, **64**, 609-615.
- [175] Huang, X., Teng, X., Chen, D., Tang, F. and He, J., '*The effect of the shape of mesoporous silica nanoparticles on cellular uptake and cell function*', *Biomaterials*, 2010, **31**, 438-448.
- [176] dos Santos, T., Varela, J., Lynch, I., Salvati, A. and Dawson, K. A., '*Effects of transport inhibitors on the cellular uptake of carboxylated polystyrene nanoparticles in different cell lines*', *PLoS ONE*, 2011, **6**, 1-10.
- [177] Michalak, G. J., Anderson, H. A. and O'Neal, D. P., '*Feasibility of using a two-wavelength photometer to estimate the concentration of circulating near-infrared extinguishing nanoparticles*', *Journal of Biomedical Nanotechnology*, 2010, **6**, 73-81.
- [178] Casciaro, S., Conversano, F., Ragusa, A., Malvindi, M. A., Franchini, R., Greco, A., Pellegrino, T. and Gigli, G., '*Optimal enhancement configuration of silica*

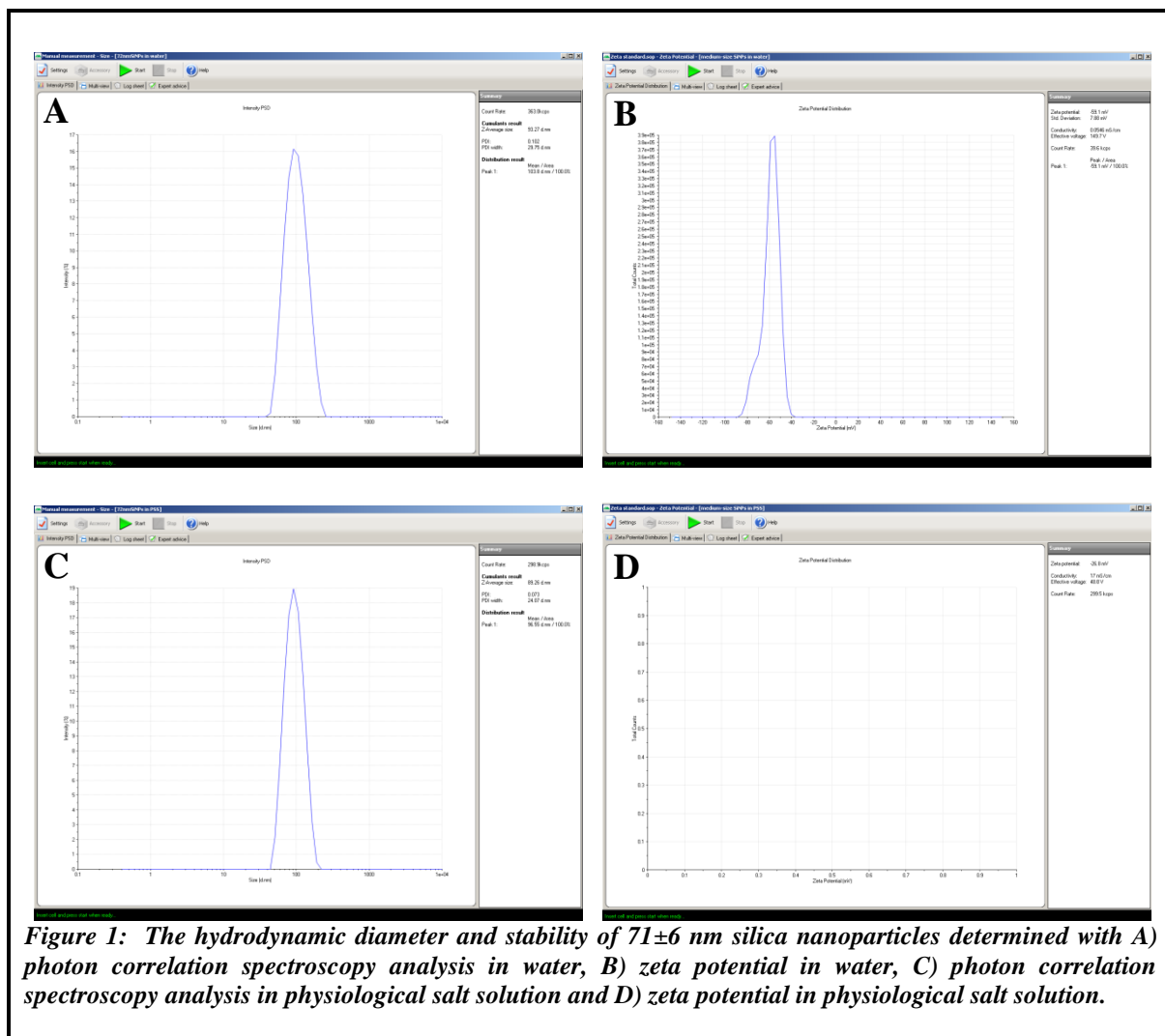
- nanoparticles for ultrasound imaging and automatic detection at conventional diagnostic frequencies*, Investigative Radiology, 2010, **45**, 715–724.
- [179] Lin, W., Huang, Y. –w., Zhou, X. –D. and Ma, Y., ‘*In vitro toxicity of silica nanoparticles in human lung cancer cells*’, Toxicology and Applied Pharmacology, 2006, **217**, 252-259.
- [180] Park, M. V. D. Z., Annema, W., Salvati, A., Lesniak, A., Elsaesser, A., Barnes, C., McKerr, G., Howard, C. V., Lynch, I., Dawson, K. A., Piersma, A. H. and de Jong, W. H., ‘*In vitro developmental toxicity test detects inhibition of stem cell differentiation by silica nanoparticles*’, Toxicology and Applied Pharmacology, 2009, **240**, 108-116.
- [181] Ahmad, J., Ahamed, M., Akhtar, M. J., Alrokayan, S. A., Siddiqui, M. A., Musarrat, J. and Al-Khedhairy, A. A., ‘*Apoptosis induction by silica nanoparticles mediated through reactive oxygen species in human liver cell line HepG2*’, Toxicol. Appl. Pharmacol., doi:10.1016/j.taap., 2011.12.020, 2012.
- [182] Miller, E. W. and Chang, C. J., ‘*Fluorescent probes for nitric oxide and hydrogen peroxide in cell signalling*’, Current Opinion in Chemical Biology, 2007, **11**, 620-625.
- [183] Kojima, H., Hirotsani, M., Nakatsubo, N., Kikuchi, K., Urano, Y., Higuchi, T., Hirata, Y. and Nagano, T., ‘*Bioimaging of Nitric Oxide with Fluorescent Indicators Based on the Rhodamine Chromophore*’, Analytical Chemistry, 2001, **73**, 1967-1973.
- [184] Fleming, I., ‘*Cytochrome P450 and vascular homeostasis*’, Circulation Research, 2001, **89**, 753-762.
- [185] Azzawi, M. and Austin, C., ‘*Extravascular pressure modulates responses of isolated rat coronary arteries to vasodilator, but not vasoconstrictor stimuli*’, American Journal of Physiology - Heart and Circulatory Physiology, 2006, **290**, H1151-1156.
- [186] Bharadwaj, L. and Prasad, K., ‘*Mediation of H<sub>2</sub>O<sub>2</sub>-induced vascular relaxation by endothelium-derived relaxing factor*’, Molecular and Cellular Biochemistry, 1995, **149**, 267-270.

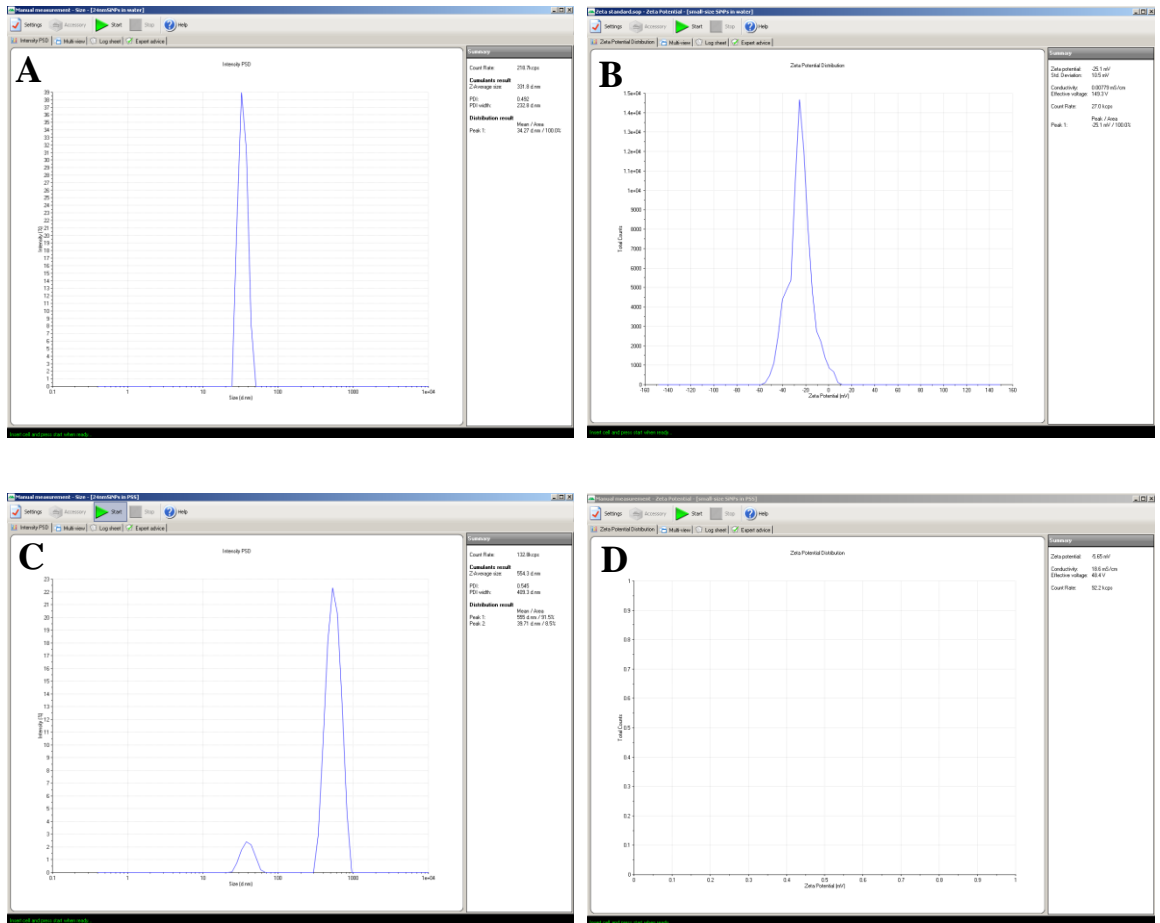
- [187] González, R., Manso, A. M. and Marin, J., '*Effect of ouabain in pressured middle cerebral arteries from normotensive and hypertensive rats*', *Clinical Pharmacology*, 1999, **21** (2), 89-97.
- [188] Dunn, W. R. and Gardiner, S. M., '*Structural and functional properties of isolated, pressurized, mesenteric resistance arteries from a vasopressin-deficient rat model of genetic hypertension*', *Hypertension*, 1995, **26**, 390-396.
- [189] Tao, Z., Toms, B. B., Goodisman, J. and Asefa, T., '*Mesoporosity and Functional Group Dependent Endocytosis and Cytotoxicity of Silica Nanomaterials*', *Chemical Research in Toxicology*, 2009, **22**, 1869-1880.
- [190] Ritter, H., Ramm, J. H. and Brühwiler, D., '*Influence of the Structural Properties of Mesoporous Silica on the Adsorption of Guest Molecules*', *Materials*, 2010, **3**, 4500-4509.
- [191] Vallet-Regi, M., Balas, F. and Arcos, D. '*Mesoporous materials for drug delivery*'. *Angewandte Chemie International Edition*, 2007, **46**, 7548-7558.
- [192] Wang, S., '*Ordered Mesoporous Materials for Drug Delivery*', *Microporous and Mesoporous Materials*, 2009, **117** (1-2), 1-9.
- [193] Fadeel, B and A. E. Garcia-Bennett, A. E., '*Better safe than sorry: Understanding the Toxicological Properties of In-organic Nanoparticles Manufactured for Biomedical Applications*', *Advanced Drug Delivery Reviews*, 2010, **62**, 362-374.
- [194] Zhao, Y. N., Trewyn, B. G., Slowing, I. I and Lin, V. S. Y., '*Mesoporous Silica Nanoparticle-Based Double Drug Delivery System for Glucose-Responsive Controlled Release of Insulin and Cyclic AMP*', *Journal of the American Chemical Society*, 2009, **131**, 8398-8400.
- [195] Rosenholm, J. M and Linden, M., '*Towards Establishing Structure-Activity Relationships for Mesoporous Silica in Drug Delivery Applications*'. *Journal of controlled release*, 2008, **128**, 157-164.
- [196] Xu, W., Gao, Q., Xu, Y., Wu, D., Sun, Y., Shen W., and Deng. F., '*Controllable release of ibuprofen from size-adjustable and surface hydrophobic mesoporous silica spheres*'. *Powder Technology*, 2009, **191**, 13-20.

- [197] Charnay, C., Be'gu, S., Tourne'-Pe'teilh, C., Nicole, L., Lerner, D. A., Devoisselle. J. M., '*Inclusion of ibuprofen in mesoporous templated silica: drug loading and release property*', European Journal of Pharmaceutics and Biopharmaceutics, 2004, **57**, 533–540.
- [198] Andersson, J., Rosenholm, J., Areva, S., and Linden, M., '*Influences of material characteristic on ibuprofen drug loading and release profiles from ordered micro- and mesoporous templated silica matrices*', Chemistry of Materials, 2004, **16**, 4160-4167.
- [199] Mashhadizadeh, M. H. and Amoli-Diva, M., '*Drug-carrying amino silane coated magnetic nanoparticles as potential vehicles for delivery of antibiotics*', Third edition, Journal of Nanomedicine and Nanotechnology, 2012, **3 (4)**, 1-7.
- [200] Shi, X., Wang, Y., Ren, L., Zhao, N., Gong, Y. and Wang, D. –A., '*Novel mesoporous silica-based antibiotic releasing scaffold for bone repair*', Acta Biomaterialia, 2009, **5**, 1697-1707.
- [201] Manoharan, P. T. and Hamilton, W. C., '*The crystal structure of sodium nitroprusside*', Inorganic Chemistry, 1963, **2 (5)**, 1043-1047.
- [202] Cho, Y., Shi, R., Borgens, R. B. B. and Ivanisevic, A., '*Functionalized mesoporous silica nanoparticle-based drug delivery system to rescue acrolein-mediated cell death*', Nanomedicine, 2008, **3 (4)**, 1-13.
- [203] Singh, N., Karambelkar, A., Gu, L., Lin, K., Miller, J. S., Chen, C. S., Sailor, M. J. and Bhatia, S. N., '*Bioresponsive mesoporous silica nanoparticles for triggered drug release*', Journal of American Chemical Society, 2011, **133**, 19582-1958.

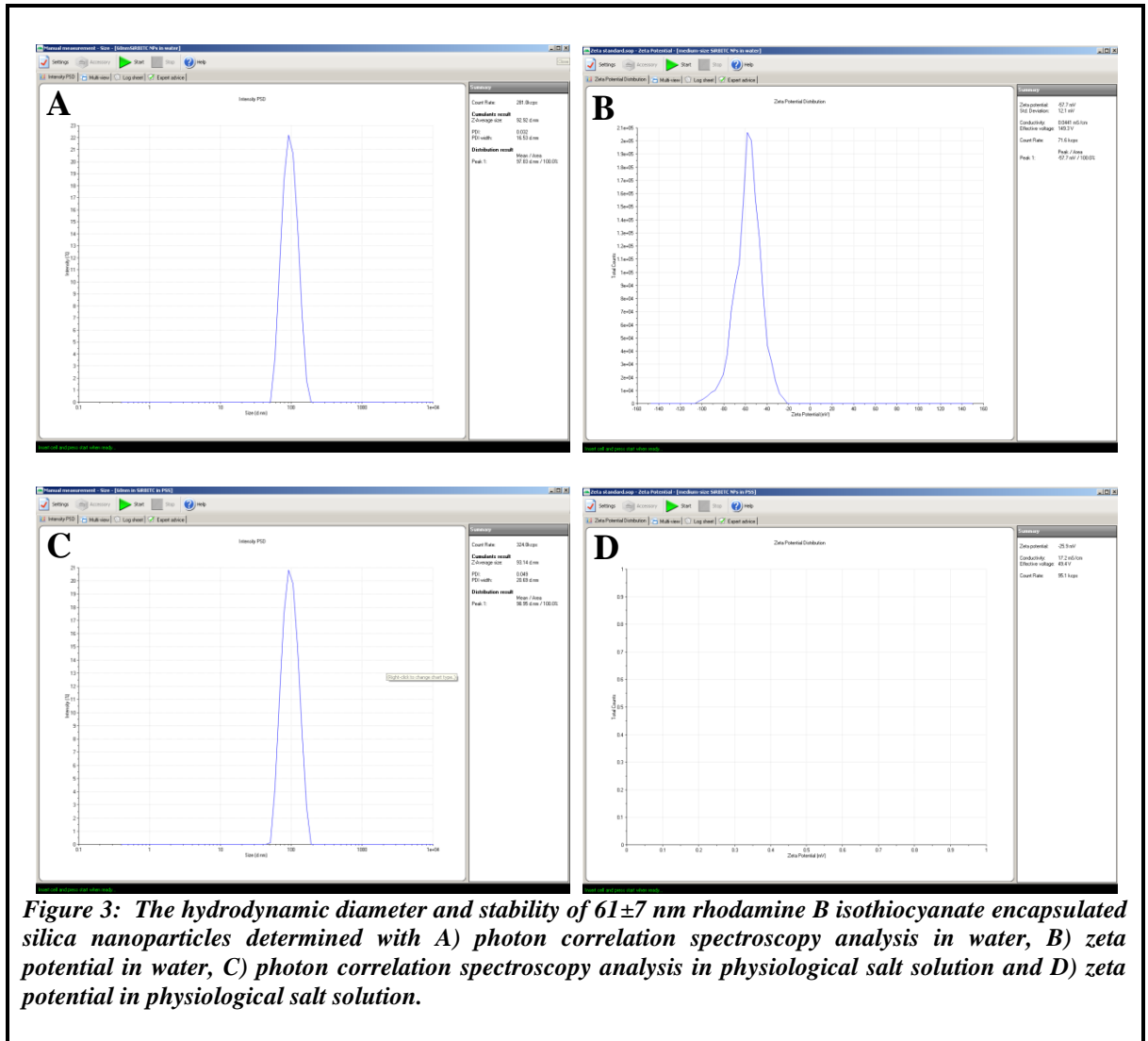
# Appendix

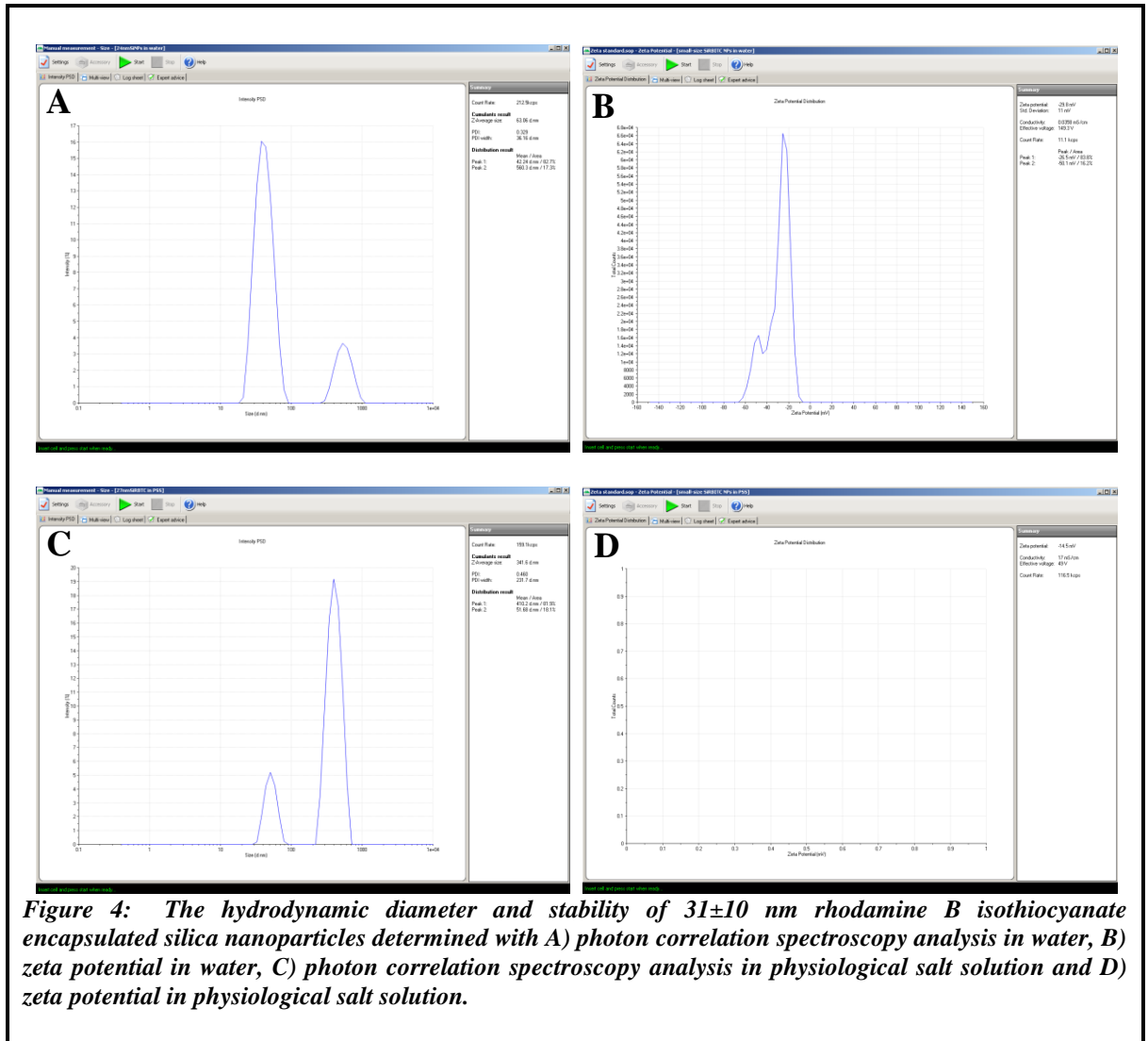
# Appendix

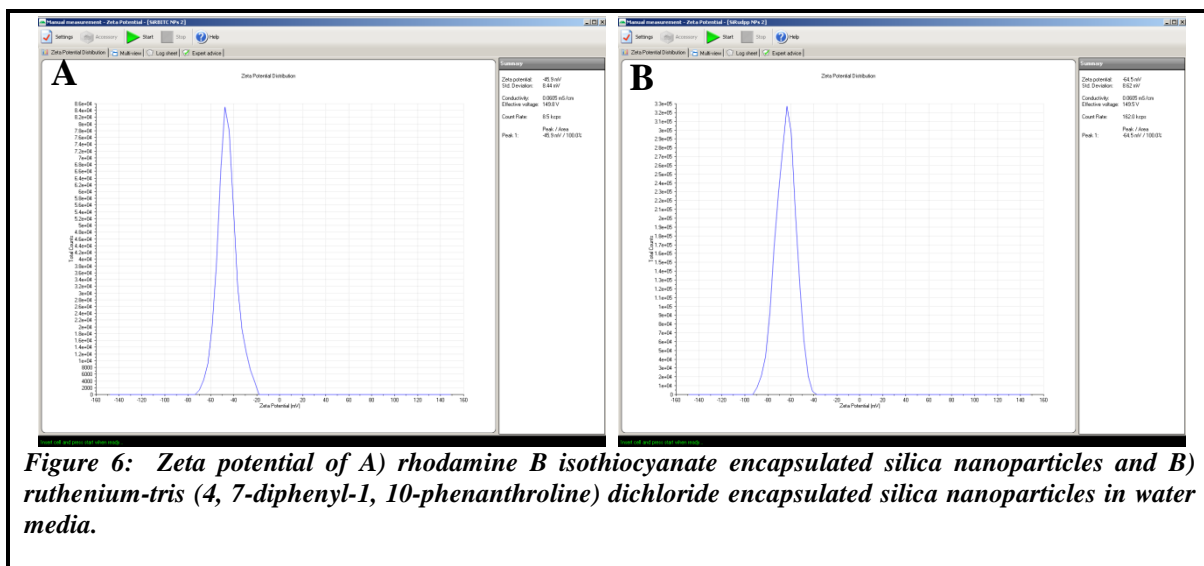
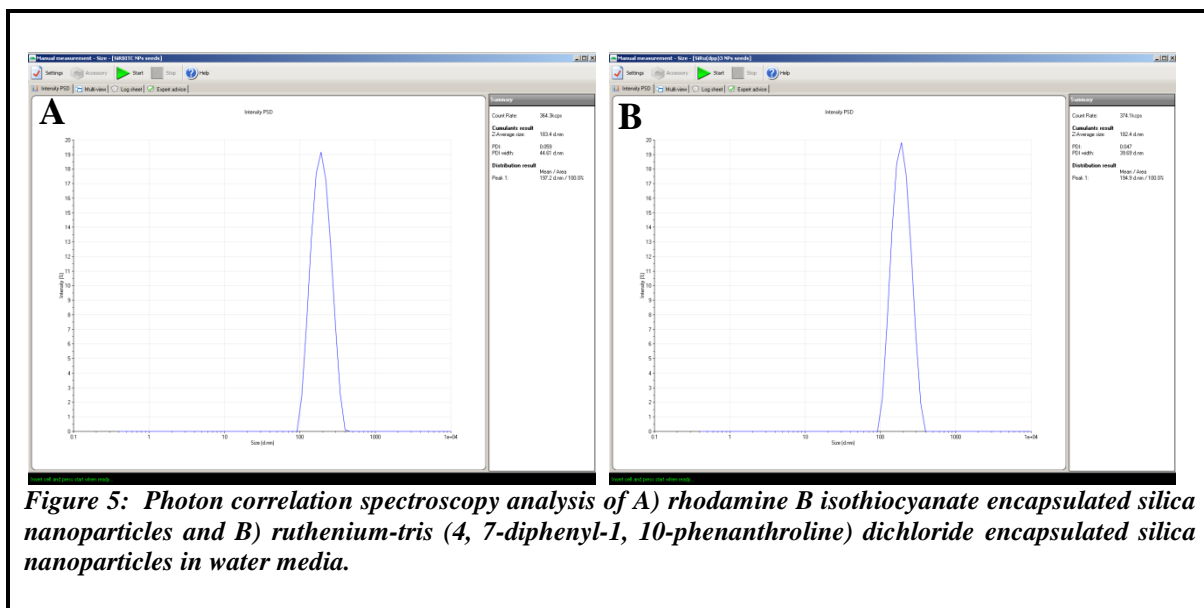


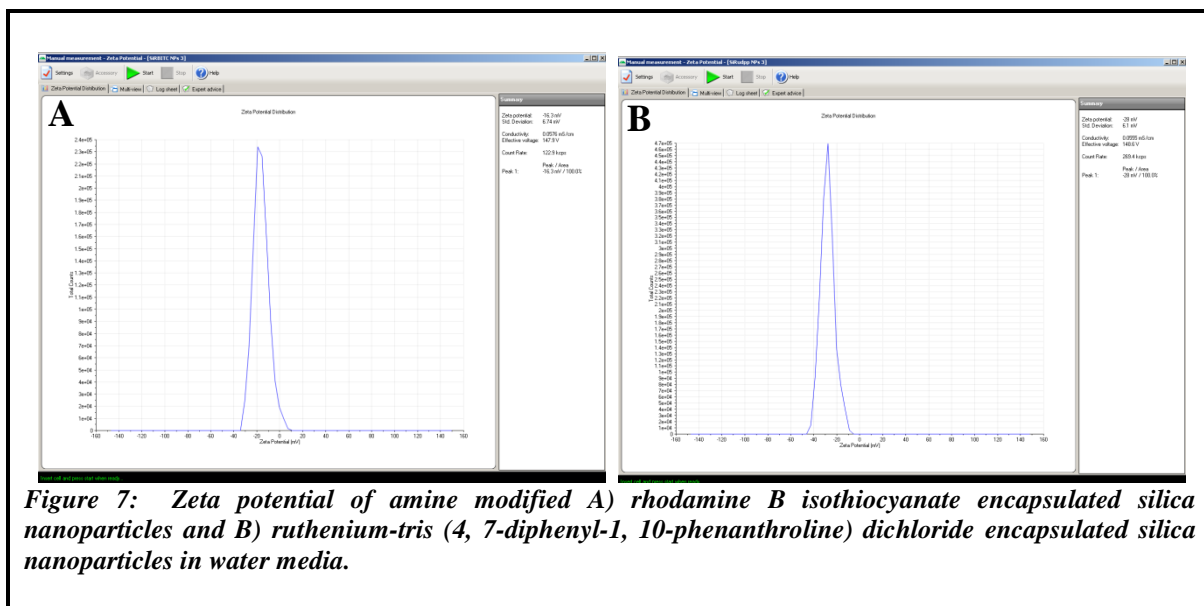


**Figure 2:** The hydrodynamic diameter and stability of  $27 \pm 7$  nm silica nanoparticles determined with A) photon correlation spectroscopy analysis in water, B) zeta potential in water, C) photon correlation spectroscopy analysis in physiological salt solution and D) zeta potential in physiological salt solution.

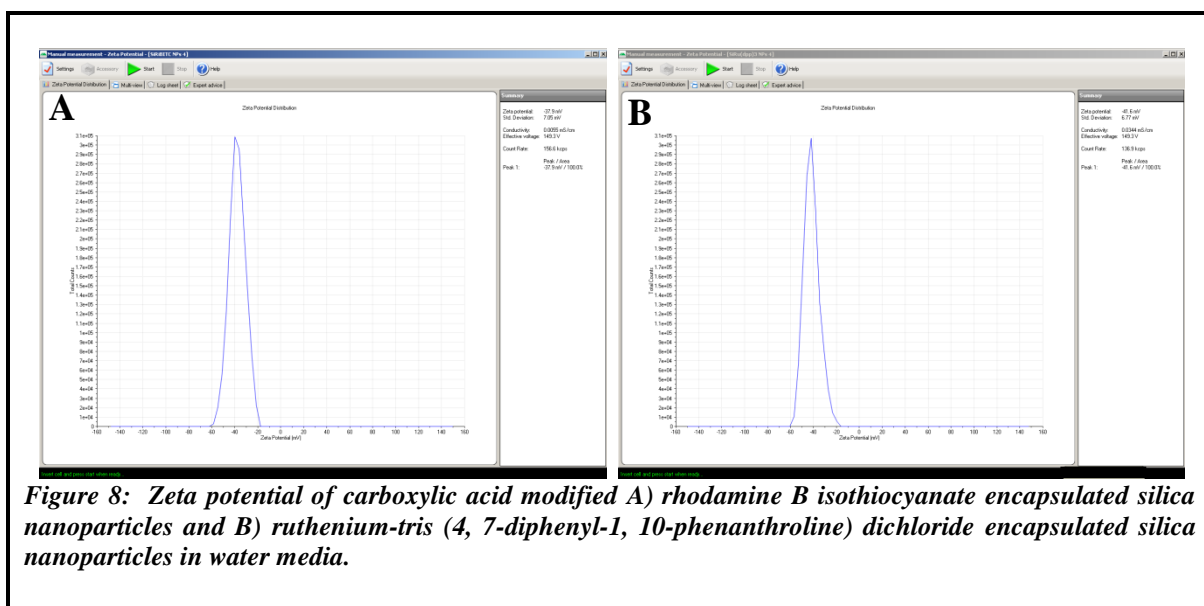




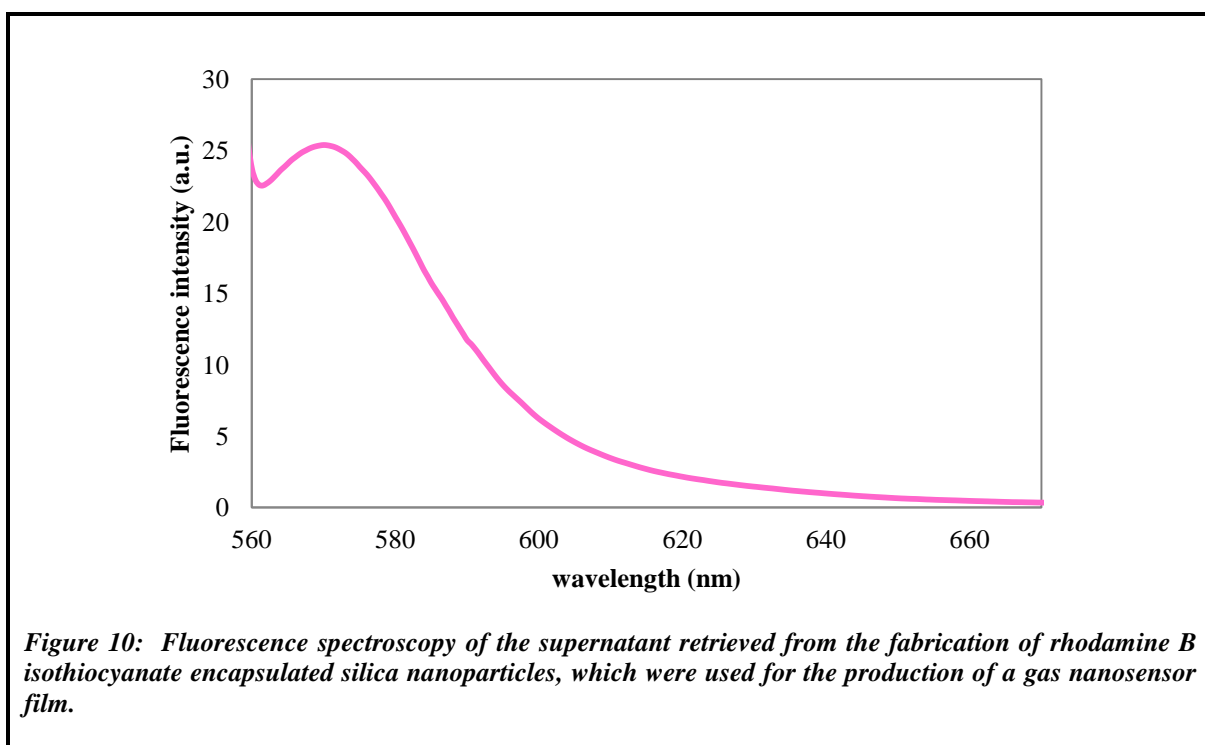
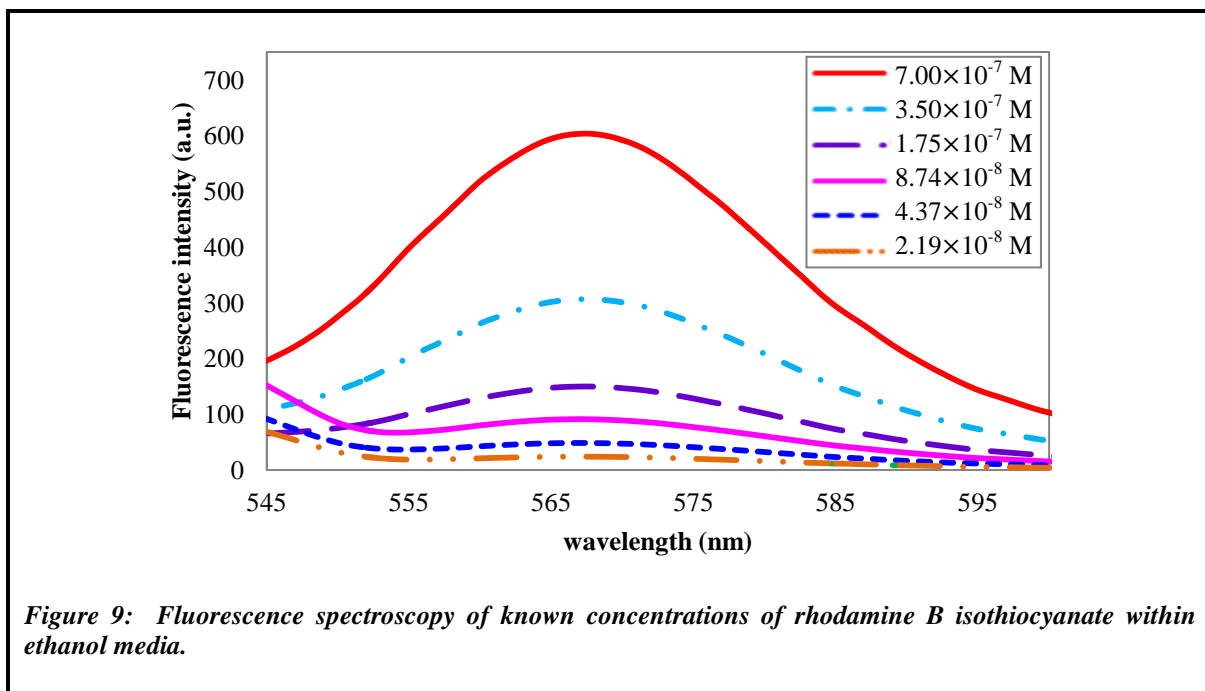


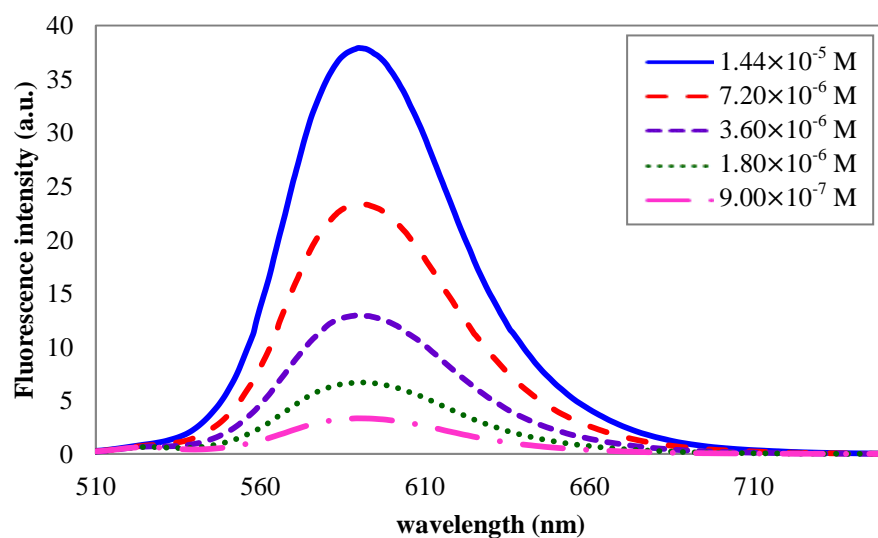


**Figure 7:** Zeta potential of amine modified **A**) rhodamine **B**) isothiocyanate encapsulated silica nanoparticles and **B**) ruthenium-tris (4, 7-diphenyl-1, 10-phenanthroline) dichloride encapsulated silica nanoparticles in water media.

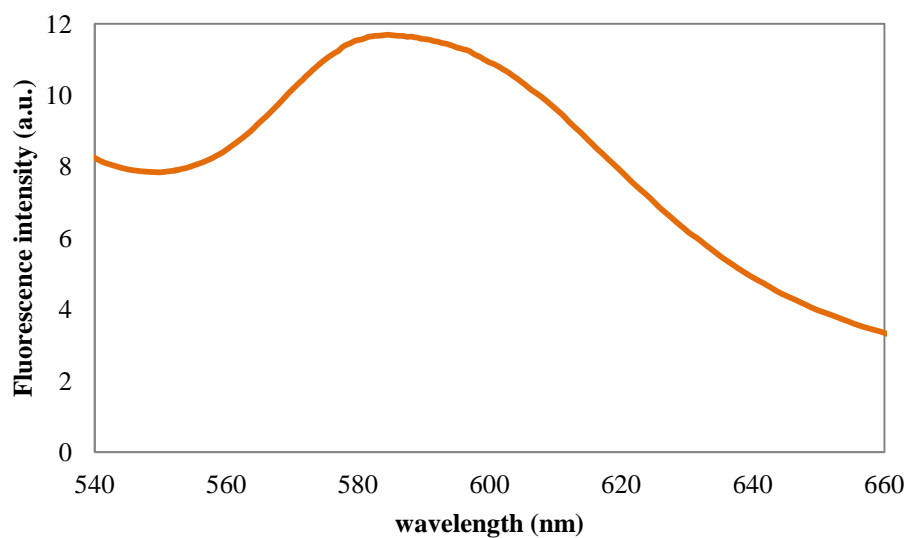


**Figure 8:** Zeta potential of carboxylic acid modified **A**) rhodamine **B**) isothiocyanate encapsulated silica nanoparticles and **B**) ruthenium-tris (4, 7-diphenyl-1, 10-phenanthroline) dichloride encapsulated silica nanoparticles in water media.

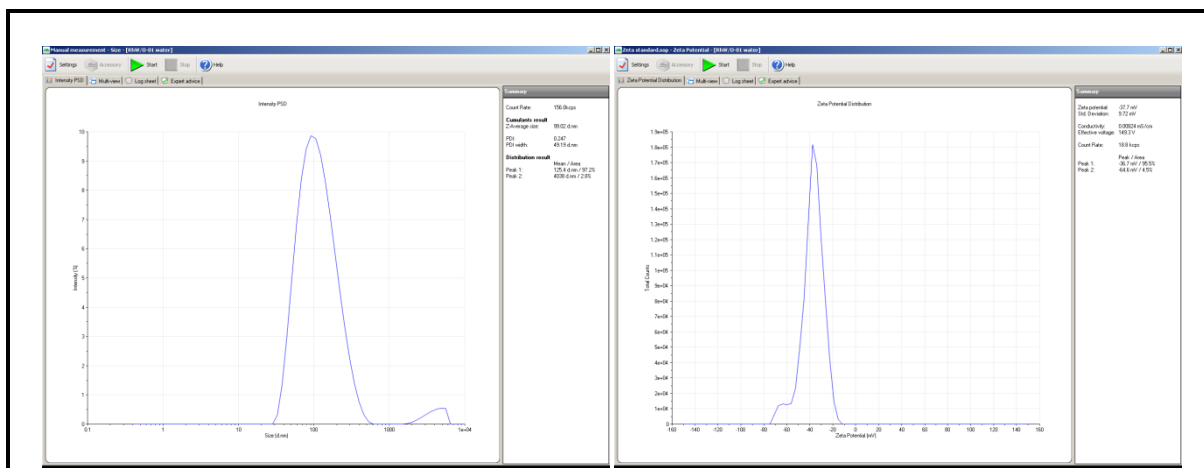




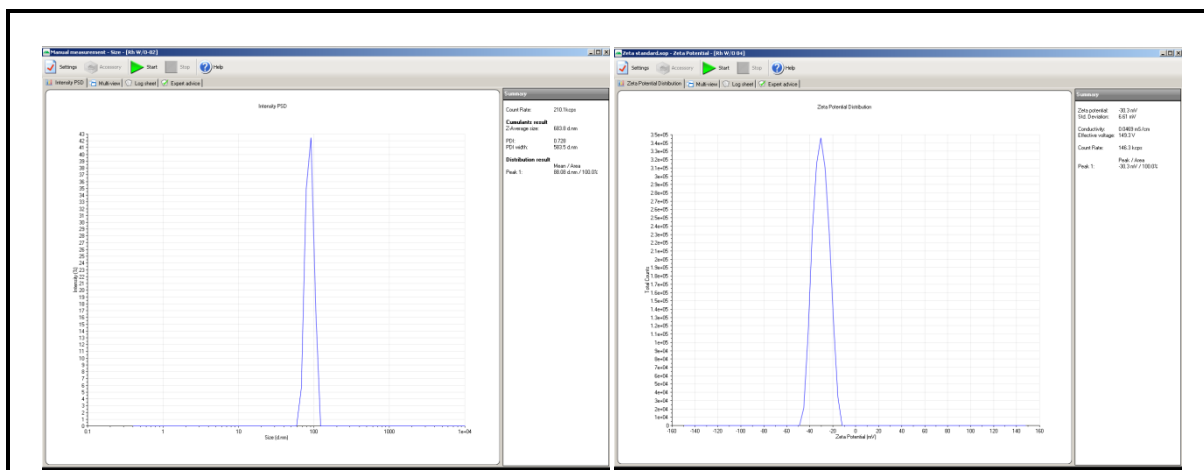
*Figure 11: Fluorescence spectroscopy of known concentrations of ruthenium-tris (4, 7-diphenyl-1, 10-phenanthroline) dichloride within ethanol media.*



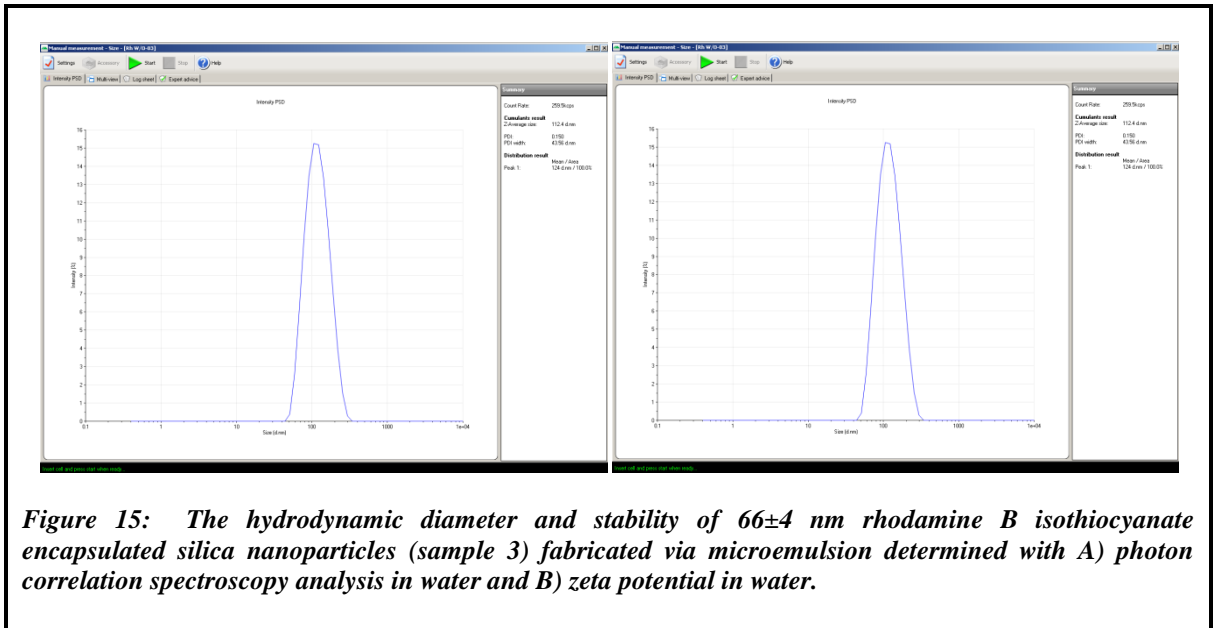
*Figure 12: Fluorescence spectroscopy of the supernatant retrieved from the fabrication of ruthenium-tris (4, 7-diphenyl-1, 10-phenanthroline) dichloride encapsulated silica nanoparticles, which were used for the production of a gas nanosensor film.*



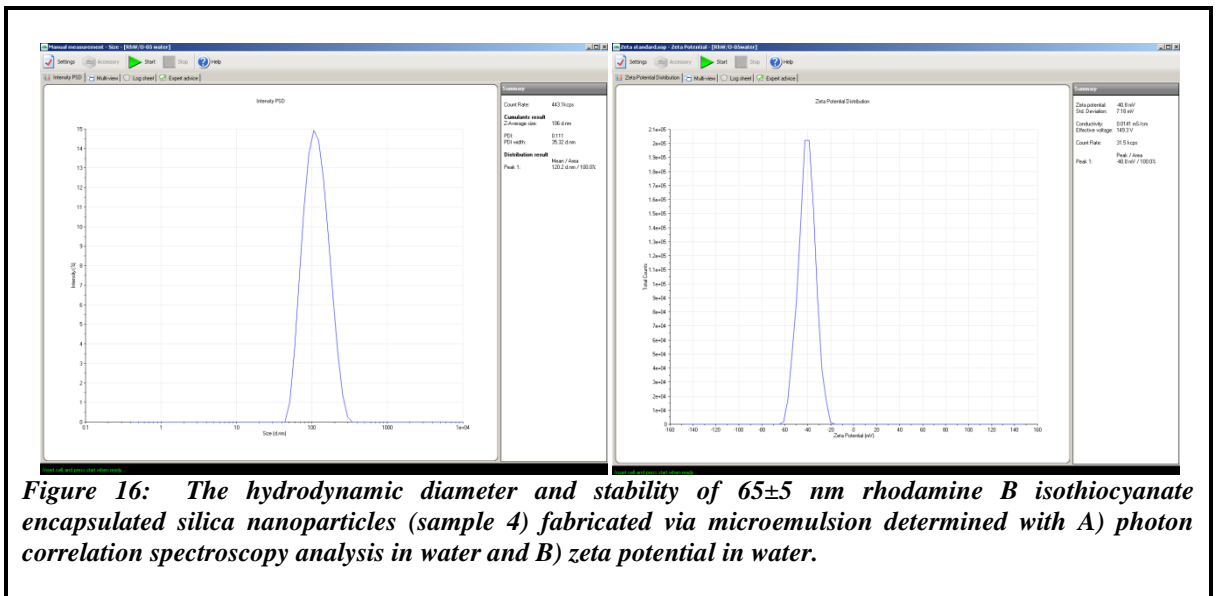
**Figure 13:** The hydrodynamic diameter and stability of  $48 \pm 4$  nm rhodamine B isothiocyanate encapsulated silica nanoparticles (sample 1) fabricated via microemulsion determined with A) photon correlation spectroscopy analysis in water and B) zeta potential in water.



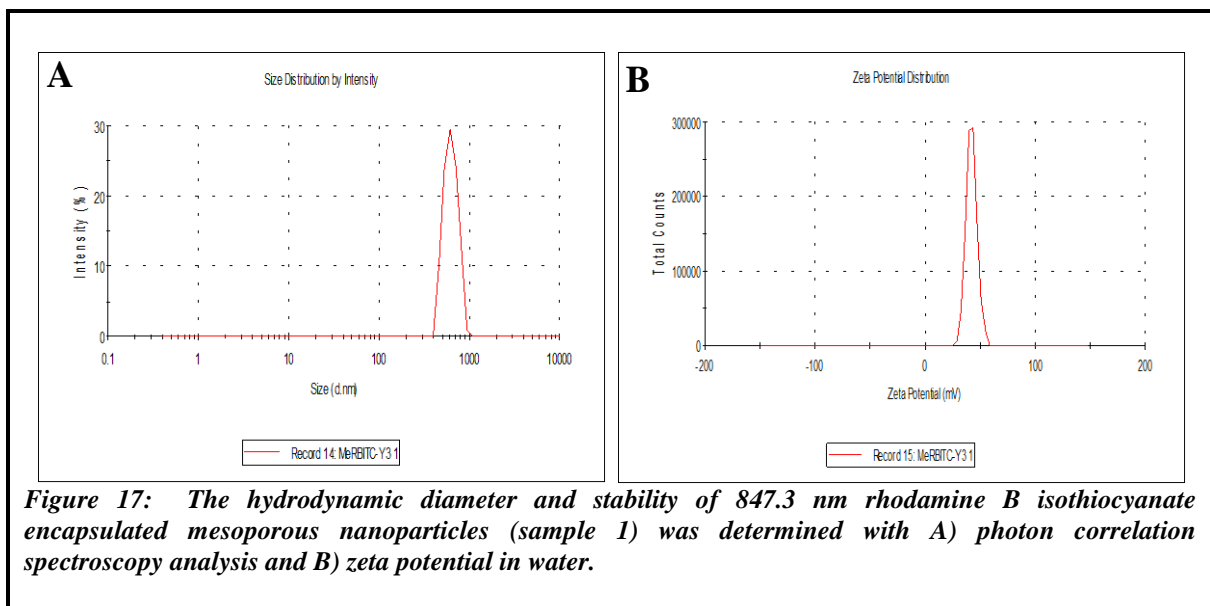
**Figure 14:** The hydrodynamic diameter and stability of  $54 \pm 9$  nm rhodamine B isothiocyanate encapsulated silica nanoparticles (sample 2) fabricated via microemulsion determined with A) photon correlation spectroscopy analysis in water and B) zeta potential in water.



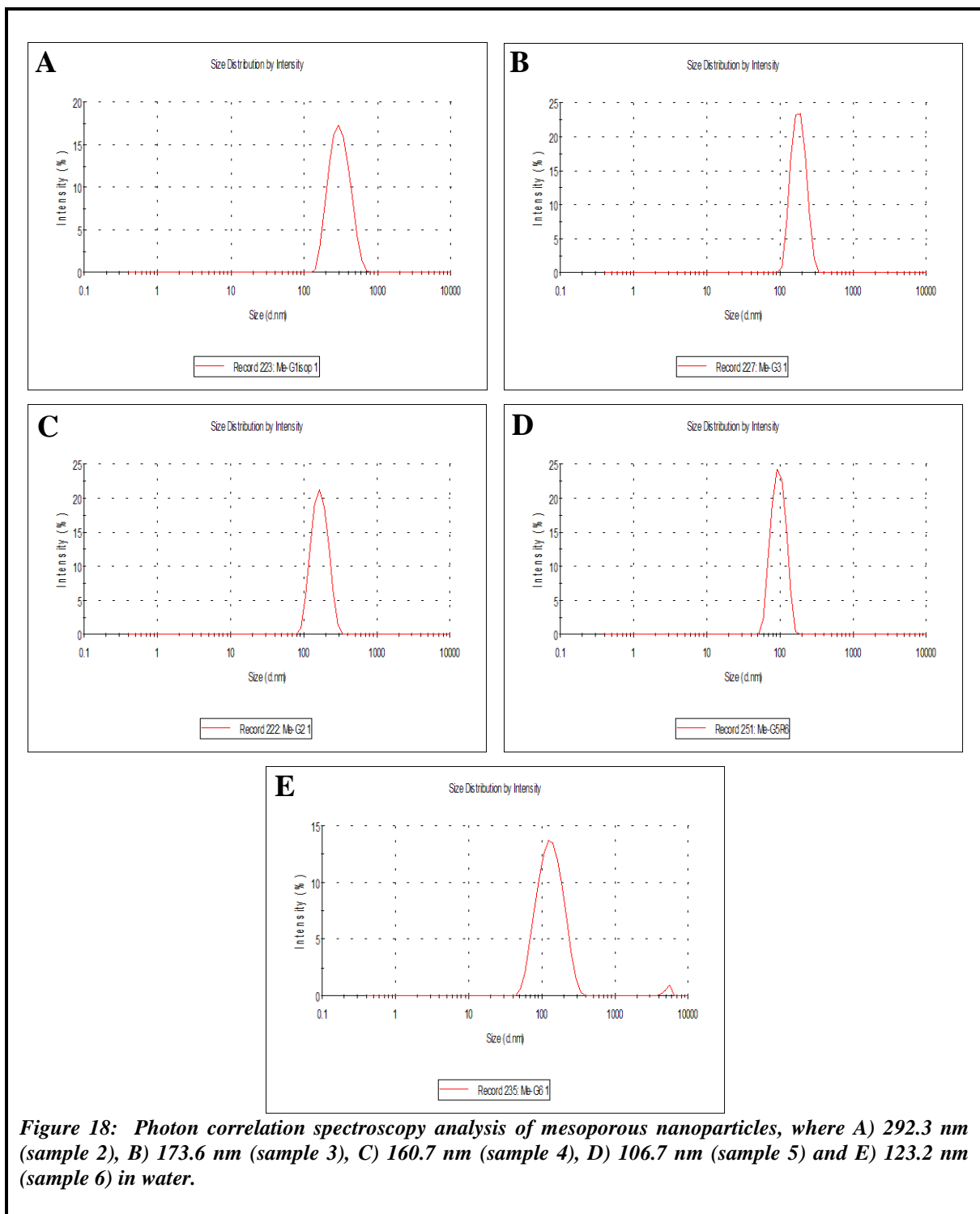
**Figure 15:** The hydrodynamic diameter and stability of  $66\pm 4$  nm rhodamine B isothiocyanate encapsulated silica nanoparticles (sample 3) fabricated via microemulsion determined with A) photon correlation spectroscopy analysis in water and B) zeta potential in water.

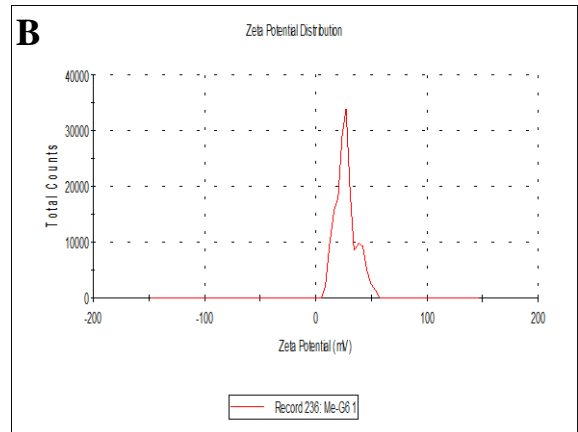
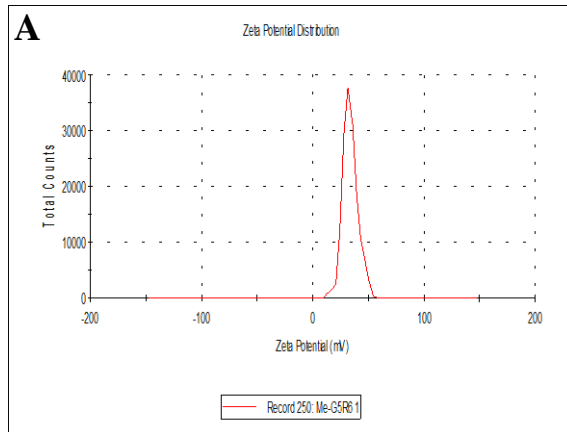


**Figure 16:** The hydrodynamic diameter and stability of  $65\pm 5$  nm rhodamine B isothiocyanate encapsulated silica nanoparticles (sample 4) fabricated via microemulsion determined with A) photon correlation spectroscopy analysis in water and B) zeta potential in water.

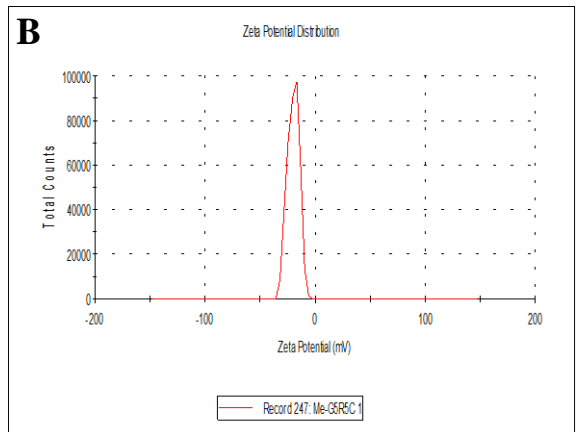
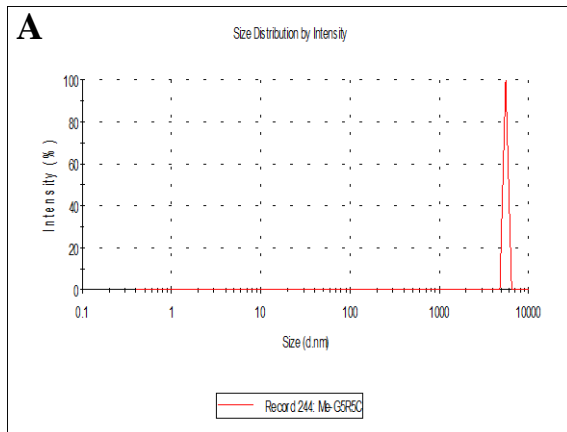


**Figure 17:** The hydrodynamic diameter and stability of 847.3 nm rhodamine B isothiocyanate encapsulated mesoporous nanoparticles (sample 1) was determined with A) photon correlation spectroscopy analysis and B) zeta potential in water.

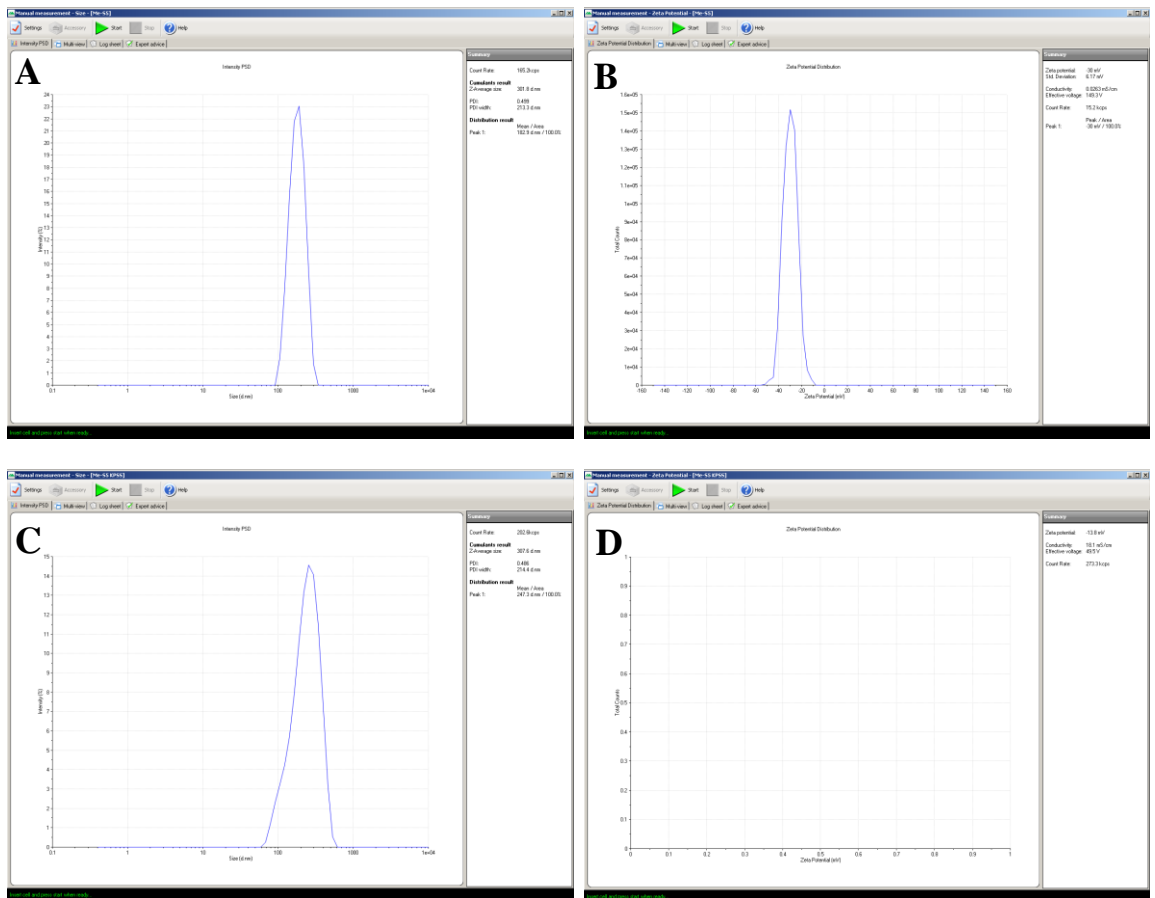




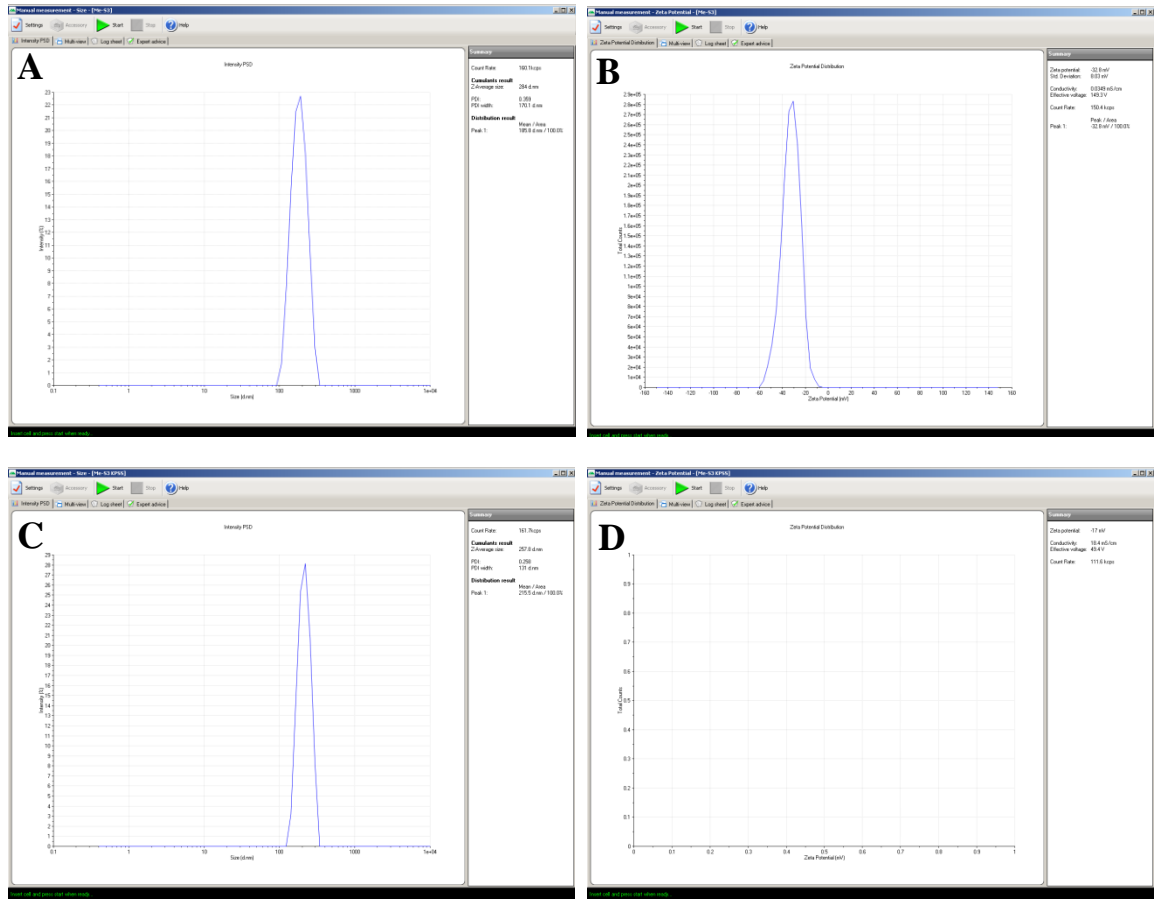
**Figure 19:** Zeta potential of mesoporous nanoparticles for A) 106.7 nm (sample 5) and B) 123.2 nm (sample 6) in water media.



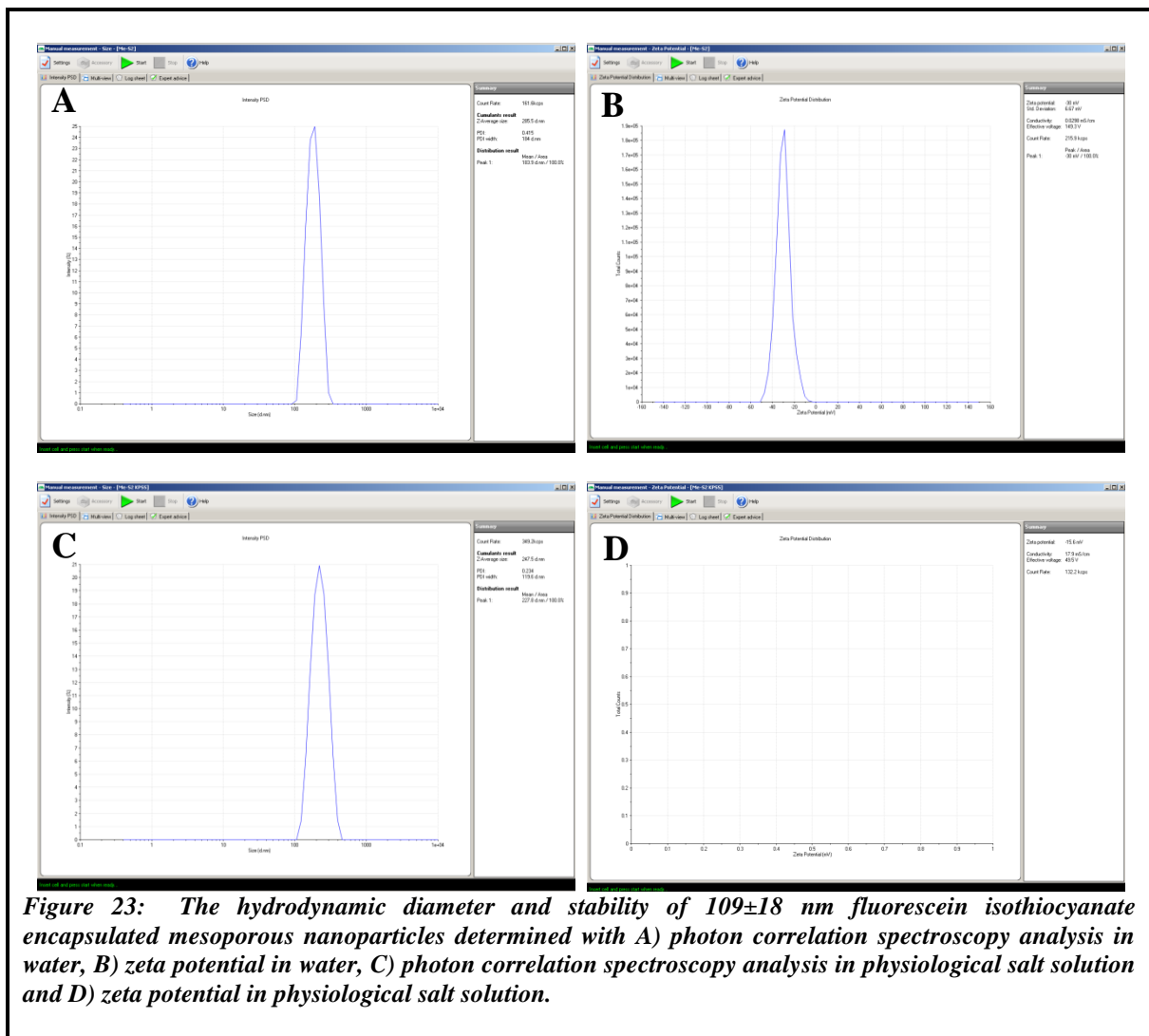
**Figure 20:** The hydrodynamic diameter and stability of mesoporous nanoparticles 8139 nm (sample 5) after calcination was determined with A) photon correlation spectroscopy analysis and B) zeta potential in water.



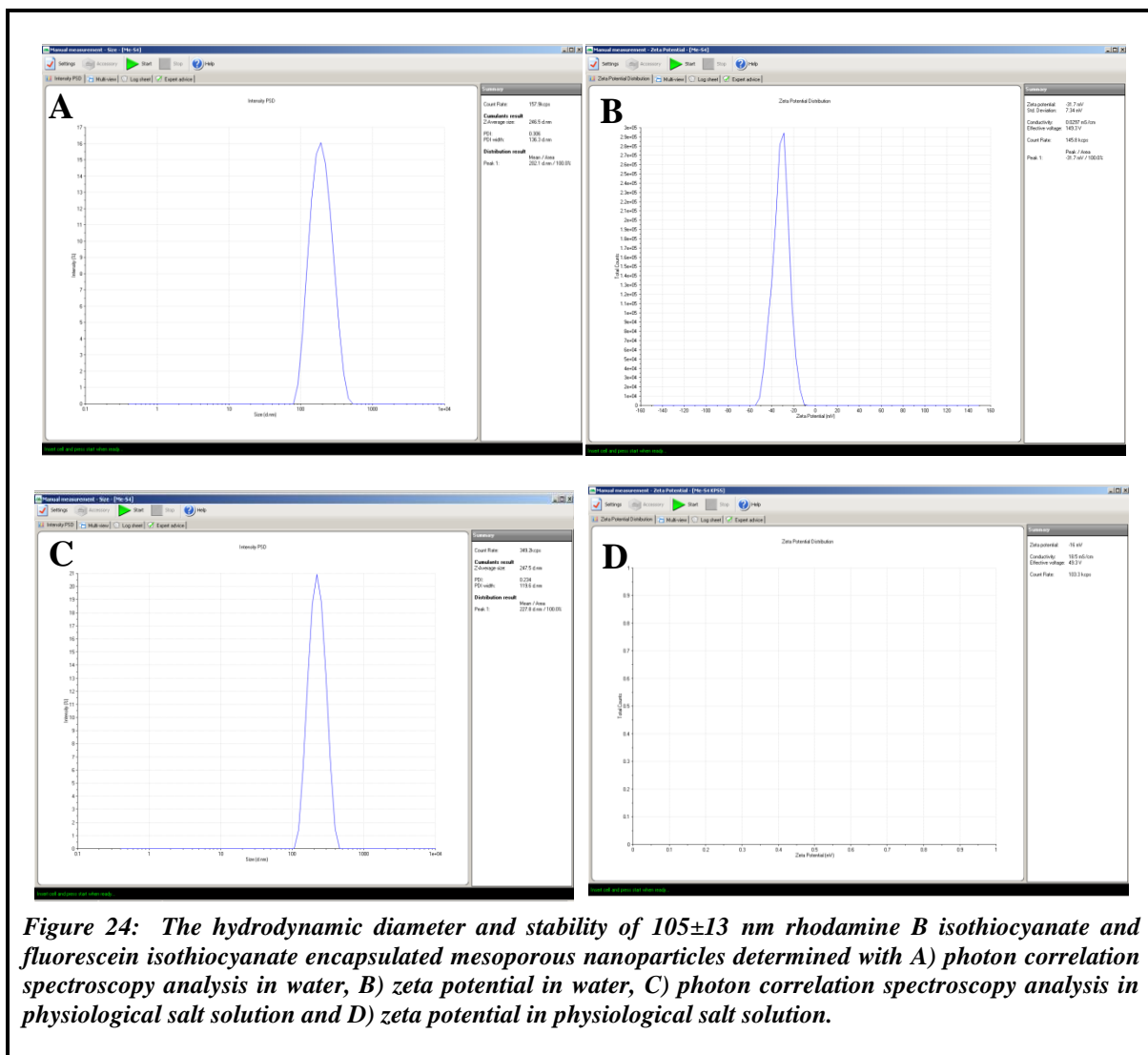
**Figure 21:** The hydrodynamic diameter and stability of  $95 \pm 13$  nm mesoporous nanoparticles determined with A) photon correlation spectroscopy analysis in water, B) zeta potential in water, C) photon correlation spectroscopy analysis in physiological salt solution and D) zeta potential in physiological salt solution.



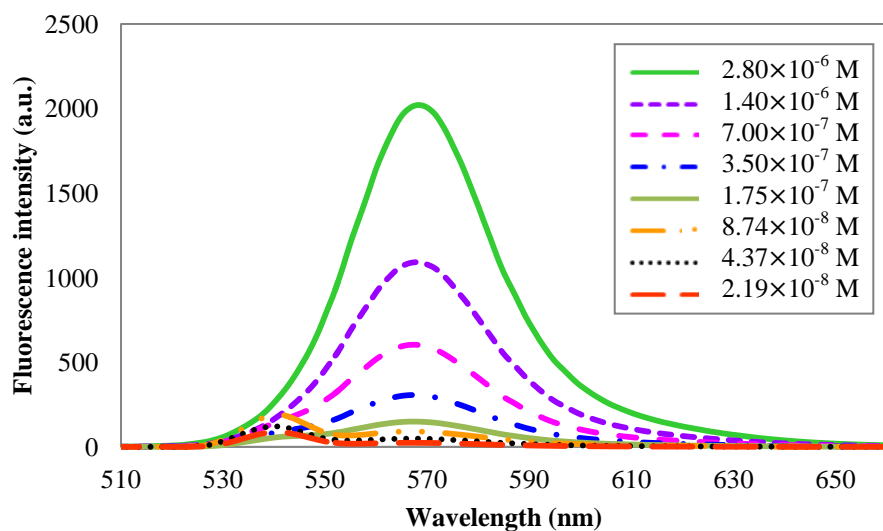
**Figure 22:** The hydrodynamic diameter and stability of  $105 \pm 13$  nm rhodamine B isothiocyanate encapsulated mesoporous nanoparticles determined with A) photon correlation spectroscopy analysis in water, B) zeta potential in water, C) photon correlation spectroscopy analysis in physiological salt solution and D) zeta potential in physiological salt solution.



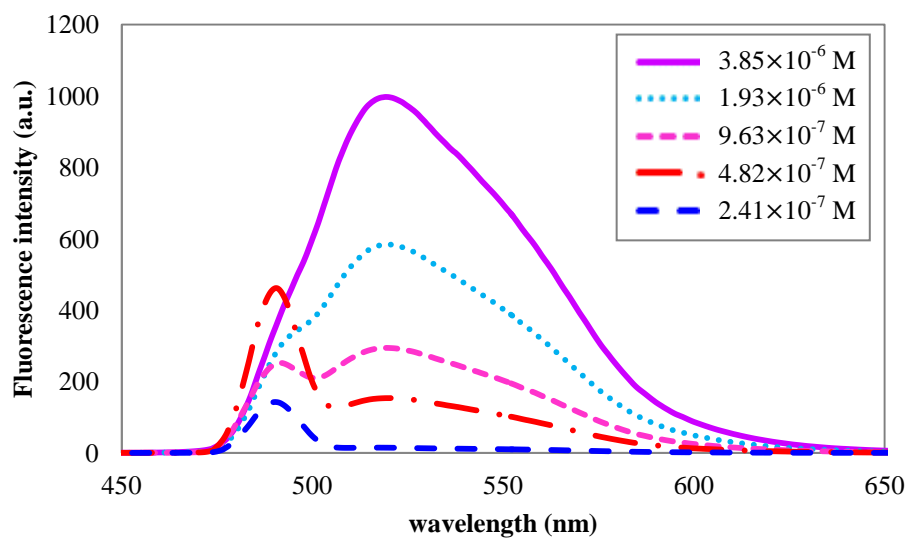
**Figure 23:** The hydrodynamic diameter and stability of  $109 \pm 18$  nm fluorescein isothiocyanate encapsulated mesoporous nanoparticles determined with A) photon correlation spectroscopy analysis in water, B) zeta potential in water, C) photon correlation spectroscopy analysis in physiological salt solution and D) zeta potential in physiological salt solution.



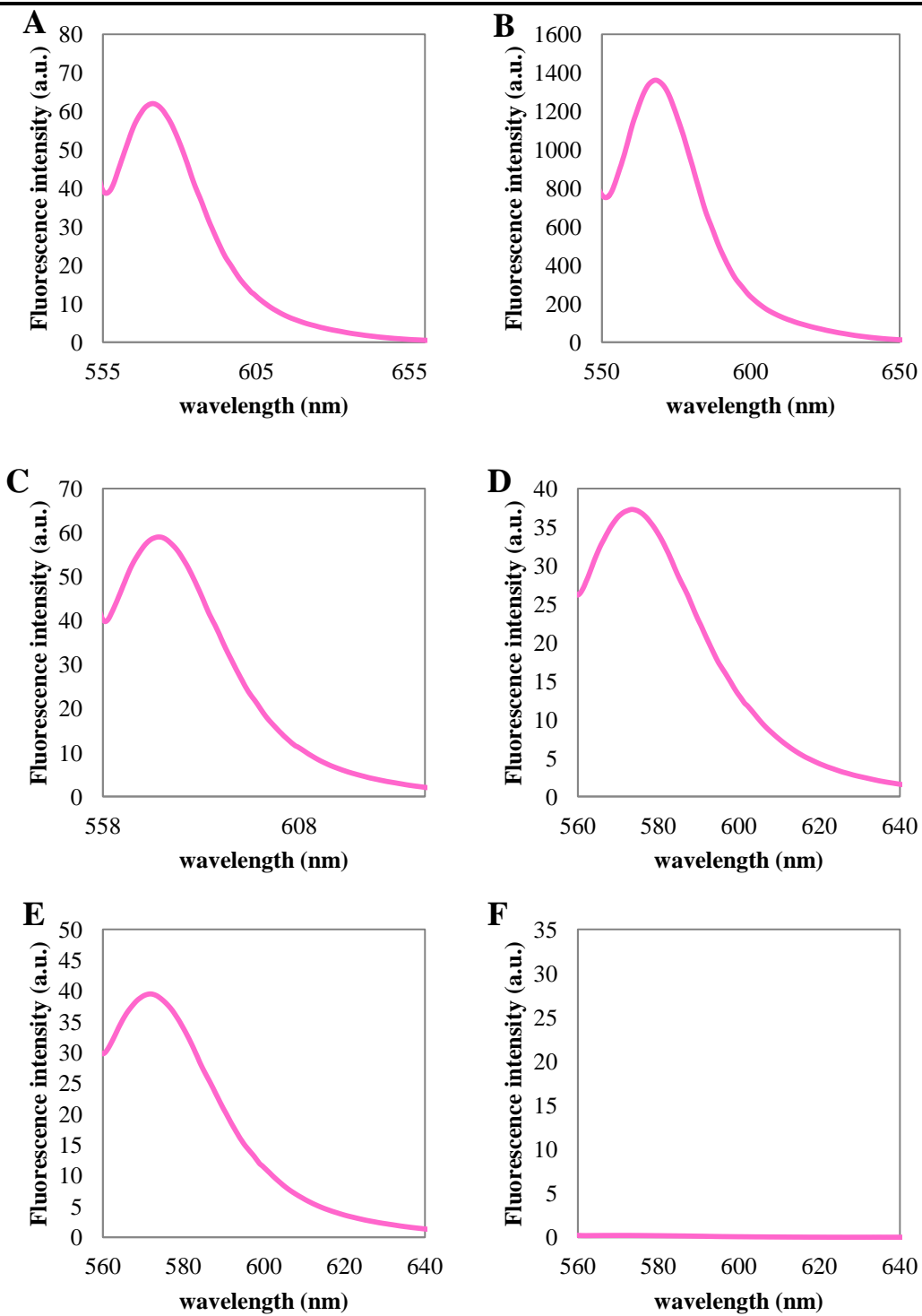
**Figure 24:** The hydrodynamic diameter and stability of  $105 \pm 13$  nm rhodamine B isothiocyanate and fluorescein isothiocyanate encapsulated mesoporous nanoparticles determined with A) photon correlation spectroscopy analysis in water, B) zeta potential in water, C) photon correlation spectroscopy analysis in physiological salt solution and D) zeta potential in physiological salt solution.



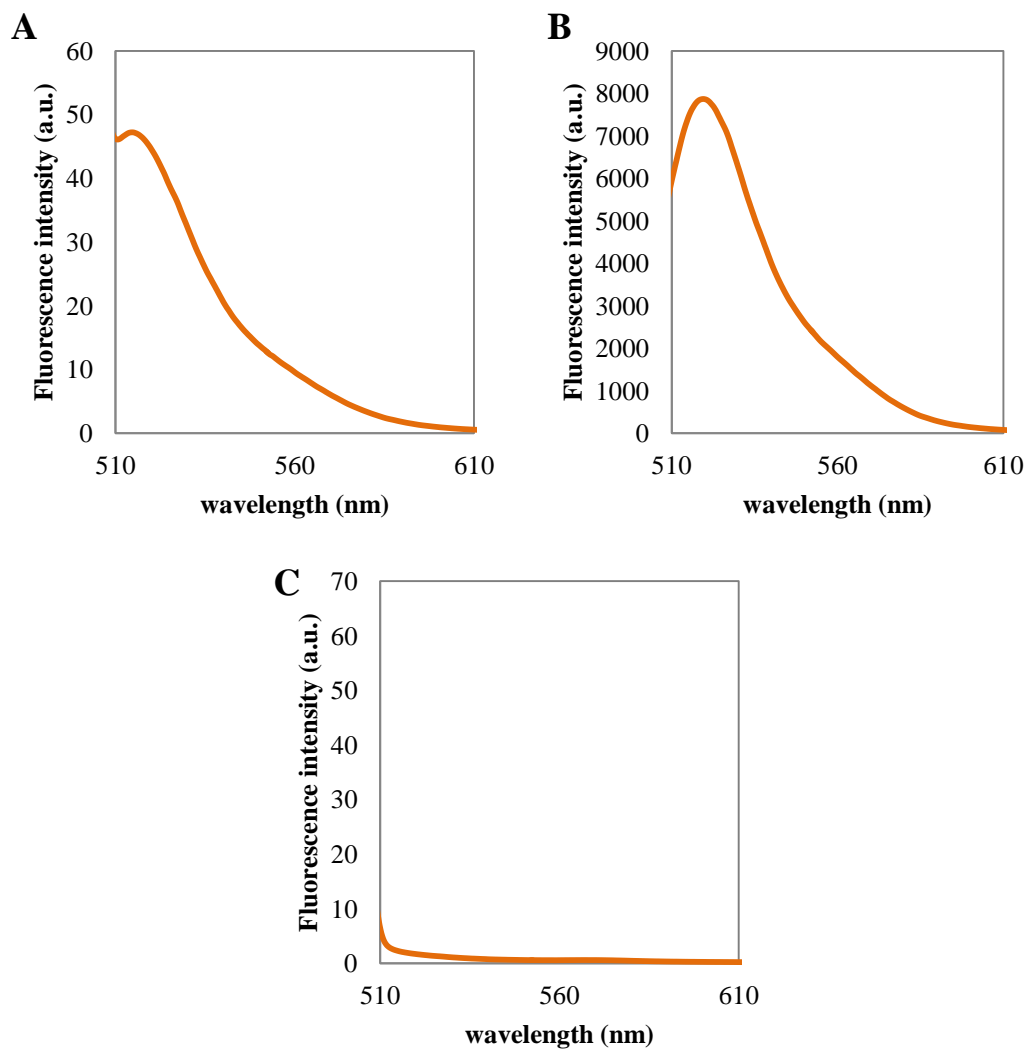
*Figure 25: Fluorescence spectroscopy of known concentrations of rhodamine B isothiocyanate in ethanol solutions (higher concentration) for calculating amount of dye molecules within mesoporous nanoparticles.*



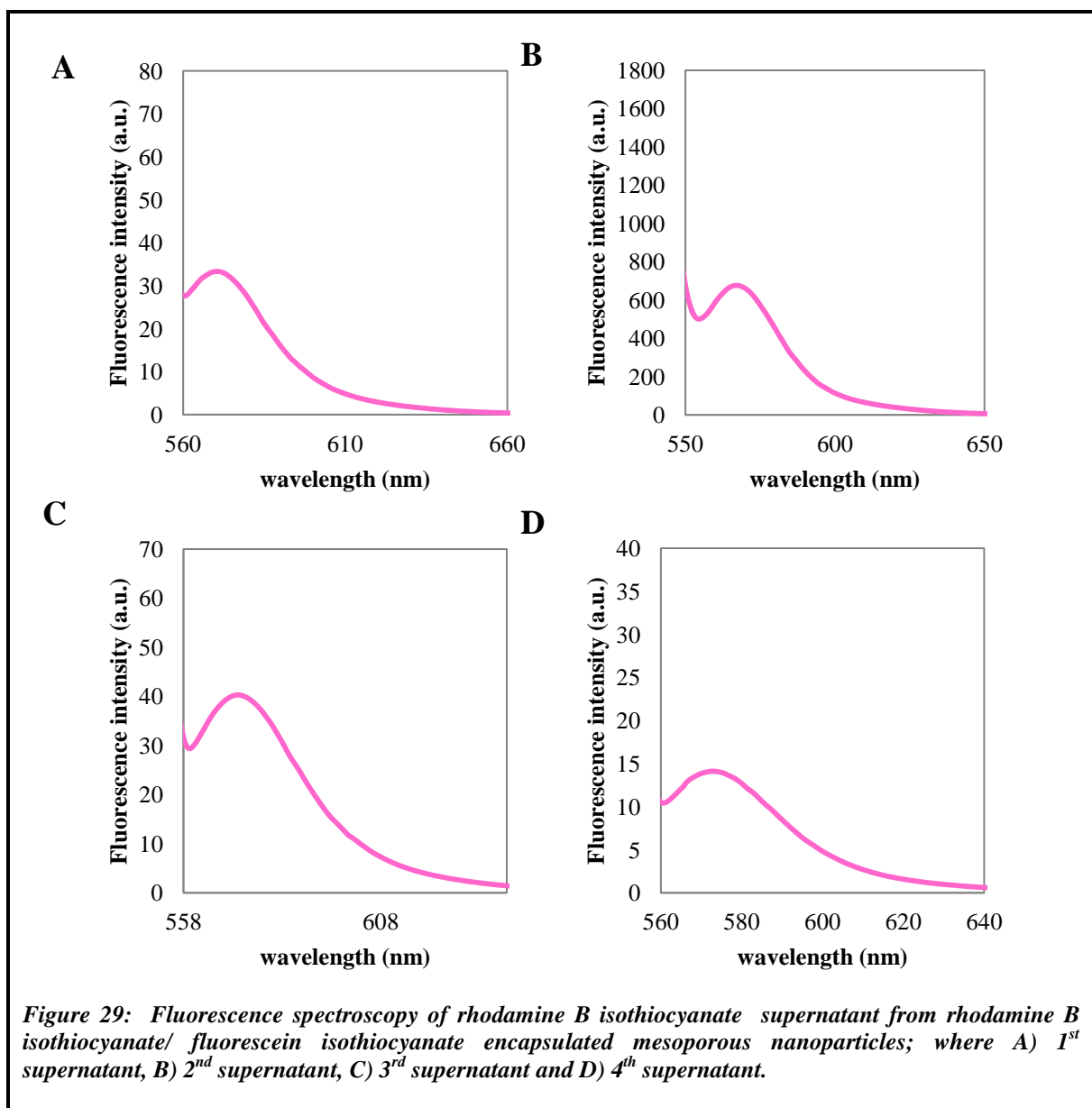
*Figure 26: Fluorescence spectroscopy of known concentration of fluorescein isothiocyanate in ethanol solutions for calculating amount of dye molecules within mesoporous nanoparticle*

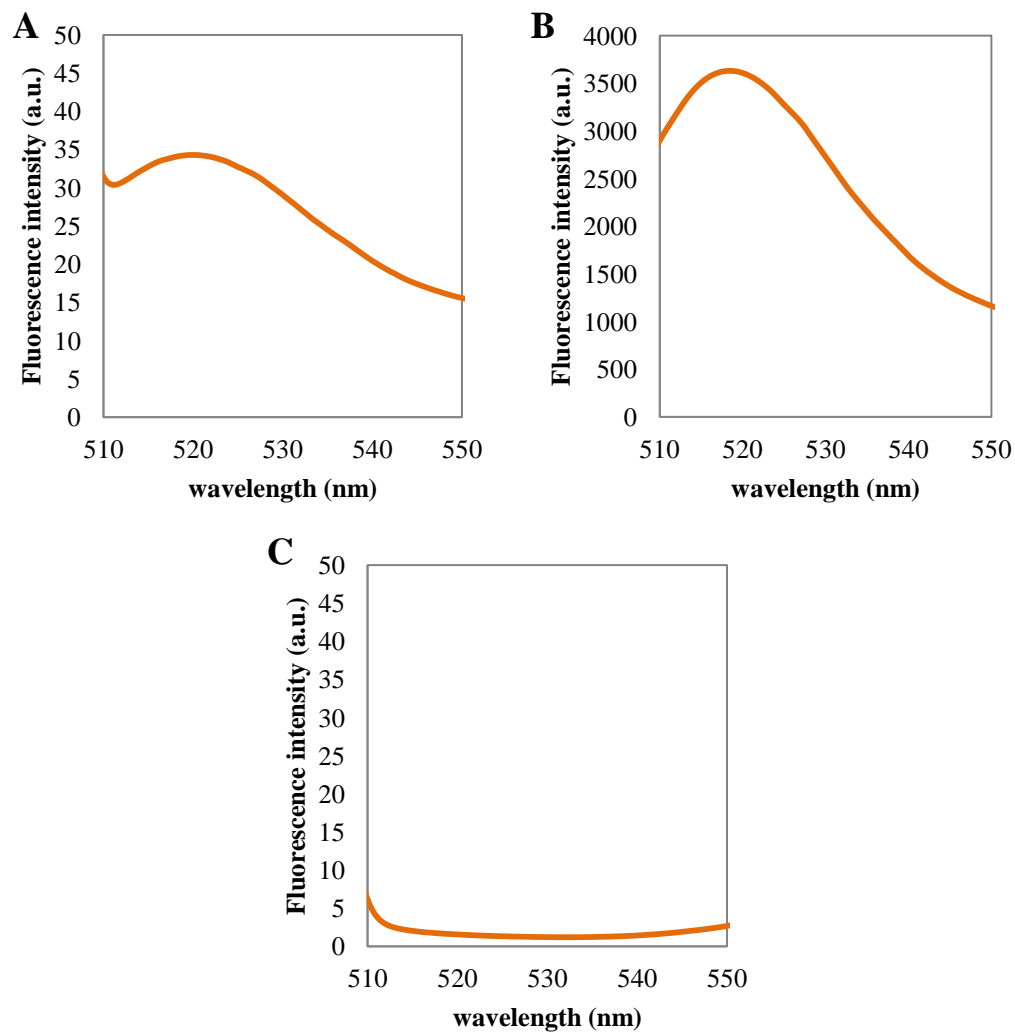


**Figure 27:** Fluorescence spectroscopy of supernatant from rhodamine B isothiocyanate mesoporous nanoparticles; where A) 1<sup>st</sup> supernatant, B) 2<sup>nd</sup> supernatant, C) 3<sup>rd</sup> supernatant, D) 4<sup>th</sup> supernatant, E) 5<sup>th</sup> supernatant and F) 6<sup>th</sup> supernatant.

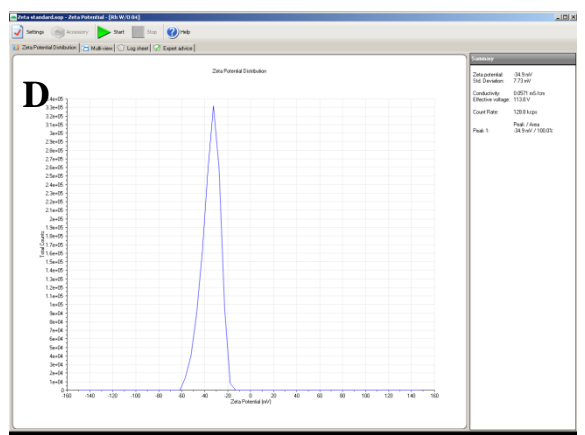
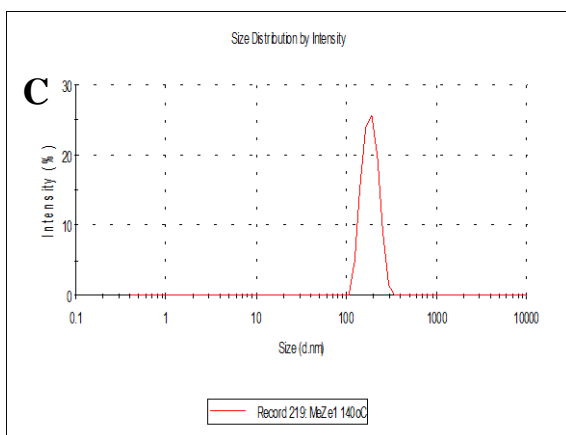
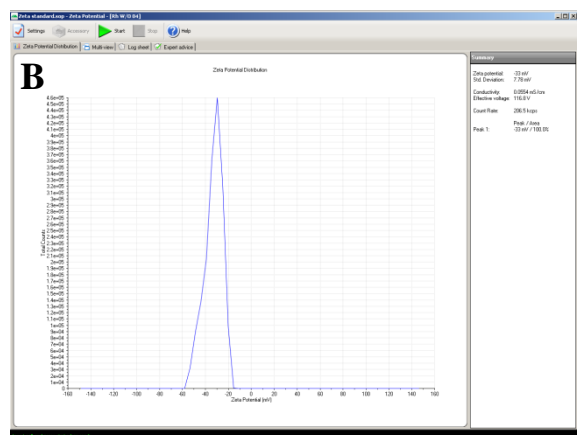
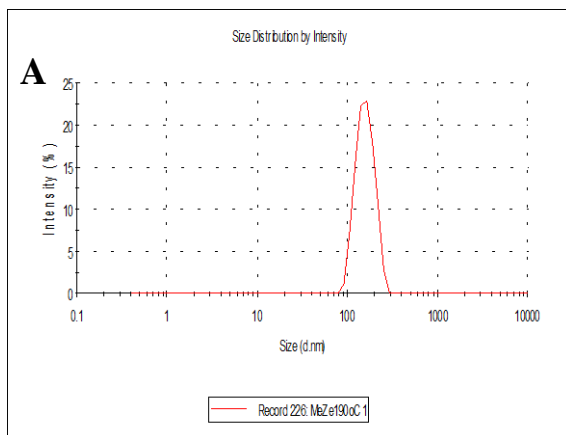


*Figure 28: Fluorescence spectroscopy of supernatant from fluorescein isothiocyanate encapsulated mesoporous nanoparticles; where A) 1<sup>st</sup> supernatant, B) 2<sup>nd</sup> supernatant and C) 3<sup>rd</sup> supernatant.*

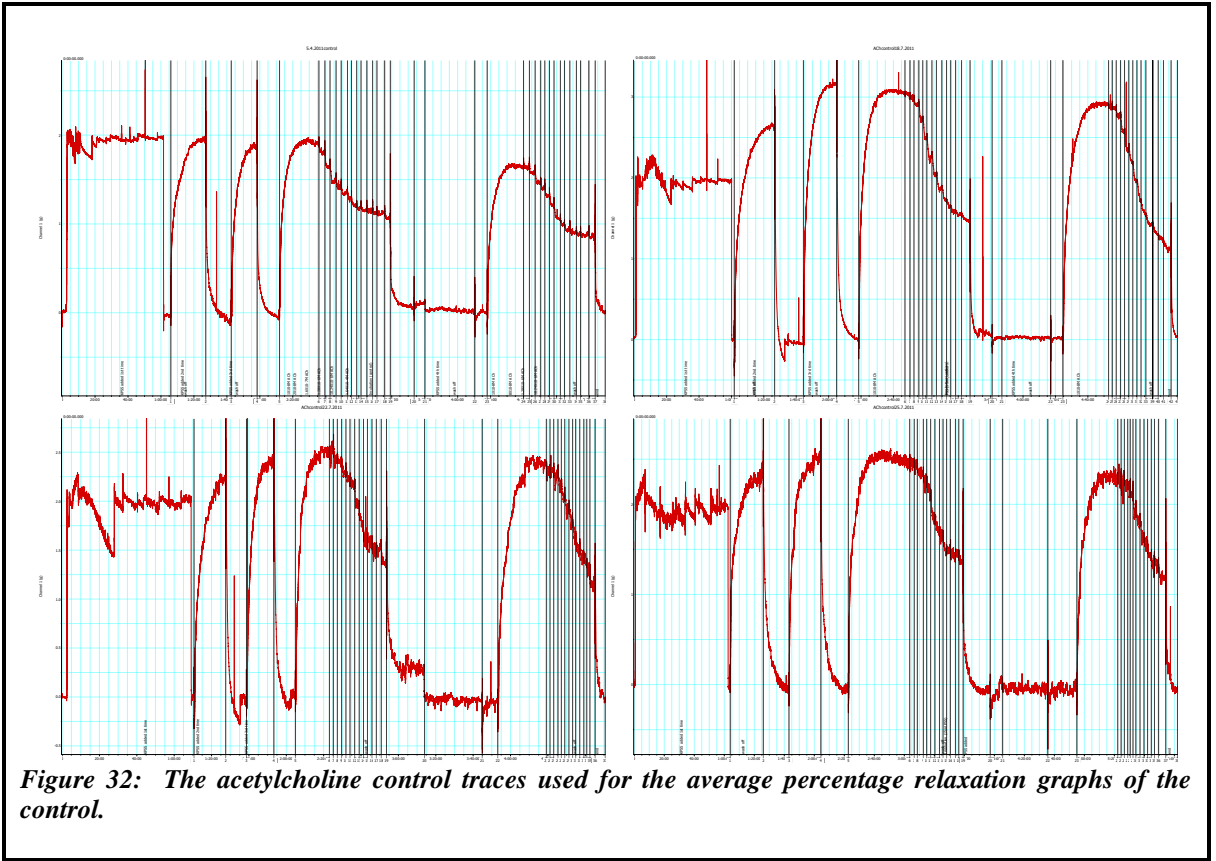




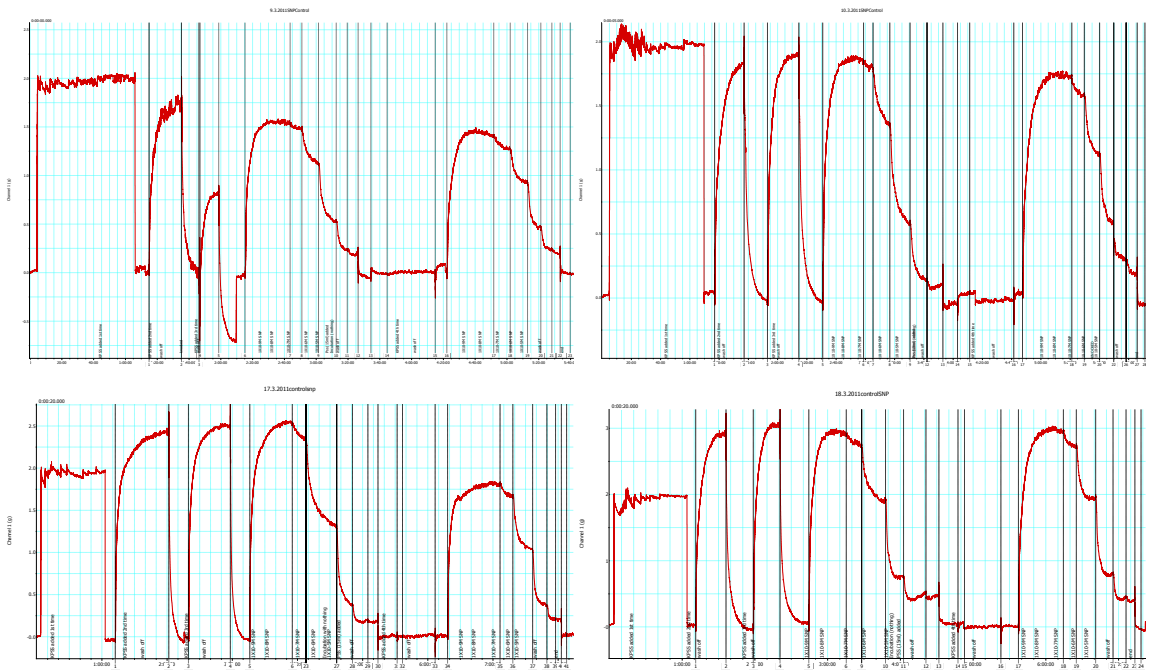
**Figure 30:** Fluorescence spectroscopy of fluorescein isothiocyanate supernatant from rhodamine B isothiocyanate/ fluorescein isothiocyanate encapsulated mesoporous nanoparticles; where A) 1<sup>st</sup> supernatant, B) 2<sup>nd</sup> supernatant and C) 3<sup>rd</sup> supernatant.



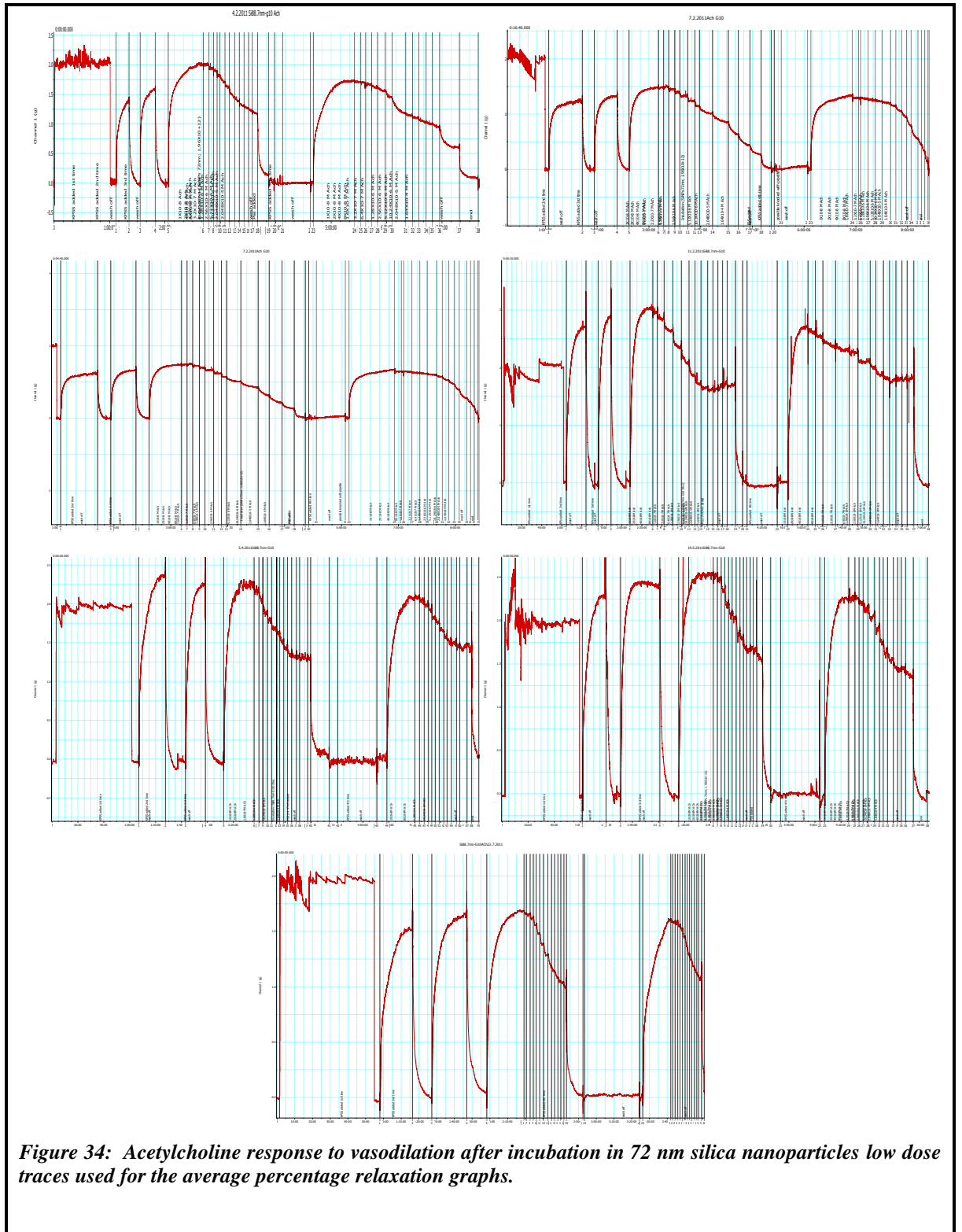
**Figure 31:** The hydrodynamic diameter and stability of silicate-1; where A) the photon correlation spectroscopy analysis of 180.6 nm, B) zeta potential of 180.6 nm, C) photon correlation spectroscopy analysis of 152.5 nm and D) zeta potential of 152.5 nm in water media.



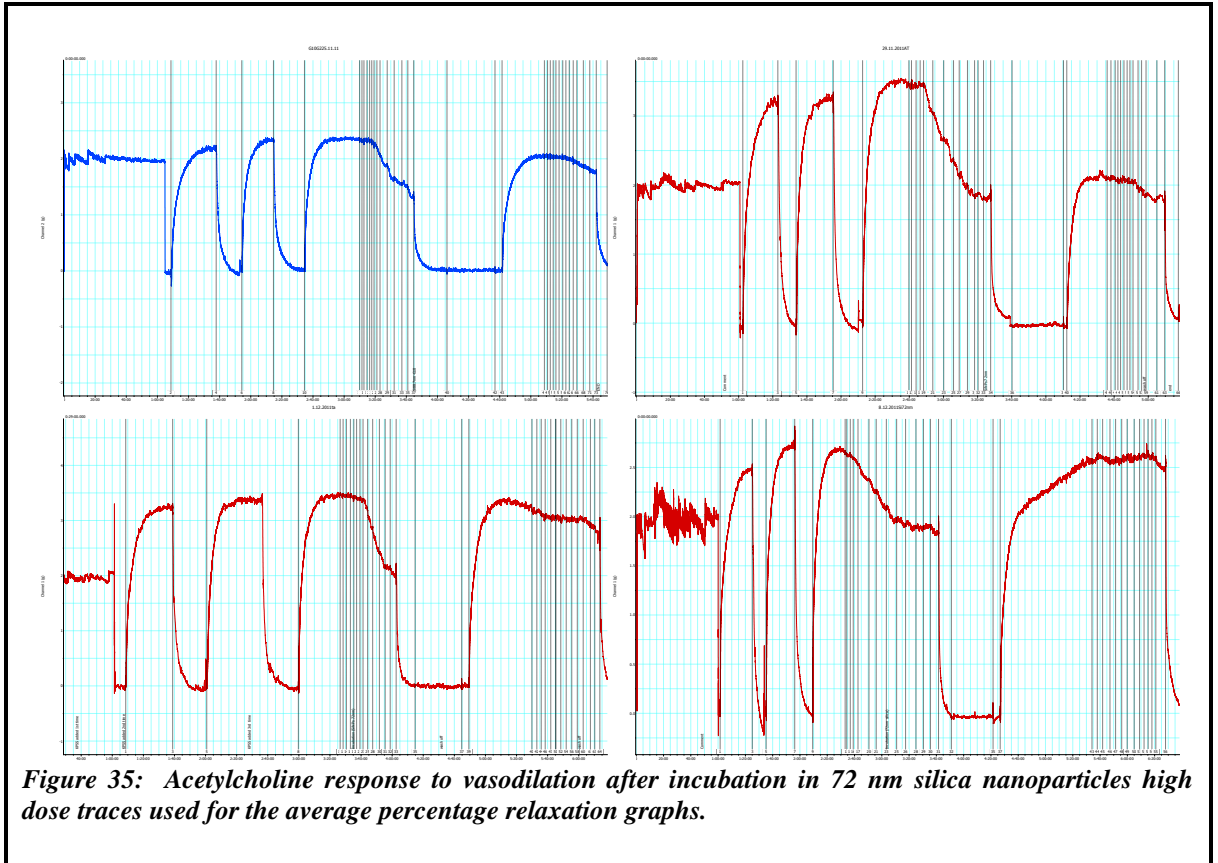
*Figure 32: The acetylcholine control traces used for the average percentage relaxation graphs of the control.*



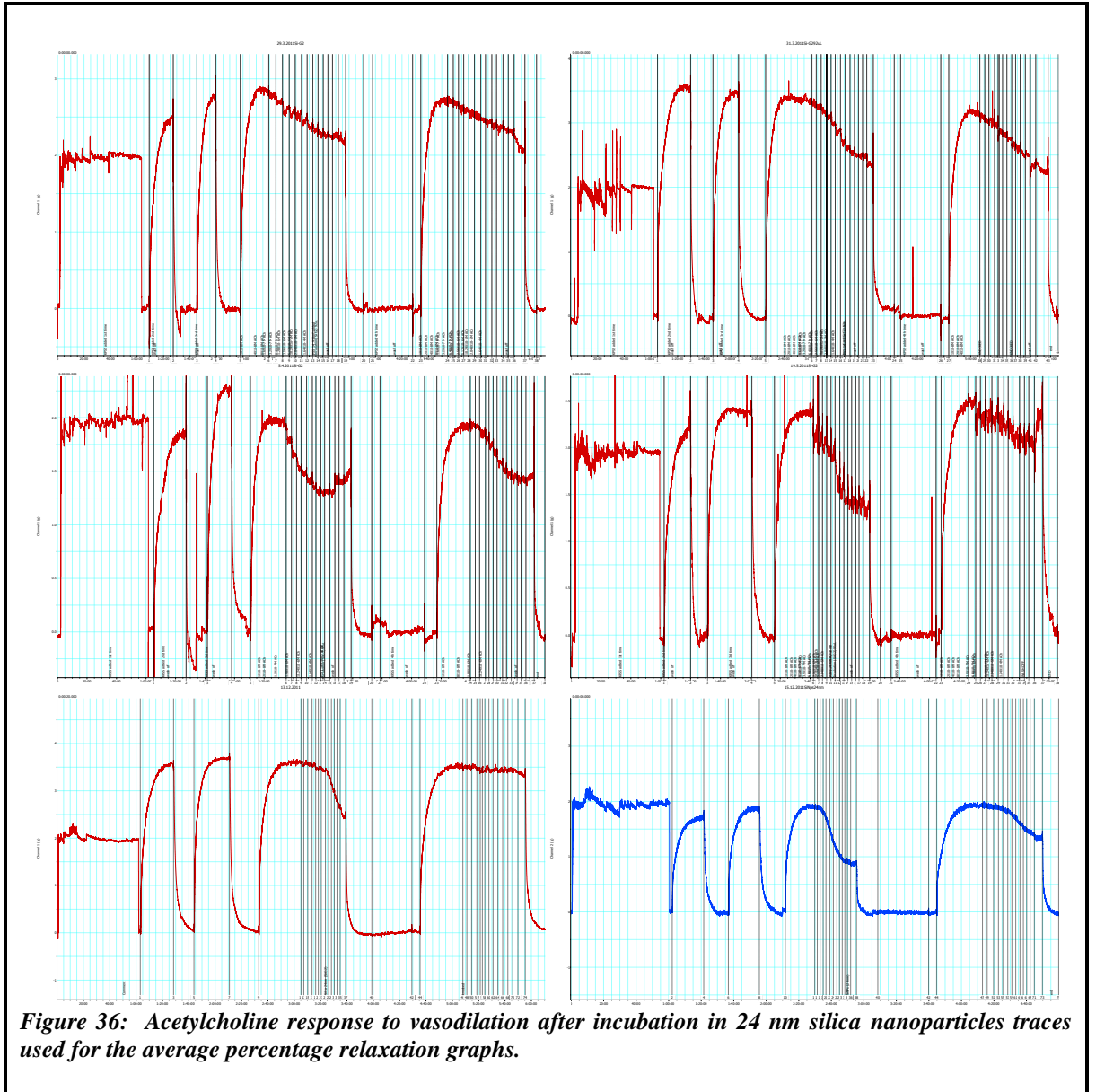
**Figure 33:** *The sodium nitroprusside control traces used for the average percentage relaxation graphs of the control.*



**Figure 34: Acetylcholine response to vasodilation after incubation in 72 nm silica nanoparticles low dose traces used for the average percentage relaxation graphs.**



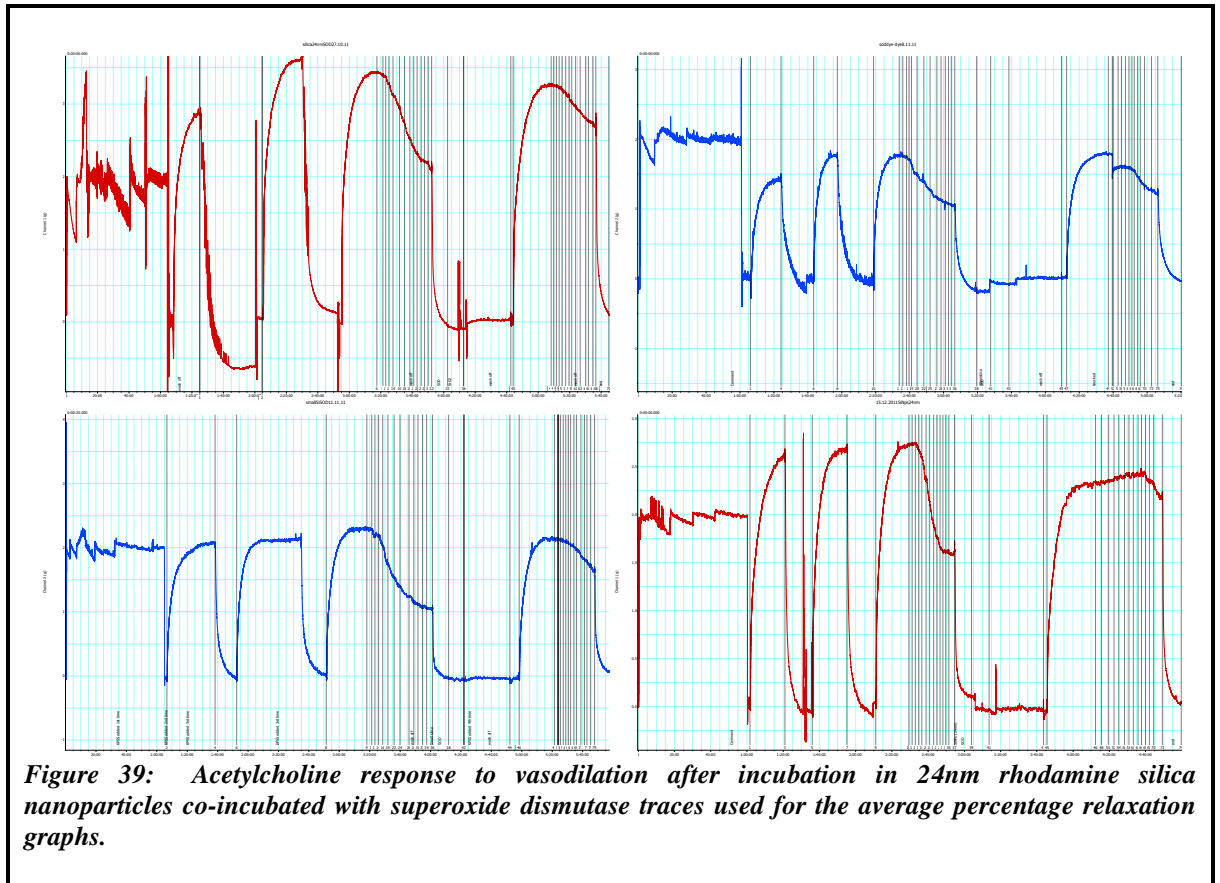
**Figure 35: Acetylcholine response to vasodilation after incubation in 72 nm silica nanoparticles high dose traces used for the average percentage relaxation graphs.**

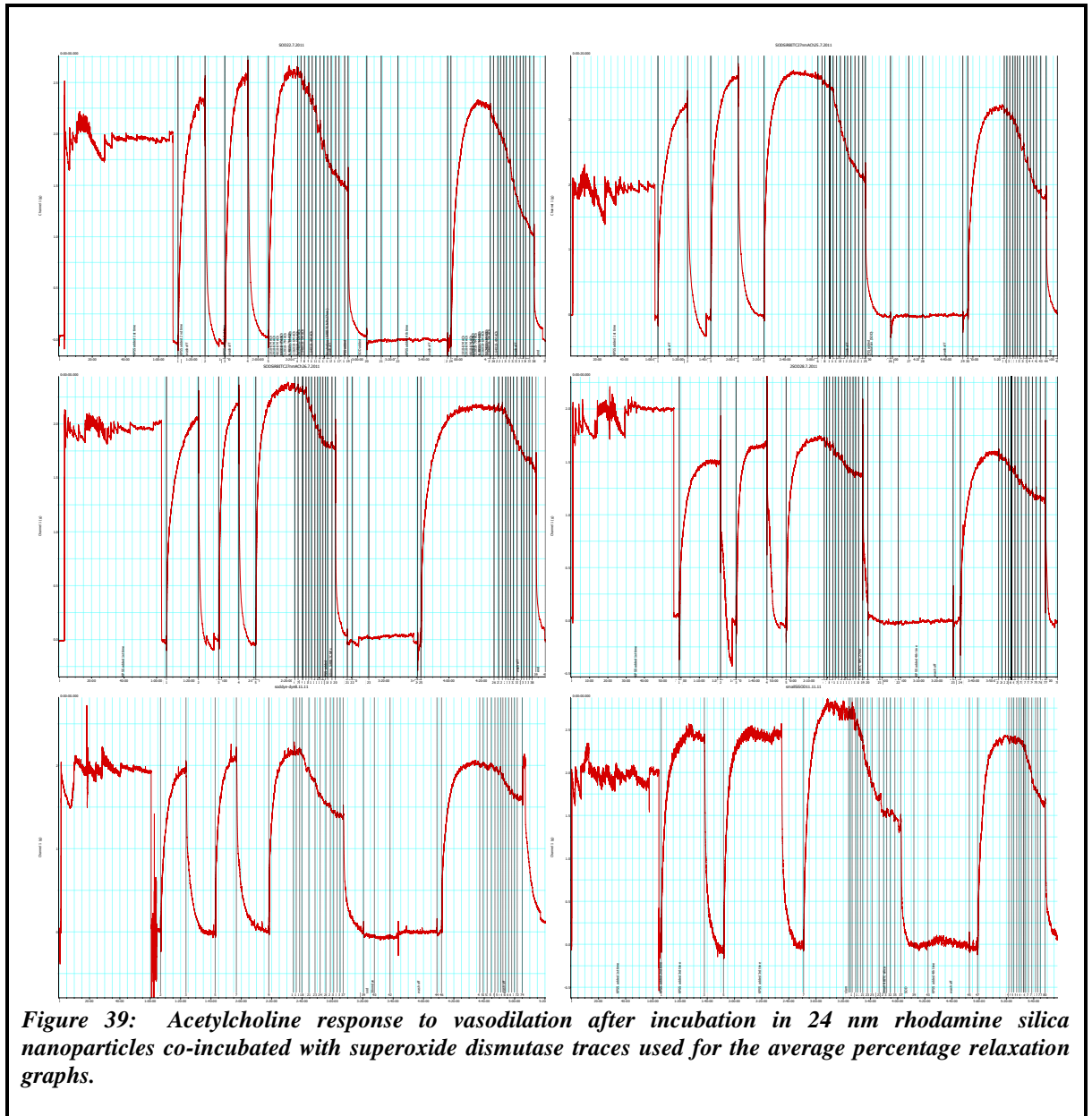


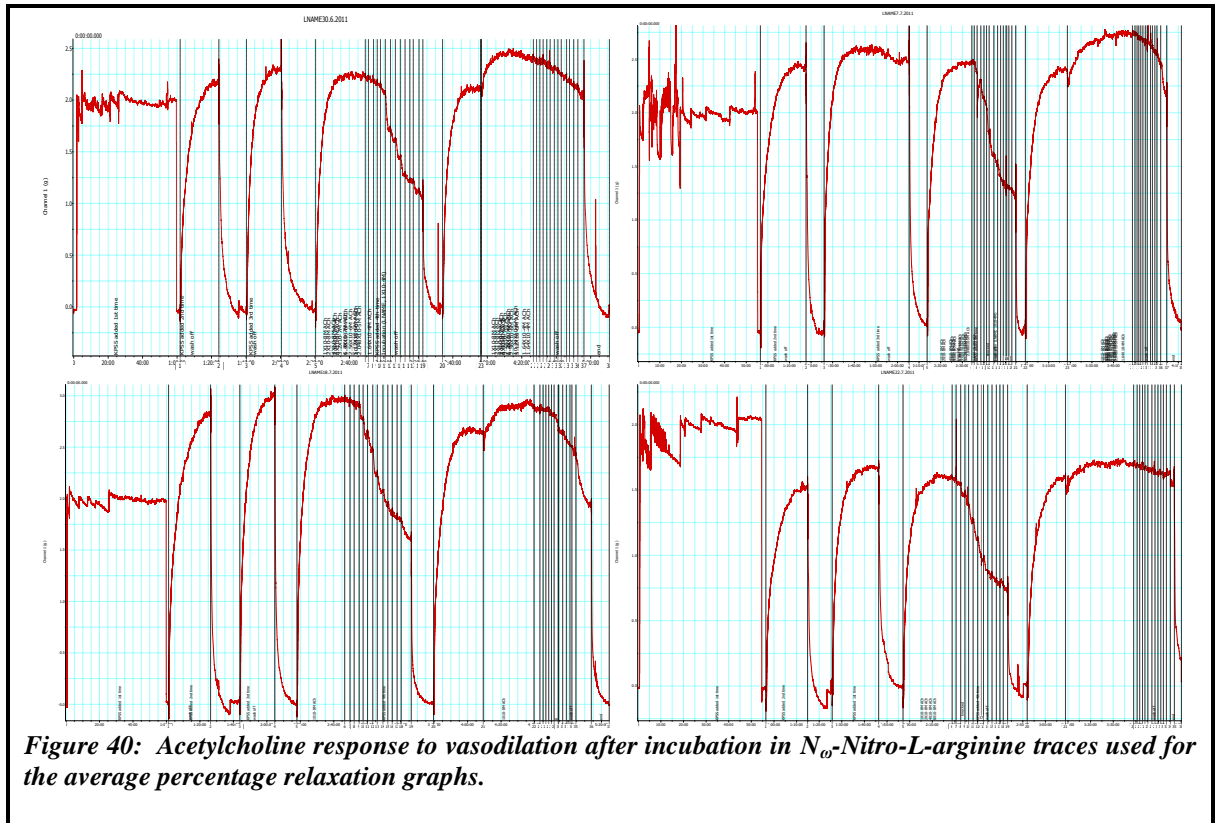
**Figure 36: Acetylcholine response to vasodilation after incubation in 24 nm silica nanoparticles traces used for the average percentage relaxation graphs.**



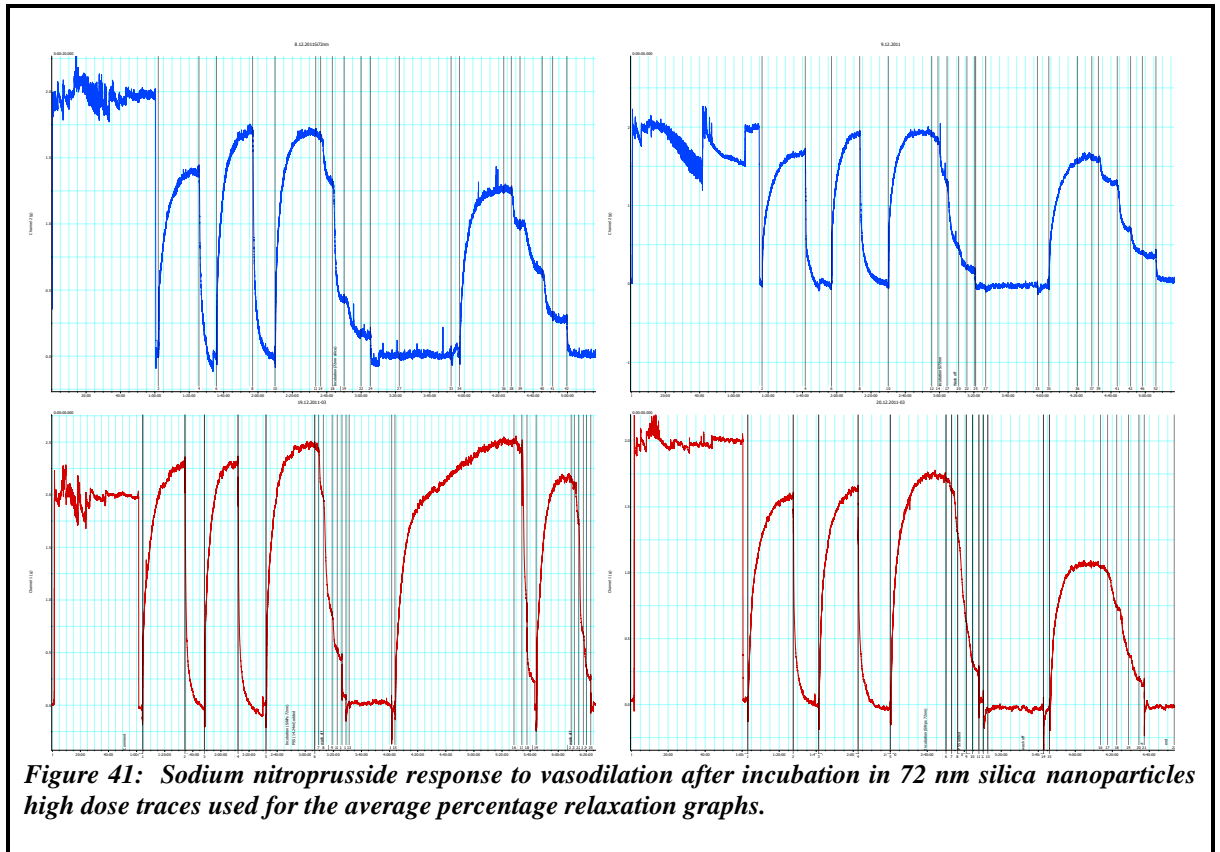


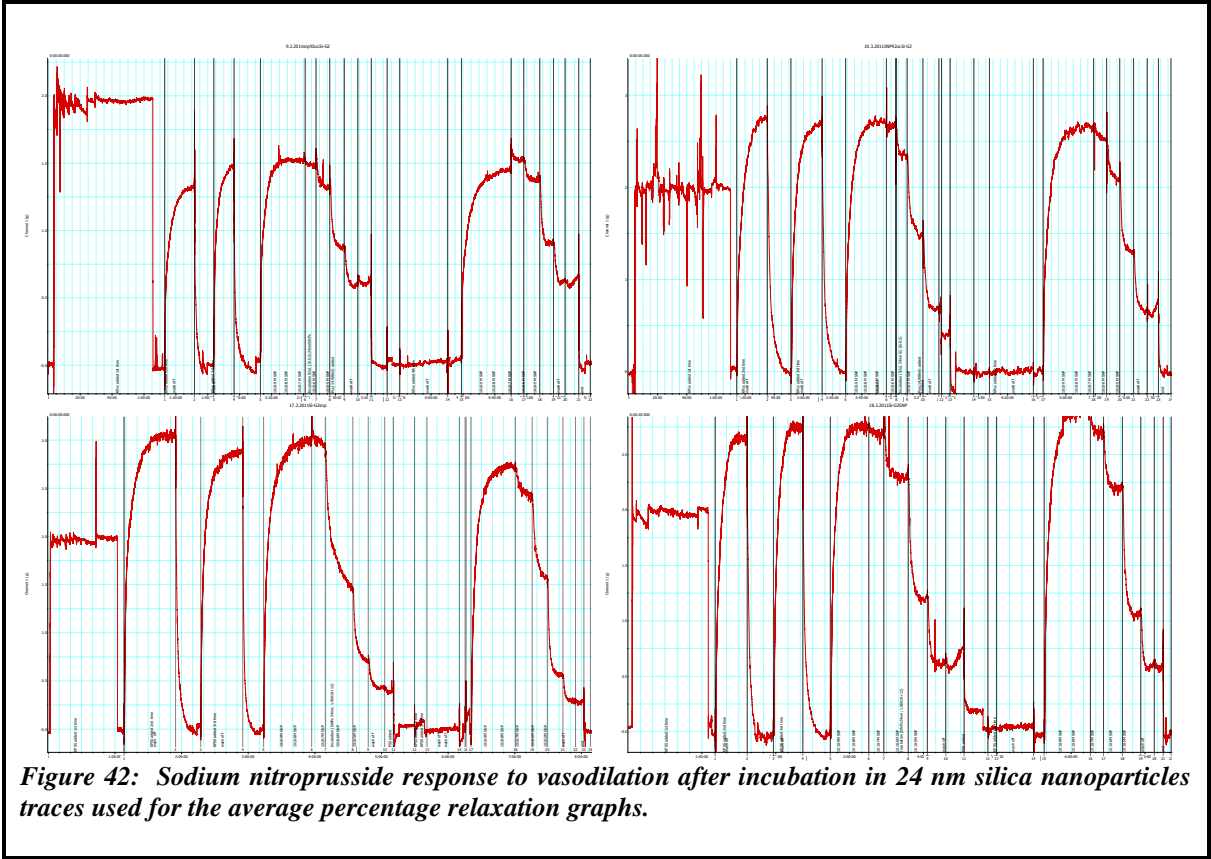




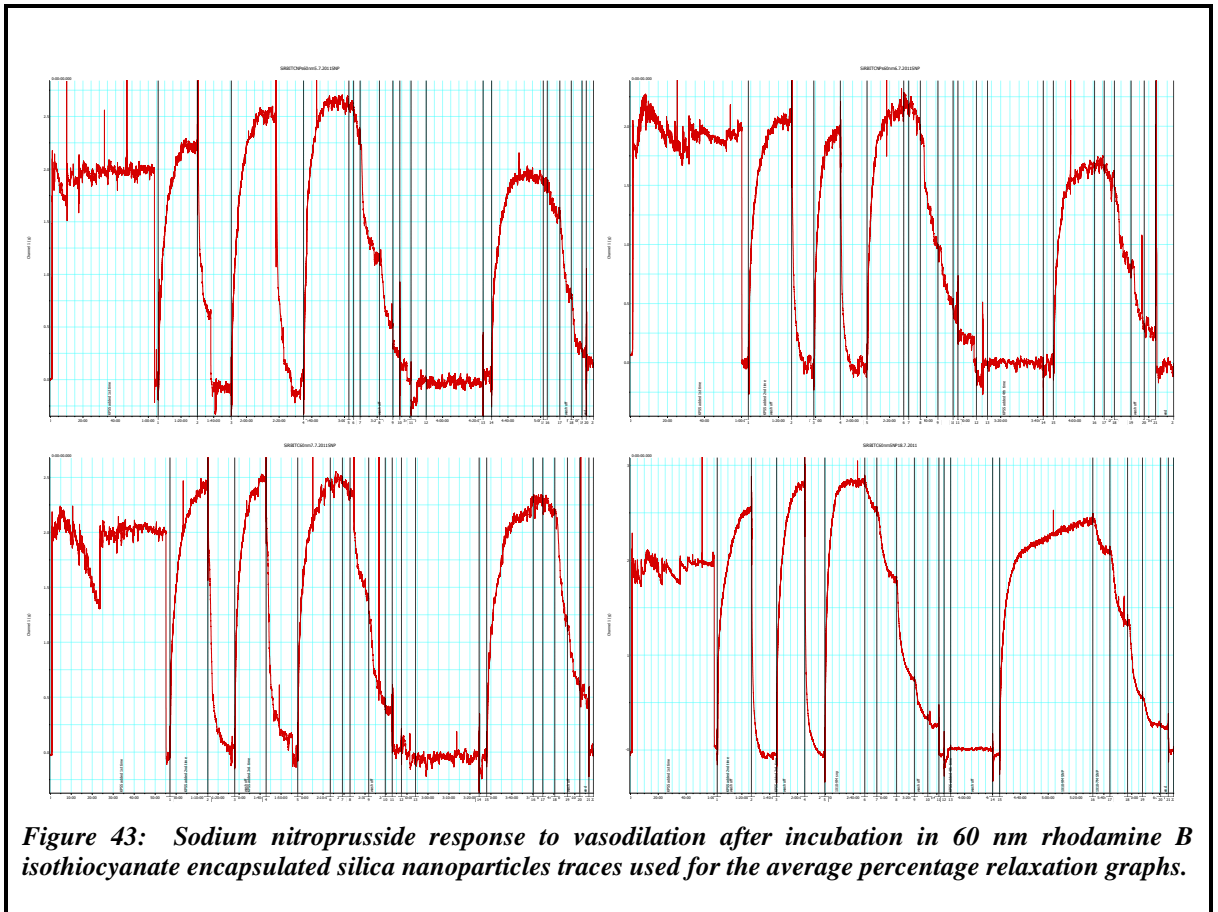


**Figure 40: Acetylcholine response to vasodilation after incubation in  $N_{\omega}$ -Nitro-L-arginine traces used for the average percentage relaxation graphs.**

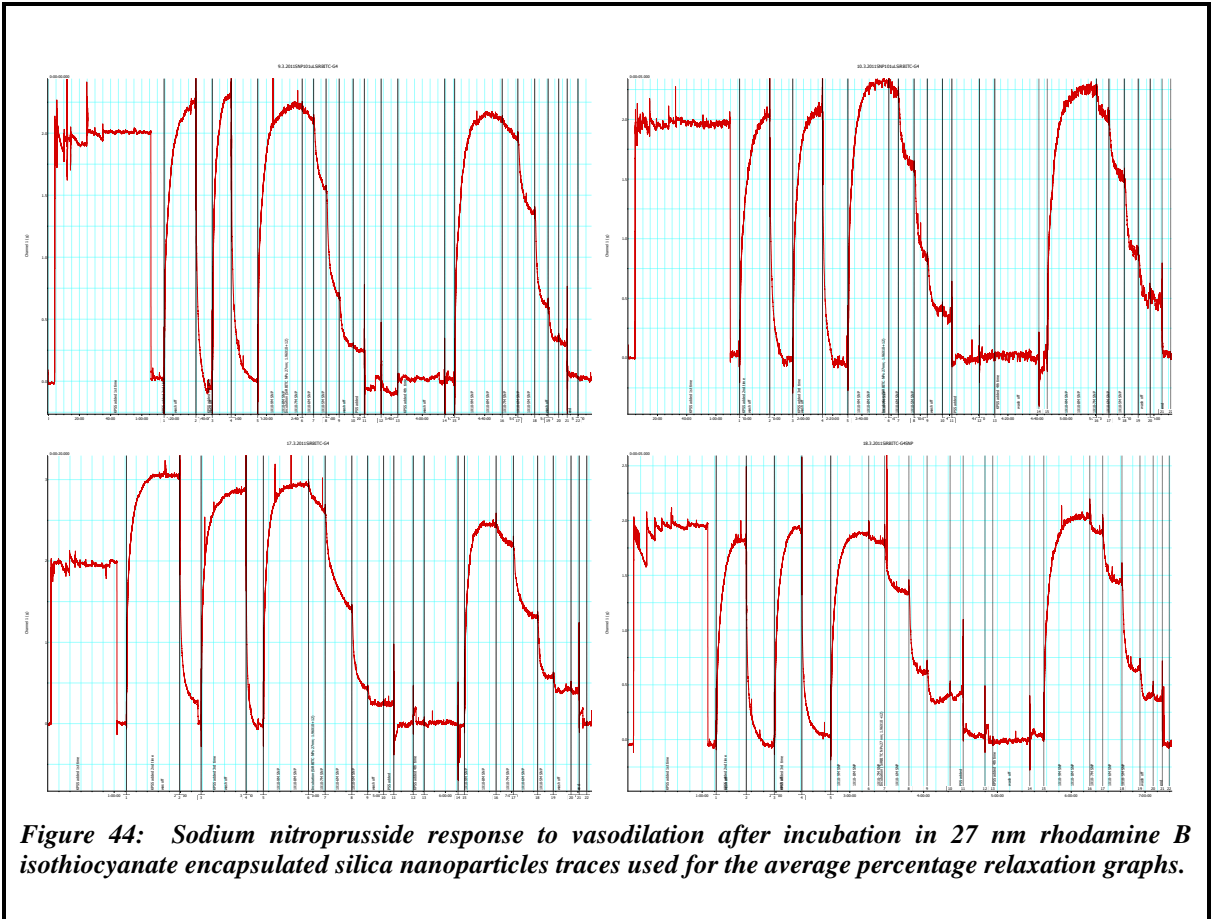




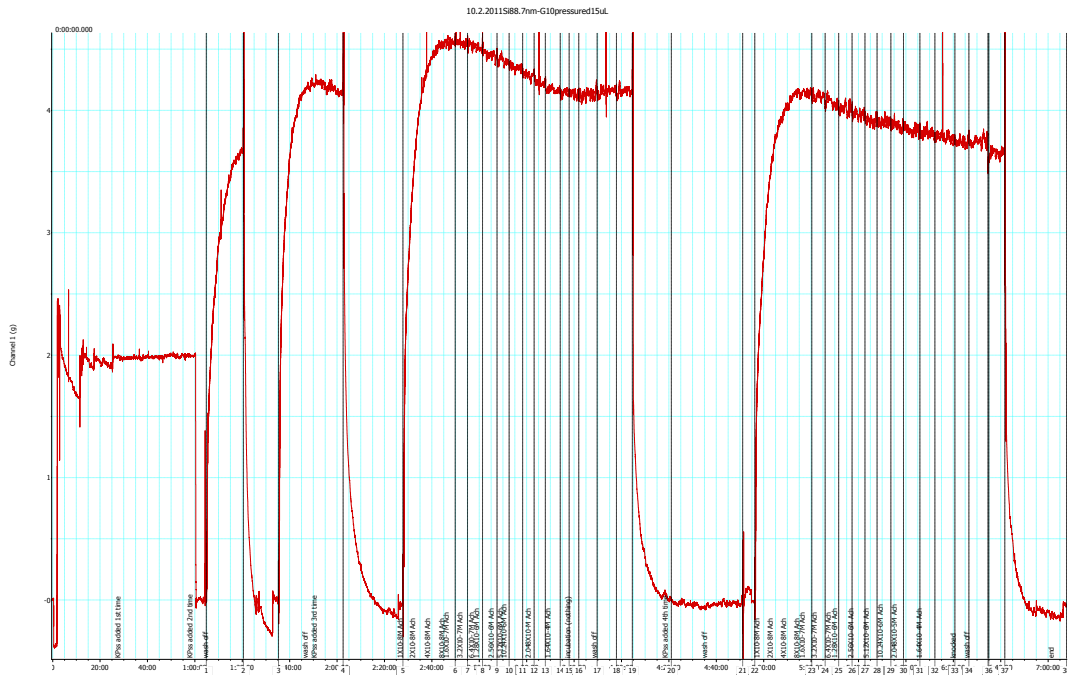
**Figure 42: Sodium nitroprusside response to vasodilation after incubation in 24 nm silica nanoparticles traces used for the average percentage relaxation graphs.**



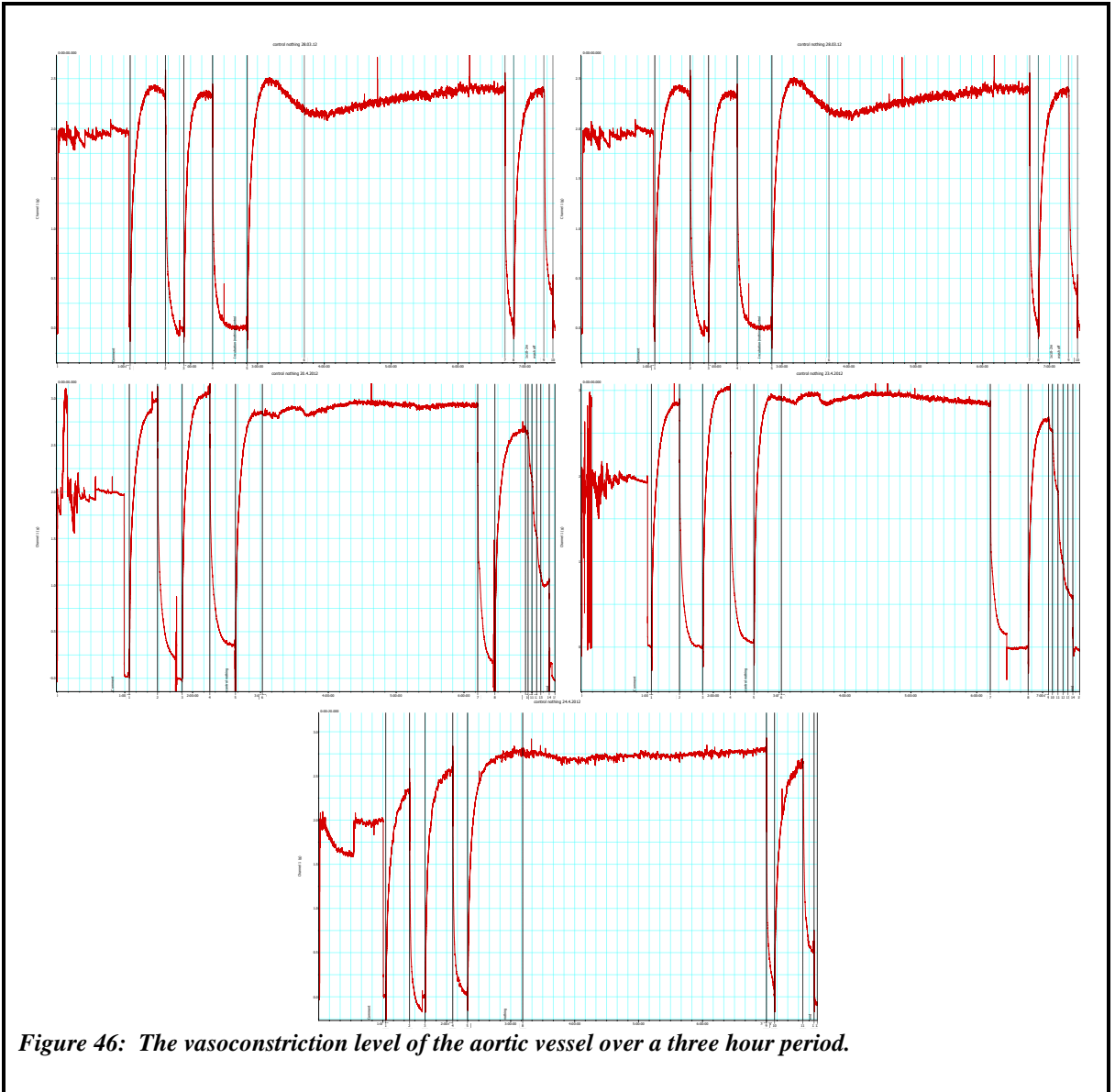
**Figure 43:** Sodium nitroprusside response to vasodilation after incubation in 60 nm rhodamine B isothiocyanate encapsulated silica nanoparticles traces used for the average percentage relaxation graphs.



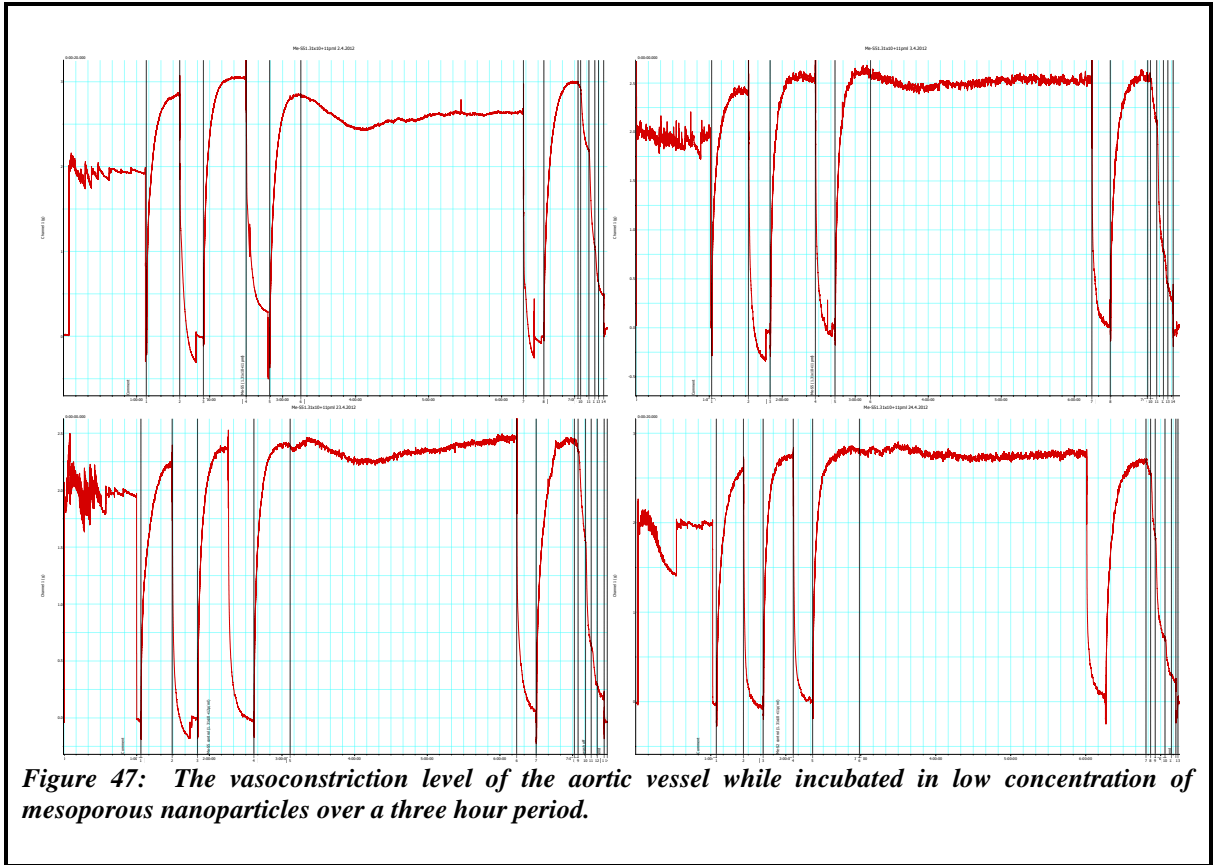
**Figure 44:** Sodium nitroprusside response to vasodilation after incubation in 27 nm rhodamine B isothiocyanate encapsulated silica nanoparticles traces used for the average percentage relaxation graphs.

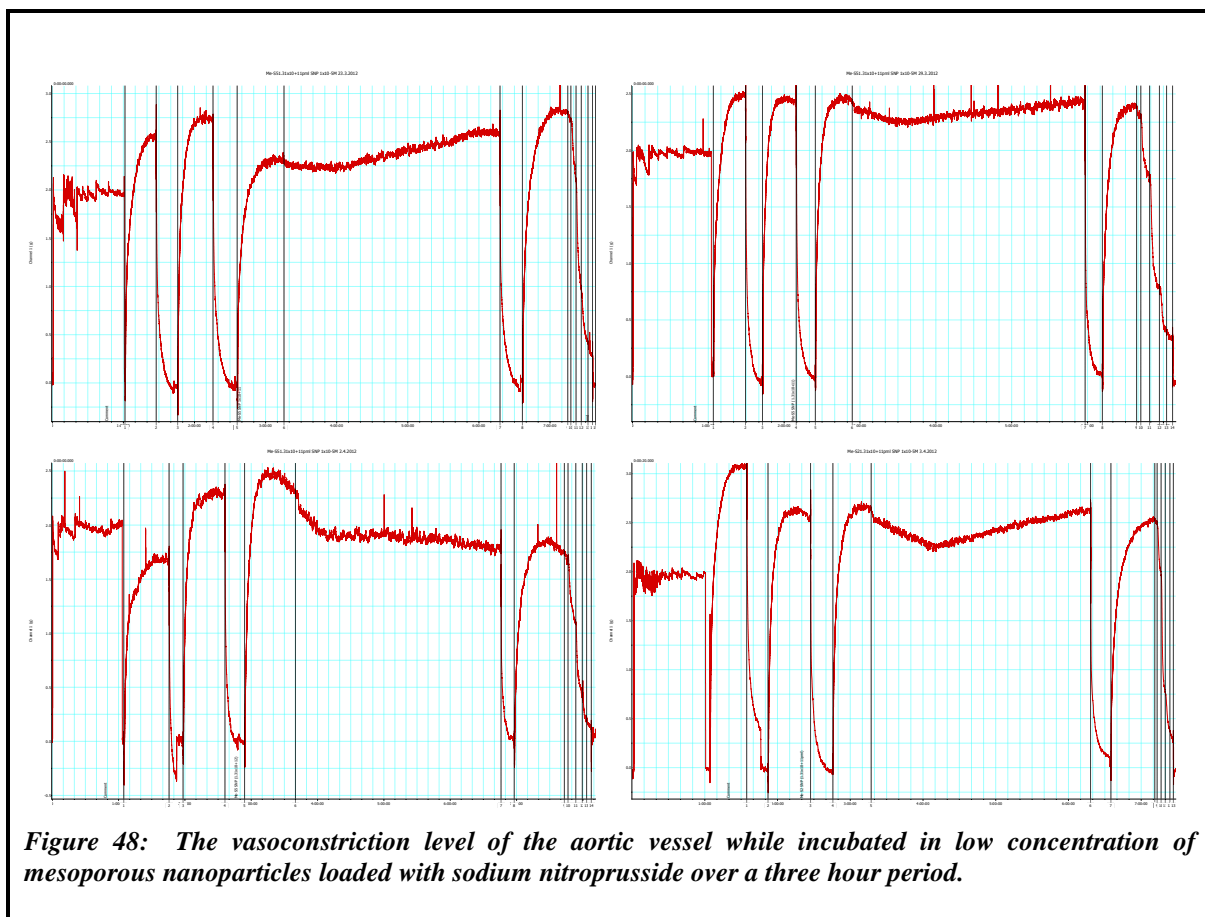


**Figure 45: Acetylcholine response to vasodilation after incubation in  $71 \pm 6$  nm silica nanoparticles under pressurised system traces used for the average percentage relaxation graphs.**

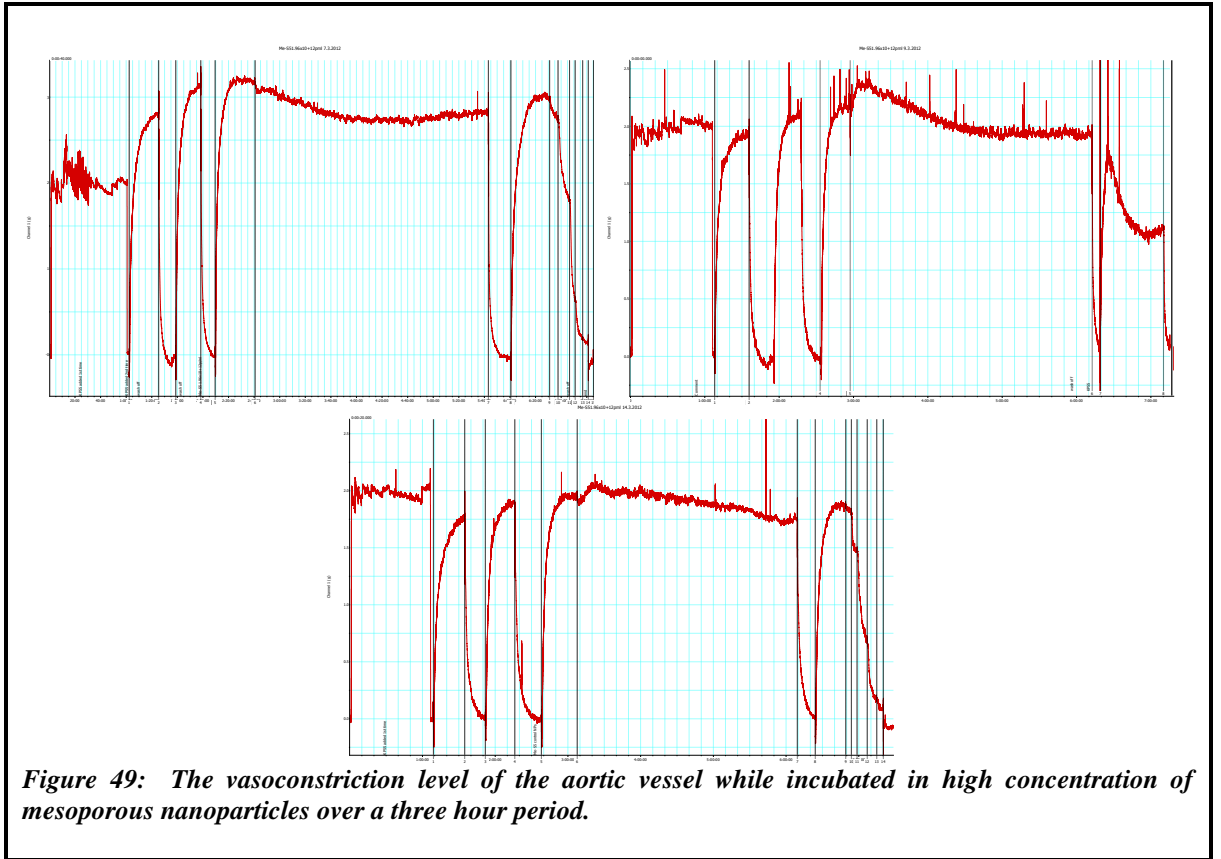


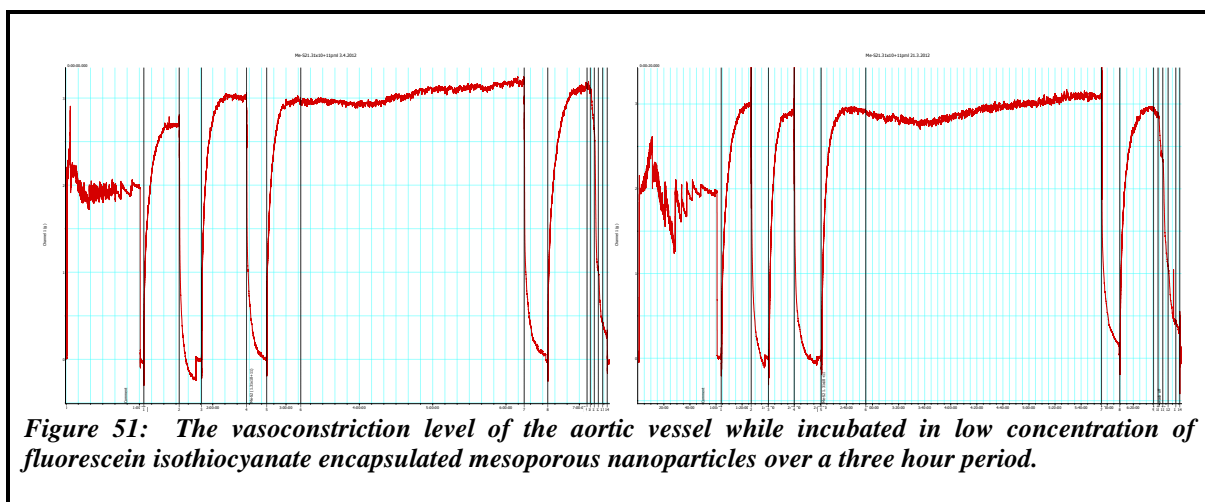
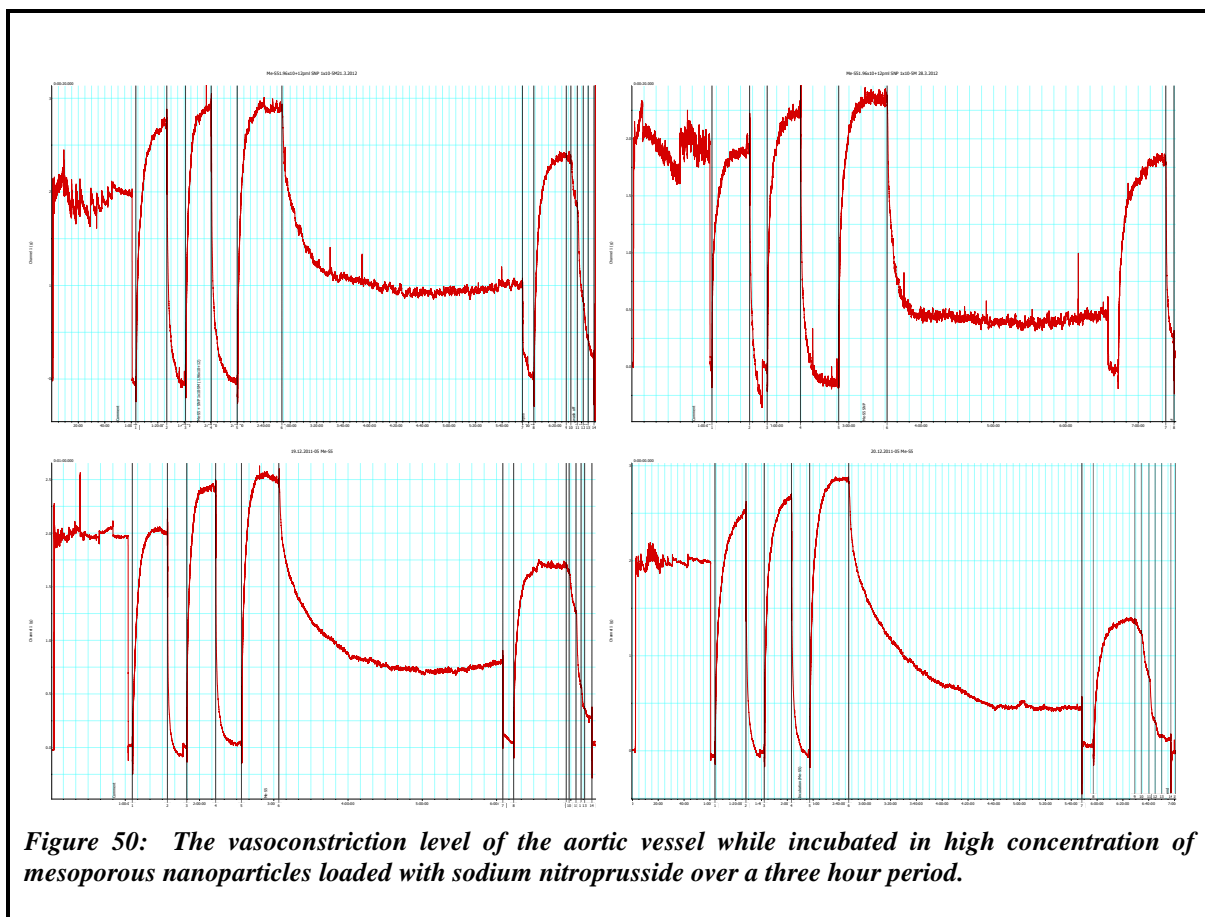
*Figure 46: The vasoconstriction level of the aortic vessel over a three hour period.*

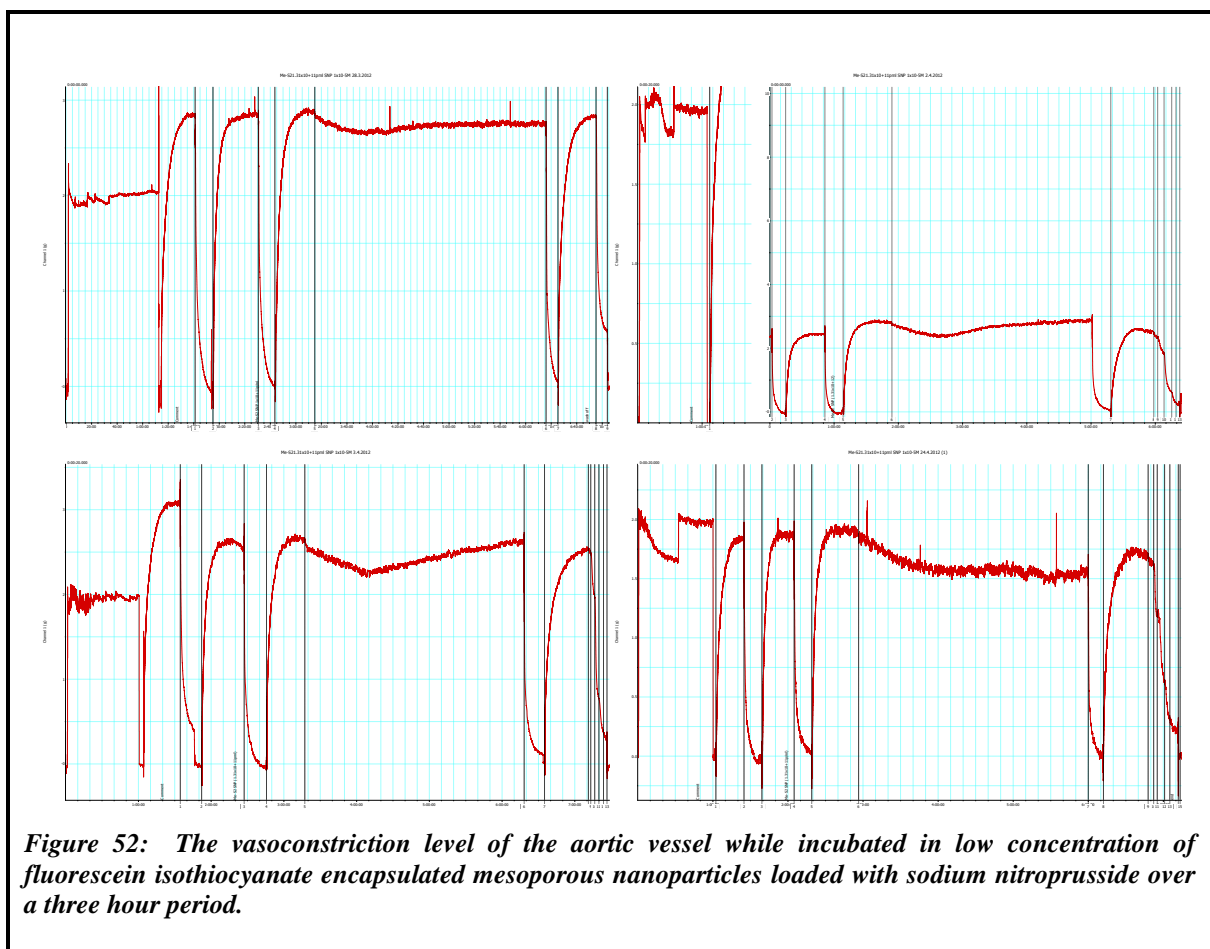




**Figure 48:** *The vasoconstriction level of the aortic vessel while incubated in low concentration of mesoporous nanoparticles loaded with sodium nitroprusside over a three hour period.*







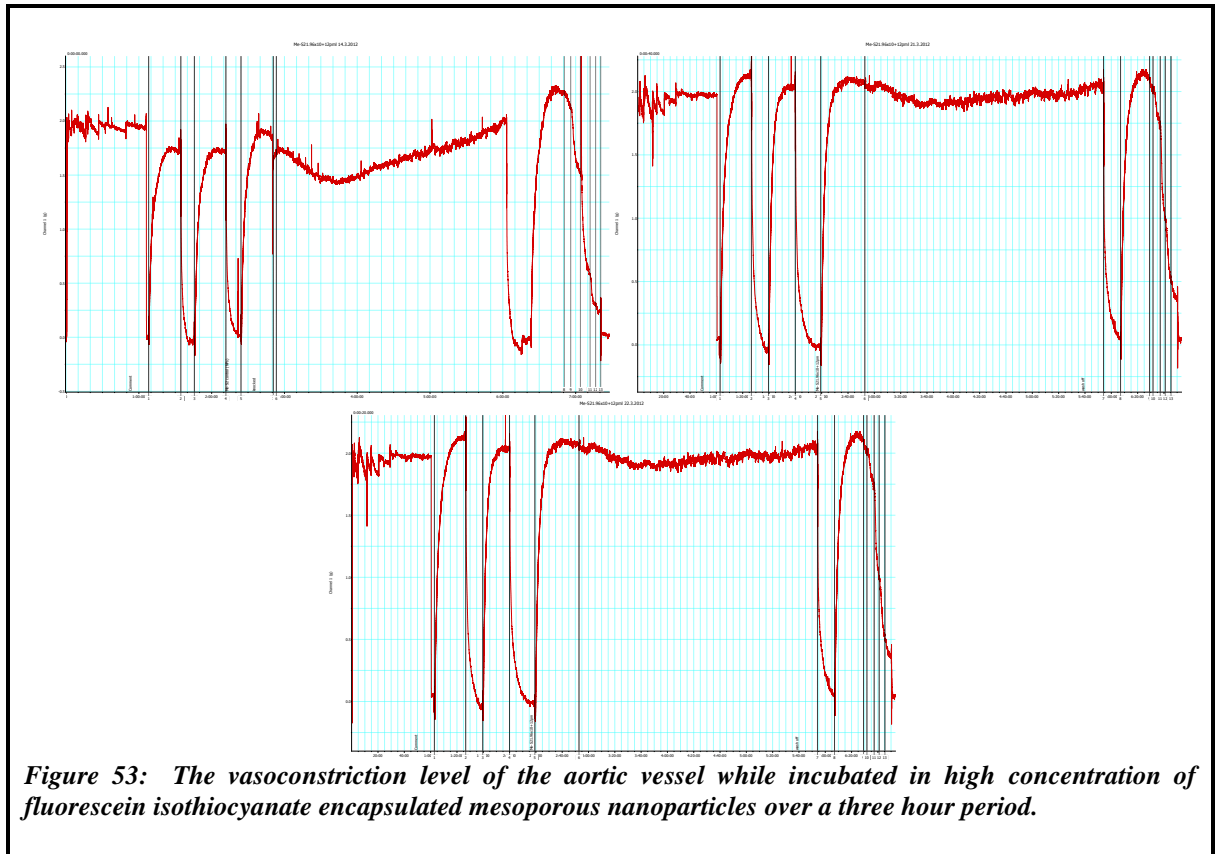


**Figure 53:** *The vasoconstriction level of the aortic vessel while incubated in high concentration of fluorescein isothiocyanate encapsulated mesoporous nanoparticles over a three hour period.*

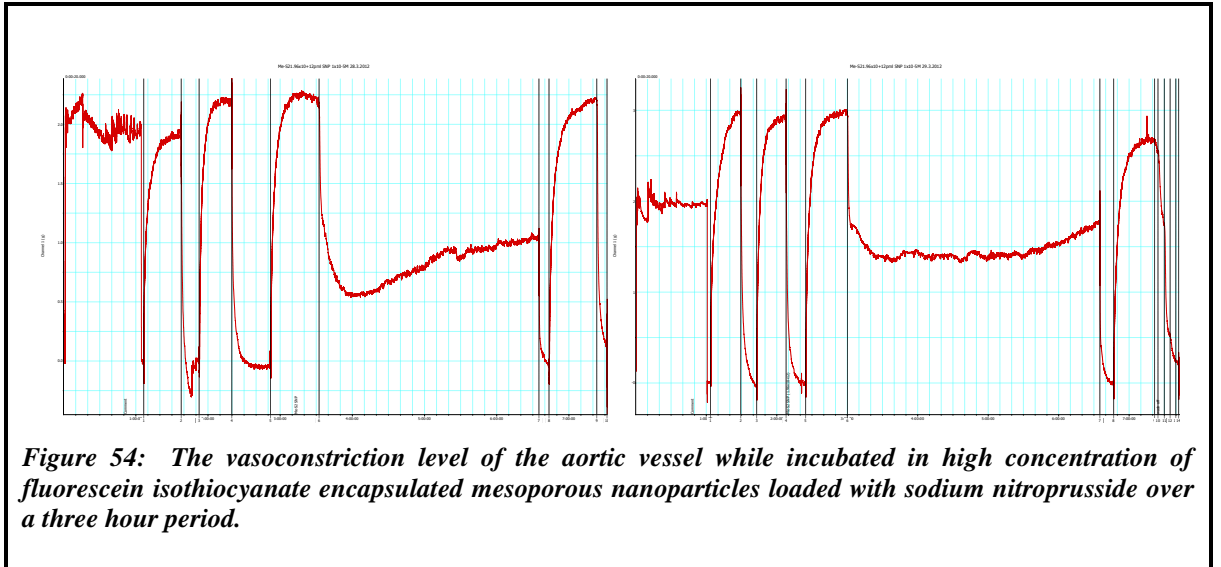


**Figure 54:** *The vasoconstriction level of the aortic vessel while incubated in high concentration of fluorescein isothiocyanate encapsulated mesoporous nanoparticles loaded with sodium nitroprusside over a three hour period.*

**Table 1: The concentration of SNP released from the MNP matrix *in vitro*, calculated from the logarithmic equation derived from the SNP control relaxation calibration graph.**

Time (min)	Concentration of SNP releases from the MNP <i>in vitro</i>	Concentration of SNP releases from the FITC MNP <i>in vitro</i>
1	$8.82 \times 10^{-10}$	$6.09 \times 10^{-9}$
2	$3.25 \times 10^{-9}$	$1.71 \times 10^{-8}$
3	$5.08 \times 10^{-9}$	$2.32 \times 10^{-8}$
4	$7.62 \times 10^{-9}$	$2.50 \times 10^{-8}$
5	$1.00 \times 10^{-8}$	$3.14 \times 10^{-8}$
6	$1.52 \times 10^{-8}$	$3.42 \times 10^{-8}$
7	$1.75 \times 10^{-8}$	$4.02 \times 10^{-8}$
8	$2.19 \times 10^{-8}$	$5.28 \times 10^{-8}$
9	$2.57 \times 10^{-8}$	$5.56 \times 10^{-8}$
10	$3.17 \times 10^{-8}$	$6.13 \times 10^{-8}$
15	$5.84 \times 10^{-8}$	$1.12 \times 10^{-7}$
20	$8.97 \times 10^{-8}$	$1.38 \times 10^{-7}$
25	$1.23 \times 10^{-7}$	$1.72 \times 10^{-7}$
30	$1.52 \times 10^{-7}$	$1.73 \times 10^{-7}$
35	$1.77 \times 10^{-7}$	$1.74 \times 10^{-7}$
40	$2.19 \times 10^{-7}$	$1.74 \times 10^{-7}$
45	$2.33 \times 10^{-7}$	$1.62 \times 10^{-7}$
50	$2.76 \times 10^{-7}$	$1.47 \times 10^{-7}$
55	$3.05 \times 10^{-7}$	$1.23 \times 10^{-7}$
60	$3.60 \times 10^{-7}$	$1.23 \times 10^{-7}$
65	$3.76 \times 10^{-7}$	$1.17 \times 10^{-7}$
70	$4.04 \times 10^{-7}$	$1.16 \times 10^{-7}$
75	$4.62 \times 10^{-7}$	$1.19 \times 10^{-7}$
80	$4.44 \times 10^{-7}$	$1.07 \times 10^{-7}$
85	$5.21 \times 10^{-7}$	$1.05 \times 10^{-7}$
90	$5.63 \times 10^{-7}$	$1.08 \times 10^{-7}$
95	$5.50 \times 10^{-7}$	$8.35 \times 10^{-8}$
100	$5.67 \times 10^{-7}$	$7.59 \times 10^{-8}$
105	$6.22 \times 10^{-7}$	$6.94 \times 10^{-8}$
110	$6.20 \times 10^{-7}$	$7.27 \times 10^{-8}$
115	$6.52 \times 10^{-7}$	$9.48 \times 10^{-8}$
120	$6.16 \times 10^{-7}$	$8.60 \times 10^{-8}$
125	$6.62 \times 10^{-7}$	$7.36 \times 10^{-8}$
130	$6.53 \times 10^{-7}$	$7.19 \times 10^{-8}$
135	$6.01 \times 10^{-7}$	$6.63 \times 10^{-8}$
140	$6.21 \times 10^{-7}$	$6.67 \times 10^{-8}$
145	$6.13 \times 10^{-7}$	$7.23 \times 10^{-8}$
150	$5.55 \times 10^{-7}$	$5.74 \times 10^{-8}$
155	$6.15 \times 10^{-7}$	$5.54 \times 10^{-8}$

160	$5.97 \times 10^{-7}$	$5.27 \times 10^{-8}$
165	$5.28 \times 10^{-7}$	$4.86 \times 10^{-8}$
170	$5.42 \times 10^{-7}$	$4.86 \times 10^{-8}$
175	$5.09 \times 10^{-7}$	$4.64 \times 10^{-8}$
180	$4.91 \times 10^{-7}$	$4.51 \times 10^{-8}$

**Table 2: One-way Anova with Bonferroni correction for relaxation of aortic vessels due to incubation in MNP and MNP loaded.**

Time (min)	Significance difference in relaxation in comparison to KPSS control							
	low MNP	low MNP+ SNP	high MNP	high MNP+ SNP	low FITC MNP	low FITC MNP+SNP	High FITC MNP	high FITC MNP+SNP
1	p>0.05	p>0.05	p>0.05	#	p>0.05	p>0.05	p>0.05	§
2	p>0.05	p>0.05	p>0.05	§	p>0.05	p>0.05	p>0.05	§
3	p>0.05	p>0.05	p>0.05	§	p>0.05	p>0.05	p>0.05	§
4	p>0.05	p>0.05	p>0.05	§	p>0.05	p>0.05	p>0.05	§
5	p>0.05	p>0.05	p>0.05	§	p>0.05	p>0.05	p>0.05	§
6	p>0.05	p>0.05	p>0.05	§	p>0.05	p>0.05	p>0.05	§
7	p>0.05	p>0.05	p>0.05	§	p>0.05	p>0.05	p>0.05	§
8	p>0.05	p>0.05	p>0.05	§	p>0.05	p>0.05	p>0.05	§
9	p>0.05	p>0.05	p>0.05	§	p>0.05	p>0.05	p>0.05	§
10	p>0.05	p>0.05	p>0.05	§	p>0.05	p>0.05	p>0.05	§
15	p>0.05	p>0.05	p>0.05	§	p>0.05	p>0.05	p>0.05	§
20	p>0.05	p>0.05	p>0.05	§	p>0.05	p>0.05	p>0.05	§
25	p>0.05	p>0.05	p>0.05	§	p>0.05	p>0.05	p>0.05	§
30	p>0.05	p>0.05	p>0.05	§	p>0.05	p>0.05	p>0.05	§
35	p>0.05	p>0.05	p>0.05	§	p>0.05	p>0.05	p>0.05	§
40	p>0.05	p>0.05	p>0.05	§	p>0.05	p>0.05	p>0.05	§
45	p>0.05	p>0.05	p>0.05	§	p>0.05	p>0.05	p>0.05	§

50	p>0.05	p>0.05	p>0.05	§	p>0.05	p>0.05	p>0.05	§
55	p>0.05	p>0.05	p>0.05	§	p>0.05	*	p>0.05	§
60	p>0.05	p>0.05	p>0.05	§	p>0.05	*	*	§
65	p>0.05	p>0.05	p>0.05	§	p>0.05	*	*	§
70	p>0.05	p>0.05	p>0.05	§	p>0.05	*	*	§
75	p>0.05	p>0.05	p>0.05	§	p>0.05	*	*	§
80	p>0.05	p>0.05	p>0.05	§	p>0.05	*	*	§
85	p>0.05	p>0.05	p>0.05	§	p>0.05	*	*	§
90	p>0.05	p>0.05	p>0.05	§	p>0.05	*	*	§
95	p>0.05	p>0.05	p>0.05	§	p>0.05	*	p>0.05	§
100	p>0.05	p>0.05	p>0.05	§	p>0.05	*	p>0.05	§
105	p>0.05	p>0.05	p>0.05	§	p>0.05	*	p>0.05	§
110	p>0.05	p>0.05	p>0.05	§	p>0.05	*	p>0.05	§
115	p>0.05	p>0.05	p>0.05	§	p>0.05	p>0.05	p>0.05	§
120	p>0.05	p>0.05	p>0.05	§	p>0.05	p>0.05	p>0.05	§
125	p>0.05	p>0.05	p>0.05	§	p>0.05	p>0.05	p>0.05	§
130	p>0.05	p>0.05	p>0.05	§	p>0.05	p>0.05	p>0.05	§
135	p>0.05	p>0.05	p>0.05	§	p>0.05	p>0.05	p>0.05	§
140	p>0.05	p>0.05	p>0.05	§	p>0.05	p>0.05	p>0.05	§
145	p>0.05	p>0.05	p>0.05	§	p>0.05	p>0.05	p>0.05	§
150	p>0.05	p>0.05	p>0.05	§	p>0.05	p>0.05	p>0.05	§
155	p>0.05	p>0.05	p>0.05	§	p>0.05	p>0.05	p>0.05	§
160	p>0.05	p>0.05	p>0.05	§	p>0.05	p>0.05	p>0.05	§
165	p>0.05	p>0.05	p>0.05	§	p>0.05	p>0.05	p>0.05	§
170	p>0.05	p>0.05	p>0.05	§	p>0.05	p>0.05	p>0.05	§

175	p>0.05	p>0.05	p>0.05	<b>§</b>	p>0.05	p>0.05	p>0.05	<b>§</b>
180	p>0.05	p>0.05	p>0.05	<b>§</b>	p>0.05	p>0.05	p>0.05	<b>§</b>

$$V = \frac{4}{3}\pi r^3 \quad [1]$$

*Equation 3.1: This equation is used to calculate the volume of a sphere*

In equation 3.1  $v$  is the volume of sphere  $\pi$  is 3.14 and  $r$  is the radius of the nanoparticles in cm. This is used to derive the number of particles per mL.

$$m = V \times D \quad [2]$$

*Equation 3.2: This equation is used to work out mass of a nanoparticles sphere*

$M$  is mass of a nanoparticles sphere,  $v$  is volume of a sphere and  $d$  is the density of a given material the nanoparticles is made of.

$$N = \frac{m}{v} \quad [3]$$

*Equation 3.3: This equation is used to obtain the number of particles within a given solution*

$V$  is the volume of a sphere at a given diameter,  $m$  is the mass of dry nanoparticle product in 1 mL.